

INFORMATION TO USERS

This manuscript has been reproduced from the microfilm master. UMI films the text directly from the original or copy submitted. Thus, some thesis and dissertation copies are in typewriter face, while others may be from any type of computer printer.

The quality of this reproduction is dependent upon the quality of the copy submitted. Broken or indistinct print, colored or poor quality illustrations and photographs, print bleedthrough, substandard margins, and improper alignment can adversely affect reproduction.

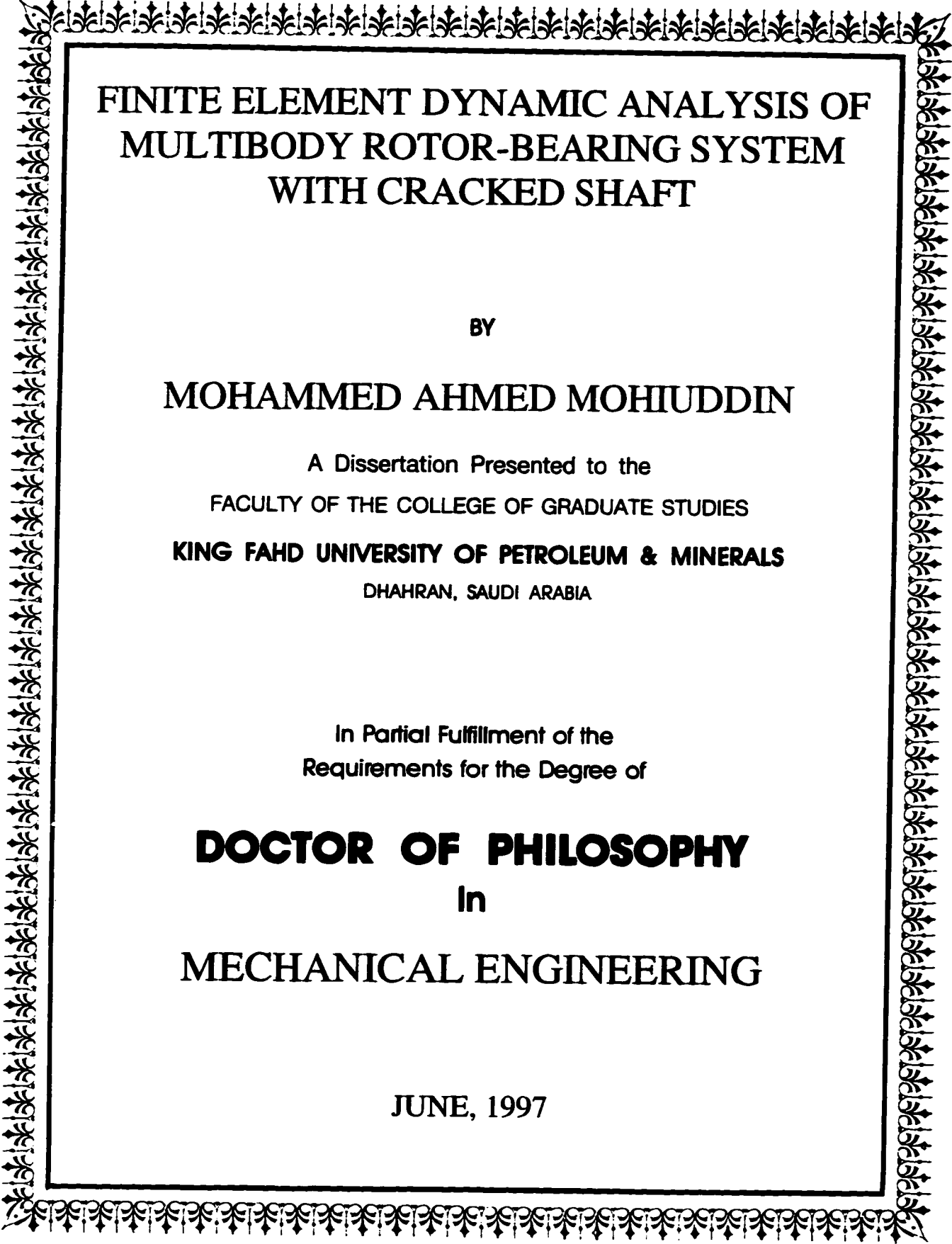
In the unlikely event that the author did not send UMI a complete manuscript and there are missing pages, these will be noted. Also, if unauthorized copyright material had to be removed, a note will indicate the deletion.

Oversize materials (e.g., maps, drawings, charts) are reproduced by sectioning the original, beginning at the upper left-hand corner and continuing from left to right in equal sections with small overlaps. Each original is also photographed in one exposure and is included in reduced form at the back of the book.

Photographs included in the original manuscript have been reproduced xerographically in this copy. Higher quality 6" x 9" black and white photographic prints are available for any photographs or illustrations appearing in this copy for an additional charge. Contact UMI directly to order.

UMI

**A Bell & Howell Information Company
300 North Zeeb Road, Ann Arbor MI 48106-1346 USA
313/761-4700 800/521-0600**



**FINITE ELEMENT DYNAMIC ANALYSIS OF
MULTIBODY ROTOR-BEARING SYSTEM
WITH CRACKED SHAFT**

BY

MOHAMMED AHMED MOHIUDDIN

A Dissertation Presented to the
FACULTY OF THE COLLEGE OF GRADUATE STUDIES
KING FAHD UNIVERSITY OF PETROLEUM & MINERALS
DHAHRAN, SAUDI ARABIA

In Partial Fulfillment of the
Requirements for the Degree of

DOCTOR OF PHILOSOPHY
In
MECHANICAL ENGINEERING

JUNE, 1997

UMI Number: 9806410

UMI Microform 9806410
Copyright 1997, by UMI Company. All rights reserved.

**This microform edition is protected against unauthorized
copying under Title 17, United States Code.**

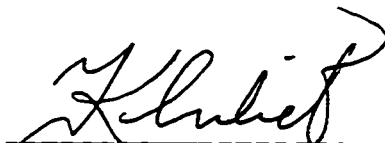
UMI
300 North Zeeb Road
Ann Arbor, MI 48103

KING FAHD UNIVERSITY OF PETROLEUM AND MINERALS
DHAHRAN 31261, SAUDI ARABIA

COLLEGE OF GRADUATE STUDIES

This dissertation, written by MOHAMMED AHMED MOHIUDDIN under the direction of his Dissertation Advisor and approved by his Dissertation Committee, has been presented to and accepted by the Dean of the College of Graduate Studies, in partial fulfillment of the requirements for the degree of DOCTOR OF PHILOSOPHY

Dissertation Committee



Dissertation Advisor: Dr. Yehia A. Khulief



Member: Dr. Abdullah A. Almusallam

 June 23, 97

Member: Dr. Kamal A. F. Moustafa

 25-6-97
Member: Dr. Mohamed El-Gebeily

Department Chairman


Dean, College of Graduate Studies

Date 28-6-97



This dissertation is dedicated to *MYMOTHER*

ACKNOWLEDGMENT

First and foremost, Praise and Thanks be to Almighty Allah, the Most Gracious, the Most Merciful and Peace be upon His Prophet.

Acknowledgment is due to King Fahd University of Petroleum and Minerals for extending all facilities and providing financial support.

I wish to express my sincere appreciation and indebtedness to my dissertation advisor Dr. Yehia A. Khulief. He has been a tremendous source of encouragement and help during my stay at KFUPM. I thank him for inculcating in me professionalism and discipline. He has imbibed in me many virtues which I find useful in life. I also greatly appreciate the invaluable cooperation and support extended by my dissertation committee members: Dr. Abdullah A. Almusallam, Dr. Kamal A. F. Moustafa and Dr. Mohamed El-Gebeily. I thank them for their critical reviews and constructive suggestions. Sincere thanks are due to the department chairman Dr. Mohammad O. Budair for immeasurable cooperation.

I wish to express my gratitude to my parents who motivated and guided me through out my career. My mother did not live to witness this day. May Allah reward her. Special thanks to my wife for her cooperation when I spent long hours working on my dissertation. My brother and sisters deserve my appreciation for their motivation and comraderie.

Finally I thank all my colleagues who have made my stay at KFUPM a memorable one. I have forged many new friendships and cemented few old ones, which I am sure will last life long.

Contents

List of Tables	ix
List of Figures	xi
Abstract (English)	xvii
Abstract (Arabic)	xviii
1 Introduction	1
1.1 Literature Survey	2
1.1.1 Cracked Non-Rotating Beams	2
1.1.2 Cracked Rotating Beams	5
1.1.3 Cracked Rotating Shafts	6
1.2 Proposed Research	10
1.2.1 Derivation of Equation of Motion	11
1.2.2 The Finite Element Discretization	11
1.2.3 Reduced-Order System	13

1.2.4	Time-Response (Numerical Integration)	13
2	The Crack Model	15
2.1	The Energy Release Rate	16
2.2	Relationship Between K and G	17
2.3	Local Flexibility of a Cracked Shaft	20
3	The Multibody Elastodynamic Model	25
3.1	Introduction	25
3.2	The Multibody System	26
3.2.1	Kinetic Energy Expression	29
3.2.2	Strain Energy Expression	32
3.2.3	The Generalized Forces	34
3.2.4	Equation of Motion	35
3.3	The Rotor-Bearing System	36
3.3.1	General Assumptions	37
3.3.2	Kinetic Energy Expression of the Shaft	37
3.3.3	The Strain Energy Expression of the Shaft	44
3.3.4	The Disk	46
3.3.5	The Bearings	47
3.3.6	Equation of Motion of the Rotor-Bearing System	48
4	Finite Element Formulation of Cracked Shaft	50

4.1	Tapered Cracked Shaft Element	51
4.1.1	Cross-Sectional Properties	51
4.1.2	Derivation of Shape Functions	55
4.2	Element Matrices	70
4.2.1	Inertia Matrices	70
4.2.2	Stiffness Matrices	72
5	Modal Reduction	102
5.1	Eigenvalue Problem	103
5.1.1	Equations in the Rotating Reference Frame	104
5.1.2	Equations in the Inertial Reference Frame	110
5.2	Modal Reduction Schemes	112
5.2.1	Planar Modal Reduction	114
5.2.2	Complex Modal Transformation	115
5.2.3	Extended Modal Reduction	117
6	Results and Discussions	122
6.1	The Computer Scheme	122
6.1.1	Input Data	123
6.1.2	System Matrices	126
6.1.3	Eigenvalue Solution	127
6.1.4	Modal Reduction Schemes	127

6.1.5	Numerical Integration	130
6.2	Modal Characteristics	132
6.2.1	Natural Frequencies	132
6.2.2	Reduction Schemes	151
6.3	Time Response	152
6.3.1	Comparison with ANSYS	159
6.3.2	Non-Rotating Uniform Shaft	161
6.3.3	Non-Rotating Tapered Shaft	173
6.3.4	Rotating Tapered Shaft	189
6.3.5	Rotating Multi-Stepped Shaft	207
7	Conclusions and Recommendations	219
7.1	Conclusions	219
7.2	Recommendations for Future Research	222
A	Fracture Mechanics	224
A.1	Fracture Modes	224
A.2	Stress Analysis of Cracks	224
A.2.1	The Stress Intensity Factor	227
A.2.2	Relationship Between K and Global Behavior	227
A.2.3	Effect of Finite Size	230

List of Tables

6.1	Frequency Ratio f_{nr} of Cylindrical Cantilever Shaft ($\rho = 0.2$)	136
6.2	Frequency Index f_n of Cylindrical	138
6.3	Frequency parameter f of tapered Timoshenko shaft overhang (taper ratio = 0.5; $\rho = 0.3$; rigid journal bearing at widest end)	141
6.4	Frequency parameter f of tapered Timoshenko shaft (taper ratio = 0.5; $\rho =$ 0.3; rigid journal bearing at both ends)	142
6.5	Frequency parameter f of tapered Timoshenko shaft	147
6.6	Multi-stepped rotor configuration data	149
6.7	Natural frequencies (rpm) of uniform stepped shaft with bearings and disks	150
6.8	The lowest thirty eigenvalues of actual finite element model	153
6.9	Eigenvalues of the reduced modal matrices	154
6.10	Reduced matrices obtained after applying planar modal reduction scheme	155
6.11	Matrix E_r obtained after applying the complex modal reduction scheme .	156
6.12	Matrix F_r obtained after applying the complex modal reduction scheme .	157

A.1	Stress fields ahead of a crack tip for Mode I and Mode II	in a	
	linear elastic, isotropic material	228
A.2	Crack tip displacement fields for Mode I and Mode II	(linear	
	elastic, isotropic material).	228
A.3	Non-zero stress and displacement components in Mode III	(lin-	
	ear elastic, isotropic material)	230

List of Figures

2-1	Through crack in an infinite plate for the general case where the principal stress is not perpendicular to the crack	18
2-2	Geometry of a cracked section of a shaft	21
3-1	Generalized coordinates of point p^{ij}	27
3-2	A rotor-bearing system: coordinates	39
3-3	Transformation of axes	40
4-1	The shaft finite element with crack	52
4-2	Free body diagram of an infinitesimal shaft finite element	58
4-3	Deformation of the shaft finite element	61
5-1	Rotation of $X'Y'Z'$ axes relative to XYZ axes	105
6-1	The control flow diagram of the developed computational scheme	124
6-2	Control flow diagram for evaluating the system matrices	128
6-3	Control flow diagram for the eigenproblem solution	129
6-4	Control flow diagram for the implementation of the modal reduction scheme	131

6-5	Control flow diagram to compute the time dependent forcing vector	133
6-6	Control flow diagram to evaluate the nodal coordinates from the modal coordinates	134
6-7	Frequency Index f_n of Cylindrical Simply Supported Shaft Rotating at $\Omega = 1000$ rad/sec ($\eta = 0.1$)	139
6-8	Frequency Parameter f of a Shaft overhang, ($\rho = 0.3$)	144
6-9	Frequency Parameter f of Simply Supported Shaft	145
6-10	Frequency Parameter f of a Shaft Overhang (Taper Ratio = 0.5)	146
6-11	The Multi-Stepped rotor-bearing shaft	148
6-12	Comparison of the deflections of the rotating shaft due to unit step force.	160
6-13	Step response of cracked non-rotating cantilever shaft using complex modal reduction	163
6-14	Step response of cracked non-rotating cantilever shaft using planar modal reduction	164
6-15	Comparison of time response of cracked and uncracked non-rotating can- tilever shaft at the free end	165
6-16	Time response of the cracked non-rotating cantilever shaft at different locations along its length	166
6-17	Comparison of impulse response of cracked and uncracked non-rotating cantilever shaft	168

6-18 Comparison of impulse response of cracked and uncracked non-rotating cantilever shaft at its free end	169
6-19 Step response of non-rotating simply supported shaft using complex modal reduction	170
6-20 Step response of non-rotating simply supported shaft using planar modal reduction	171
6-21 Step response of the cracked simply supported shaft at different locations along its length due to unit step force at node 5	172
6-22 Impulse response of non-rotating simply supported shaft	174
6-23 Deflection of the cracked non-rotating simply supported shaft at different locations along its length due to unit impulse at node 5	175
6-24 Step response of non-rotating tapered simply supported shaft using complex modal reduction	177
6-25 Step response of non-rotating tapered simply supported shaft using planar modal reduction	178
6-26 Step response of the non-rotating tapered shaft near the widest end	179
6-27 Step response of non-rotating tapered shaft near the narrow end	180
6-28 Impulse response of non-rotating simply supported shaft using complex modal reduction	182
6-29 Impulse response of non-rotating simply supported shaft using planar modal reduction	183

6-30	Deflection of cracked non-rotating simply supported shaft at different locations along its length due to unit impulse at node 5	184
6-31	Step response of non-rotating tapered cantilever shaft using complex modal reduction	185
6-32	Step response of non-rotating tapered cantilever shaft using planar modal reduction	186
6-33	Comparison of step response of the cracked and uncracked non-rotating tapered cantilever shaft at the free end	187
6-34	Step response of cracked non-rotating tapered cantilever shaft at different locations along the length of the shaft	188
6-35	Comparison of impulse response of the cracked and uncracked tapered cantilever shaft at the free end	190
6-36	Comparison of impulse response of the cracked and uncracked tapered cantilever shaft at node 5	191
6-37	Step response of the rotating tapered cracked cantilever shaft using complex modal reduction	193
6-38	Step response of the rotating tapered uncracked cantilever shaft	194
6-39	Step response of the rotating tapered cracked cantilever shaft using planar modal reduction	195
6-40	Impulse response of the rotating tapered cracked cantilever shaft using planar modal reduction	196

6-41	Step response of a cracked rotating tapered simply supported shaft using planar modal reduction	198
6-42	Torsional response of a cracked rotating tapered simply supported shaft due to inertial coupling	199
6-43	Step response of an uncracked rotating tapered simply supported shaft	200
6-44	Impulse response of cracked rotating tapered simply supported shaft using planar modal reduction	201
6-45	Time response of cracked rotating tapered cantilever shaft due to a force $\sin(1000 t)$	203
6-46	Time response of cracked rotating tapered cantilever shaft due to a force $\sin(3000 t)$	204
6-47	Time response of cracked rotating tapered cantilever shaft due to a force $\sin(965 t)$	205
6-48	Time response of cracked rotating tapered cantilever shaft due to a force $\sin(1425 t)$	206
6-49	Time response of cracked rotating tapered simply supported shaft due to a force $\sin(3000 t)$	208
6-50	Time response of cracked rotating tapered simply supported shaft due to a force $\sin(2167 t) + \cos(1632 t)$	209
6-51	Time response of uncracked multi-stepped shaft due to unit force at the disk	211
6-52	Time response of cracked multi-stepped shaft due to unit force at the disk	212

6-53	Step response of the multi-stepped uncracked rotor-bearing system using planar modal reduction	214
6-54	Step response of uncracked multi-stepped system an node 1 due to excitation at node 13	215
6-55	Step response of multi-stepped shaft at node 1 with expanded simulation time	216
6-56	Step response of cracked multi-stepped system due to excitation at node 13	217
6-57	Step response of cracked multi-stepped shaft at node 1 due to excitation at node 13	218
A-1	The different modes of fracture of a solid	225
A-2	Definition of the coordinate axis ahead of a crack tip. The Z direction is normal to the page	226
A-3	A through-thickness crack in an infinitely wide plate subjected to a remote tensile stress	229
A-4	Edge crack in a semi-infinite plate subjected to a remote tensile stress . .	231
A-5	Stress concentration effects due to a through crack in finite and infinite width plates.	233

DISSERTATION ABSTRACT

FULL NAME OF STUDENT MOHAMMED AHMED MOHIUDDIN

TITLE OF STUDY FINITE ELEMENT DYNAMIC ANALYSIS
OF MULTIBODY ROTOR-BEARING
SYSTEM WITH CRACKED SHAFT

MAJOR FIELD MECHANICAL ENGINEERING

DATE OF DEGREE JUNE 1997

The equations of motion of a general multibody system are derived using the Lagrangian approach. The multibody system can be an assemblage of flexible as well as rigid bodies. The equations of motion of a rotor-bearing system are deduced from those of the general multibody system. A cracked rotor shaft finite element is developed to model the rotor shaft. The shape functions of the cracked rotor shaft finite element are derived using Timoshenko beam theory and crack flexibility compliance as a parameter. The explicit expressions of the element mass, stiffness and gyroscopic matrices are developed thus obviating the need for extensive numerical computations. A computer scheme is developed to assemble the system equations of motion from the elemental level using finite element assembly procedure. It can invoke either complex or planar modal reduction scheme to reduce the order of the full-order finite element model. The complex modal reduction scheme is implemented for the first time in this dissertation. The reduced order modal equations of motion are integrated forward in time. The mass matrix of the rotor-bearing system is function of time and couples the flexural and torsional vibrations. The numerical scheme updates the mass matrix with time. The vibration characteristics and the transient dynamic response of the cracked rotor-bearing system are studied.

DOCTOR OF PHILOSOPHY DEGREE
KING FAHD UNIVERSITY OF PETROLEUM & MINERALS
Dhahran, Saudi Arabia
June 1997

خلاصة الرسالة

إسم الطالب الكامل : محمد أحمد محي الدين
عنوان الدراسة : تحليل ديناميكي لنظام محمل دوار متعدد الأجسام ذي شق في عمود الإدارة باستخدام العناصر المنتهية .
التخصص : هندسة ميكانيكية
تاريخ الشهادة : يونيو ١٩٩٧م

إشتقت معادلات الحركة لنظام متعدد الأجسام باستخدام تقريب لا جرانج . يمكن اعتبار النظام المتعدد الأجسام مجموعة من أجسام لينة وصلبة. إستنتجت معادلات الحركة لنظام محمل دوار من معادلات نظام متعدد الأجسام. طُور شق في عمود الإدارة باستخدام العنصر المنتهي لصياغة المحور الدوار . كما اشتقت دوال الأشكال لعمود الإدارة بالعنصر المنتهي لأول مرة في هذه الأطروحة باستخدام مطاوعة اللدانة في الشق المشكل كوسيط. إشتقت كذلك العبارات الصريحة لمصفوفات الكتلة والصلبية والجير وسكوبية. كما طور برنامج كمبيوتر لتجميع جملة معادلات الحركة من العنصر إلى المجموعة كلها باستخدام طريقة التجميع في العناصر المنتهية. بالإضافة فقد طور برنامج ثانٍ يحتوي على تخفيض عدد المعادلات المراد حلها وذلك بواسطة التخفيض البسيط والتخفيض المركب الذي ينشر لأول مرة في هذه الأطروحة وأجري تكامل المعادلات الناتجة عن هذا التخفيض في حل المسألة بالنسبة للزمن . ويجدر الإشارة إلى أن مصفوفة الكتلة لنظام محمل الدوار فهي متغيرة بالنسبة للزمن وتزدوج كلاً من اهتزازات الاثناء واللي . كما يقوم البرنامج بتطوير مصفوفة الكتلة مع الزمن. درست خواص الاهتزازات والتجاوب الديناميكي العابر لتشكيل اتشقاقي في محور ذي محمل .

درجة الدكتوراه في الفلسفة
جامعة الملك فهد للبترول والمعادن
الظهران - المملكة العربية السعودية
يونيو ١٩٩٧م

Chapter 1

Introduction

Cracks may occur due to presence of notches and slots in a rotating shaft. Cracks can also appear as a result of the accidental mechanical damage which often occurs in the blades of axial compressors of aircraft engines. In this case, the damage arises as a result of air suction when the air contains fine stones and sand. Other reasons for the appearance of cracks are erosion and corrosion as well as fatigue of the rotor material.

According to Muszynska [1], at least 28 rotor failures, which can be attributed to shaft cracks, have occurred within a period of ten years in the North American utility industry alone. Clearly, the timely detection of cracks would obviate expensive and dangerous machine failures and plant shutdowns.

A crack on a machine element introduces considerable local flexibility due to the stress concentration at the vicinity of the crack tip. Due to change in stiffness, the presence of crack changes the dynamical characteristics of the machine element. Because

of the increasing demands for safety, reliability and efficiency, it is now believed that monitoring of the global dynamics of a mechanical system offers a promising alternative for damage detection. Consequently, the study of dynamics of cracked rotors, which represent essential elements in all rotating machinery, is of great importance.

1.1 Literature Survey

Complex mechanical systems are an assemblage of simple structural components. These simple structural elements include beams, bars, plates, frames, etc. To understand the effect of cracks on the dynamics of complex structures it is imperative that we understand their effect on simple structures. The simplest form of a rotor component is one that is modeled by a uniform beam. In the literature survey that follows, the effect of a crack on the dynamics of beams has been addressed.

1.1.1 Cracked Non-Rotating Beams

Petroski [2] presented a simple model for the effect of a crack on the response of an elastic beam. In the model, the crack is represented by an equivalent slot accounting for the ineffective material adjacent to a crack and a pair of concentrated couples acting on the beam. Using Fourier series expansion for the response of the beam he determined the vibration response of the beam to a step load. He concluded that the presence of crack increases the overall vibration amplitude by a factor of three over that of the uncracked beam and introduces higher frequency vibrations more noticeably into the

total response. Christides and Barr [3] introduced a modification of Bernoulli-Euler beam theory by incorporating symmetric cracks. The stress field around the crack is modeled by an approximate exponential decay parameter which is estimated from the experimental data on the natural frequency change as a function of crack depth. Shen and Pierre [4] proposed an approximate Galerkin solution to the theory developed by Christides and Barr [3] for the free bending motion of beams with pairs of symmetric open cracks. The Galerkin procedure involves the expansion of the cracked beam deflection in a series using eigenfunctions of the corresponding uncracked beam. However, the stress-decay parameter, which is used to model the concentration of stress around the crack, had to be redetermined to increase the convergence speed of the Galerkin solution. Shen and Pierre [5] extended the cracked beam theory presented in reference [4]. In this formulation, they assumed that the damage can be viewed as a single surface crack normal to the beam neutral axis. The assumption of single-edge crack, introduces discontinuities in the slope of the neutral axis and in the axial displacement along the neutral axis. The equations of motion of the beam are derived using the variational principle. The Galerkin and Ritz methods are then applied to predict the free vibration modes of cracked beams, with simply supported and cantilevered configurations. Papadopoulos and Dimarogonas [6] derived the equation of motion for the transverse and torsional vibration of a clamped-free Timoshenko beam of circular cross-section and stated its boundary condition and crack-compatibility conditions. They investigated the coupling of bending and torsional vibrations of the beam by solving the differential equations of motion using the assumed

modes method. Rajab and Al-Sabeeh [7] studied the vibration characteristics of a cracked simply supported Timoshenko shaft. They assumed discontinuities in deflection and slope of the shaft at the location of the crack. The four boundary conditions and the four continuity equations at the crack location were substituted in the assumed solution of the equation of motion of the non-rotating shaft. They addressed the change of the natural frequencies as a function of crack depth and crack location.

The study of dynamics, using analytical methods is limited to simple structures. Complicated structures can be better modelled using the finite element method. Therefore, investigators have recently focussed their interest in this direction. Gounaris and Dimarogonas [8] presented a finite element formulation of a cracked prismatic beam for structural analysis. They developed the consistent stiffness matrix of the finite element model by assuming that a discontinuity at the crack location occurs in both deflection and slope due to bending and shear compliance, respectively. The assumption of a discontinuity in deflection would imply that the structure is broken. Hence the reduction in stiffness due to the presence of crack need to be modelled by considering discontinuity in slope only. Haisty and Springer [9] proposed a finite beam element for damage assessment of complex structures. In this beam element formulation, the stiffness due to crack is modelled by equivalent springs between two undamaged beams. The finite element is developed by determining the force-displacement relationships for two undamaged beams connected by a set of springs.

Ostachowicz and Krawczuk [10] analyzed the vibrations of a cracked beam by dividing

the beam into triangular finite elements with two degrees of freedom per node, while modeling the crack as a point finite element. The local flexibility due to the crack is taken care of by the stiffness of the point finite element. They outlined a procedure to calculate the stiffness of the point finite element and to incorporate it in the assembled stiffness matrix of the structure. Krawczuk [11] presented a finite Timoshenko-type beam element with a crack. The crack is modelled by including an additional flexibility matrix to the flexibility matrix of the uncracked element. The terms of the additional flexibility matrix due to crack are evaluated according to the laws of fracture mechanics. The Timoshenko effect is included by adding the strain energy due to shear deformation to the strain energy of the uncracked beam element. The stiffness matrix is obtained by inverting the flexibility matrix of the cracked beam element. However, for small cracks, the crack flexibilities are very small and the elements of the stiffness matrix are correspondingly larger. This might lead to numerical solution problems [8].

Although, all the previously cited investigations were dedicated to studying the effect of a crack on the dynamic behavior of non-rotating beams, they addressed the basic approaches that were adopted in the investigations of cracks on rotating beams.

1.1.2 Cracked Rotating Beams

Chen and Chen [12] studied the vibrations of cracked thick rotating blades wherein the rotating blade is modelled by a number of Timoshenko beam elements. The presence of a crack is modelled by introducing a local flexibility matrix. They concluded that the crack

flexibilities and crack position have significant effects on the free vibration frequencies of the rotating blade. Wauer [13] derived equations of motion for a cracked rotating blade. He considered the cracked blade as a Bernoulli-Euler beam with a single transverse crack. The reduced stiffness of the crack region is characterized by a local spring element connecting two uncracked beam segments. The governing nonlinear boundary value problem is derived and linearized for small superimposed oscillations. However, shear was not included in the analysis and quantitative results were not presented in reference [13]. Krawczuk [14] presented a finite element for a rotating cracked beam. He derived the shape functions of the beam element by taking into account only the discontinuity in slope due to bending at the cracked location. The discontinuities in deflection and shear deformation were not considered. Using the derived shape functions, he constructed the stiffness and mass matrices for the rotating beam element.

1.1.3 Cracked Rotating Shafts

All of the previously cited formulations, however, were dedicated to either nonrotating or rotating beams. In recent years, investigators have given more attention to the presence of cracks in rotating shafts due to their importance in practical situations. Davies and Mayes [15] studied the effect of a propagating transverse crack on the dynamics of a rotor-bearing system using an experimental spin rig. They concluded that except for very large cracks, the vibrational behavior is similar to that of a slotted shaft with additional excitation due to the crack opening and closing. Grabowski [16] investigated the vibrational

behavior of the flexible turbine rotor containing a transverse crack. The shaft deflections are modeled, using the assumed modes method, by a series expansion of the first few eigenfunctions. Strong dependence of the vibrational behavior of the cracked rotating shaft on the crack position is demonstrated. Papadopoulos and Dimarogonas [17, 18] investigated the coupling of longitudinal and bending vibrations of a rotating shaft due to an open transverse surface crack. The assumed modes method was employed in deriving the model, wherein shear deformations were not considered. Wauer [19] formulated the equations of motion for cracked rotating shafts. A rotating Timoshenko shaft with six degrees of freedom is considered. Due to the presence of crack, the shaft is considered as two uniform fields, one on either side of the crack. The open crack is simulated by a local spring, with reduced stiffness and damping, that connects the two uniform fields. The equations of motion are rewritten replacing the geometric discontinuity by a load discontinuity at the crack location. Galerkin method is applied to solve the simplified equations of motion.

In addition to the previously cited assumed modes method, the finite element method has been employed in modeling rotating cracked shafts. Nelson and Nataraj [20] presented a theoretical analysis of the dynamics of cracked rotor-bearing system using the finite element method. The rotor shaft is modelled using a finite shaft element with a transverse crack. The additional flexibility due to the crack is not accounted for according to the laws of fracture mechanics. Instead, the variation in stiffness of the cracked shaft with its rotation is evaluated. The variation in stiffness is modelled by a perturbation parameter,

thus resulting in a nonlinear parametrically excited system of equations. These equations are solved by applying perturbation techniques to an assumed solution in terms of a Fourier series. The equations of motion are then converted to the frequency domain. Only the frequency response of unbalance excitation is presented. The solution methodology adopted is not suitable for predicting time response, however. The perturbation parameter, which is also called the crack parameter that accounts for the variation of stiffness of the cracked shaft, is not physically related to any crack property like depth, type of crack, etc. Hamidi et al. [21] presented a finite element model for the study of modal parameters of cracked rotors, wherein the open crack is modelled by additional local flexibility. The stiffness matrix of the finite element model is found by inverting the flexibility matrix, which is computed using the principles of fracture mechanics. Since the inversion of the flexibility matrix is involved, the numerical scheme could be inefficient for small crack sizes when the associated flexibility is small. They have investigated the effect of a crack only on the modal characteristics of a uniformly cylindrical Euler-Bernoulli shaft. Their study was not carried out to the stage of dynamic response calculations.

In practice, shafts have stepped geometry to allow for adequate strength as well as tapered segments for mounting other mechanical elements. In addition, actual rotors include disks and anisotropic bearings. A realistic dynamic analysis of rotors with such a complex geometry, can be made feasible using the powerful finite element method. The literature review reveals that only cylindrical cracked rotating shafts were tackled using the finite element method. In such formulations, the reduced stiffness due to the presence

of a crack is modelled by an additional flexibility matrix, which is inverted to obtain the stiffness matrix. For small flexibility values, however, the inversion procedure could be numerically sensitive. Moreover, the reported formulations did not account for the shear deformations, which are significant for rotor systems with short shafts.

The current status of the reported work in the area of dynamic analysis of cracked rotors reveals the following observations:

1. The crack stiffness effects were obtained by inverting the flexibility matrix. However, for small cracks, the crack flexibilities are very small and the inversion of the flexibility matrix often results in numerical difficulties.
2. The finite element used did not permit the tapered geometry of the shaft element.
3. For dynamic response analysis, the modal reduction was carried out using only planar modal transformations.
4. Time response to a general input, (e.g., step, impulse) was not addressed. Most of the work was carried out for predicting the response due to a rotating unbalance.

The purpose of the present study is to develop a consistent finite element scheme for the efficient evaluation of the dynamic characteristics and prediction of the time-responses of cracked rotor-bearing systems. In this regard, a finite element formulation of the elastodynamic equations of motion is developed, and the eigenvalue problem is then defined. For discretization, a tapered cracked shaft finite element is introduced to account for translational inertia, rotary inertia, gyroscopic moments, torsional and

shear deformations. This cracked finite element formulation is based on a consistent mass approach that accounts for shear as a deformation parameter. For the developed finite element, the shape functions are derived taking into account the crack geometry as well as the associated boundary and continuity conditions. Explicit expressions of the mass, stiffness and gyroscopic matrices are formulated, and the eigenvalue solutions are obtained for a wide range of parameter variations. The equations of motion of the rotor-bearing system, when written in nodal coordinates are of very high order. It is numerically inefficient to integrate forward in time such high order of equations. Three modal reduction schemes are discussed. The planar and complex modal reduction schemes are implemented and reduced order equations of motion are obtained. The resulting reduced order equations of motion are integrated forward in time to predict the response for different types of loads. The developed scheme has been utilized to produce useful numerical results beyond those available in the current literature.

1.2 Proposed Research

A complete dynamic model for a general rotor-bearing system with a cracked shaft is derived for the purpose of studying the dynamic response behavior of such systems. The following tasks will be carried out:

1.2.1 Derivation of Equation of Motion

A general rotor-bearing system is an assemblage of flexible as well as rigid components. Therefore, a multibody formulation capable of accommodating flexible and rigid bodies will be adopted. The shear stiffness, torsional stiffness, rotary inertia, gyroscopic effects and inertia coupling of flexural and torsional motions will be included in the general multibody formulation.

1.2.2 The Finite Element Discretization

The flexible components of the rotor-bearing system such as the shaft will be modelled using the finite element method.

The Finite Element Mesh

The cracked elastic shaft is divided into finite elements. A general cracked shaft finite element which has two nodes, with each node having five degrees of freedom is developed. The five degrees of freedom comprise of two deflections which are perpendicular to the axis of the element and three rotations about the three axes. The vanishingly small axial deflection is neglected. The mesh of the cracked rotor shaft can contain unequal shaft finite element lengths. It is proposed to develop the formulation of the finite cracked element such that it lends itself to both cylindrical and conical geometry of the element which may have solid or hollow cross-section.

Shape Functions

In finite element method, the elastic displacement field over an element is expressed in terms of the nodal coordinates using shape functions. In the literature, the shape functions for a cracked shaft element are not derived. It is proposed to derive the shape functions incorporating the flexibility of the crack as a crack compliance. The deformation due to shear (Timoshenko effect) will also be included in the derivation of shape functions.

Explicit Form of Matrices

The literature survey shows that researchers have modelled the cracked rotor shaft using standard finite beam elements. The total flexibility matrix of the cracked beam element is obtained by adding the additional flexibility due to crack to the flexibility matrix of the uncracked beam element. The stiffness matrix of the cracked beam element is obtained by inverting the total flexibility matrix. If the flexibility is small, the inversion of the flexibility matrix creates numerical problems. Hence, a method to directly compute the stiffness matrix of the cracked beam element is desirable. The calculation of the element matrices involve integration of shape functions. It is desirable to avoid numerical integration to minimize round off errors and to increase efficiency of the numerical computations. It is proposed to derive the explicit form of the non-zero entries of the element mass, stiffness and gyroscopic matrices.

Assembled Equation of Motion

The element matrices are assembled into the system matrices which represent the rotor-bearing system. The order of the system matrices, before applying the constraints is equal to the total number of degrees of freedom of the system. In the finite element method, the number of total degrees of freedom of a system is very large, thus resulting in equation of motion with very large dimensionality.

1.2.3 Reduced-Order System

Modal transformations can be invoked to obtain a reduced-order model. In the literature, planar modes are used to reduce the order of the system matrices. However, actual modes of a rotor-bearing system are complex. Due to the associated numerical difficulties, complex modal transformations were not adopted by any reported dynamic response analysis investigation. In this proposed research work, complex modal transformations are invoked using a set of significant complex as a basis for the reduced-order modal space. The modal form of the equations of motion will be obtained.

1.2.4 Time-Response (Numerical Integration)

The reduced modal forms of the system matrices are used for time response analysis. The reduced-order equations of motion are numerically integrated forward in time to obtain the system's time response. The response obtained from the reduced-order system is compared to that of the full-order FEM model to validate the reduced-order system. It

is proposed to study the dynamic response of the cracked shaft for different types of forcing functions.

Chapter 2

The Crack Model

The presence of crack introduces flexibility in a solid. The amount of flexibility introduced depends upon the crack geometry and type of crack. Due to cyclic loading and fatigue, the crack propagates, thus resulting in a possible catastrophic fracture of the mechanical component. The different fracture modes of a solid material and stresses induced by them are presented in the appendix.

Using fracture mechanics concepts, the effect of crack on the solid can be represented by a single parameter called the stress intensity factor. The stress intensity factor is found by considering the boundary conditions and type of loading on the solid. A relationship between the additional strain energy due to crack and its stress intensity factor can be established. The flexibility influence coefficient of the crack is then found using the relationship between the additional strain energy and the stress intensity factor. The flexibility influence coefficient of the crack will be used in the derivation of shape functions

of the cracked shaft finite element to be developed in this investigation. In this chapter, the derivation of flexibility influence coefficient of a transverse surface crack using fracture mechanics concepts is presented.

2.1 The Energy Release Rate

Griffith [22] realised that for an infinitesimally small amount of crack extension, the decrease in stored elastic strain energy of a cracked body under fixed grip conditions is identical to the decrease in potential energy under conditions of constant loading. The energy release for an increase in crack length δa is given by

$$GB\delta a = \frac{1}{2}P\delta u \quad (2.1)$$

where G is the energy release rate per unit area, B is the thickness of the plate and P is the load. The displacement u of the plate can be written as

$$u = CP \quad (2.2)$$

where C is the reciprocal of the slope of the load-deflection curve at a particular value of crack length a , and is known as the crack compliance of the system. For constant load, we can write

$$GB\delta a = \frac{1}{2}P^2\delta C \quad (2.3)$$

therefore as $\delta a \rightarrow 0$, the energy release rate can be written as

$$G = \frac{1}{2} \frac{P^2}{B} \frac{\partial C}{\partial a} \quad (2.4)$$

2.2 Relationship Between K and G

The crack tip region is small compared to the body as a whole but sufficiently large with respect to the atomic dimensions. Therefore the linear theory of elasticity can be applied with reasonable accuracy. From Westergaard's solution [23], referring to Figure 2-1, one gets

$$\sigma_{xx} = \frac{\sigma y}{(y^2 - a^2)^{\frac{1}{2}}} \quad (2.5)$$

Considering plane strain, the displacement u_{xx} can be written as

$$u_{xx} = 2(1 - \nu^2) \frac{\sigma}{E} [(a + \delta a)^2 - y^2]^{\frac{1}{2}} \quad (2.6)$$

Now substituting

$$r = y - a \quad (2.7)$$

the stress and displacement can be written as

$$\sigma_{xx} = \frac{\sigma \sqrt{\pi a}}{\sqrt{2\pi r}} = \frac{K}{\sqrt{2\pi r}} \quad (2.8)$$

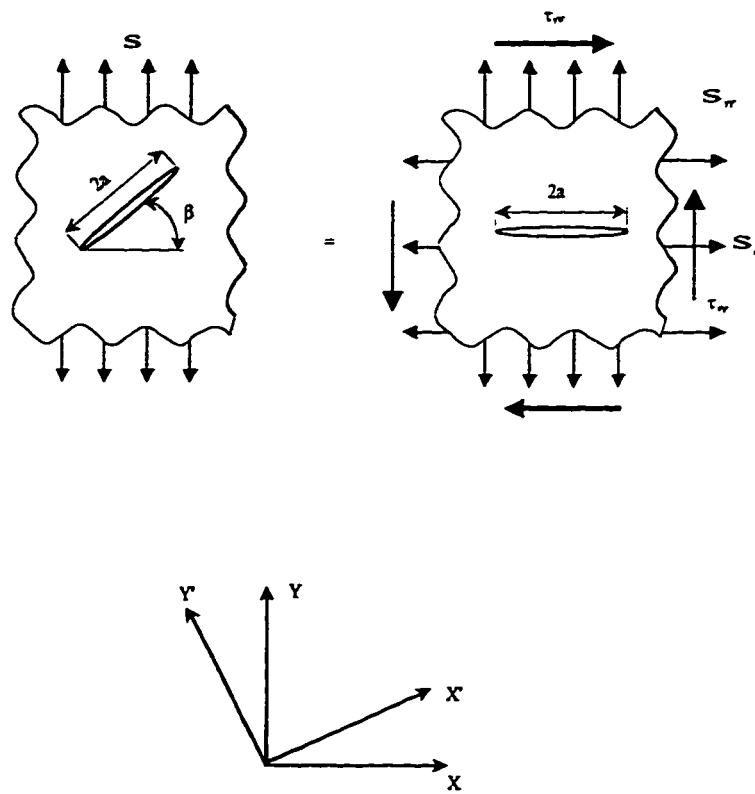


Figure 2-1: Through crack in an infinite plate for the general case where the principal stress is not perpendicular to the crack.

and

$$u_{xx} = 2(1 - \nu^2) \frac{\sigma}{E} \sqrt{2a} [\delta a - r]^{\frac{1}{2}} \quad (2.9)$$

The energy change per unit thickness can be expressed as

$$G\delta a = \int_0^{\delta a} \sigma_{xx} u_{xx} dr = 2(1 - \nu^2) \frac{\sigma^2 a}{E} \int_0^{\delta a} \left(\frac{\delta a - r}{r} \right)^{\frac{1}{2}} dr \quad (2.10)$$

After evaluating the integral, the change in energy is written as

$$G\delta a = \frac{\sigma^2 \pi a}{E} (1 - \nu^2) \delta a \quad (2.11)$$

putting

$$K = \sigma \sqrt{\pi a} \quad (2.12)$$

where K is defined as the stress intensity factor, then the expression for G can be written as

$$G = \frac{K^2}{E} (1 - \nu^2) \quad (2.13)$$

Consider a crack situated in an infinite body is subjected to a tensile stress (Mode I opening), to a shear stress (Mode II sliding) and to an antiplane shear stress (Mode III). The local crack tip stresses which could do work are σ_{xx} (Mode I), the shear σ_{xy} (Mode II) and the shear σ_{zx} (Mode III), which are characterized by the stress intensity parameters K_I , K_{II} and K_{III} , respectively. Work is done only when these stresses move in the appropriate directions. The expression of the strain energy release rate per unit

thickness is given by

$$G = \lim_{\delta a \rightarrow 0} \frac{1}{\delta a} \int_0^{\delta a} (\sigma_{xx} u_{xx} + \sigma_{xy} u_{xy} + \sigma_{xz} u_{xz}) d\tau \quad (2.14)$$

Evaluating the integral and assuming plane strain conditions for modes I and II, one obtains [24]

$$EG = (1 - \nu^2) K_I^2 + (1 - \nu^2) K_{II}^2 + (1 + \nu) K_{III}^2 \quad (2.15)$$

2.3 Local Flexibility of a Cracked Shaft

A transverse crack of depth a is considered on a shaft of radius R (Figure 2-2). The shaft has local flexibility due to a crack in many directions, depending on the direction of the applied forces. In this model, only bending deformation is considered. Axial forces which give coupling with transverse motions of the cracked shaft will not be considered. Therefore, the shaft is bent by a pure bending moment M and the additional angular deflection of one end of the shaft relative to the other will be computed.

Paris [25] computed the displacement u per unit width of a cracked structure due to the action of a force P as

$$u = \frac{\partial}{\partial P} \int_0^a G(\tau) d\tau \quad (2.16)$$

where a is the crack depth and $G(\tau)$ is the strain energy release rate. The energy release

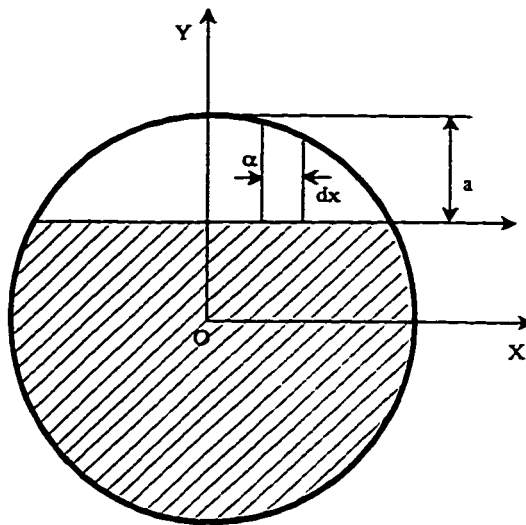


Figure 2-2: Geometry of a cracked section of a shaft

rate for mode I fracture, referring to Eq.(2.13) can be written as

$$G = \frac{1 - \nu^2}{E} K_I^2 \quad (2.17)$$

For a crack with varying depth, referring to Figure 2-2 the strain energy density function will have the form [26]

$$G = \int_{-b}^b \frac{(1 - \nu^2) K_I^2(X)}{E} dX \quad (2.18)$$

where E is Young's modulus, ν is Poisson's ratio and $2b$ is the crack width. The flexibility influence coefficient can be written as

$$c = \frac{\partial u}{\partial P} = \frac{\partial^2}{\partial P^2} \int_0^a \int_{-b}^b \frac{(1 - \nu^2) K_I^2(X)}{E} dX da \quad (2.19)$$

The solution of the stress intensity factor K_I is not available, however. The solution for the strip with width dX and depth $\alpha = a + \sqrt{R^2 - X^2} - R$ will be used. This solution is reported in reference [25] as

$$K_I = \frac{4M}{\pi R^4} \sqrt{R^2 - X^2} \sqrt{\pi \alpha} F_2 \left(\frac{\alpha}{h} \right) \quad (2.20)$$

where

$$F_2 \left(\frac{\alpha}{h} \right) = \sqrt{\frac{2h}{\pi \alpha} \tan \left(\frac{\pi \alpha}{2h} \right)} \frac{0.923 + 0.199 \left(1 - \sin \frac{\pi \alpha}{2h} \right)^4}{\cos \frac{\pi \alpha}{2h}} \quad (2.21)$$

and h is the local height:

$$h = 2\sqrt{R^2 - X^2} \quad (2.22)$$

Therefore, for $p = M$, Eq.(2.19) becomes [26]

$$c_x = \frac{1 - \nu^2}{E} \int_0^a \int_{-b}^b \frac{32}{\pi^2 R^8} (R^2 - X^2) \pi \alpha F_2^2 \left(\frac{\alpha}{h} \right) dX d\alpha \quad (2.23)$$

In dimensionless form, this can be written as

$$\frac{\pi^2 R^3 E c_x}{1 - \nu^2} = \int_0^a \int_{-b}^b 32 \left[1 - \left(\frac{X}{R} \right)^2 \right] \pi \left(\frac{\alpha}{R} \right) F_2^2 \left(\frac{\alpha}{h} \right) d \left(\frac{X}{R} \right) d \left(\frac{\alpha}{R} \right) \quad (2.24)$$

The expression on the right side is a function of $\frac{\alpha}{R}$ only and can be computed by numerical integration.

For the moment about the y -axis, the cracked shaft has another flexibility coefficient, which is given by

$$c_y = \frac{1 - \nu^2}{E} \int_0^a \int_{-b}^b \frac{32 \xi^2 \pi \alpha F_1^2 \left(\frac{\alpha}{h} \right)}{\pi^2 R^8} dX d\alpha \quad (2.25)$$

where

$$F_1 \left(\frac{\alpha}{h} \right) = \sqrt{\frac{2h}{\pi \alpha} \tan \left(\frac{\pi \alpha}{2h} \right)} \frac{0.752 + 2.02 \left(\frac{\alpha}{h} \right) + 0.37 \left(1 - \sin \frac{\pi \alpha}{2h} \right)^3}{\cos \frac{\pi \alpha}{2h}} \quad (2.26)$$

In dimensionless form

$$\frac{\pi^2 R^3 E c_y}{1 - \nu^2} = \int_0^a \int_0^b 32 \left(\frac{X}{R} \right)^2 \pi \left(\frac{\alpha}{R} \right) F_1^2 \left(\frac{\alpha}{h} \right) d \left(\frac{X}{R} \right) d \left(\frac{\alpha}{R} \right) \quad (2.27)$$

The integral on the right is a function of $\frac{a}{R}$ only. The integration is carried out over only half the crack width because only positive tension stresses cause extension and opening of the crack.

The flexibility influence coefficients c_x and c_y of Eqs.(2.23) and (2.25) will be employed in the derivation of shape functions of a cracked rotor shaft finite element to be developed later in chapter 4.

Chapter 3

The Multibody Elastodynamic

Model

3.1 Introduction

A rotor-bearing system is comprised of a number of mechanical components that can be treated as rigid (e.g. disks, bearing brackets, etc.) or flexible (blades, shafts, bearings, etc.). In this chapter, a general multibody system is considered. A multibody system, in general, is an assemblage of elastic as well as rigid bodies. The kinetic and potential energy expressions are obtained and the governing differential equations of motion are derived by means of the Lagrangian approach. The equations of motion of a rotor-bearing system are then deduced from the general multibody system model.

3.2 The Multibody System

One may start by deriving the equations of motion of a general elastic body. Referring to Figure 3-1, the XYZ Cartesian coordinate system represents an inertial frame and the $X^iY^iZ^i$ axes represent a body fixed Cartesian coordinate system that is rigidly attached to an infinitesimal volume on the i^{th} body. Using the finite element approach, the body is divided into a number of elements which are attached to each other. The location of an arbitrary infinitesimal volume on the j^{th} element of this body is defined in terms of two sets of generalized coordinates. The first set represents reference coordinates that locate the position of a body fixed coordinate system $X^iY^iZ^i$ with respect to the inertial XYZ frame. The second set consists of elastic coordinates that characterize the elastic deformation of the body. Elastic coordinates represent relative translational and angular displacements of infinitesimal volumes at the nodal points on a body with respect to the body fixed coordinate system $X^iY^iZ^i$.

Let $X^{ij}Y^{ij}Z^{ij}$ be a Cartesian coordinate system with its origin affixed to an infinitesimal volume at some point on the j^{th} element of the i^{th} body, and the $\bar{X}^{ij}\bar{Y}^{ij}\bar{Z}^{ij}$ be a coordinate system parallel to the $X^{ij}Y^{ij}Z^{ij}$ but with its origin coincident with the origin of the body-fixed axes, as shown in Figure 3-1. If e^{ij} represents the nodal coordinates of element ij , with respect to the $X^{ij}Y^{ij}Z^{ij}$ coordinate system, then the position of point p^{ij} with respect to the $\bar{X}^{ij}\bar{Y}^{ij}\bar{Z}^{ij}$ coordinate system can be defined by u^{ij} as:

$$u^{ij} = N^{ij}e^{ij} \quad (3.1)$$

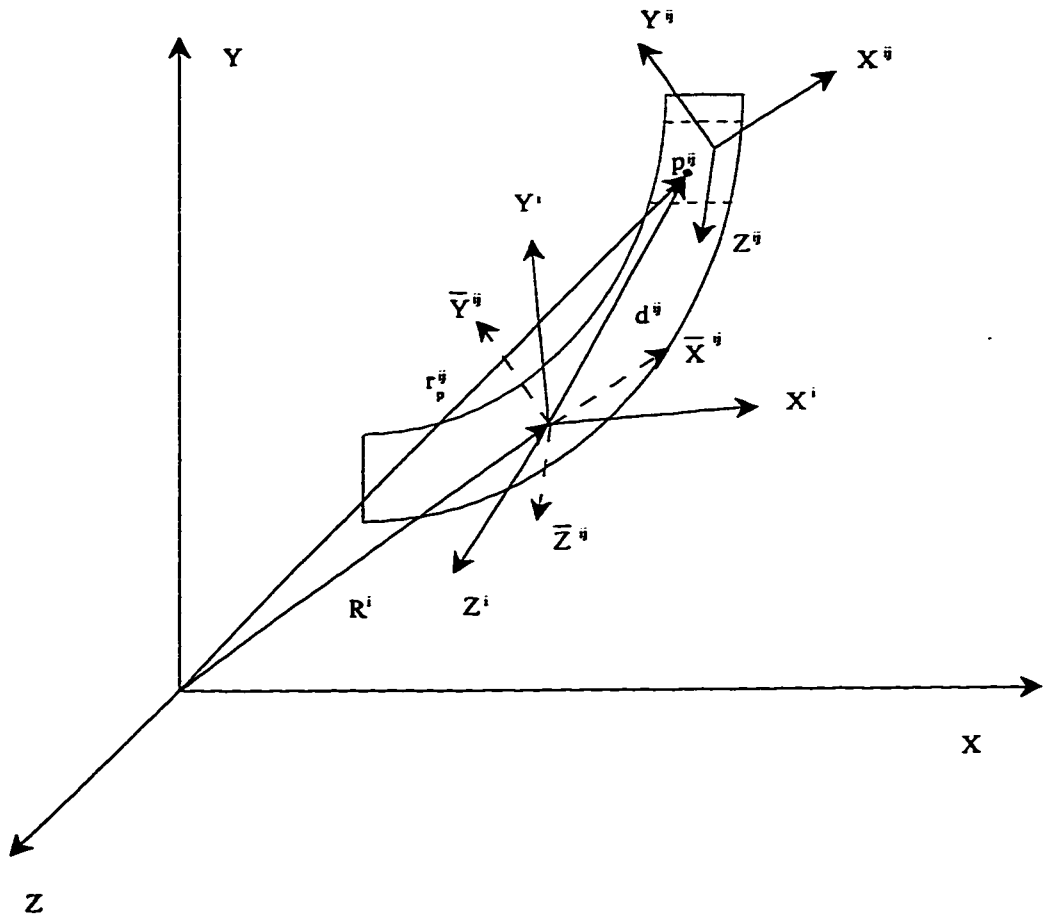


Figure 3-1: Generalized coordinates of point p^{ij}

where N^{ij} is the modified shape function of element ij which takes into account the transformation from $X^{ij}Y^{ij}Z^{ij}$ to $\overline{X}^{ij}\overline{Y}^{ij}\overline{Z}^{ij}$ axes. As shown in Figure 3-1, the global position vector r_p^{ij} of the point p^{ij} can be written as

$$r_p^{ij} = R^i + d^{ij} \quad (3.2)$$

where

$$d^{ij} = \Psi^i \Gamma^{ij} u^{ij} \quad (3.3)$$

is the position vector of point p^{ij} from body fixed axes in global coordinates, $\Psi^i(\theta^i)$ is the transformation matrix from the i^{th} body fixed $X^i Y^i Z^i$ coordinate system to the global XYZ coordinate system and Γ^{ij} is the transformation matrix from the element $\overline{X}^{ij}\overline{Y}^{ij}\overline{Z}^{ij}$ coordinate system to the i^{th} body fixed coordinate system. Substituting Eq.(3.3) in Eq.(3.2), we can write r_p^{ij} as

$$r_p^{ij} = R^i + \Psi^i \Gamma^{ij} u^{ij} \quad (3.4)$$

To evaluate kinetic energy of element ij , it is first necessary to derive an expression for the velocity vector of an infinitesimal volume at point p^{ij} on the element. Differentiating Eq.(3.4) with respect to time yields the velocity of point p^{ij} ,

$$\dot{r}_p^{ij} = \dot{R}^i + \dot{\Psi}^i \Gamma^{ij} N^{ij} e^{ij} + \Psi^i \dot{\Gamma}^{ij} N^{ij} e^{ij} + \Psi^i \Gamma^{ij} \dot{N}^{ij} e^{ij} \quad (3.5)$$

where (\cdot) denotes differentiation with respect to time. The second term on the right side of Eq.(3.5) is defined as

$$\dot{\Psi}^i \Gamma^{ij} N^{ij} e^{ij} = B^{ij} \dot{\theta}^i \quad (3.6)$$

and the third term on the right hand side of Eq.(3.5) is defined as

$$\Psi^i \dot{\Gamma}^{ij} N^{ij} e^{ij} = D^{ij} \dot{e}^{ij} \quad (3.7)$$

The matrices $B^{ij}(\theta^i, e^{ij})$ and $D^{ij}(\theta^i, e^{ij})$ are functions of the reference rotational coordinates of body i and the elastic coordinates of element ij . Equation (3.5) is then expressed as

$$\bar{r}_p^{ij} = \left[I \quad B^{ij} \quad D^{ij} + \Psi^i \Gamma^{ij} N^{ij} \right] \begin{Bmatrix} \dot{R}^i \\ \dot{\theta}^i \\ \dot{e}^{ij} \end{Bmatrix} \quad (3.8)$$

where I is an identity matrix.

3.2.1 Kinetic Energy Expression

The kinetic energy of the element ij is obtained by integrating the kinetic energy of the infinitesimal volume at point p^{ij} over the volume V^{ij} ,

$$T^{ij} = \frac{1}{2} \int_{V^{ij}} \mu^{ij} \bar{r}_p^{ijT} \bar{r}_p^{ij} dV^{ij} \quad (3.9)$$

The parameter μ^{ij} is the mass density of the element, and the superscript T implies transpose of a matrix. Using the vector notation $q^{ij} = [R^{i^T}, \theta^{i^T}, e^{ij^T}]^T$ and substituting Eq.(3.8) into Eq.(3.9), the kinetic energy expression becomes

$$T^{ij} = \frac{1}{2} \dot{q}^{ij^T} M^{ij} \dot{q}^{ij} \quad (3.10)$$

where M^{ij} is the mass matrix of element ij ,

$$M^{ij} = \int_{V^{ij}} \mu^{ij} \begin{bmatrix} I & B^{ij} \\ B^{ij^T} & B^{ij^T} B^{ij} \\ D^{ij^T} + N^{ij^T} \Gamma^{ij^T} \Psi^{i^T} & (D^{ij^T} + N^{ij^T} \Gamma^{ij^T} \Psi^{i^T}) B^{ij} \\ (D^{ij} + \Psi^i \Gamma^{ij} N^{ij}) & \\ B^{ij^T} (D^{ij} + \Psi^i \Gamma^{ij} N^{ij}) & \\ (D^{ij^T} + N^{ij^T} \Gamma^{ij^T} \Psi^{i^T}) (D^{ij} + \Psi^i \Gamma^{ij} N^{ij}) & \end{bmatrix} dV^{ij} \quad (3.11)$$

Orthonormality of the transformation matrices Ψ^i and Γ^{ij} , i.e., $\Psi^{i^T} \Psi^i = I$, $\Gamma^{ij^T} \Gamma^{ij} = I$, is utilized to simplify the lower right submatrix of Eq.(3.11). Note that the mass matrix M^{ij} is function of the generalized coordinates, but the submatrix $N^{ij^T} N^{ij}$ associated with the element elastic coordinates is constant. The individual elements of the mass matrix given in Eq.(3.11), when simplified, gives the following matrices:

$$\begin{aligned}
\int_{V^{ij}} \mu^{ij} B^{ijT} B^{ij} dV^{ij} &\equiv \text{the mass matrix due to rigid body rotations} \\
\int_{V^{ij}} \mu^{ij} D^{ijT} D^{ij} dV^{ij} &\equiv \text{the matrices due to torsion, rotary inertia} \\
&\quad \text{and inertia coupling of elastic coordinates} \\
\int_{V^{ij}} \mu^{ij} N^{ijT} N^{ij} dV^{ij} &\equiv \text{the mass matrix due to elastic translations} \\
\int_{V^{ij}} \mu^{ij} B^{ijT} D^{ij} dV^{ij} &\equiv \text{matrix due to gyroscopic moments}
\end{aligned}$$

All the above discussed matrices are constant matrices except the matrix due to inertia coupling of elastic coordinates, which is nonlinear and function of elastic nodal coordinates.

The kinetic energy T^i of the i^{th} body is obtained by summing up the kinetic energies of all elements in the body. Denoting the number of elements by n^i , T^i is given by

$$T^i = \sum_{j=1}^{n^i} T^{ij} = \frac{1}{2} \dot{q}^{iT} M^i \dot{q}^i \quad (3.12)$$

where q^i is the vector of generalized coordinates of body i given by $q^i = [R^{iT}, \theta^{iT}, e^{iT}]^T$, where e^i is the vector of nodal coordinates of all the elements of body i . The matrix M^i is

$$M^i = \begin{bmatrix} M_{11}^i & M_{12}^i & M_{13}^i \\ M_{21}^i & M_{22}^i & M_{23}^i \\ M_{31}^i & M_{32}^i & M_{33}^i \end{bmatrix} \quad (3.13)$$

where

$$\begin{aligned}
M_{11}^i &= \sum_{j=1}^{n^i} \int_{V^{ij}} \mu^{ij} I \, dV^{ij} \\
M_{12}^i &= \sum_{j=1}^{n^i} \int_{V^{ij}} \mu^{ij} B^{ij} \, dV^{ij} \\
M_{13}^i &= \sum_{j=1}^{n^i} \int_{V^{ij}} \mu^{ij} (D^{ij} + \Psi^i \Gamma^{ij} N^{ij}) \, dV^{ij} \\
M_{22}^i &= \sum_{j=1}^{n^i} \int_{V^{ij}} \mu^{ij} B^{ijT} B^{ij} \, dV^{ij} \\
M_{23}^i &= \sum_{j=1}^{n^i} \int_{V^{ij}} \mu^{ij} B^{ijT} (D^{ij} + \Psi^i \Gamma^{ij} N^{ij}) \, dV^{ij} \\
M_{33}^i &= \sum_{j=1}^{n^i} \int_{V^{ij}} \mu^{ij} (D^{ijT} + N^{ijT} \Gamma^{ijT} \Psi^{iT}) (D^{ij} + \Psi^i \Gamma^{ij} N^{ij}) \, dV^{ij}
\end{aligned}$$

The other submatrices M_{21}^i , M_{31}^i , M_{32}^i are the transpose of M_{12}^i , M_{13}^i , M_{23}^i , respectively.

3.2.2 Strain Energy Expression

The strain energy of the finite element ij can be written in the form

$$\begin{aligned}
U^{ij} &= \frac{1}{2} \int_{V^{ij}} \left[E^{ij} \left\{ \epsilon_x^{ij^2} + \epsilon_y^{ij^2} + \epsilon_z^{ij^2} \right\} + G^{ij} \left\{ \epsilon_{xy}^{ij^2} + \epsilon_{yz}^{ij^2} + \epsilon_{zx}^{ij^2} \right\} \right] dV^{ij} \\
&= \frac{1}{2} \int_{V^{ij}} \left[E^{ij} \left\{ \epsilon_x^{ijT} \epsilon_x^{ij} + \epsilon_y^{ijT} \epsilon_y^{ij} + \epsilon_z^{ijT} \epsilon_z^{ij} \right\} \right. \\
&\quad \left. + G^{ij} \left\{ \epsilon_{xy}^{ijT} \epsilon_{xy}^{ij} + \epsilon_{yz}^{ijT} \epsilon_{yz}^{ij} + \epsilon_{zx}^{ijT} \epsilon_{zx}^{ij} \right\} \right] dV^{ij} \tag{3.14}
\end{aligned}$$

where ε_x^{ij} , ε_y^{ij} , ε_z^{ij} are the strains in the X^{ij} , Y^{ij} and Z^{ij} directions respectively, and ε_{xy}^{ij} , ε_{yz}^{ij} , ε_{zx}^{ij} are the shear strains of the finite element ij . The other parameters represent modulus of elasticity E^{ij} and the shear modulus G^{ij} . The strains, in general, can be written in terms of nodal coordinates as

$$\varepsilon^{ij} = \hat{B}^{ij} e^{ij} \quad (3.15)$$

where \hat{B}^{ij} is called the curvature matrix. Equation (3.15) is valid for all the subscripts of ε shown in Eq.(3.14). Substituting Eq.(3.15) in Eq.(3.14) the strain energy expression can be written as

$$U^{ij} = \frac{1}{2} e^{ijT} K^{ij} e^{ij} \quad (3.16)$$

where

$$K^{ij} = \int_{V^{ij}} \left[E^{ij} \left\{ \hat{B}_x^{ijT} \hat{B}_x^{ij} + \hat{B}_y^{ijT} \hat{B}_y^{ij} + \hat{B}_z^{ijT} \hat{B}_z^{ij} \right\} + G^{ij} \left\{ \hat{B}_{xy}^{ijT} \hat{B}_{xy}^{ij} + \hat{B}_{yz}^{ijT} \hat{B}_{yz}^{ij} + \hat{B}_{zx}^{ijT} \hat{B}_{zx}^{ij} \right\} \right] dV^{ij} \quad (3.17)$$

The individual terms of the stiffness matrix of Eq.(3.17) gives the following matrices:

$$\int_{V^{ij}} E^{ij} \left\{ \hat{B}_x^{ijT} \hat{B}_x^{ij} + \hat{B}_y^{ijT} \hat{B}_y^{ij} + \hat{B}_z^{ijT} \hat{B}_z^{ij} \right\} dV^{ij} \equiv \text{the elastic stiffness matrix}$$

due to normal strains

$$\int_{V^{ij}} G^{ij} \left\{ \hat{B}_{xy}^{ijT} \hat{B}_{xy}^{ij} + \hat{B}_{yz}^{ijT} \hat{B}_{yz}^{ij} + \hat{B}_{zx}^{ijT} \hat{B}_{zx}^{ij} \right\} dV^{ij} \equiv \text{the stiffness matrices due to}$$

shear and torsion

All the individual matrices discussed above, that contribute to the strain energy, are constant matrices. The total strain energy of the i^{th} body is the sum of the strain energies of all the individual elements, and is given by

$$U^i = \sum_{j=1}^{n^i} U^{ij} = \frac{1}{2} q^{iT} K^i q^i \quad (3.18)$$

where

$$K^i = \begin{bmatrix} 0 & 0 & 0 \\ 0 & 0 & 0 \\ 0 & 0 & \bar{K}^i \end{bmatrix} \quad (3.19)$$

where \bar{K}^i is the assembled stiffness matrix of the body i .

3.2.3 The Generalized Forces

The virtual work expression of all forces acting on element ij can be written as

$$\delta W^{ij} = Q^{ijT} \delta q^{ij} \quad (3.20)$$

where Q^{ij} is the vector of generalized forces associated with generalized coordinates q^{ij} . The effect of all forces, except the workless constraint forces between elements, is included in δW^{ij} of Eq.(3.20). The virtual work expression for body i is given by

$$\begin{aligned}\delta W^i &= \sum_{j=1}^{n^i} \delta W^{ij} \\ &= Q^{iT} \delta q^i\end{aligned}\tag{3.21}$$

3.2.4 Equation of Motion

Let $q = [q^{1T}, q^{2T}, \dots, q^{n_b T}]^T$, where n_b is the total number of bodies in the system, be the composite vector of the multibody system generalized coordinates. The holonomic constraints between different bodies in the system can be written in a vector function form as

$$\Theta(q, t) = 0\tag{3.22}$$

where $\Theta(q, t) = [\Theta_1(q, t), \dots, \Theta_m(q, t)]^T$ and all equations are assumed to be independent. The subscript m denotes the number of constraints. The variational form of the equation of motion for the i^{th} body, for all virtual displacements δq^i that are consistent with the constraints given by Eq.(3.22), is

$$\left[\frac{d}{dt} (T_{\dot{q}^i}^i) - T_{q^i}^i + U_{q^i}^i - Q^{iT} \right] \delta q^i = 0\tag{3.23}$$

where subscript q denotes differentiation with respect to a vector q . Making use of the Lagrange multiplier vector $F \in R^m$, the equation of motion can be written as

$$\frac{d}{dt} (T_{\dot{q}^i}^i)^T - (T_{q^i}^i)^T + (U_{q^i}^i)^T - Q^i + \Theta_{q^i}^T F = 0 \quad (3.24)$$

After carrying out the differentiation, the equation of motion can be written in the form

$$M^i \ddot{q}^i + C^i \dot{q}^i + K^i q^i = Q^i - \Theta_{q^i}^T F \quad (3.25)$$

where M^i is the mass matrix, C^i is the matrix associated with the gyroscopic moments and Coriolis forces, K^i is the stiffness matrix of the body i , and Θ_{q^i} is the Jacobian matrix of the constraints on body i .

3.3 The Rotor-Bearing System

In this section, the generalized multibody formulation of equation (3.25) will be applied to a rotor-bearing system. In this context, all the coefficient matrices will be explicitly evaluated to include the contributions of all the basic rotor components, e.g. shafts, disks, bearings, etc. For complete dynamic modeling of rotors, the following important features need to be included:

1. Shear deflection and rotary inertia effects.
2. Gyroscopic effects which couple motions in two directions.

3. Variable shaft geometry, e.g. tapered, stepped, solid as well as hollow shaft sections.
4. Type of bearings, e.g. rigid, isotropic, or orthotropic.

3.3.1 General Assumptions

One may start by stating all the assumptions that underlie the formulation.

1. The material of the rotor is elastic, homogeneous and isotropic.
2. The plane cross-section initially perpendicular to the neutral axis of the rotor remain plane, but no longer perpendicular to the neutral axis during bending.
3. The deflection of the rotor is represented by the displacements of points of its center line.
4. The axial deformation of the rotor is small and can be neglected.
5. The shaft is flexible, while disks are treated as rigid.
6. Aerodynamic forces are neglected

3.3.2 Kinetic Energy Expression of the Shaft

Referring to Figure 3-2, the rotor-bearing system is defined by an inertial frame XYZ and a body fixed Cartesian coordinate system $X^iY^iZ^i$. The rotor shaft is considered as the body i and is divided into a number of finite elements. The rotor shaft is rotating

about its X^i -axis with a constant spin speed of $\dot{\theta}_x^i$. Therefore the transformation matrix between the body fixed $X^i Y^i Z^i$ axis and the inertial frame XYZ is

$$\Psi^i(\theta^i) = \begin{bmatrix} 1 & 0 & 0 \\ 0 & \cos \theta_x^i & -\sin \theta_x^i \\ 0 & \sin \theta_x^i & \cos \theta_x^i \end{bmatrix} \quad (3.26)$$

Consider a point p^{ij} on the ij^{th} element of the rotor shaft. The ij^{th} element undergoes two bending deformations v^{ij} and w^{ij} in the Y^{ij} and Z^{ij} directions, respectively. Referring to Figure 3-3, any cross section of the element undergoes the following three elastic rotations: torsional deformation ϕ^{ij} about X_1^{ij} , β^{ij} about Y_2^{ij} and γ^{ij} about Z_3^{ij} . The transformation matrix Γ^{ij} between the elemental coordinate system $X^{ij} Y^{ij} Z^{ij}$ and the body fixed coordinate system $X^i Y^i Z^i$ is calculated as

$$\Gamma^{ij} = \begin{bmatrix} 1 & -\gamma & -\beta \\ \gamma - \phi\beta & 1 + \phi\beta\gamma & -\phi \\ \phi\gamma + \beta & \phi - \beta\gamma & 1 \end{bmatrix} \quad (3.27)$$

where ϕ , β and γ are elastic rotations which belong to the small deformations within the hypothesis of the linear theory of elasticity. Therefore the following substitutions have been made in Eq.(3.27):

$$\cos \phi = \cos \beta = \cos \gamma = 1$$

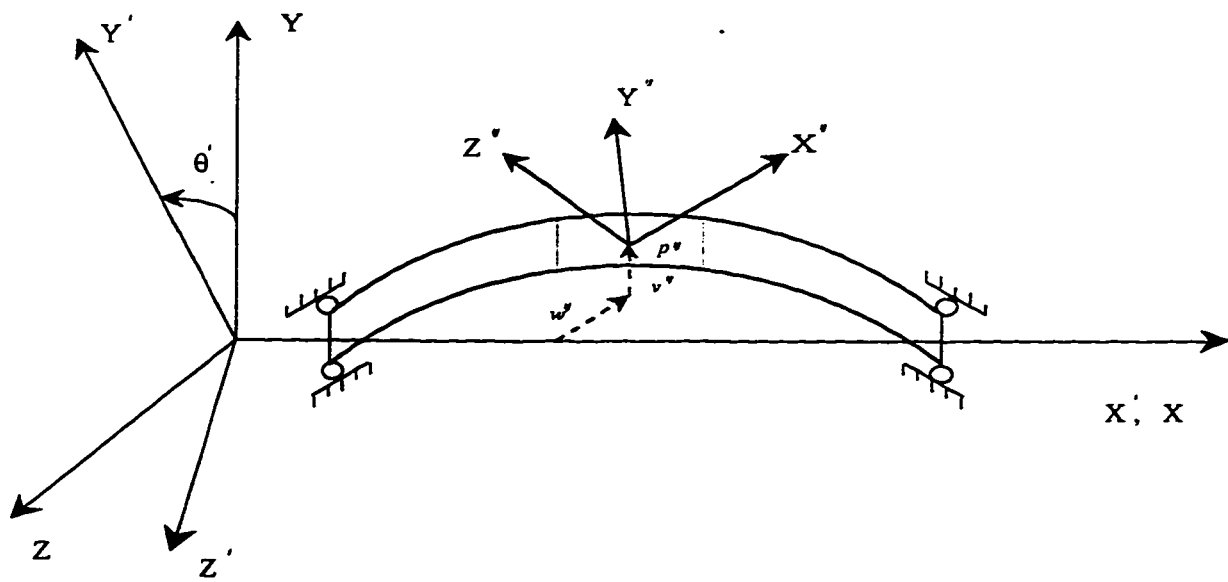


Figure 3-2: A rotor-bearing system: coordinates

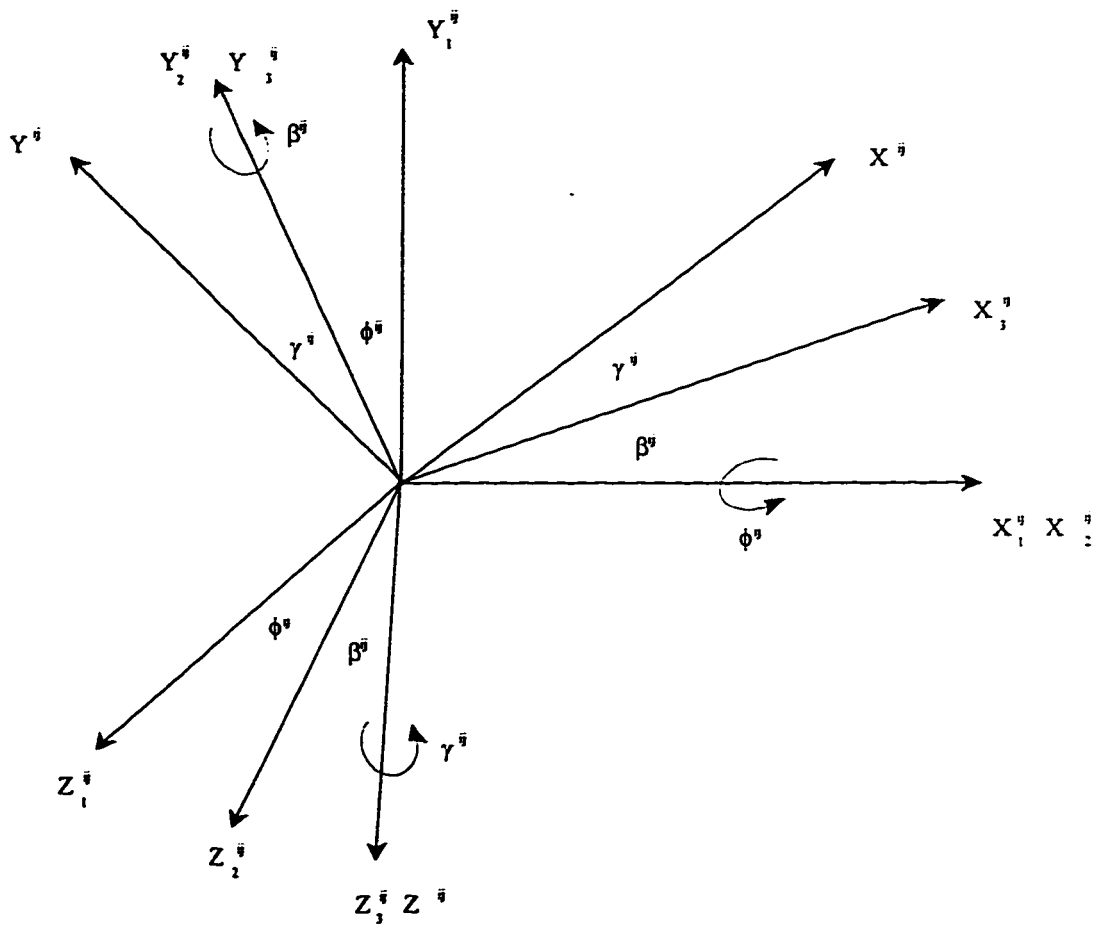


Figure 3-3: Transformation of axes

$$\sin \phi = \phi, \sin \beta = \beta, \sin \gamma = \gamma$$

Neglecting second order terms, the transformation matrix Γ^{ij} can be further simplified as

$$\Gamma^{ij} = \begin{bmatrix} 1 & -\gamma & -\beta \\ \gamma & 1 & -\phi \\ \beta & \phi & 1 \end{bmatrix} \quad (3.28)$$

It is observed that the transformation matrix Γ^{ij} is an antisymmetric matrix. As mentioned earlier in this section, the rotor shaft rotates about its X^i -axis only with a constant spin speed of $\dot{\theta}_x^i$. Considering the reference rotation θ_x^i together with the elastic degrees of freedom, the kinetic energy of the finite element ij is

$$T^{ij} = \frac{1}{2} \dot{q}^{ijT} M^{ij} \dot{q}^{ij} \quad (3.29)$$

where

$$q^{ij} = \left\{ \theta_x^i, e^{ijT} \right\}^T \quad (3.30)$$

and M^{ij} , the mass matrix of element ij is

$$M^{ij} = \int_{V^{ij}} \mu^{ij} \begin{bmatrix} B^{ijT} B^{ij} & B^{ijT} (D^{ij} + \Psi^i \Gamma^{ij} N^{ij}) \\ (D^{ijT} + N^{ijT} \Gamma^{ijT} \Psi^{iT}) B^{ij} & (D^{ijT} + N^{ijT} \Gamma^{ijT} \Psi^{iT}) (D^{ij} + \Psi^i \Gamma^{ij} N^{ij}) \end{bmatrix} dV^{ij} \quad (3.31)$$

Simplifying, the mass matrix can be written as

$$M^{ij} = \int_{l^{ij}} \mu^{ij} \begin{bmatrix} I_p^{ij} & e^{ijT} \bar{g}^{ij} \\ \bar{g}^{ijT} e^{ij} & \bar{m}^{ij} \end{bmatrix} dl^{ij} \quad (3.32)$$

where

$$\begin{aligned} I_p^{ij} &= \int_{A^{ij}} B^{ijT} B^{ij} dA^{ij} \\ e^{ijT} \bar{g}^{ij} &= \int_{A^{ij}} B^{ijT} (D^{ij} + \Psi^i \Gamma^{ij} N^{ij}) dA^{ij} \\ \bar{g}^{ijT} e^{ij} &= \int_{A^{ij}} (D^{ijT} + N^{ijT} \Gamma^{ijT} \Psi^{iT}) B^{ij} dA^{ij} \end{aligned}$$

and

$$\bar{m}^{ij} = \int_{A^{ij}} (D^{ijT} + N^{ijT} \Gamma^{ijT} \Psi^{iT}) (D^{ij} + \Psi^i \Gamma^{ij} N^{ij}) dA^{ij}$$

where l^{ij} is the length and A^{ij} is the cross-sectional area of the ij^{th} element. Substituting the above simplified mass matrix in the kinetic energy expression and writing

$$\dot{e}^{ijT} \bar{g}^{ijT} e^{ij} + e^{ijT} \bar{g}^{ij} \dot{e}^{ij} = -2\dot{e}^{ijT} \hat{g}^{ij} e^{ij}$$

the kinetic energy can be written in expanded form as

$$T^{ij} = \frac{1}{2} \Gamma^{ij} \dot{\theta}_x^2 + \frac{1}{2} \dot{e}^{ijT} m^{ij} \dot{e}^{ij} - \dot{\theta}_x^i e^{ijT} g^{ij} e^{ij} \quad (3.33)$$

where

$$\Gamma^{ij} = \int_{V^{ij}} \mu^{ij} \Gamma_p^{ij} dx^{ij} \quad (3.34)$$

$$m^{ij} = \int_{V^{ij}} \mu^{ij} \bar{m}^{ij} dx^{ij} \quad (3.35)$$

and

$$g^{ij} = \int_{V^{ij}} \mu^{ij} \bar{g}^{ij} dx^{ij} \quad (3.36)$$

The matrix g^{ij} is the gyroscopic matrix and m^{ij} is called the composite mass matrix which can be written as

$$m^{ij} = m_t^{ij} + m_r^{ij} + m_\phi^{ij} + m_e^{ij} \quad (3.37)$$

where m_t^{ij} is the mass matrix due to elastic flexural deflections of the shaft finite element in the Y and Z - directions, m_r^{ij} is the mass matrix due to rotary inertia, m_ϕ^{ij} is the mass matrix due to torsion and m_e^{ij} is the inertia coupling matrix which couples the flexural and torsional motions and is a function of nodal coordinates.

Now, recalling Eq.(3.12) the kinetic energy of the shaft can be written as

$$T^i = \sum_{j=1}^{n^i} T^{ij} = \frac{1}{2} \dot{q}^{iT} M^i \dot{q}^i \quad (3.38)$$

where $q^i = [\theta_x^i, e^{iT}]^T$, the vector e^i contains all the nodal coordinates of the shaft, and

the matrix M^i is given by

$$M^i = \begin{bmatrix} m_{11}^i & m_{12}^i \\ m_{21}^i & m_{22}^i \end{bmatrix} \quad (3.39)$$

where

$$m_{11}^i = \sum_{j=1}^{n^i} \Gamma^{ij} \quad (3.40)$$

$$m_{12}^i = -m_{21}^i = \sum_{j=1}^{n^i} \hat{g}^{ij} \quad (3.41)$$

$$m_{22}^i = \sum_{j=1}^{n^i} m^{ij} \quad (3.42)$$

3.3.3 The Stain Energy Expression of the Shaft

The finite element ij of the rotor shaft deforms by v^{ij} and w^{ij} in the Y^{ij} and Z^{ij} directions. Its axial deformation is neglected. The deformations in the Y^{ij} and Z^{ij} directions cause axial strain in the X^{ij} direction only. The strains in Y^{ij} and Z^{ij} directions are zeros. Hence, the strain energy of the shaft finite element ij can be written in the form

$$\begin{aligned} U^{ij} &= \frac{1}{2} \int_0^{l^{ij}} E^{ij} \Gamma^{ij} \left\{ \left(\frac{\partial \beta^{ij}}{\partial X^{ij}} \right)^2 + \left(\frac{\partial \gamma^{ij}}{\partial X^{ij}} \right)^2 \right\} dX^{ij} \\ &+ \frac{1}{2} \int_0^{l^{ij}} \kappa G^{ij} A^{ij} \left\{ \left(\frac{\partial v^{ij}}{\partial X^{ij}} - \gamma^{ij} \right)^2 + \left(\frac{\partial w^{ij}}{\partial X^{ij}} + \beta^{ij} \right)^2 \right\} dX^{ij} \\ &+ \frac{1}{2} \int_0^{l^{ij}} G^{ij} J^{ij} \left(\frac{\partial \phi^{ij}}{\partial X^{ij}} \right)^2 dX^{ij} \end{aligned} \quad (3.43)$$

where v^{ij} and w^{ij} are flexural deformations in Y^{ij} and Z^{ij} directions, while ϕ^{ij} , β^{ij} and γ^{ij} represent small rotations about the X_1^{ij} , Y_2^{ij} and Z_3^{ij} axes, respectively, of the point p^{ij} . The other parameters represent modulus of elasticity E^{ij} , the shear modulus G^{ij} , the second moment of the cross-sectional area I^{ij} , the polar moment of inertia J^{ij} and the shear correction factor κ . Now, Eq.(3.43) can be written in matrix form as

$$U^{ij} = \frac{1}{2} e^{ijT} K^{ij} e^{ij} \quad (3.44)$$

The matrix $K^{ij} = K_e^{ij} + K_s^{ij} + K_\phi^{ij}$ is the element composite stiffness matrix, where K_e^{ij} represents the elastic stiffness, K_s^{ij} accounts for the shear stiffness, and K_ϕ^{ij} represents the torsional stiffness. These can be expressed as

$$K_e^{ij} = \int_0^{l^{ij}} \left(\frac{\partial N_\beta^{ij}}{\partial X^{ij}} \right)^T E^{ij} I^{ij} \left(\frac{\partial N_\beta^{ij}}{\partial X^{ij}} \right) dX^{ij} \quad (3.45)$$

$$K_\phi^{ij} = \int_0^{l^{ij}} \left(\frac{\partial N_\phi^{ij}}{\partial X^{ij}} \right)^T G^{ij} J^{ij} \left(\frac{\partial N_\phi^{ij}}{\partial X^{ij}} \right) dX^{ij} \quad (3.46)$$

$$K_s^{ij} = \int_0^{l^{ij}} \kappa G^{ij} A^{ij} \begin{bmatrix} \frac{\partial N_{\gamma\gamma}^{ij}}{\partial X^{ij}} - N_{\beta\gamma}^{ij} \\ \frac{\partial N_{\gamma\gamma}^{ij}}{\partial X^{ij}} + N_{\beta\beta}^{ij} \end{bmatrix}^T \begin{bmatrix} \frac{\partial N_{\gamma\gamma}^{ij}}{\partial X^{ij}} - N_{\beta\gamma}^{ij} \\ \frac{\partial N_{\gamma\gamma}^{ij}}{\partial X^{ij}} + N_{\beta\beta}^{ij} \end{bmatrix} dX^{ij} \quad (3.47)$$

Here, the different shape functions are defined by the following relationships:

$$\begin{Bmatrix} v^{ij} \\ w^{ij} \end{Bmatrix} = N_v^{ij} e^{ij} = \begin{bmatrix} N_{vw}^{ij} \\ N_{vw}^{ij} \end{bmatrix} e^{ij} \quad (3.48)$$

$$\begin{Bmatrix} \beta^{ij} \\ \gamma^{ij} \end{Bmatrix} = N_{\beta}^{ij} e^{ij} = \begin{bmatrix} N_{\beta\beta}^{ij} \\ N_{\beta\gamma}^{ij} \end{bmatrix} e^{ij} \quad (3.49)$$

$$\phi^{ij} = N_{\phi}^{ij} e^{ij} \quad (3.50)$$

The strain energy of the shaft is now given by

$$U^i = \sum_{j=1}^{n^i} U^{ij} = \frac{1}{2} q^{iT} K^i q^i \quad (3.51)$$

where

$$K^i = \begin{bmatrix} 0 & 0 \\ 0 & \bar{K}^i \end{bmatrix} \quad (3.52)$$

where \bar{K}^i is the assembled stiffness matrix of the body i .

3.3.4 The Disk

Let the number of disks present in the rotor-bearing system be n^d . The disk is assumed to be rigid and is solely characterized by its contribution to the system's kinetic energy. Following the same procedure of section 3.2.1, the kinetic energy for a disk can be written as

$$T^{dj} = \frac{1}{2} I^{dj} \dot{\theta}_x^2 + \frac{1}{2} \dot{e}^{djT} m^{dj} e^{dj} - \dot{\theta}_x \dot{e}^{djT} g^{dj} e^{dj} \quad (3.53)$$

The kinetic energy of all the disks can be written as

$$T^d = \sum_{j=1}^{n^d} T^{dj} = \frac{1}{2} \dot{q}^{d^T} M^d \dot{q}^d \quad (3.54)$$

where $q^d = [\theta_x^{d^T}, e^{d^T}]^T$, the vector e^d contains the nodal coordinates of all the nodes at which the disks are located on the shaft. The matrix M^d is similar to the matrix M^i of Eq.(3.39).

3.3.5 The Bearings

Let the number of bearings present in the rotor-bearing system be n^b . The bearings are modelled as flexible with damping. The deflection of the rotor inside the ports of the bearings results in generalized forces acting on the shaft. The virtual work expression of all the forces acting on the shaft element ij is

$$\delta W^{bj} = Q^{bj^T} \delta e^{ij} \quad (3.55)$$

The generalized force vector Q^{bj^T} is given by

$$Q^{bj^T} = -C^{bj} \dot{e}^{ij} - K^{bj} e^{ij} \quad (3.56)$$

where C^{bj} is the damping matrix and K^{bj} is the stiffness matrix of the j^{th} bearing. The virtual work expression for all the bearings can be written as

$$\delta W^b = \sum_{j=1}^{n^b} \delta W^{bj} = Q^{b^T} \delta q^b \quad (3.57)$$

where

$$Q^{b^T} = \sum_{j=1}^{n^b} (-C^{bj} e^{ij} - K^{bj} e^{ij}) \quad (3.58)$$

3.3.6 Equation of Motion of the Rotor-Bearing System

The equation of motion of the rotor-bearing system can be derived using Lagrange's equation of the unconstrained system (with embedded constraints) as

$$\frac{d}{dt} \left(\frac{\partial L}{\partial \dot{q}} \right) - \frac{\partial L}{\partial q} = Q \quad (3.59)$$

where

$$L = T - U \quad = \text{Lagrangian function}$$

$$q = [q^{i^T}, q^{a^T}, q^{b^T}]^T \quad = \text{generalized coordinates}$$

$$Q \quad = \text{vector of generalized forces}$$

Here, the vector q represents only the independent nodal degrees of freedom, where other constrained nodal displacements according to the boundary conditions were embedded.

The term T is the total kinetic energy of the rotor-bearing system which is the sum of kinetic energies of the shaft and disks. The term U is the total strain energy of the system with the shaft being the only contributor. Substituting L in the above equation,

the equation of motion are obtained as

$$m_{11}^i \ddot{\theta}_x^i = Q_1 \quad (3.60)$$

where m_{11}^i is as defined in Eq.(3.40), Q_1 is the external torque acting in the direction of θ_x^i and

$$m_{22}^i \ddot{e}^i + \dot{\theta}_x^i g^i \dot{e}^i + k^i e^i = Q_2 \quad (3.61)$$

where

$$g^i = m_{12}^i - m_{21}^i \quad (3.62)$$

m^i , g^i and k^i are the system mass, gyroscopic and stiffness matrices, respectively, and $Q_2 = F^{iT} + Q^{bT}$ is the vector of generalized forces. The vector F^i contains all the external forces acting on the shaft. It is noted that $Q = \{Q_1^T, Q_2^T\}^T$.

Chapter 4

Finite Element Formulation of Cracked Shaft

This chapter represents the derivation of a new tapered cracked shaft finite element. When the rotor-bearing system is modelled using the finite element method, its configuration can be defined by a properly generated mesh of finite shaft elements. The disk and bearing properties are added at respective nodes. Combination of unequal shaft elements are permitted by the model developed in this study. In this chapter, the cross-sectional properties of the tapered shaft finite element will be expressed in non-dimensional forms. The shape functions of the tapered shaft finite element will be derived. Finally, the closed form expressions of the cracked tapered shaft finite element matrices will be presented.

4.1 Tapered Cracked Shaft Element

In this formulation, linearly tapered shaft elements are considered. A linearly tapered shaft element of circular cross-section has its radius varying linearly with length, so that its area and moment of inertia are second and fourth order functions of axial position, respectively. The element consists of two nodes and each node has five degrees of freedom; two transverse displacements (v^{ij}, w^{ij}) , two bending rotations $(\beta^{ij}, \gamma^{ij})$ and a torsional rotation (ϕ^{ij}) . A crack is present at an arbitrary location between the two nodes of the tapered shaft finite element. The presence of crack introduces local flexibility in the element. The local flexibility of the element is modelled using a parameter called the crack compliance.

4.1.1 Cross-Sectional Properties

A typical axial cross-section of a linearly tapered finite shaft element is shown in Figure 4-1. It is assumed that the cross-sectional properties in a given element are continuous functions of the axial position, and the element cross-section has two planes of symmetry $X^{ij} - Z^{ij}$ and $X^{ij} - Y^{ij}$. In this formulation, the general case of a hollow tapered shaft element will be considered. In this regard, the notations of reference [27, 28] will be adopted in describing the cross-sectional geometrical parameters.

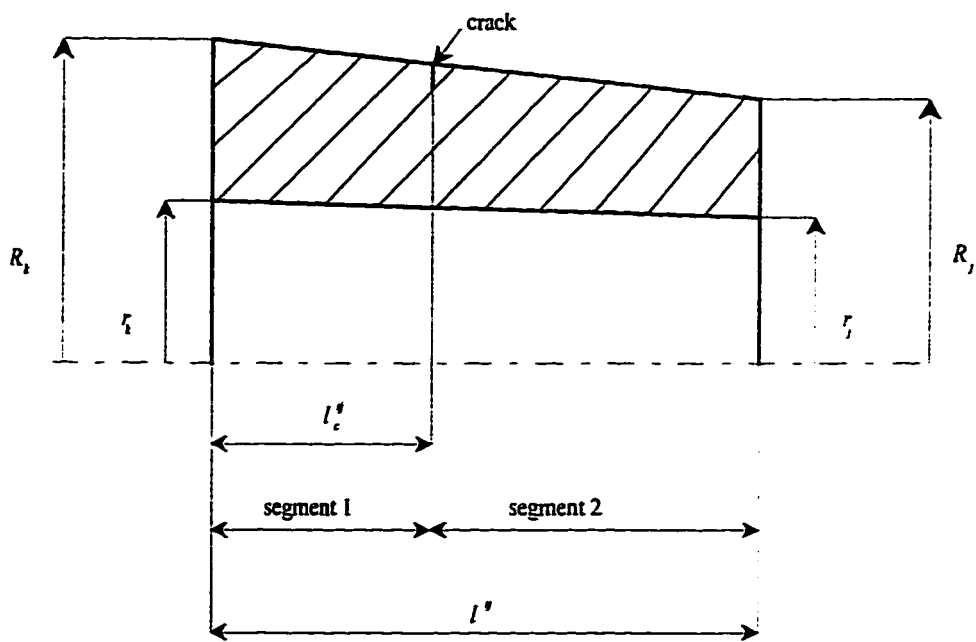


Figure 4-1: The shaft finite element with crack

Hollow Tapered Shaft Element

The cross-section at each end of the element is associated with an inner radius r and an outer radius R . Defining a non-dimensional position coordinate ξ^{ij} equal to the ratio $\frac{x^{ij}}{l^{ij}}$, the inner and outer radii may be expressed as

$$r = r_k (1 - \xi^{ij}) + r_j \xi^{ij} \quad (4.1a)$$

$$R = R_k (1 - \xi^{ij}) + R_j \xi^{ij} \quad (4.1b)$$

where the subscripts k and j refer to the left end ($x^{ij} = 0$) and right end ($x^{ij} = l^{ij}$) of the element, respectively.

Representing the ratios of inner and outer radii on each end as ρ and α , which are equal to $\frac{r_j}{r_k}$ and $\frac{R_j}{R_k}$, respectively, one can write equations (4.1a) and (4.1b) in the form

$$r = r_k (1 + (\rho - 1) \xi^{ij}) \quad (4.2a)$$

$$R = R_k (1 + (\alpha - 1) \xi^{ij}) \quad (4.2b)$$

Using equations (4.2a) and (4.2b) in the cross-sectional area expression results in the following second order polynomial expressions:

$$A^{ij} = \pi (R^2 - r^2) = A_k \left[1 + \alpha_1 \xi^{ij} + \alpha_2 \xi^{ij^2} \right] \quad (4.3)$$

where the following expressions are introduced:

$$A_k = \pi (R_k^2 - r_k^2) \quad (4.4)$$

$$\alpha_1 = \frac{2 [R_k^2 (\alpha - 1) - r_k^2 (\rho - 1)]}{(R_k^2 - r_k^2)} \quad (4.5)$$

$$\alpha_2 = \frac{[R_k^2 (\alpha - 1)^2 - r_k^2 (\rho - 1)^2]}{(R_k^2 - r_k^2)} \quad (4.6)$$

Similarly for cross-sectional moments of inertia, the use of equations (4.2a) and (4.2b) results in a fourth order polynomial expression

$$I^{ij} = \frac{\pi (R^4 - r^4)}{4} = I_k \left[1 + \delta_1 \xi^{ij} + \delta_2 \xi^{ij^2} + \delta_3 \xi^{ij^3} + \delta_4 \xi^{ij^4} \right] \quad (4.7)$$

where the coefficients are given by

$$I_k = \frac{\pi (R_k^4 - r_k^4)}{4} \quad (4.8)$$

$$\delta_1 = \frac{4 [R_k^4 (\alpha - 1) - r_k^4 (\rho - 1)]}{(R_k^4 - r_k^4)} \quad (4.9)$$

$$\delta_2 = \frac{6 [R_k^4 (\alpha - 1)^2 - r_k^4 (\rho - 1)^2]}{(R_k^4 - r_k^4)} \quad (4.10)$$

$$\delta_3 = \frac{4 [R_k^4 (\alpha - 1)^3 - r_k^4 (\rho - 1)^3]}{(R_k^4 - r_k^4)} \quad (4.11)$$

$$\delta_4 = \frac{[R_k^4 (\alpha - 1)^4 - r_k^4 (\rho - 1)^4]}{(R_k^4 - r_k^4)} \quad (4.12)$$

Solid Tapered Shaft Element

If the shaft is solid the inner radius r does not exist. Hence the cross-sectional properties are evaluated by ignoring r in the Eqs.(4.1-4.12).

4.1.2 Derivation of Shape Functions

As discussed earlier, the presence of crack introduces additional local flexibility in the cracked finite element. There are two approaches to model the stiffness of the cracked shaft finite element. In the first approach, the stiffness matrix of the cracked shaft finite element is computed by inverting the total flexibility matrix of the finite element. The total flexibility matrix is the sum of the flexibility of uncracked shaft finite element and the additional flexibility due to crack. When the additional flexibility of the crack is small, i.e., when the crack is of small size, the inversion of the flexibility matrix often results in numerical difficulties. Avoiding the inversion of matrices in a numerical scheme is desirable. Hence, the second approach which incorporates the additional flexibility of the crack in the shape functions of the cracked shaft with the help of the crack compliance parameter is a better way of modeling. This approach is a consistent approach of computing the stiffness matrix of the cracked shaft finite element directly using the shape functions which include the crack compliance parameter. There is no need to invert any matrix in this approach. The detailed procedure of deriving the shape functions of the cracked tapered shaft finite element is presented below.

Let the finite element of length l^{ij} has a crack at a distance l_c^{ij} from its left end, where

$0 < l_c^{ij} < l^{ij}$. It is assumed that the crack introduces a discontinuity at l_c^{ij} in slope due to bending. Consequently, two different displacement fields are assumed; one on each side of the crack. Therefore, referring to Figure 4-1, the deflection of segment 1 and segment 2 of the finite element in the Y^{ij} - direction will be approximated by the following two different third order polynomial shape functions

$$v_1^{ij} = a_1 + a_2x^{ij} + a_3x^{ij^2} + a_4x^{ij^3} \quad (4.13a)$$

$$v_2^{ij} = a_5 + a_6x^{ij} + a_7x^{ij^2} + a_8x^{ij^3} \quad (4.13b)$$

where v_1^{ij} represents the displacement field over segment 1, and v_2^{ij} represents the displacement field over segment 2. The total deformation v_1^{ij} is the sum of deformations due to bending $v_{1_b}^{ij}$ and shear $v_{1_s}^{ij}$. Hence one can write

$$v_1^{ij} = v_{1_b}^{ij} + v_{1_s}^{ij} \quad (4.14)$$

Differentiating Eq.(4.14) with respect to x^{ij} , we get the following relationship:

$$\begin{aligned} \frac{dv_1^{ij}}{dx^{ij}} &= \frac{dv_{1_b}^{ij}}{dx^{ij}} + \frac{dv_{1_s}^{ij}}{dx^{ij}} \\ &= \beta_1^{ij} + \theta_{1_s}^{ij} \end{aligned} \quad (4.15)$$

where

$$\frac{dv_{1_b}^{ij}}{dx^{ij}} = \beta_1^{ij} \quad (4.16)$$

is the slope of the deflection curve and

$$\frac{dv_{1s}^{ij}}{dx^{ij}} = \theta_{1s}^{ij} \quad (4.17)$$

is the shear strain. It is assumed that the transverse shear strain θ_{1s}^{ij} , which is consistent with the cubic polynomial of v_1^{ij} is independent of x^{ij} . Referring to Figure 4-2, taking equilibrium of an infinitesimal shaft segment yields

$$\frac{\partial M_o^{ij}}{\partial x^{ij}} - V_f^{ij} = 0 \quad (4.18)$$

where M_o^{ij} is the bending moment and V_f^{ij} is the shear force. The bending moment and the curvature relationship can be written as

$$M_o^{ij} = -E^{ij} I^{ij} \frac{d\beta_1^{ij}}{dx^{ij}} \quad (4.19)$$

The shear force is related to the transverse shear strain θ_{1s}^{ij} by

$$V_f^{ij} = \kappa G^{ij} A^{ij} \theta_{1s}^{ij} \quad (4.20)$$

Using Eq.(4.15) along with Eq.(4.13a), the slope of the deflection curve β_1^{ij} can be written as

$$\beta_1^{ij} = a_2 + 2a_3 x^{ij} + 3a_4 x^{ij^2} - \theta_{1s}^{ij} \quad (4.21)$$

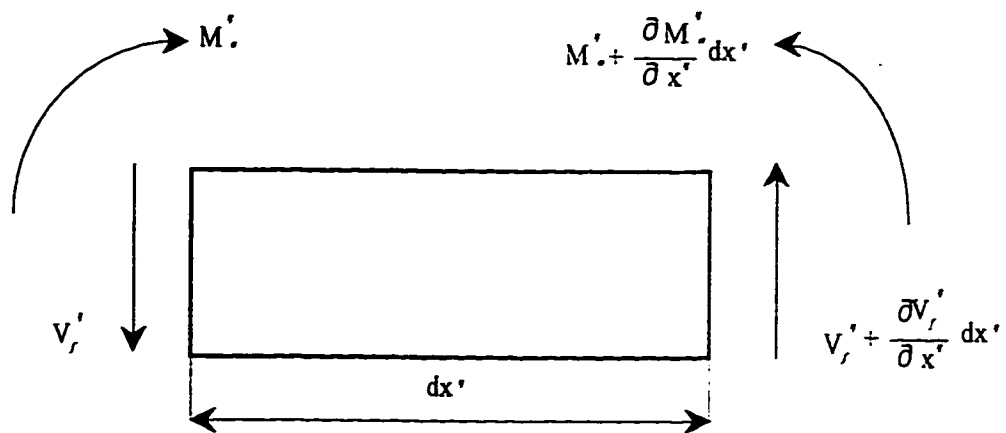


Figure 4-2: Free body diagram of an infinitesimal shaft finite element

Now, differentiating Eq.(4.21) with respect to x^{ij} , we can write

$$\frac{d\beta_1^{ij}}{dx^{ij}} = 2a_3 + 6a_4x^{ij} \quad (4.22)$$

Substituting Eq.(4.22) in Eq.(4.19), we get

$$M_o^{ij} = -E^{ij} \Gamma^{ij} (2a_3 + 6a_4x^{ij}) \quad (4.23)$$

Differentiating Eq.(4.23), with respect to x^{ij} , we can write

$$\frac{dM_o^{ij}}{dx^{ij}} = -6E^{ij} \Gamma^{ij} a_4 \quad (4.24)$$

Substituting Eq.(4.24) and Eq.(4.20) in Eq.(4.18) and simplifying, we get a relationship for the constant shear strain

$$\theta_{1*}^{ij} = -6\bar{g}a_4 \quad (4.25)$$

where

$$\bar{g} = \frac{E^{ij} \Gamma^{ij}}{\kappa G^{ij} A^{ij}} \quad (4.26)$$

Substituting Eq.(4.25) in Eq.(4.21), the slope of the deflection curve can be written as

$$\beta_1^{ij} = a_2 + 2a_3x^{ij} + (3x^{ij^2} + 6\bar{g}) a_4 \quad (4.27)$$

Following the procedure described above, the slope of deflection curve for segment 2 of

the finite element can be written similarly as

$$\beta_2^{ij} = a_6 + 2a_7 x^{ij} + (3x^{ij^2} + 6\bar{g}) a_8 \quad (4.28)$$

For a shaft finite element which is deformed in the Y^{ij} - direction due to bending, four boundary conditions can be specified. They are displacements $(v_1^{ij}(0), v_2^{ij}(l^{ij}))$ and slopes of deflection curves $(\beta_1^{ij}(0), \beta_2^{ij}(l^{ij}))$ at the two ends of the finite element. As shown in Figure 4-3, any shaft finite element can deform in four different ways. Hence, four sets of boundary conditions can be specified. They are as follows:

Referring to Figure 4-3a

Boundary Conditions (set I)

$$v_1^{ij}(0) = 1 \quad (4.29a)$$

$$v_{1,b}^{ij'}(0) = 0 \quad (4.29b)$$

$$v_2^{ij}(l^{ij}) = 0 \quad (4.29c)$$

$$v_{2,b}^{ij'}(l^{ij}) = 0 \quad (4.29d)$$

Referring to Figure 4-3b

Boundary Conditions (set II)

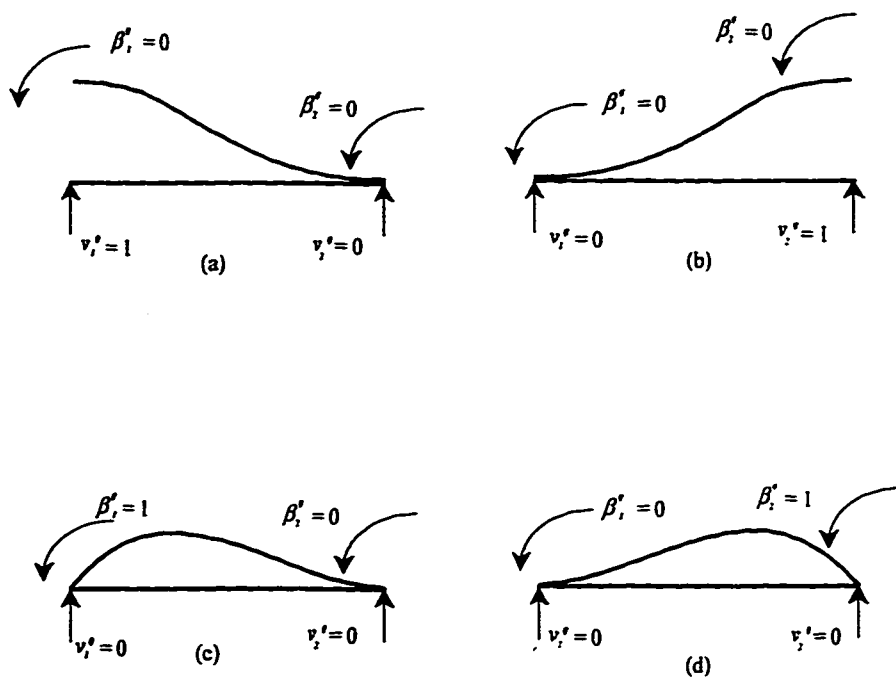


Figure 4-3: Deformation of the shaft finite element

$$v_1^{ij}(0) = 0 \quad (4.30a)$$

$$v_{1_b}^{ij'}(0) = 0 \quad (4.30b)$$

$$v_2^{ij}(l^{ij}) = 1 \quad (4.30c)$$

$$v_{2_b}^{ij'}(l^{ij}) = 0 \quad (4.30d)$$

Referring to Figure 4-3c

Boundary Conditions (set III)

$$v_1^{ij}(0) = 0 \quad (4.31a)$$

$$v_{1_b}^{ij'}(0) = 1 \quad (4.31b)$$

$$v_2^{ij}(l^{ij}) = 0 \quad (4.31c)$$

$$v_{2_b}^{ij'}(l^{ij}) = 0 \quad (4.31d)$$

Referring to Figure 4-3d

Boundary Conditions (set IV)

$$v_1^{ij}(0) = 0 \quad (4.32a)$$

$$v_{1_b}^{ij'}(0) = 0 \quad (4.32b)$$

$$v_2^{ij}(l^{ij}) = 0 \quad (4.32c)$$

$$v_{2_b}^{ij'}(l^{ij}) = 1 \quad (4.32d)$$

At the location of the crack in the finite element it is assumed that (a) the deflection is continuous, (b) there is discontinuity in slope, (c) the bending moment is continuous, and (d) the shear force is continuous. Taking into account that the effect of the crack is expressed in terms of crack compliance coefficients which are directly related to the change in stiffness due to the presence of crack. Several investigators [6, 7, 18, 21] have adopted the idea of accounting for the change in stiffness due to the presence of crack by assuming discontinuity in the slope at the crack location. However, they have preserved the continuity of moments and shear forces at the crack location since there are no actual impulses taking place due to the presence of crack. Impulsive moments and forces are known to appear due to sudden disturbances [29, 30]. This approach may seem incongruous with mathematical logic where discontinuity in slope would introduce Dirac delta function in the derivatives of the slope and correspondingly in the moments and shear forces.

In the following derivations, the same assumptions introduced by Papadopoulos and Dimarogonas [6] and adopted by other investigators [7, 18, 21] will be invoked.

Continuity Conditions

$$v_1^{ij} (l_c^{ij}) = v_2^{ij} (l_c^{ij}) \quad (4.33a)$$

$$v_{2_b}^{ij'} (l_c^{ij}) = v_{1_b}^{ij'} (l_c^{ij}) + c_y v_{1_b}^{ij''} (l_c^{ij}) \quad (4.33b)$$

$$v_{1_b}^{ij''} (l_c^{ij}) = v_{2_b}^{ij''} (l_c^{ij}) \quad (4.33c)$$

$$v_{1_b}^{ij'''} (l_c^{ij}) = v_{2_b}^{ij'''} (l_c^{ij}) \quad (4.33d)$$

where (') denotes differentiation with respect to x^{ij} , c_y is the crack compliance due to bending in the Y^{ij} - direction. Using a set of boundary conditions along with the continuity conditions, the eight unknowns in equations (4.13a) and (4.13b) can be determined.

Now Substituting Eqs.(4.13, 4.27-4.28) in the first set of boundary conditions represented by Eqs.(4.29a-4.29b), we can write

$$a_1 = 1 \quad (4.34a)$$

$$a_2 + 6\bar{g}a_4 = 0 \quad (4.34b)$$

$$a_5 + a_6 l^{ij} + a_7 l^{ij^2} + a_8 l^{ij^3} = 0 \quad (4.34c)$$

$$a_6 + 2a_7 l^{ij} + (3l^{ij^2} + 6\bar{g}) a_8 = 0 \quad (4.34d)$$

Substituting Eqs.(4.13, 4.27-4.28) in the crack continuity conditions, represented by Eq.(4.33), and simplifying we get

$$a_4 = a_8 \quad (4.35a)$$

$$a_3 = a_7 \quad (4.35b)$$

$$a_6 = a_2 + 2a_3c_y + 6a_4l_c^{ij}c_y \quad (4.35c)$$

$$a_5 = 1 - 2a_3l_c^{ij}c_y - 6a_4l_c^{ij^2}c_y \quad (4.35d)$$

Solving Eqs.(4.34) and Eqs.(4.35) simultaneously, we find the eight unknowns of Eqs.(4.13).

Therefore the shape functions for the first set of boundary conditions can be written as

$$v_1^{ij} = N_{v_{11}}^{ij} = \frac{1}{1 + \Phi^{ij}} \left[1 - 3\xi^{ij^2} + 2\xi^{ij^3} + \Phi^{ij} (1 - \xi^{ij}) \right] \quad (4.36a)$$

$$v_2^{ij} = N_{v_{21}}^{ij} = \frac{1}{1 + \Phi^{ij}} \left[1 - 3\xi^{ij^2} + 2\xi^{ij^3} + \Phi^{ij} (1 - \xi^{ij}) \right] \quad (4.36b)$$

$$\beta_1^{ij} = N_{\beta_{11}}^{ij} = \frac{6}{(1 + \Phi^{ij}) l^{ij}} \left[-\xi^{ij} + \xi^{ij^2} \right] \quad (4.36c)$$

$$\beta_2^{ij} = N_{\beta_{21}}^{ij} = \frac{6}{(1 + \Phi^{ij}) l^{ij}} \left[-\xi^{ij} + \xi^{ij^2} \right] \quad (4.36d)$$

where

$$\xi^{ij} = \frac{x^{ij}}{l^{ij}} \text{ and } \Phi^{ij} = \frac{12E^{ij}I^{ij}}{\kappa A^{ij}G^{ij}l^{ij^2}}$$

The parameter Φ^{ij} is known as the shear deformation parameter (the ratio between bending stiffness and shear stiffness), E^{ij} is the modulus of elasticity, I^{ij} is the second moment of the cross-sectional area, A^{ij} is the cross-sectional area of the shaft finite element, G^{ij} is the shear modulus, l^{ij} is the element length, and κ is the shear correction factor depending on the shape of the cross-section. The shear correction factor κ for a

solid circular cross-section is given by

$$\kappa = \frac{6(1+\nu)}{7+6\nu} \quad (4.37)$$

and for hollow circular cross-section

$$\kappa = \frac{6(1+\nu)(1+m^2)^2}{(7+6\nu)(1+m^2)^2 + (20+12\nu)m^2} \quad (4.38)$$

where ν is the Poisson's ratio and m is the ratio of inner radius to the outer radius.

Using the second set of boundary conditions represented by Eqs.(4.30) along with the crack continuity conditions represented by Eqs.(4.33) and following the procedure described above, the shape functions can be derived as

$$v_1^{ij} = N_{v_{13}}^{ij} = \frac{1}{1+\Phi^{ij}} \left[3\xi^{ij^2} - 2\xi^{ij^3} + \Phi^{ij}\xi^{ij} \right] \quad (4.39a)$$

$$v_2^{ij} = N_{v_{23}}^{ij} = \frac{1}{1+\Phi^{ij}} \left[3\xi^{ij^2} - 2\xi^{ij^3} + \Phi^{ij}\xi^{ij} \right] \quad (4.39b)$$

$$\beta_1^{ij} = N_{\beta_{13}}^{ij} = \frac{6}{(1+\Phi^{ij})l^{ij}} \left[\xi^{ij} - \xi^{ij^2} \right] \quad (4.39c)$$

$$\beta_2^{ij} = N_{\beta_{23}}^{ij} = \frac{6}{(1+\Phi^{ij})l^{ij}} \left[\xi^{ij} - \xi^{ij^2} \right] \quad (4.39d)$$

Using the third set of boundary conditions represented by Eqs.(4.31) along with the crack continuity conditions represented by Eqs.(4.33) and following the procedure described

earlier, the shape functions can be derived as

$$v_1^{ij} = N_{v_{12}}^{ij} = \frac{1}{1 + \Phi^{ij}} \left[l^{ij} \xi^{ij} - \left\{ \frac{3}{2l^{ij}} + \frac{1}{2(c_y + l^{ij})} \right\} l^{ij^2} \xi^{ij^2} + l^{ij} \xi^{ij^3} + \Phi^{ij} \left\{ \frac{l^{ij} \xi^{ij}}{2} - \frac{l^{ij^2} \xi^{ij^2}}{2(c_y + l^{ij})} \right\} \right] \quad (4.40a)$$

$$v_2^{ij} = N_{v_{22}}^{ij} = \frac{1}{1 + \Phi^{ij}} \left[\frac{c_y l^{ij}}{2(c_y + l^{ij})} + \frac{l^{ij^2}}{(c_y + l^{ij})} \xi^{ij} - \left\{ \frac{3}{2l^{ij}} + \frac{1}{2(c_y + l^{ij})} \right\} l^{ij^2} \xi^{ij^2} + l^{ij} \xi^{ij^3} + \Phi^{ij} \left\{ \frac{c_y l^{ij}}{2(c_y + l^{ij})} + \left(\frac{l^{ij}}{(c_y + l^{ij})} - \frac{1}{2} \right) l^{ij} \xi^{ij} - \frac{l^{ij^2} \xi^{ij^2}}{2(c_y + l^{ij})} \right\} \right] \quad (4.40b)$$

$$\beta_1^{ij} = N_{\beta_{12}}^{ij} = \frac{1}{1 + \Phi^{ij}} \left[1 - 2l^{ij} \xi^{ij} \left\{ \frac{3}{2l^{ij}} + \frac{1}{2(c_y + l^{ij})} \right\} + 3\xi^{ij^2} + \Phi^{ij} \left\{ 1 - \frac{l^{ij} \xi^{ij}}{(c_y + l^{ij})} \right\} \right] \quad (4.40c)$$

$$\beta_2^{ij} = N_{\beta_{22}}^{ij} = \frac{1}{1 + \Phi^{ij}} \left[\frac{l^{ij}}{(c_y + l^{ij})} - l^{ij} \xi^{ij} \left\{ \frac{3}{l^{ij}} + \frac{1}{(c_y + l^{ij})} \right\} + 3\xi^{ij^2} + \frac{\Phi^{ij} l^{ij}}{(c_y + l^{ij})} \{1 - \xi^{ij}\} \right] \quad (4.40d)$$

Using the fourth set of boundary conditions represented by Eqs.(4.32) along with the crack continuity conditions represented by Eqs.(4.33) and following the procedure described above, the shape functions can be derived as

$$v_1^{ij} = N_{v_{14}}^{ij} = \frac{1}{1 + \Phi^{ij}} \left[\left\{ \frac{1}{2(c_y + l^{ij})} - \frac{3}{2l^{ij}} \right\} l^{ij^2} \xi^{ij^2} + l^{ij} \xi^{ij^3} + \Phi^{ij} \left\{ \frac{l^2 \xi^{ij^2}}{2(c_y + l^{ij})} - \frac{l^{ij} \xi^{ij}}{2} \right\} \right] \quad (4.41a)$$

$$v_2^{ij} = N_{v_{24}}^{ij} = \frac{1}{1 + \Phi^{ij}} \left[\frac{-c_y l^{ij}}{2(c_y + l^{ij})} + \frac{c_y l^{ij}}{(c_y + l^{ij})} \xi^{ij} + \left\{ \frac{1}{2(c_y + l^{ij})} - \frac{3}{2l^{ij}} \right\} l^{ij^2} \xi^{ij^2} + l^{ij} \xi^{ij^3} + \Phi^{ij} \left\{ \frac{-c_y l^{ij}}{2(c_y + l^{ij})} + \left(\frac{c_y}{(c_y + l^{ij})} - \frac{1}{2} \right) l^{ij} \xi^{ij} + \frac{l^{ij^2} \xi^{ij^2}}{2(c_y + l^{ij})} \right\} \right] \quad (4.41b)$$

$$\beta_1^{ij} = N_{\beta_{14}}^{ij} = \frac{1}{1 + \Phi^{ij}} \left[2l^{ij} \xi^{ij} \left\{ \frac{1}{2(c_y + l^{ij})} - \frac{3}{2l^{ij}} \right\} + 3\xi^{ij^2} + \Phi^{ij} \frac{l^{ij} \xi^{ij}}{(c_y + l^{ij})} \right] \quad (4.41c)$$

$$\beta_2^{ij} = N_{\beta_{24}}^{ij} = \frac{1}{1 + \Phi^{ij}} \left[\frac{c_y}{(c_y + l^{ij})} + 2l^{ij} \xi^{ij} \left\{ \frac{1}{2(c_y + l^{ij})} - \frac{3}{2l^{ij}} \right\} + 3\xi^{ij^2} + \Phi^{ij} \left\{ \frac{c_y}{(c_y + l^{ij})} + \frac{l^{ij} \xi^{ij}}{(c_y + l^{ij})} \right\} \right] \quad (4.41d)$$

The shape functions $N_{v_{1i}}^{ij}$ and $N_{\beta_{1i}}^{ij}$, $i = 1..4$, are valid for the left side, and the shape functions $N_{v_{2i}}^{ij}$ and $N_{\beta_{2i}}^{ij}$, $i = 1..4$, are valid for the right side of the cracked finite element.

The shape functions to approximate the deformation w^{ij} of the shaft finite element in the Z^{ij} - direction can also be assumed as third order polynomials, similar to those of Eqs.(4.13). The boundary conditions and the crack continuity conditions can be specified by replacing v_1^{ij} by w_1^{ij} , v_2^{ij} by w_2^{ij} , β_1^{ij} by γ_1^{ij} , β_2^{ij} by γ_2^{ij} and c_y by c_z , in the relevant equations, where c_z is the crack compliance due to bending in the Z^{ij} - direction. The eight unknowns of the assumed third order polynomial shape functions can be obtained and shape functions established. Using the obtained shape functions, the translational deformation of an arbitrary point on the left side of the cracked finite element can be represented as

$$\begin{aligned} \begin{Bmatrix} v_1^{ij}(\xi^{ij}, t) \\ w_1^{ij}(\xi^{ij}, t) \end{Bmatrix} &= \begin{bmatrix} N_{v_{11}}^{ij} & 0 & 0 & N_{v_{12}}^{ij} & 0 & N_{v_{13}}^{ij} & 0 & 0 & N_{v_{14}}^{ij} & 0 \\ 0 & N_{v_{11}}^{ij} & -N_{v_{12}}^{ij} & 0 & 0 & 0 & N_{v_{13}}^{ij} & -N_{v_{14}}^{ij} & 0 & 0 \end{bmatrix} \{e^{ij}(t)\} \\ &= \begin{bmatrix} N_{v_{v_1}}^{ij}(\xi^{ij}) \\ N_{v_{w_1}}^{ij}(\xi^{ij}) \end{bmatrix} \{e^{ij}(t)\} = [N_{v_1}^{ij}(\xi^{ij})] \{e^{ij}(t)\} \end{aligned} \quad (4.42)$$

The rotation of a typical cross-section of the element is represented by

$$\begin{aligned} \begin{Bmatrix} \beta_1^{ij}(\xi^{ij}, t) \\ \gamma_1^{ij}(\xi^{ij}, t) \end{Bmatrix} &= \begin{bmatrix} 0 & -N_{\beta_{11}}^{ij} & N_{\beta_{12}}^{ij} & 0 & 0 & 0 & -N_{\beta_{13}}^{ij} & N_{\beta_{14}}^{ij} & 0 & 0 \\ N_{\beta_{11}}^{ij} & 0 & 0 & N_{\beta_{12}}^{ij} & 0 & N_{\beta_{13}}^{ij} & 0 & 0 & N_{\beta_{14}}^{ij} & 0 \end{bmatrix} \{e(t)\} \\ &= \begin{bmatrix} N_{\beta_{\beta_1}}^{ij}(\xi^{ij}) \\ N_{\beta_{\gamma_1}}^{ij}(\xi^{ij}) \end{bmatrix} \{e^{ij}(t)\} = [N_{\beta_1}^{ij}(\xi^{ij})] \{e^{ij}(t)\} \end{aligned} \quad (4.43)$$

The torsional displacement of a typical cross-section of the element is then approximated by

$$\begin{aligned} \{\phi_1^{ij}(\xi^{ij}, t)\} &= \begin{bmatrix} 0 & 0 & 0 & 0 & N_{\phi_{11}}^{ij} & 0 & 0 & 0 & 0 & N_{\phi_{12}}^{ij} \end{bmatrix} \{e^{ij}(t)\} \\ &= [N_{\phi_1}^{ij}(\xi^{ij})] \{e^{ij}(t)\} \end{aligned} \quad (4.44)$$

Similar relationships can be written for the deflection of segment 2 of the cracked beam element as

$$\begin{aligned} \begin{Bmatrix} v_2^{ij}(\xi^{ij}, t) \\ w_2^{ij}(\xi^{ij}, t) \end{Bmatrix} &= \begin{bmatrix} N_{v_{21}}^{ij} & 0 & 0 & N_{v_{22}}^{ij} & 0 & N_{v_{23}}^{ij} & 0 & 0 & N_{v_{24}}^{ij} & 0 \\ 0 & N_{v_{21}}^{ij} & -N_{v_{22}}^{ij} & 0 & 0 & 0 & N_{v_{23}}^{ij} & -N_{v_{24}}^{ij} & 0 & 0 \end{bmatrix} \{e^{ij}(t)\} \\ &= \begin{bmatrix} N_{vv_2}^{ij}(\xi^{ij}) \\ N_{vw_2}^{ij}(\xi^{ij}) \end{bmatrix} \{e^{ij}(t)\} = [N_{v_2}^{ij}(\xi^{ij})] \{e^{ij}(t)\} \end{aligned} \quad (4.45)$$

$$\begin{aligned}
\begin{Bmatrix} \beta_2^{ij}(\xi^{ij}, t) \\ \gamma_2^{ij}(\xi^{ij}, t) \end{Bmatrix} &= \begin{bmatrix} 0 & -N_{\beta_{21}}^{ij} & N_{\beta_{22}}^{ij} & 0 & 0 & 0 & -N_{\beta_{23}}^{ij} & N_{\beta_{24}}^{ij} & 0 & 0 \\ N_{\beta_{21}}^{ij} & 0 & 0 & N_{\beta_{22}}^{ij} & 0 & N_{\beta_{23}}^{ij} & 0 & 0 & N_{\beta_{24}}^{ij} & 0 \end{bmatrix} \{e(t)\} \\
&= \begin{bmatrix} N_{\beta\beta_2}^{ij}(\xi^{ij}) \\ N_{\beta\gamma_2}^{ij}(\xi^{ij}) \end{bmatrix} \{e^{ij}(t)\} = [N_{\beta_2}^{ij}(\xi^{ij})] \{e^{ij}(t)\} \quad (4.46)
\end{aligned}$$

$$\begin{aligned}
\{\phi_2^{ij}(\xi^{ij}, t)\} &= \begin{bmatrix} 0 & 0 & 0 & 0 & N_{\phi_{21}}^{ij} & 0 & 0 & 0 & 0 & N_{\phi_{22}}^{ij} \end{bmatrix} \{e^{ij}(t)\} \\
&= [N_{\phi_2}^{ij}(\xi^{ij})] \{e^{ij}(t)\} \quad (4.47)
\end{aligned}$$

It is noteworthy to mention that the shape functions of Eqs.(4.36, 4.39-4.41) derived in this investigation are presented here for the first time. These shape functions form the basis for deriving the explicit forms of the tapered cracked shaft elemental matrices.

4.2 Element Matrices

4.2.1 Inertia Matrices

The kinetic energy expression of a rotating tapered shaft element of length l^{ij} which is derived in chapter 3 may be rewritten as

$$T^{ij} = \frac{1}{2}I^{ij}\dot{\theta}_x^2 + \frac{1}{2}\dot{e}^{ijT} m_e^{ij} \dot{e}^{ij} - \dot{\theta}_x \dot{e}^{ijT} \hat{g}^{ij} e^{ij} \quad (4.48)$$

The matrix m^{ij} is the composite mass matrix given by

$$m^{ij} = m_t^{ij} + m_r^{ij} + m_\phi^{ij} - 2m_e^{ij} \quad (4.49)$$

This is known as the consistent mass matrix because it is formulated from the same shape functions N_v^{ij} , N_β^{ij} and N_ϕ^{ij} that are used to formulate the stiffness matrix. The matrix m_e^{ij} accounts for the coupling between torsional and transverse vibrations and is time dependent. The components of the mass matrix are given by

$$m_t^{ij} = \int_0^{l_1^{ij}} N_{v_1}^{ijT} \mu^{ij} A^{ij} N_{v_1}^{ij} dx^{ij} + \int_{l_1^{ij}}^{l_2^{ij}} N_{v_2}^{ijT} \mu^{ij} A^{ij} N_{v_2}^{ij} dx^{ij} \quad (4.50)$$

$$m_r^{ij} = \int_0^{l_1^{ij}} N_{\beta_1}^{ijT} I_D^{ij} N_{\beta_1}^{ij} dx^{ij} + \int_{l_1^{ij}}^{l_2^{ij}} N_{\beta_2}^{ijT} I_D^{ij} N_{\beta_2}^{ij} dx^{ij} \quad (4.51)$$

$$m_\phi^{ij} = \int_0^{l_1^{ij}} N_{\phi_1}^{ijT} I_P^{ij} N_{\phi_1}^{ij} dx^{ij} + \int_{l_1^{ij}}^{l_2^{ij}} N_{\phi_2}^{ijT} I_P^{ij} N_{\phi_2}^{ij} dx^{ij} \quad (4.52)$$

where m_t^{ij} is the translational mass matrix, m_r^{ij} is the rotary inertia mass matrix, m_ϕ^{ij} is the torsional mass matrix, I_D^{ij} is the diametral mass moment of inertia and I_P^{ij} is the polar mass moment of inertia. The explicit expressions for the element translational mass matrix m_t^{ij} , the rotary inertia mass matrix m_r^{ij} and the elemental torsional mass

matrix m_ϕ^{ij} are obtained by carrying out the integration of Eqs.(4.50), (4.51) and (4.52), respectively. The nonzero entries of m_t^{ij} , m_r^{ij} and m_ϕ^{ij} are presented in Tables 4.1, 4.2 and 4.3, respectively.

The gyroscopic matrix g^{ij} is given by

$$g^{ij} = \hat{g}^{ij} - \hat{g}^{ijT} \quad (4.53)$$

where, for constant rotating speed, \hat{g}^{ij} can be calculated by

$$\hat{g}^{ij} = \int_0^{l_1^{ij}} N_{\beta\gamma_1}^{ijT} I_P^{ij} N_{\beta\beta_1}^{ij} dx^{ij} + \int_{l_1^{ij}}^{l_2^{ij}} N_{\beta\gamma_2}^{ijT} I_P^{ij} N_{\beta\beta_2}^{ij} dx^{ij} \quad (4.54)$$

The explicit expressions for the elemental gyroscopic matrix g^{ij} are obtained by integrating Eq.(4.54), and then substituting into Eq.(4.53). The nonzero entries of g^{ij} are presented in Table 4.4.

4.2.2 Stiffness Matrices

The strain energy expression of a rotating tapered shaft element of length l^{ij} , in matrix form is given by

$$U^{ij} = \frac{1}{2} e^{ijT} K^{ij} e^{ij} \quad (4.55)$$

The matrix K^{ij} is the composite stiffness matrix given by

$$K^{ij} = K_e^{ij} + K_s^{ij} + K_\phi^{ij} \quad (4.56)$$

where

$$K_e^{ij} = \int_0^{l_1^{ij}} \hat{B}_{e_1}^{ijT} E^{ij} I^{ij} \hat{B}_{e_1}^{ij} dx^{ij} + \int_{l_1^{ij}}^{l_2^{ij}} \hat{B}_{e_2}^{ijT} E^{ij} I^{ij} \hat{B}_{e_2}^{ij} dx^{ij} \quad (4.57)$$

$$K_s^{ij} = \int_0^{l_1^{ij}} \hat{B}_{s_1}^{ijT} \kappa G^{ij} A^{ij} \hat{B}_{s_1}^{ij} dx^{ij} + \int_{l_1^{ij}}^{l_2^{ij}} \hat{B}_{s_2}^{ijT} \kappa G^{ij} A^{ij} \hat{B}_{s_2}^{ij} dx^{ij} \quad (4.58)$$

$$K_\phi^{ij} = \int_0^{l_1^{ij}} \hat{B}_{\phi_1}^{ijT} G^{ij} J^{ij} \hat{B}_{\phi_1}^{ij} dx^{ij} + \int_{l_1^{ij}}^{l_2^{ij}} \hat{B}_{\phi_2}^{ijT} G^{ij} J^{ij} \hat{B}_{\phi_2}^{ij} dx^{ij} \quad (4.59)$$

As defined earlier, K_e^{ij} is the elastic stiffness matrix, K_s^{ij} is the shear stiffness matrix and K_ϕ^{ij} is the torsional stiffness matrix. where

$$\hat{B}_{\phi_1}^{ij} = \frac{dN_{\phi_1}^{ij}}{dx^{ij}} \quad (4.60)$$

$$\hat{B}_{e_1}^{ij} = \frac{dN_{\beta_1}^{ij}}{dx^{ij}} \quad (4.61)$$

$$\hat{B}_{s_1}^{ij} = \frac{dN_{v_1}^{ij}}{dx^{ij}} - N_{\beta_1}^{ij} \quad (4.62)$$

Equations (4.60–4.62) are applicable to the left side of the cracked beam element. Similar expressions can be written for the right side of the cracked beam element.

Carrying out the integration of Eq.(4.57), the elastic stiffness matrix K_e^{ij} is obtained with nonzero entries as presented in Table 4.5. The explicit expression for the element shear stiffness matrix K_s^{ij} is obtained by carrying out the integration of Eq.(4.58). the shear stiffness matrix K_s^{ij} is obtained with nonzero entries as presented in Table 4.6. Similarly, the torsional stiffness matrix K_ϕ^{ij} is established by evaluating the integral of Eq.(4.59). The nonzero entries of torsional stiffness matrix K_ϕ^{ij} are presented in Table 4.7.

The elemental matrices presented below are derived for a crack located at the midpoint of the finite element, i.e. $l_c^{ij} = \frac{l^{ij}}{2}$. This should not impose any limitations on the use of these matrices, since the developed formulation, allows for a variable length finite element. In addition, the dynamic analyst can always select a finite element mesh that matches the problem at hand. It is noted that the superscript ij denoting the ij^{th} finite element is dropped in the following expressions for the sake of brevity.

TABLE: 4.1a

Any nonzero entry of the translational mass matrix for the left side of the rotating cracked shaft element can be expressed in the following form:

$$M_{ij1}^t = \frac{\mu A_i L}{(1 + \Phi)^2} \left[\frac{P_0}{2} + \frac{P_1}{8} + \frac{P_2}{24} + \frac{P_3}{64} + \frac{P_4}{160} + \frac{P_5}{384} + \frac{P_6}{896} + \frac{P_7}{2048} + \frac{P_8}{4608} \right]$$

where $i, j = 1, \dots, 10$ and the constants $P_i, i = 0, 1, \dots, 8$ are defined as

$$P_0 = C_0$$

$$P_1 = C_1 + \alpha_1 C_0$$

$$P_2 = C_2 + \alpha_1 C_1 + \alpha_2 C_0$$

$$P_3 = C_3 + \alpha_1 C_2 + \alpha_2 C_1$$

$$P_4 = C_4 + \alpha_1 C_3 + \alpha_2 C_2$$

$$P_5 = C_5 + \alpha_1 C_4 + \alpha_2 C_3$$

$$P_6 = C_6 + \alpha_1 C_5 + \alpha_2 C_4$$

$$P_7 = \alpha_1 C_6 + \alpha_2 C_5$$

$$P_8 = \alpha_2 C_6$$

The constants $C_i, i = 0, 1, \dots, 6$ for different entries M_{ij1}^t are as follows:

For M_{111}^t, M_{221}^t

$$C_0 = (1 + \Phi)^2,$$

$$C_1 = -2\Phi(1 + \Phi),$$

$$C_2 = \Phi^2 - 6(1 + \Phi),$$

$$C_3 = 4 + 10\Phi,$$

$$C_4 = 9 - 4\Phi,$$

$$C_5 = -12,$$

$$C_6 = 4.$$

For $M_{141}^t, -M_{231}^{t*}$

$$C_0 = 0,$$

$$C_1 = l(1 + \Phi) \left(1 + \frac{\Phi}{2}\right),$$

$$C_2 = -l^2(1 + \Phi) \left(\frac{3}{2l} + \frac{1 + \Phi}{2(c_v + l)}\right) - \Phi l \left(1 + \frac{\Phi}{2}\right),$$

$$C_3 = l(1 + \Phi) + \Phi l^2 \left(\frac{3}{2l} + \frac{1 + \Phi}{2(c_v + l)}\right) - 3l \left(1 + \frac{\Phi}{2}\right),$$

$$C_4 = -\Phi l + 3l^2 \left(\frac{3}{2l} + \frac{1 + \Phi}{2(c_v + l)}\right) + 2l \left(1 + \frac{\Phi}{2}\right),$$

$$C_5 = -3l - 2l^2 \left(\frac{3}{2l} + \frac{1 + \Phi}{2(c_v + l)}\right),$$

$$C_6 = 2l.$$

For $M_{16,1}^t, M_{27,1}^t$

$$C_0 = 0,$$

$$C_1 = \Phi(1 + \Phi),$$

$$C_2 = 3(1 + \Phi) - \Phi^2,$$

$$C_3 = -2 - 8\Phi,$$

$$C_4 = 4\Phi - 9,$$

$$C_5 = 12,$$

$$C_6 = -4.$$

For $M_{19,1}^t, M_{28,1}^t$

$$C_0 = 0,$$

$$C_1 = -l(1 + \Phi) \frac{\Phi}{2},$$

$$C_2 = l^2(1 + \Phi) \left(\frac{1 + \Phi}{2(c_v + l)} - \frac{3}{2l} \right) + \frac{\Phi^2 l}{2},$$

$$C_3 = l(1 + \Phi) - \Phi l^2 \left(\frac{1 + \Phi}{2(c_v + l)} - \frac{3}{2l} \right) + \frac{3l\Phi}{2},$$

$$C_4 = -2\Phi l - 3l^2 \left(\frac{1 + \Phi}{2(c_v + l)} - \frac{3}{2l} \right),$$

$$C_5 = -3l + 2l^2 \left(\frac{1 + \Phi}{2(c_v + l)} - \frac{3}{2l} \right),$$

$$C_6 = 2l.$$

For $M_{33_1}^t, M_{44_1}^{t*}$

$$C_0 = 0,$$

$$C_1 = 0,$$

$$C_2 = l^2 \left(1 + \frac{\Phi}{2}\right)^2,$$

$$C_3 = -2l^3 \left(1 + \frac{\Phi}{2}\right) \left(\frac{3}{2l} + \frac{1+\Phi}{2(c_y+l)}\right),$$

$$C_4 = l^4 \left(\frac{3}{2l} + \frac{1+\Phi}{2(c_y+l)}\right) + 2l^2 \left(1 + \frac{\Phi}{2}\right),$$

$$C_5 = -2l^3 \left(\frac{3}{2l} + \frac{1+\Phi}{2(c_y+l)}\right),$$

$$C_6 = l^2.$$

For $M_{37_1}^t, -M_{46_1}^{t*}$

$$C_0 = 0,$$

$$C_1 = 0,$$

$$C_2 = l \left(1 + \frac{\Phi}{2}\right),$$

$$C_3 = -\Phi l^2 \left(\frac{3}{2l} + \frac{1+\Phi}{2(c_y+l)}\right) + 3l \left(1 + \frac{\Phi}{2}\right),$$

$$C_4 = \Phi l - 3l^2 \left(\frac{3}{2l} + \frac{1+\Phi}{2(c_y+l)}\right) - 2l \left(1 + \frac{\Phi}{2}\right),$$

$$C_5 = 3l + 2l^2 \left(\frac{3}{2l} + \frac{1+\Phi}{2(c_y+l)}\right),$$

$$C_6 = -2l.$$

For $M_{38_1}^t, M_{49_1}^{t*}$

$$C_0 = 0,$$

$$C_1 = 0,$$

$$C_2 = -\frac{\Phi l^2}{2} \left(1 + \frac{\Phi}{2}\right),$$

$$C_3 = l^3 \left(1 + \frac{\Phi}{2}\right) \left(\frac{1+\Phi}{2(c_v+l)} - \frac{3}{2l}\right) - \frac{\Phi l^3}{2} \left(\frac{3}{2l} + \frac{1+\Phi}{2(c_v+l)}\right),$$

$$C_4 = l^2 - l^4 \left(\frac{3}{2l} + \frac{1+\Phi}{2(c_v+l)}\right) \left(\frac{1+\Phi}{2(c_v+l)} - \frac{3}{2l}\right),$$

$$C_5 = -l^3 \left(\frac{3}{2l} + \frac{1+\Phi}{2(c_v+l)}\right) + l^3 \left(\frac{1+\Phi}{2(c_v+l)} - \frac{3}{2l}\right),$$

$$C_6 = l^2.$$

For $M_{66_1}^t, M_{77_1}^t$

$$C_0 = 0,$$

$$C_1 = 0,$$

$$C_2 = \Phi^2,$$

$$C_3 = 6\Phi,$$

$$C_4 = 9 - 4\Phi,$$

$$C_5 = -12,$$

$$C_6 = 4.$$

For $M_{69_1}^t, M_{78_1}^{t*}$

$$C_0 = 0,$$

$$C_1 = 0,$$

$$C_2 = -\frac{\Phi l^2}{2},$$

$$C_3 = \Phi l^2 \left(\frac{1+\Phi}{2(c_v+l)} - \frac{3}{2l} \right) - \frac{3\Phi l}{2},$$

$$C_4 = 2\Phi l + 3l^2 \left(\frac{1+\Phi}{2(c_v+l)} - \frac{3}{2l} \right),$$

$$C_5 = 3l - 2l^2 \left(\frac{1+\Phi}{2(c_v+l)} - \frac{3}{2l} \right),$$

$$C_6 = -2l.$$

For $M_{88_1}^t, M_{99_1}^{t*}$

$$C_0 = 0,$$

$$C_1 = 0,$$

$$C_2 = \frac{\Phi^2 l^2}{4},$$

$$C_3 = -\Phi l^3 \left(\frac{1+\Phi}{2(c_v+l)} - \frac{3}{2l} \right),$$

$$C_4 = -\Phi l^2 + l^4 \left(\frac{1+\Phi}{2(c_v+l)} - \frac{3}{2l} \right),$$

$$C_5 = 2l^3 \left(\frac{1+\Phi}{2(c_v+l)} - \frac{3}{2l} \right),$$

$$C_6 = l^2.$$

TABLE: 4.1b

Any nonzero entry of the translation mass matrix for the right side of the rotating cracked shaft element can be expressed in the form

$$M_{ij2}^t = \frac{\mu A_i L}{(1 + \Phi)^2} \left[\frac{P_0}{2} + \frac{3P_1}{8} + \frac{7P_2}{24} + \frac{15P_3}{64} + \frac{31P_4}{160} + \frac{63P_5}{384} + \frac{127P_6}{896} + \frac{255P_7}{2048} + \frac{511P_8}{4608} \right]$$

where $i, j = 1, \dots, 10$ and the constants $P_i, i = 0, 1, \dots, 8$ are as defined for the left side of the cracked shaft element in Table 3.1a. The constants $C_i, i = 0, 1, \dots, 6$ for different entries M_{ij2}^t are as follows:

For M_{112}^t, M_{222}^t the constants C_i are equal to those of M_{111}^t

For M_{142}^t, M_{232}^t

$$C_0 = \frac{c_y l (1 + \Phi)^2}{2(c_y + l)},$$

$$C_1 = l(1 + \Phi) \left\{ \Phi \left(\frac{1}{2} - \frac{c_y}{c_y + l} \right) + \frac{l}{c_y + l} \right\} - \frac{c_y l \Phi (1 + \Phi)}{2(c_y + l)},$$

$$C_2 = -l^2(1 + \Phi) \left(\frac{3}{2l} + \frac{1 + \Phi}{2(c_y + l)} \right) - \Phi l \left\{ \Phi \left(\frac{1}{2} - \frac{c_y}{c_y + l} \right) + \frac{l}{c_y + l} \right\} - \frac{3c_y l (1 + \Phi)}{2(c_y + l)},$$

$$C_3 = l(1 + \Phi) + \Phi l^2 \left(\frac{3}{2l} + \frac{1 + \Phi}{2(c_y + l)} \right) - 3l \left\{ \Phi \left(\frac{1}{2} - \frac{c_y}{c_y + l} \right) + \frac{l}{c_y + l} \right\} - \frac{c_y l (1 + \Phi)}{2(c_y + l)},$$

$$C_4 = -\Phi l + 3l^2 \left(\frac{3}{2l} + \frac{1 + \Phi}{2(c_y + l)} \right) + 2l \left\{ \Phi \left(\frac{1}{2} - \frac{c_y}{c_y + l} \right) + \frac{l}{c_y + l} \right\},$$

$$C_5 = -3l - 2l^2 \left(\frac{3}{2l} + \frac{1 + \Phi}{2(c_y + l)} \right),$$

$$C_6 = 2l.$$

For $M_{16_2}^t$, $M_{27_2}^t$ the constants C_i are equal to those of $M_{16_1}^t$.

For $M_{19_2}^t$, $-M_{28_2}^{t*}$

$$C_0 = -\frac{c_y l (1+\Phi)^2}{2(c_y+l)},$$

$$C_1 = l(1+\Phi) \left\{ \Phi \left(\frac{c_y}{c_y+l} - \frac{1}{2} \right) + \frac{c_y}{c_y+l} \right\} + \frac{c_y l \Phi (1+\Phi)}{2(c_y+l)},$$

$$C_2 = l^2(1+\Phi) \left(\frac{1+\Phi}{2(c_y+l)} - \frac{3}{2l} \right) - \Phi l \left\{ \Phi \left(\frac{c_y}{c_y+l} - \frac{1}{2} \right) + \frac{c_y}{c_y+l} \right\} + \frac{3c_y l (1+\Phi)}{2(c_y+l)},$$

$$C_3 = l(1+\Phi) - \Phi l^2 \left(\frac{1+\Phi}{2(c_y+l)} - \frac{3}{2l} \right) - 3l \left\{ \Phi \left(\frac{c_y}{c_y+l} - \frac{1}{2} \right) + \frac{c_y}{c_y+l} \right\} - \frac{c_y l (1+\Phi)}{2(c_y+l)},$$

$$C_4 = -\Phi l - 3l^2 \left(\frac{1+\Phi}{2(c_y+l)} - \frac{3}{2l} \right) + 2l \left\{ \Phi \left(\frac{c_y}{c_y+l} - \frac{1}{2} \right) + \frac{c_y}{c_y+l} \right\},$$

$$C_5 = -3l + 2l^2 \left(\frac{1+\Phi}{2(c_y+l)} - \frac{3}{2l} \right),$$

$$C_6 = 2l.$$

For $M_{33_2}^t$, $M_{44_2}^{t*}$

$$C_0 = \frac{c_y^2 l^2 (1+\Phi)^2}{4(c_y+l)^2},$$

$$C_1 = \frac{c_y l^2 (1+\Phi)}{(c_y+l)} \left\{ \Phi \left(\frac{1}{2} - \frac{c_y}{c_y+l} \right) + \frac{l}{c_y+l} \right\},$$

$$C_2 = l^2 \left\{ \Phi \left(\frac{1}{2} - \frac{c_y}{c_y+l} \right) + \frac{l}{c_y+l} \right\}^2 - \frac{c_y l^3 (1+\Phi)}{(c_y+l)} \left(\frac{3}{2l} + \frac{1+\Phi}{2(c_y+l)} \right),$$

$$C_3 = \frac{c_y l^2 (1+\Phi)}{(c_y+l)} - 2l^3 \left\{ \Phi \left(\frac{1}{2} - \frac{c_y}{c_y+l} \right) + \frac{l}{c_y+l} \right\} \left(\frac{3}{2l} + \frac{1+\Phi}{2(c_y+l)} \right),$$

$$C_4 = l^4 \left(\frac{3}{2l} + \frac{1+\Phi}{2(c_y+l)} \right)^2 + 2l^2 \left\{ \Phi \left(\frac{1}{2} - \frac{c_y}{c_y+l} \right) + \frac{l}{c_y+l} \right\},$$

$$C_5 = -2l^3 \left(\frac{3}{2l} + \frac{1+\Phi}{2(c_y+l)} \right),$$

$$C_6 = l^2.$$

For $M_{372}^t, -M_{462}^{t*}$

$$C_0 = 0,$$

$$C_1 = \frac{c_y l (1+\Phi) \Phi}{2(c_y+l)},$$

$$C_2 = l\Phi \left\{ \Phi \left(\frac{1}{2} - \frac{c_y}{c_y+l} \right) + \frac{l}{c_y+l} \right\} + \frac{3c_y l (1+\Phi)}{2(c_y+l)},$$

$$C_3 = -\Phi l^2 \left(\frac{3}{2l} + \frac{1+\Phi}{2(c_y+l)} \right) + 3l \left\{ \Phi \left(\frac{1}{2} - \frac{c_y}{c_y+l} \right) + \frac{l}{c_y+l} \right\} - \frac{c_y l (1+\Phi)}{(c_y+l)},$$

$$C_4 = \Phi l - 3l^2 \left(\frac{3}{2l} + \frac{1+\Phi}{2(c_y+l)} \right) - 2l \left\{ \Phi \left(\frac{1}{2} - \frac{c_y}{c_y+l} \right) + \frac{l}{c_y+l} \right\},$$

$$C_5 = 3l + 2l^2 \left(\frac{3}{2l} + \frac{1+\Phi}{2(c_y+l)} \right),$$

$$C_6 = -2l.$$

For M_{382}^t, M_{492}^{t*}

$$C_0 = -\frac{c_y^2 l^2 (1+\Phi)^2}{4(c_y+l)^2},$$

$$C_1 = \frac{c_y l^2 (1+\Phi)}{2(c_y+l)} \left\{ \Phi \left(\frac{c_y}{c_y+l} - \frac{1}{2} \right) + \frac{c_y}{c_y+l} \right\} - \frac{c_y l^2 (1+\Phi)}{2(c_y+l)} \left\{ \Phi \left(\frac{1}{2} - \frac{c_y}{c_y+l} \right) + \frac{l}{c_y+l} \right\},$$

$$C_2 = \frac{c_y l^3 (1+\Phi)^2}{2(c_y+l)^2} + l^2 \left\{ \Phi \left(\frac{1}{2} - \frac{c_y}{c_y+l} \right) + \frac{l}{c_y+l} \right\} \left\{ \Phi \left(\frac{c_y}{c_y+l} - \frac{1}{2} \right) + \frac{c_y}{c_y+l} \right\},$$

$$C_3 = l^3 \left\{ \Phi \left(\frac{1}{2} - \frac{c_y}{c_y+l} \right) + \frac{l}{c_y+l} \right\} \left(\frac{1+\Phi}{2(c_y+l)} - \frac{3}{2l} \right) - l^3 \left(\frac{3}{2l} + \frac{1+\Phi}{2(c_y+l)} \right) \left\{ \Phi \left(\frac{c_y}{c_y+l} - \frac{1}{2} \right) + \frac{c_y}{c_y+l} \right\},$$

$$C_4 = l^2 \left\{ \Phi \left(\frac{1}{2} - \frac{c_y}{c_y+l} \right) + \frac{l}{c_y+l} \right\} - l^4 \left(\frac{3}{2l} + \frac{1+\Phi}{2(c_y+l)} \right) \left(\frac{1+\Phi}{2(c_y+l)} - \frac{3}{2l} \right) + l^2 \left\{ \Phi \left(\frac{c_y}{c_y+l} - \frac{1}{2} \right) + \frac{c_y}{c_y+l} \right\},$$

$$C_5 = -l^3 \left(\frac{3}{2l} + \frac{1+\Phi}{2(c_y+l)} \right) + l^3 \left(\frac{1+\Phi}{2(c_y+l)} - \frac{3}{2l} \right),$$

$$C_6 = l^2.$$

For M_{662}^t, M_{772}^t the constants C_i are equal to those of M_{661}^t .

For $M_{692}^t, -M_{782}^{t*}$

$$C_0 = 0,$$

$$C_1 = -\frac{c_y l (1+\Phi) \Phi}{2(c_y+l)},$$

$$C_2 = l\Phi \left\{ \Phi \left(\frac{c_y}{c_y+l} - \frac{1}{2} \right) + \frac{c_y}{c_y+l} \right\} - \frac{3c_y l (1+\Phi)}{2(c_y+l)},$$

$$C_3 = \Phi l^2 \left(\frac{1+\Phi}{2(c_y+l)} - \frac{3}{2l} \right) + 3l \left\{ \Phi \left(\frac{c_y}{c_y+l} - \frac{1}{2} \right) + \frac{c_y}{c_y+l} \right\} + \frac{c_y l (1+\Phi)}{(c_y+l)},$$

$$C_4 = \Phi l + 3l^2 \left(\frac{1+\Phi}{2(c_y+l)} - \frac{3}{2l} \right) - 2l \left\{ \Phi \left(\frac{c_y}{c_y+l} - \frac{1}{2} \right) + \frac{c_y}{c_y+l} \right\},$$

$$C_5 = 3l - 2l^2 \left(\frac{1+\Phi}{2(c_y+l)} - \frac{3}{2l} \right),$$

$$C_6 = -2l.$$

For M_{882}^t, M_{992}^{t*}

$$C_0 = \frac{c_y^2 l^2 (1+\Phi)^2}{4(c_y+l)^2},$$

$$C_1 = -\frac{c_y l^2 (1+\Phi)}{(c_y+l)} \left\{ \Phi \left(\frac{c_y}{c_y+l} - \frac{1}{2} \right) + \frac{c_y}{c_y+l} \right\},$$

$$C_2 = l^2 \left\{ \Phi \left(\frac{c_y}{c_y+l} - \frac{1}{2} \right) + \frac{c_y}{c_y+l} \right\}^2 - \frac{c_y l^3 (1+\Phi)}{(c_y+l)} \left(\frac{1+\Phi}{2(c_y+l)} - \frac{3}{2l} \right),$$

$$C_3 = 2l^3 \left\{ \Phi \left(\frac{c_y}{c_y+l} - \frac{1}{2} \right) + \frac{c_y}{c_y+l} \right\} \left(\frac{1+\Phi}{2(c_y+l)} - \frac{3}{2l} \right) - \frac{c_y l^2 (1+\Phi)}{(c_y+l)},$$

$$C_4 = l^4 \left(\frac{1+\Phi}{2(c_y+l)} - \frac{3}{2l} \right)^2 + 2l^2 \left\{ \Phi \left(\frac{c_y}{c_y+l} - \frac{1}{2} \right) + \frac{c_y}{c_y+l} \right\},$$

$$C_5 = 2l^3 \left(\frac{1+\Phi}{2(c_y+l)} - \frac{3}{2l} \right),$$

$$C_6 = l^2.$$

TABLE: 4.2a

Any nonzero entry of the rotational mass matrix for the left side of the rotating cracked shaft element can be expressed in the form

$$M_{ij1}^r = \frac{\mu I_i}{(1 + \Phi)^2} \left[\frac{P_0}{2} + \frac{P_1}{8} + \frac{P_2}{24} + \frac{P_3}{64} + \frac{P_4}{160} + \frac{P_5}{384} + \frac{P_6}{896} + \frac{P_7}{2048} + \frac{P_8}{4608} \right]$$

where $i, j = 1, \dots, 10$ and the constants $P_i, i = 0, 1, \dots, 8$ are defined as

$$P_0 = C_0$$

$$P_1 = C_1 + \delta_1 C_0$$

$$P_2 = C_2 + \delta_1 C_1 + \delta_2 C_0$$

$$P_3 = C_3 + \delta_1 C_2 + \delta_2 C_1 + \delta_3 C_0$$

$$P_4 = C_4 + \delta_1 C_3 + \delta_2 C_2 + \delta_3 C_1 + \delta_4 C_0$$

$$P_5 = \delta_1 C_4 + \delta_2 C_3 + \delta_3 C_2 + \delta_4 C_1$$

$$P_6 = \delta_2 C_4 + \delta_3 C_3 + \delta_4 C_2$$

$$P_7 = \delta_3 C_4 + \delta_4 C_3$$

$$P_8 = \delta_4 C_4$$

The constants $C_i, i = 0, 1, \dots, 4$ for different entries M_{ij1}^r are as follows:

For $M_{11_1}^r, -M_{16_1}^r, M_{22_1}^r, -M_{27_1}^r, M_{66_1}^r, M_{77_1}^r$

$$C_0 = 0,$$

$$C_1 = 0,$$

$$C_2 = \frac{36}{l},$$

$$C_3 = -\frac{72}{l},$$

$$C_4 = \frac{36}{l}.$$

For $M_{14_1}^r, -M_{23_1}^{r*}, M_{37_1}^r, -M_{46_1}^{r*}$

$$C_0 = 0,$$

$$C_1 = -6(1 + \Phi),$$

$$C_2 = 6l \left(\frac{3}{l} + \frac{1+\Phi}{(c_y+l)} \right) + 6(1 + \Phi),$$

$$C_3 = -18 - 6l \left(\frac{3}{l} + \frac{1+\Phi}{(c_y+l)} \right),$$

$$C_4 = 3.$$

For $M_{19_1}^r, M_{28_1}^{r*}, -M_{69_1}^r, M_{78_1}^{r*}$

$$C_0 = 0,$$

$$C_1 = 0,$$

$$C_2 = -6l \left(\frac{1+\Phi}{(c_y+l)} - \frac{3}{l} \right),$$

$$C_3 = -18 + 6l \left(\frac{1+\Phi}{(c_y+l)} - \frac{3}{l} \right),$$

$$C_4 = 18.$$

For $M_{33_1}^r, M_{44_1}^{r*}$

$$C_0 = l(1 + \Phi)^2,$$

$$C_1 = -2l^2(1 + \Phi) \left(\frac{3}{l} + \frac{1+\Phi}{(c_v+l)} \right),$$

$$C_2 = 6l(1 + \Phi) + l^3 \left(\frac{3}{l} + \frac{1+\Phi}{(c_v+l)} \right)^2,$$

$$C_3 = -6l^2 \left(\frac{3}{2l} + \frac{1+\Phi}{2(c_v+l)} \right),$$

$$C_4 = 9l.$$

For $M_{38_1}^r, M_{49_1}^{r*}$

$$C_0 = 0,$$

$$C_1 = l^2(1 + \Phi) \left(\frac{1+\Phi}{(c_v+l)} - \frac{3}{l} \right),$$

$$C_2 = 3l(1 + \Phi) - l^3 \left(\frac{3}{l} + \frac{1+\Phi}{(c_v+l)} \right) \left(\frac{1+\Phi}{(c_v+l)} - \frac{3}{l} \right),$$

$$C_3 = -18l,$$

$$C_4 = 9l.$$

For $M_{88_1}^r, M_{99_1}^{r*}$

$$C_0 = 0,$$

$$C_1 = 0,$$

$$C_2 = l^3 \left(\frac{1+\Phi}{(c_v+l)} - \frac{3}{l} \right)^2,$$

$$C_3 = 6l^2 \left(\frac{1+\Phi}{(c_v+l)} - \frac{3}{l} \right),$$

$$C_4 = 9l.$$

TABLE: 4.2b

Any nonzero entry of the rotational mass matrix for the right side of the rotating cracked shaft element can be expressed in the form

$$M_{ij2}^r = \frac{\mu I_i}{(1 + \Phi)^2} \left[\frac{P_0}{2} + \frac{3P_1}{8} + \frac{7P_2}{24} + \frac{15P_3}{64} + \frac{31P_4}{160} + \frac{63P_5}{384} + \frac{127P_6}{896} + \frac{255P_7}{2048} + \frac{511P_8}{4608} \right]$$

where $i, j = 1, \dots, 10$ and the constants P_i , $i = 0, 1, \dots, 8$ are as defined for the left side of the cracked shaft element. The constants C_i , $i = 0, 1, \dots, 4$ for different entries M_{ij2}^r are as follows:

For $M_{11_2}^r, -M_{16_2}^r, M_{22_2}^r, -M_{27_2}^r, M_{66_2}^r, M_{77_2}^r$
the constants C_i are equal to those of $M_{11_1}^r$.

For $M_{14_2}^r, -M_{23_2}^{r*}, M_{37_2}^r, -M_{46_2}^{r*}$
$C_0 = 0,$ $C_1 = -\frac{6l(1+\Phi)}{c_y+l},$ $C_2 = 18 + \frac{12l(1+\Phi)}{c_y+l},$ $C_3 = -36 - \frac{6l(1+\Phi)}{(c_y+l)},$ $C_4 = 18.$

For M_{192}^r , M_{282}^{r*} , $-M_{692}^r$, M_{782}^{r*}

$$C_0 = 0,$$

$$C_1 = -\frac{6c_y(1+\Phi)}{c_y+l},$$

$$C_2 = -6l \left(\frac{1+\Phi}{(c_y+l)} - \frac{3}{l} \right) + \frac{6c_y(1+\Phi)}{c_y+l},$$

$$C_3 = -18 + 6l \left(\frac{1+\Phi}{(c_y+l)} - \frac{3}{l} \right),$$

$$C_4 = 18.$$

For M_{332}^r , M_{442}^{r*}

$$C_0 = \frac{l^3(1+\Phi)^2}{(c_y+l)^2},$$

$$C_1 = \frac{-2l^3(1+\Phi)}{c_y+l} \left(\frac{3}{l} + \frac{1+\Phi}{(c_y+l)} \right),$$

$$C_2 = \frac{6l^2(1+\Phi)}{c_y+l} + l^3 \left(\frac{3}{l} + \frac{1+\Phi}{(c_y+l)} \right),$$

$$C_3 = -6l^2 \left(\frac{3}{2l} + \frac{1+\Phi}{2(c_y+l)} \right),$$

$$C_4 = 9l.$$

For M_{382}^r , M_{492}^{r*}

$$C_0 = \frac{c_y l^2 (1+\Phi)^2}{(c_y+l)^2},$$

$$C_1 = \frac{l^3(1+\Phi)}{c_y+l} \left(\frac{1+\Phi}{c_y+l} - \frac{3}{l} \right) - \frac{c_y l^2 (1+\Phi)}{c_y+l} \left(\frac{1+\Phi}{c_y+l} + \frac{3}{l} \right),$$

$$C_2 = \frac{3l^2(1+\Phi)}{c_y+l} - l^3 \left(\frac{3}{l} + \frac{1+\Phi}{c_y+l} \right) \left(\frac{1+\Phi}{c_y+l} - \frac{3}{l} \right) + \frac{3c_y l (1+\Phi)}{c_y+l},$$

$$C_3 = -18l,$$

$$C_4 = 9l.$$

For $M_{88_2}^r, M_{99_2}^{r*}$

$$C_0 = \frac{c_y l (1+\Phi)^2}{(c_y + l)^2},$$

$$C_1 = \frac{2c_y l^2 (1+\Phi)}{c_y + l} \left(\frac{1+\Phi}{c_y + l} - \frac{3}{l} \right),$$

$$C_2 = l^3 \left(\frac{1+\Phi}{c_y + l} - \frac{3}{l} \right)^2 + \frac{6c_y l (1+\Phi)}{c_y + l},$$

$$C_3 = 6l^2 \left(\frac{1+\Phi}{c_y + l} - \frac{3}{l} \right),$$

$$C_4 = 9l.$$

TABLE: 4.3a

Any nonzero entry of the torsional mass matrix for the left side of the rotating cracked shaft element can be expressed in the form

$$M_{ij1}^{\phi} = 2\mu I_i \left[\frac{P_0}{2} + \frac{P_1}{8} + \frac{P_2}{24} + \frac{P_3}{64} + \frac{P_4}{160} + \frac{P_5}{384} + \frac{P_6}{896} \right]$$

where $i, j = 1, \dots, 10$ and the constants $P_i, i = 0, 1, \dots, 6$ are defined as

$$P_0 = C_0$$

$$P_1 = C_1 + \delta_1 C_0$$

$$P_2 = C_2 + \delta_1 C_1 + \delta_2 C_0$$

$$P_3 = \delta_1 C_2 + \delta_2 C_1 + \delta_3 C_0$$

$$P_4 = \delta_2 C_2 + \delta_3 C_1 + \delta_4 C_0$$

$$P_5 = \delta_3 C_2 + \delta_4 C_1$$

$$P_6 = \delta_4 C_2$$

The constants $C_i, i = 0, 1, 2$ for different entries M_{ij1}^{ϕ} are as follows:

For $M_{55_1}^\phi$

$$C_0 = 1,$$

$$C_1 = -2,$$

$$C_2 = 1,$$

For $M_{5,10_1}^\phi, M_{10,5_1}^\phi$

$$C_0 = 0,$$

$$C_1 = 1,$$

$$C_2 = -1,$$

For $M_{10,10_1}^\phi$

$$C_0 = 0,$$

$$C_1 = 0,$$

$$C_2 = 1,$$

TABLE: 4.3b

Any nonzero entry of the torsional mass matrix for the right side of the rotating cracked shaft element can be expressed in the form

$$M_{ij2}^{\phi} = 2\mu I_i \left[\frac{P_0}{2} + \frac{3P_1}{8} + \frac{7P_2}{24} + \frac{15P_3}{64} + \frac{31P_4}{160} + \frac{63P_5}{384} + \frac{127P_6}{896} \right]$$

where $i, j = 1, \dots, 10$ and the constants P_i and C_i are as defined for the left side of the cracked shaft element in Table 3.3b for all the entries M_{ij2}^{ϕ} .

TABLE: 4.4a

The nonzero entries of the gyroscopic matrix for the left and right side of the rotating cracked shaft element can be written as

For $-G_{12_1}, G_{17_1}, -G_{17_1}$

the constants P_i and C_i are equal to those of $M_{11_1}^r$.

For $-G_{13_1}, G_{47_1}$

the constants P_i and C_i are equal to those of $M_{14_1}^r$.

For $-G_{18_1}, G_{68_1}$

the constants P_i and C_i are equal to those of $M_{19_1}^r$.

For $-G_{48_1}$

the constants P_i and C_i are equal to those of $M_{38_1}^r$.

TABLE: 4.5a

Any nonzero entry of the elastic stiffness matrix for the left side of the rotating cracked shaft element can be expressed in the form

$$K_{ij1}^e = \frac{EI_i}{(1 + \Phi)^2} \left[\frac{P_0}{2} + \frac{P_1}{8} + \frac{P_2}{24} + \frac{P_3}{64} + \frac{P_4}{160} + \frac{P_5}{384} + \frac{P_6}{896} \right]$$

where $i, j = 1, \dots, 10$ and the constants P_i , $i = 0, 1, \dots, 6$ are defined as

$$P_0 = C_0$$

$$P_1 = C_1 + \delta_1 C_0$$

$$P_2 = C_2 + \delta_1 C_1 + \delta_2 C_0$$

$$P_3 = \delta_1 C_2 + \delta_2 C_1 + \delta_3 C_0$$

$$P_4 = \delta_2 C_2 + \delta_3 C_1 + \delta_4 C_0$$

$$P_5 = \delta_3 C_2 + \delta_4 C_1$$

$$P_6 = \delta_2 C_4$$

The constants C_i , $i, j = 0, 1, 2$ for different entries K_{ij1}^e are as follows:

For $K_{11_1}^e, -K_{16_1}^e, K_{22_1}^e, -K_{27_1}^e, K_{66_1}^e, K_{77_1}^e$

$$C_0 = \frac{36}{l},$$

$$C_1 = -\frac{4 \times 36}{l},$$

$$C_2 = \frac{4 \times 36}{l}.$$

For $K_{14_1}^e, -K_{23_1}^{e*}, K_{37_1}^e, -K_{46_1}^{e*}$

$$C_0 = 18 + \frac{6l(1+\Phi)}{c_v+l},$$

$$C_1 = -6 \left(12 + \frac{2l(1+\Phi)}{c_v+l} \right),$$

$$C_2 = 72.$$

For $K_{19_1}^e, -K_{28_1}^{e*}, -K_{69_1}^e, K_{78_1}^{e*}$

$$C_0 = 18 - \frac{6l(1+\Phi)}{c_v+l},$$

$$C_1 = 6 \left(-12 + \frac{2l(1+\Phi)}{c_v+l} \right),$$

$$C_2 = 72.$$

For $K_{33_1}^e, K_{44_1}^{e*}$

$$C_0 = l^3 \left(\frac{3}{l} + \frac{1+\Phi}{c_v+l} \right)^2,$$

$$C_1 = -12l^2 (1+\Phi) \left(\frac{3}{l} + \frac{1+\Phi}{c_v+l} \right),$$

$$C_2 = 36l.$$

For $K_{38_1}^e, K_{49_1}^{es}$
$C_0 = -l^3 \left(\frac{3}{l} + \frac{1+\Phi}{c_y+l} \right) \left(\frac{1+\Phi}{c_y+l} - \frac{3}{l} \right),$
$C_1 = -36l,$
$C_2 = 36l.$

For $K_{88_1}^e, K_{99_1}^{es}$
$C_0 = l^3 \left(\frac{1+\Phi}{c_y+l} - \frac{3}{l} \right)^2,$
$C_1 = 12l^2 \left(\frac{1+\Phi}{c_y+l} - \frac{3}{l} \right),$
$C_2 = 36l.$

TABLE: 4.5b

Any nonzero entry of the elastic stiffness matrix for the right side of the rotating cracked shaft element can be expressed in the form

$$K_{ij_2}^e = \frac{EI_i}{(1+\Phi)^2} \left[\frac{P_0}{2} + \frac{3P_1}{8} + \frac{7P_2}{24} + \frac{15P_3}{64} + \frac{31P_4}{160} + \frac{63P_5}{384} + \frac{127P_6}{896} \right]$$

where the constants P_i and C_i are as defined for the left side of the cracked shaft element for all the entries $K_{ij_2}^e$.

TABLE: 4.6a

Any nonzero entry of the shear stiffness matrix for the left side of the rotating cracked shaft element can be expressed in the form

$$K_{ij}^s = \frac{\kappa G A_i}{(1 + \Phi)^2} \left[\frac{P_0}{2} + \frac{P_1}{8} + \frac{P_2}{24} + \frac{P_3}{64} + \frac{P_4}{160} + \frac{P_5}{384} + \frac{P_6}{896} \right]$$

where $i, j = 1, \dots, 10$ and the constants P_i , $i = 0, 1, \dots, 6$ are defined as

$$P_0 = C_0$$

$$P_1 = C_1 + \alpha_1 C_0$$

$$P_2 = C_2 + \alpha_1 C_1 + \alpha_2 C_0$$

$$P_3 = \alpha_1 C_2 + \alpha_2 C_1 + C_3$$

$$P_4 = \alpha_1 C_3 + \alpha_2 C_2 + C_4$$

$$P_5 = \alpha_1 C_4 + \alpha_2 C_3$$

$$P_6 = \alpha_2 C_4$$

The constants C_i , $i, j = 0, 1, \dots, 4$, for different entries K_{ij}^s are as follows:

For $K_{11_1}^s, -K_{16_1}^s, K_{22_1}^s, -K_{27_1}^s, K_{66_1}^s, K_{77_1}^s$

$$C_0 = \frac{\Phi^2}{l},$$

$$C_1 = 0,$$

$$C_2 = 0,$$

$$C_3 = 0,$$

$$C_4 = 0$$

For $K_{14_1}^s, K_{19_1}^s, -K_{23_1}^{s*}, K_{37_1}^s, -K_{46_1}^{s*}, -K_{69_1}^s$

$$C_0 = \frac{\Phi^2}{2},$$

$$C_1 = 0$$

$$C_2 = 0$$

$$C_3 = 0,$$

$$C_4 = 0,$$

For $K_{33_1}^s, K_{44_1}^{s*}, -K_{38_1}^s$

$$C_0 = \frac{\Phi^2}{4},$$

$$C_1 = 0,$$

$$C_2 = 0,$$

$$C_3 = 0,$$

$$C_4 = 0.$$

For $K_{88_1}^s, K_{99_1}^{s*}$
$C_0 = \frac{\Phi^2}{4}$
$C_1 = 0,$
$C_2 = 0,$
$C_3 = 0,$
$C_4 = 0,$

TABLE: 4.6b

Any nonzero entry of the shear stiffness matrix for the right side of the rotating cracked shaft element can be expressed in the form

$$K_{ij_2}^s = \frac{EI_i}{(1 + \Phi)^2} \left[\frac{P_0}{2} + \frac{3P_1}{8} + \frac{7P_2}{24} + \frac{15P_3}{64} + \frac{31P_4}{160} + \frac{63P_5}{384} + \frac{127P_6}{896} \right]$$

where the constants P_i and C_i are as defined for the left side of the cracked shaft element for all the entries $K_{ij_2}^s$.

TABLE: 4.7

The nonzero entries of the torsional stiffness matrix for the left and right side of the rotating cracked shaft element are

$$K_{55_1}^\phi = K_{55_2}^\phi = \frac{2GI_t}{l} \left[\frac{1}{2} + \frac{\delta_1}{8} + \frac{\delta_2}{24} + \frac{\delta_3}{64} + \frac{\delta_4}{160} \right]$$

$$-K_{5,10_1}^\phi = -K_{10,5_1}^\phi = K_{10,10_1}^\phi = K_{55_1}^\phi$$

$$-K_{5,10_2}^\phi = -K_{10,5_2}^\phi = K_{10,10_2}^\phi = K_{55_2}^\phi$$

Remark 1 For the entries with (*) sign, the crack compliance c_y appearing in the constants C_i should be replaced by c_z .

Chapter 5

Modal Reduction

In this chapter, the strategy for solving the assembled equations of motion of the rotor-bearing system derived in chapter 3 is outlined. First the homogeneous form of the equations of motion is used to define the eigenvalue problem. The natural frequencies of the system are obtained from the eigenvalues. Different schemes to solve the eigenvalue problem are discussed. Second, the equations of motion of the rotor-bearing system have to be arranged in the state space form and integrated forward in time to study the time response of the system. The equations of motion of the system when written in nodal coordinates are of very high order spanning a wide-spread frequency spectrum. It is not only time consuming to integrate such a large number of equations but also numerically inefficient. Furthermore, the presence of high frequencies could result in a numerically stiff problem. Hence, a reduction of the order of the equations of motion is desirable while retaining the important dynamic characteristics of the actual system. It is well

known that the dynamics of a rotor-bearing system is dominated by the lower part of its frequency spectrum. Therefore, the lower set of frequencies can be retained in the reduced form of the equations of motion, thus resulting in a numerically more efficient system without sacrificing the accuracy of the obtained solution.

5.1 Eigenvalue Problem

The equations of motion of the rotor-bearing system derived in chapter 4 is

$$m_{22}^i \ddot{e}^i + \dot{\theta}_x^i g^i \dot{e}^i + k^i e^i = Q_2 \quad (5.1)$$

where m_{22}^i , g^i , k^i are the assembled mass, gyroscopic and stiffness matrices respectively and e^i is the assembled vector of nodal coordinates. These constituent matrices are highly banded in nature. The matrices m_{22}^i and k^i are symmetric, whereas g^i is skew symmetric. The vector Q_2 contains all the forces, external as well as generalized, acting on the shaft. Neglecting the external forces and rearranging the generalized forces acting on the shaft due to the bearings to the left side of Eq.(5.1), the free vibrational equation of motion of the rotor-bearing system can be written as

$$m\ddot{e} + g\dot{e} + ke = 0 \quad (5.2)$$

where g is the sum of the gyroscopic matrix and bearing damping matrix and k is the sum of stiffness matrices of shaft and bearings. The mass matrix m_{22}^i and the nodal coordinate vector e^i are now denoted as m and e respectively. The matrix g is skew symmetric only if the bearings are undamped, otherwise it is a general real matrix. The matrix k is symmetric only when the bearings are rigid or when they have stiffness coefficients in the principal directions, otherwise it is a general real matrix.

The homogeneous equations of motion Eq.(5.2) can be solved in two different coordinate systems: (a) the rotating reference system $X'Y'Z'$ and (b) the inertial coordinate system XYZ .

5.1.1 Equations in the Rotating Reference Frame

The homogeneous system of equations given by Eq.(5.2) is transformed into the rotating frame $X'Y'Z'$. The $X'Y'Z'$ frame is rotating about the X' axis with a speed of ω , as shown in Figure 5-1. In this method, only bending frequencies can be found as the transformation to the rotating frame loses track of the torsional motion. The transformation from XYZ to $X'Y'Z'$ is given by

$$e = \Upsilon p \quad (5.3)$$

where e and p are the vectors of nodal coordinates in XYZ and $X'Y'Z'$ coordinate systems, respectively, and Υ is the transformation matrix which is function of the rotational speed ω and time t . The nodal coordinate vectors e and p of the unconstrained

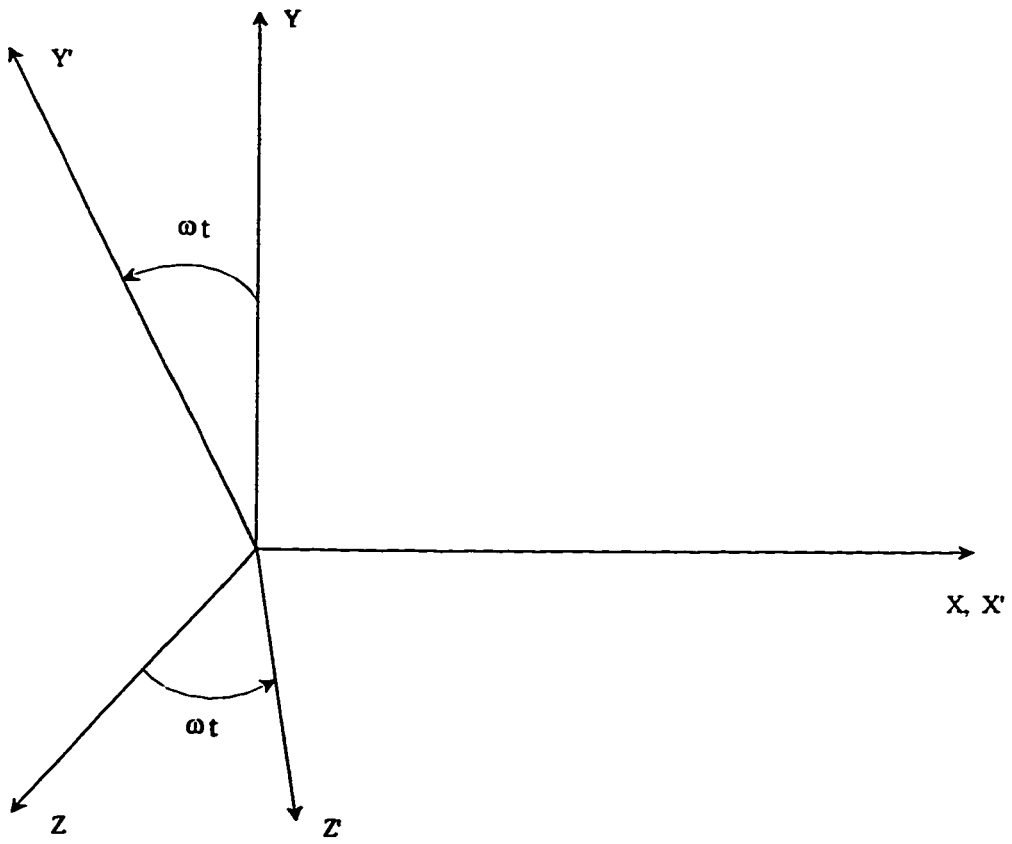


Figure 5-1: Rotation of $X'Y'Z'$ axes relative to XYZ axes

rotor-bearing system are of the form

$$e = \{v_1, w_1, \beta_1, \gamma_1, \dots, v_n, w_n, \beta_n, \gamma_n\}^T \quad (5.4)$$

and

$$p = \{v'_1, w'_1, \beta'_1, \gamma'_1, \dots, v'_n, w'_n, \beta'_n, \gamma'_n\}^T \quad (5.5)$$

respectively, where n is the number of nodes present in the system. The above vectors in equations (5.4) and (5.5) are written by neglecting the torsional degree of freedom ϕ .

The transformation matrix Υ is then of the form

$$\Upsilon = \begin{bmatrix} s & & & 0 \\ & s & & \\ & & \cdot & \\ 0 & & & s_n \end{bmatrix} \quad (5.6)$$

where

$$s = \begin{bmatrix} \cos \omega t & -\sin \omega t & 0 & 0 \\ \sin \omega t & \cos \omega t & 0 & 0 \\ 0 & 0 & \cos \omega t & -\sin \omega t \\ 0 & 0 & \sin \omega t & \cos \omega t \end{bmatrix} \quad (5.7)$$

The first two time derivatives of Eq.(5.3) can be written as

$$\dot{e} = \omega \bar{\Upsilon} p + \Upsilon \dot{p} \quad (5.8)$$

$$\bar{e} = \Upsilon (\bar{p} - \omega^2 p) + 2\omega \bar{\Upsilon} \dot{p} \quad (5.9)$$

where

$$\bar{\Upsilon} = \begin{bmatrix} \bar{s} & 0 \\ & \bar{s} \\ 0 & \bar{s}_n \end{bmatrix} \quad (5.10)$$

The submatrix \bar{s} in Eq.(5.10) is defined as

$$\bar{s} = \frac{1}{\omega} \dot{\bar{s}} = \begin{bmatrix} -\sin \omega t & -\cos \omega t & 0 & 0 \\ \cos \omega t & -\sin \omega t & 0 & 0 \\ 0 & 0 & -\sin \omega t & -\cos \omega t \\ 0 & 0 & \cos \omega t & -\sin \omega t \end{bmatrix} \quad (5.11)$$

Substituting Eq.(5.3) and Eqs.(5.8-5.10) in Eq.(5.2) and premultiplying by Υ^T , one can write

$$m\bar{p} + (2\omega\hat{m} + g)\dot{p} + (\omega\hat{g} - \omega^2 m + k)p = 0 \quad (5.12)$$

where

$$\hat{m} = \Upsilon^T m \bar{\Upsilon} \quad (5.13)$$

$$\hat{g} = \Upsilon^T g \bar{\Upsilon} \quad (5.14)$$

Now assuming that the bearings are undamped, then for constant spin speed i.e. $\dot{\theta}_x^i = \Omega$, the matrix g can be expressed as

$$g = \Omega g^i \quad (5.15)$$

Further, we know that neglecting the torsional and coupling effects, the mass matrix m is

$$m = m_t + m_r \quad (5.16)$$

where m_t and m_r are the mass matrices due to flexural deflections and rotary inertia respectively. Substituting equations (5.15) and (5.16) in Eq.(5.12), one can write

$$m\ddot{p} + \omega [2\hat{m} + \lambda g^i] \dot{p} + [\omega^2 (\lambda \hat{g}^i - (m_t + m_r)) + k] p = 0 \quad (5.17)$$

where $\lambda = \frac{\Omega}{\omega}$ is the whirl ratio. After some algebraic manipulations of Eqs.(5.6), (5.10) and (4.51) one can establish the following relationship between the gyroscopic matrix g^i and the rotary inertia matrix m_r :

$$g^i = 2\Upsilon^T m_r \bar{\Upsilon} = 2\hat{m}_r \quad (5.18)$$

Substituting Eq.(5.18) in Eq.(5.17), one can write

$$m\ddot{p} + \omega [2\hat{m} + \lambda g^i] \dot{p} + [\omega^2 (2\lambda m_r - m) + k] p = 0 \quad (5.19)$$

The natural whirl speeds and the mode shapes with respect to the rotating frame $X'Y'Z'$ can be obtained from Eq.(5.19). These modes are constant relative to $X'Y'Z'$ frame. Assuming $p = p_o = \text{constant}$ as a solution, the associated eigenvalue problem becomes

$$kp_o = \omega^2 (m - 2\lambda m_r) p_o \quad (5.20)$$

The solution of Eq.(5.20) gives eigenvalues ω together with the associated eigenvectors p_o . The eigenvalues represent the natural whirl speeds and the eigenvectors represent the mode shapes relative to $X'Y'Z'$ frame at the specified whirl ratio λ . The total number of eigenvalues obtained are equal to the dimension of the matrices in Eq.(5.20). The eigenvalues are real and have positive values.

The above procedure may be simply viewed as solving the eigenvalue problem of a rotor-bearing system by restructuring its mass matrix so as to accommodate the gyroscopic effects. By such restructuring of the mass matrix, the eigenvalue problem is transformed into the classical eigenvalue problem denoted by

$$(k - \omega^2 m) p = 0 \quad (5.21)$$

The limitations of this method of eigensolution are evident. The bearings used have to be undamped and isotropic. The eigenvalue problem cannot be solved for any given spin speed Ω , thus inhibiting its wide application. It can only be solved for a specified whirl ratio λ .

5.1.2 Equations in the Inertial Reference Frame

The homogeneous equations of motion Eq.(5.2) can be represented in the following state space form

$$\begin{bmatrix} 0 & -m \\ m & g \end{bmatrix} \begin{Bmatrix} \bar{e} \\ \dot{e} \end{Bmatrix} + \begin{bmatrix} m & 0 \\ 0 & k \end{bmatrix} \begin{Bmatrix} \dot{e} \\ e \end{Bmatrix} = 0 \quad (5.22)$$

Or, simply as

$$E\dot{q} + Fq = 0 \quad (5.23)$$

in which

$$q = \begin{bmatrix} \dot{e}^T, & e^T \end{bmatrix}^T \quad (5.24)$$

The matrices E and F are highly banded. If the bearings are undamped then the matrix E is skew symmetric. The matrix F is symmetric when the bearings are isotropic with cross coupling terms equal to zero. If the bearings are damped or orthotropic or both, then nothing can be said about the symmetry or skew-symmetry of the matrices. Thus, the type of bearings used in the rotor-bearing system play an important role in selecting a numerical strategy to solve the equation of motion. The eigenvalues of the rotor-bearing system can be extracted from Eq.(5.23) by assuming a solution of the form

$$q = \bar{q}e^{\bar{\omega}t} \quad (5.25)$$

Substituting Eq.(5.25) in Eq.(5.23) we can write

$$(\bar{\omega}E + F) \bar{q}e^{\bar{\omega}t} = 0 \quad (5.26)$$

Equation (5.26) yields both forward and backward whirl speeds from the same eigenvector. The eigenvalues are found in complex form as

$$\bar{\omega} = \omega_r + i\omega \quad (5.27)$$

where the imaginary part ω is the whirl speed. The real part of Eq.(5.27) is used to express the logarithmic decrement

$$\underline{\Delta} = \frac{-2\pi\omega_r}{\omega} \quad (5.28)$$

The logarithmic decrement is a measure of the rate of decay of free oscillations and is defined as the natural logarithm of the ratio of any two successive amplitudes. It is a convenient way of determining the amount of damping present in a system. There is no restriction on the type of bearings when this method is used to solve the system's eigenvalue problem.

5.2 Modal Reduction Schemes

The finite element method is often used to model complex rotor-bearing systems, which involves writing the equations of motion in terms of nodal coordinates. The use of nodal coordinates, however, results in a large dimensionality, thus inhibiting the efficiency of the finite element solution. Moreover, the use of nodal coordinates results in a dynamic model of widely spread eigen-spectrum that includes many insignificant modes. Consequently, a numerically stiff system is often created which causes the numerical integration scheme to search inefficiently for a solution or may even fail to find one.

In order to alleviate this problem, reduced order models using modal coordinates were introduced. Likins [31] introduced modal reduction using complex modes in his early formulation of the elastic appendage equations. Gunter et al.[32] utilized modal transformations to obtain a reduced order modal form of the equations of motion. Although they recognized that the actual vibration modes of a rotor system are complex, they have used planar modes in their evaluation of the unbalance response of the rotor. They have also referred to the numerical difficulties associated with using complex modes. Nevertheless, they recommended that complex modes (damped modes) be considered in the final analysis. Laurenson [33] addressed the issue of complex mode shapes in rotating flexible structures. It was suggested, however, that planar modes be used in modal reduction of complex geometric configurations by employing the technique presented in [34] for converting the complex eigenvalue problem to one defined by real matrices. Stephenson and Rouch [35] invoked modal reduction using planar modes, wherein the mass matrix

was modified to include the gyroscopic effects. Modal transformations using planar modes were also utilized in evaluating the unbalance response [36, 37], stability [38], and the gyroscopic effect in rotor systems [39]. In this regard, one can also refer to the general area of flexible multibody applications [40-43] where planar modes were employed to obtain reduced order models inspite of the existence of damping and gyroscopic forces. Kane and Torby [44] referred to the different methods for reducing the size of the finite element model while preserving the lower (significant) frequencies. It was stated that the static reduction usually results in poor accuracy at higher modes, therefore, cannot be applied to general rotor systems because it is derived for systems having symmetric mass and stiffness matrices. Therefore, they introduced a modal transformation based on complex modes that resulted in reduced mass and stiffness matrices, and demonstrated how the reduced model preserved the same modal characteristics of the original finite element model. Their work, however, was not carried out to the dynamic response analysis stage.

Having examined the previously cited investigations, one recognizes a strong view in support of using complex modes in modal transformations of systems with gyroscopic matrices, though acknowledging the associated numerical complexities. To avoid such numerical difficulties, another view suggested the use of planar modes obtained after modifying the mass matrix to include the gyroscopic effects. Nevertheless, other investigators, especially those concerned with dynamic response analysis, have consistently employed planar modal transformations. It is noteworthy to mention, to the best of the author's knowledge, that no dynamic response analysis study that invoked complex

modal transformations was reported in the available literature.

In the following sections, first the planar modal reduction scheme which is widely used in the dynamic analysis of the flexible system is presented. This scheme utilizes planar modes obtained by solving the self-adjoint eigenvalue problem. Second, the complex modal reduction scheme is applied to rotor-bearing systems. The complex modal reduction scheme invokes the complex modes of the non-self-adjoint eigenvalue problem. Lastly, the modal reduction scheme presented by Kane and Torby [44] which is called the extended modal reduction is discussed.

5.2.1 Planar Modal Reduction

In order to obtain the real eigenvalues and the associated planar modes, one must ignore the matrix g in Eq.(5.2). To this end, the associated homogenous adjoint equation can be written as

$$m\ddot{e} + ke = 0 \quad (5.29)$$

Upon solving the self-adjoint eigenvalue problem associated with Eq.(5.29), which is of the form presented in Eq.(5.21), one obtains a set of real eigenvalues and eigenvectors. Let H denote the modal matrix that comprises a selected subset of the resulting real eigenvectors (planar modes). Now, a modal transformation can be defined as

$$e = Hv \quad (5.30)$$

where ν is the vector of modal coordinates. If only a truncated set of significant modes are retained, the corresponding truncated form of Eq.(5.1) can be written as

$$H^T m H \ddot{\nu} + H^T g H \dot{\nu} + H^T k H \nu = H^T F \quad (5.31)$$

Or simply as

$$M_r \ddot{\nu} + G_r \dot{\nu} + K_r \nu = H^T F \quad (5.32)$$

where M_r , G_r , and K_r are the reduced modal mass, gyroscopic, and stiffness matrices, respectively. Equation (5.32) represent the reduced order model using planar mode truncation.

5.2.2 Complex Modal Transformation

The elastodynamic model of Eq.(5.1) can be represented in the state-space form as

$$\begin{bmatrix} 0 & -m \\ m & g \end{bmatrix} \begin{Bmatrix} \bar{e} \\ \dot{e} \end{Bmatrix} + \begin{bmatrix} m & 0 \\ 0 & k \end{bmatrix} \begin{Bmatrix} \dot{e} \\ e \end{Bmatrix} = \begin{Bmatrix} 0 \\ F \end{Bmatrix} \quad (5.33)$$

Or simply as

$$E\dot{q} + Fq = f \quad (5.34)$$

where E , F and q are as defined in section 5.1.2. One can write the following two homogeneous adjoint equations:

$$E\dot{q} + Fq = 0 \quad (5.35)$$

and

$$E^T \dot{q}' + F^T q' = 0 \quad (5.36)$$

Assuming a solution in the form of Eq.(5.25) and substituting in Eq.(5.35), one can write

$$(\bar{\omega}_i E + F) R_i = 0 \quad (5.37)$$

where $\bar{\omega}_i$ is the i^{th} eigenvalue associated with the right hand eigenvector R_i . Similarly substituting Eq.(5.25) in Eq.(5.36), we can write

$$(\bar{\omega}_i E^T + F^T) L_i = 0 \quad (5.38)$$

where $\bar{\omega}_i$ is the i^{th} eigenvalue associated with the left hand eigenvector L_i . For non-symmetric E and F , R_i does not equal L_i and for symmetric E and F , R_i equals L_i . Let R and L denote the complex modal matrices of the differential operators of equations (5.35) and (5.36), respectively, [45]. Introducing the transformation

$$q = Ru \quad (5.39)$$

where u is the vector of modal coordinates. If only a subset of significant modes are to be retained, the truncated modal form of the equations of motion can be written as

$$L^T E R \dot{u} + L^T F R u = L^T f \quad (5.40)$$

Or, simply as

$$E_r \dot{u} + F_r u = L^T f \quad (5.41)$$

where R and L contain only those complex eigenvectors that represent a subset of selected modes. Now Eq.(5.41) represents truncated model using complex modal transformation. In general, a subset of eigenvectors which spans the frequency spectrum of the forcing function are retained as significant modes.

5.2.3 Extended Modal Reduction

In the extended modal reduction scheme, the degrees of freedom of the rotor-bearing system are divided into two parts. One part contains only those degrees of freedom which are very important for the motion of the rotor-bearing system. Such degrees of freedom are chosen as retained degrees of freedom a . The other part which contains the non-essential degrees of freedom is chosen as omitted degrees of freedom o . The reduced size mode shapes will represent only the motion of the retained degrees of freedom. In determining which modes to keep, it is usually desirable to retain the lowest system frequencies. The choice of retained degrees of freedom affects the resulting reduced system matrices and the degrees of freedom represented in the eigenvectors, but the eigenvalues and the mode shapes are not affected.

Having chosen the degrees of freedom and modes to be retained, the $[E]$ and $[F]$ matrices and the right and left hand mode shapes R and L may be partitioned into the retained degrees of freedom, a , and the omitted degrees of freedom, o . The unwanted

modes are also removed. The partitioned matrices and the eigenvectors are given as follows,

$$E_p = \begin{bmatrix} E_{aa} & E_{ao} \\ E_{oa} & E_{oo} \end{bmatrix} \quad (5.42)$$

$$F_p = \begin{bmatrix} F_{aa} & F_{ao} \\ F_{oa} & F_{oo} \end{bmatrix} \quad (5.43)$$

$$R_{ip} = \begin{bmatrix} R_{ia} \\ R_{io} \end{bmatrix}, \quad i = 1 \text{ to the number of retained modes} \quad (5.44)$$

$$L_{ip} = \begin{bmatrix} L_{ia} \\ L_{io} \end{bmatrix}, \quad i = 1 \text{ to the number of retained modes} \quad (5.45)$$

Any number of degrees of freedom may be retained, but the number of modes retained should be equal to or less than the number of degrees of freedom ($\leq a$). The vector q can also be expressed in terms of the truncated and partitioned right hand vector matrix and the associated normal coordinates y . Namely,

$$q = \begin{Bmatrix} q_a \\ q_o \end{Bmatrix} = \begin{bmatrix} R_a \\ R_o \end{bmatrix} y \quad (5.46)$$

From Eq.(5.46),

$$q_a = R_a y \quad (5.47)$$

Premultiplying by R_a^T gives,

$$R_a^T q_a = R_a^T R_a y \quad (5.48)$$

The generalized inverse may now be used to solve for y

$$y = (R_a^T R_a)^{-1} R_a^T q_a \quad (5.49)$$

Equation (5.49) substituted into Eq.(5.46) gives,

$$q_o = D_R q_a$$

where,

$$D_R = R_o (R_a^T R_a)^{-1} R_a^T \quad (5.50)$$

Similarly, for the left hand modes,

$$q = \begin{Bmatrix} q_a \\ q_o \end{Bmatrix} = \begin{bmatrix} L_a \\ L_o \end{bmatrix} \{y'\} \quad (5.51)$$

where y' is the normal coordinate vector for the transposed system. In a similar manner,

it can be shown that

$$q_o = D_L q_a \quad (5.52)$$

where,

$$D_L = L_o (L_a^T L_a)^{-1} L_a^T \quad (5.53)$$

Now define

$$T_R = \begin{bmatrix} I \\ D_R \end{bmatrix} \quad (5.54)$$

$$T_L = \begin{bmatrix} I \\ D_L \end{bmatrix} \quad (5.55)$$

Then,

$$R_p = T_R R_a \quad (5.56)$$

and similarly,

$$L_p = T_L L_a \quad (5.57)$$

The reduced matrices E_R and F_R are then defined by

$$E_R = T_L^T E_p T_R \quad (5.58)$$

$$F_R = T_L^T F_p T_R \quad (5.59)$$

The equations of motion formed using these reduced matrices can be integrated forward in time. The procedure to determine the reduced matrices is numerically sensitive as the evaluation of the generalized inversion of matrices is involved in Eq.(5.50) and Eq.(5.53). Furthermore, the above procedure may yield complex reduced matrices which

often complicate the numerical integration of the equations of motion. Due to these numerical difficulties which are associated with the extended modal reduction scheme, the direct complex modal reduction scheme presented in section 5.2.2 appears to be the most appropriate in the sense of both efficiency and accuracy requirements.

Chapter 6

Results and Discussions

The eigenvalue solution and the modal reduction schemes discussed in the previous chapter will be applied to obtain the natural frequencies and time response for different rotor bearing systems. The results will be compared to some available results in literature, wherever possible.

6.1 The Computer Scheme

A Computer program is developed for the free and forced vibration analysis of a cracked multibody rotor-bearing system. The developed computer program carries out the following tasks:

- Evaluation of the system matrices

- Solution of the eigenvalue problem in the rotating reference frame as well as in the inertial frame to evaluate the modal characteristics.
- Implementation of the modal reduction schemes to generate the reduced order matrices
- Numerical solution of the reduced order equations of motion to evaluate the time response in terms of the modal coordinates
- Recovering the nodal coordinate vector using the modal coordinate vector and updates the forcing vector which is a function of the nodal coordinates.

A flow chart of the developed computer scheme is presented in Figure 6-1. The important tasks carried out by the program are further explained in details.

6.1.1 Input Data

The input to the computer scheme developed in this investigation is given in a separate subroutine. Since the rotor-bearing system is being treated as a multibody system, the number of bodies in the system have to be defined. The details pertaining to each body which are required by the computer scheme are discussed below.

Type of body: The type of each body i.e. whether it is rigid or flexible is to be defined. A rigid body is characterized by its mass and the reference positions of its centre of mass. A flexible body is then discretized into a number of finite elements and

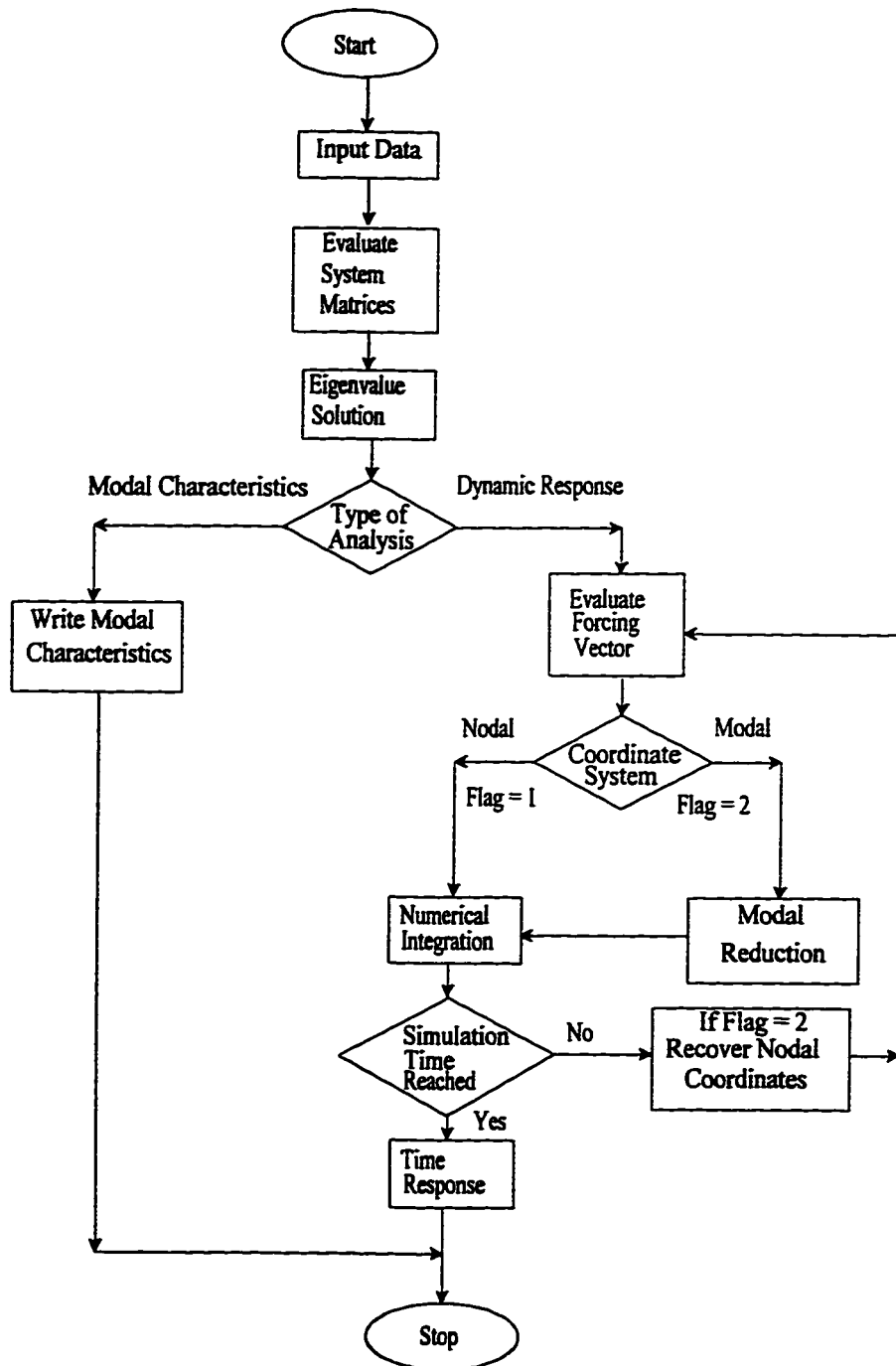


Figure 6-1: The control flow diagram of the developed computational scheme

properties of each finite element are defined. If the flexible body under consideration is the rotor shaft, its spin speed is to be specified.

Element Properties: There are two types of properties namely; geometrical and material that need to be specified for each finite element of the flexible body. The geometrical properties include length, outer radii at each end of the element, flag to indicate whether the element is solid or hollow. If the element is hollow, the inner radii at each end of the element as well as the position of each element along the inertial axes must be defined. The taperness of the finite element is defined by specifying two different radii at the two ends of the element. The developed computational scheme can accommodate tapered hollow shaft parts, as well. The material properties include the mass density, Young's modulus, Poisson's ratio and shear coefficient.

Crack: A crack may be present in any finite element of the rotor shaft. There is a flag associated with each finite element of the rotor shaft to indicate the presence of a crack. If a crack is present, its flexibility compliance need to be specified.

Bearings: The total number of the bearings and their locations are required by the computational scheme. The bearings could be anisotropic, flexible and damped. The flexibility of the bearings, are expressed in terms of stiffness coefficients. The properties of each bearing which may include different values of stiffness and damping coefficients in different directions need to be specified.

Disks: Disks are assumed to be rigid. The total number of disks and their respective positions are to be specified. The properties of the disk which are needed for the

computational scheme are the mass of the disk and its mass moment of inertia about the centroidal axes.

Type of Analysis: One need to specify the type of analysis required. (a) For modal analysis, one must specify whether planar or complex modal characteristics are required, as well as specifying the number of eigenvalues and the corresponding eigenvectors to be printed. (b) For dynamic response analysis, one must specify whether the equations of motion are generated in terms of nodal or modal coordinates. If nodal coordinates are chosen, the user must indicate whether a planar or complex modal reduction scheme is to be invoked, as well as the number of significant modes to be retained in the dynamic model. In either case of the dynamic simulations, however, the total simulation time must be specified.

6.1.2 System Matrices

The cracked rotor-bearing system consists of rigid as well as flexible components. The flexible rotor shaft is cracked at some location along its axis. When the flexible rotor shaft is divided into finite elements, only one finite element will contain the crack and all the other elements are uncracked. The element mass, stiffness and gyroscopic matrices of each element for which the nonzero entries are presented in Tables 4.1 to 4.7 are evaluated. The boundary conditions are applied and the matrix entries are stored in a master array after assigning pointers for every entry. The element matrices for all the elements are evaluated and stored in master array. The pointers created are used to

assemble the system matrices. The control flow chart for creating the system matrices is shown in Figure 6-2.

6.1.3 Eigenvalue Solution

The system matrices are used to establish the eigenvalue problem. The eigenvalue problem can be solved in either the rotating reference frame or in the Inertial frame. When using rotating reference frame, the matrices involved are symmetric (Eq.(5.20)), whereas when the inertial frame is used the matrices are, in general, not symmetric (Eq.(5.26)). The eigenvalue problem is solved using EISPACK subroutines. The control flow diagram for this purpose is shown in Figure 6-3.

6.1.4 Modal Reduction Schemes

Two modal reduction schemes, namely planar and complex are implemented. The modal transformation matrices are constructed using a subset of eigenvectors. The subset of eigenvectors are selected such that the reduced modal matrices span the lower or significant part of the frequency spectrum of the system. The complex reduction scheme is numerically difficult to implement. The entries in the modal transformation matrix are complex. when the complex modal transformation matrices are multiplied with real full order matrices, the resulting reduced matrices of Eq.(5.41) are, in general, be complex. This implies that the reduced modal equations have complex coefficients. It needs considerable programming effort to take care of the resulting complex modal equations.

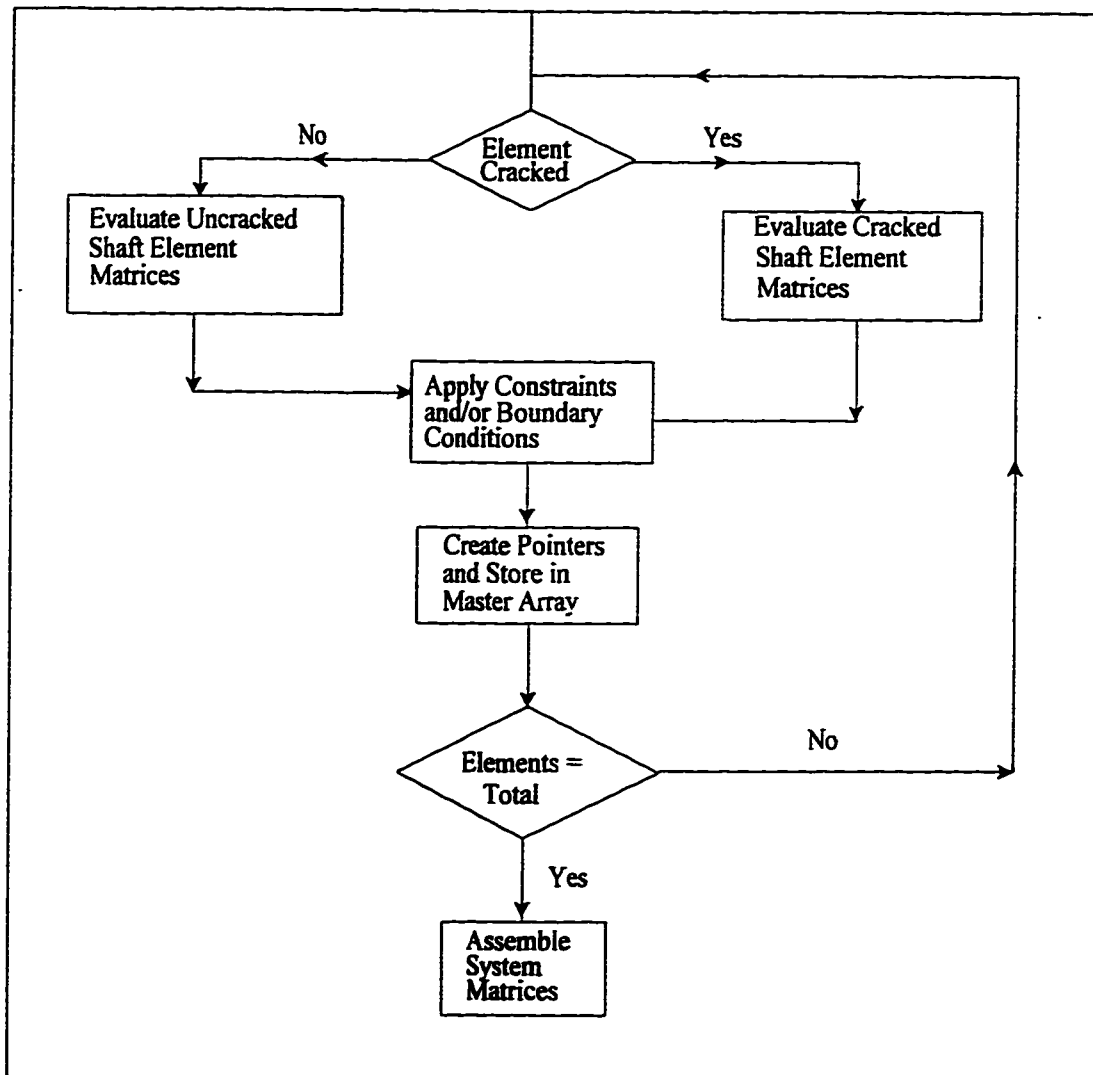


Figure 6-2: Control flow diagram for evaluating the system matrices
128

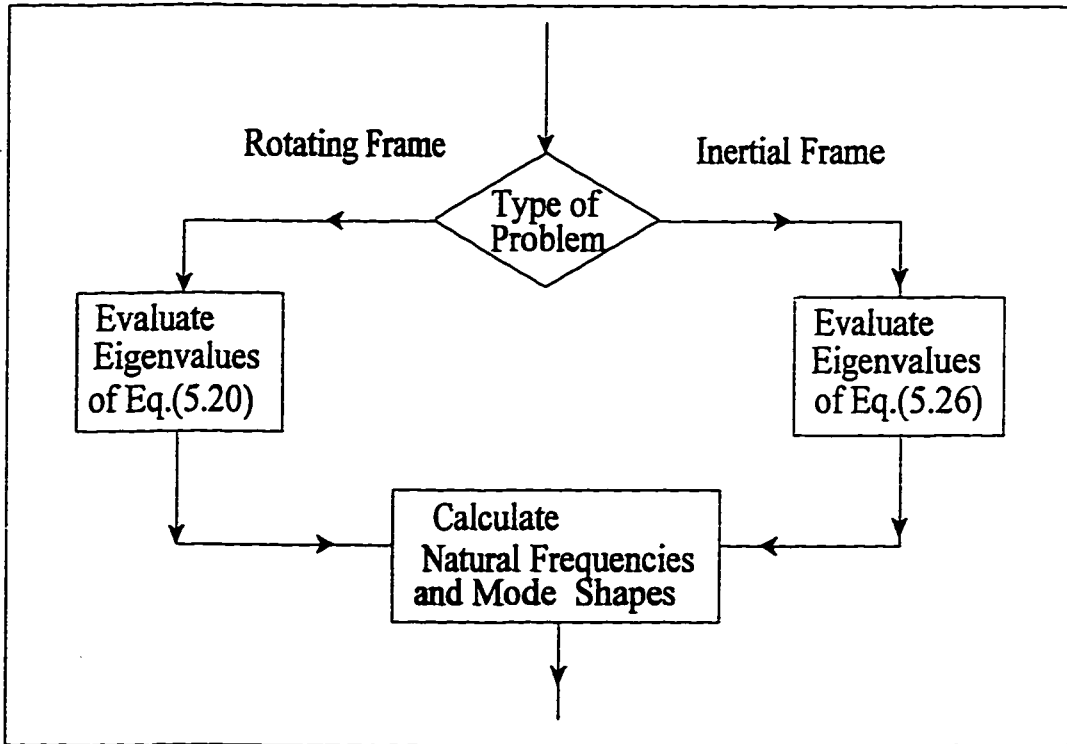


Figure 6-3: Control flow diagram for the eigenproblem solution

Numerical integration of the complex modal equations is also time consuming.

The difficulty of complex modal transformations is avoided when the planar modal reduction is utilized. In planar modal reduction, the planar modes obtained from Eq.(5.29) are used to reduce the order of equations of motion. The resulting reduced order equation of motion i.e. Eq.(5.32) has real coefficients. The control flow diagram showing the implementation of the modal reduction scheme is shown in Figure 6-4.

6.1.5 Numerical Integration

The reduced order modal equations are integrated forward in time to predict the time response. The Runge-Kutta-Fehlberg fourth and fifth order numerical solution scheme for a system of first order differential equations is used for numerically integrating the modal equations.

The equations of motion are arranged such that the inertia coupling term is kept on the right side along with the forcing terms. In this way, the coefficient matrices of the equations of motion are constant whereas the forcing vector becomes a function of nodal coordinates. Therefore, the forcing vector needs to be updated at every time step.

At the end of each numerical integration step, the modal coordinate vector is computed. The nodal coordinates can be recovered using the modal transformation. The computed nodal coordinate vector is associated with the system matrix. Therefore, the unconstrained elemental nodal coordinate vector is obtained from the system's nodal vector, and then used in computing the inertia coupling matrix. The inertia coupling matrix

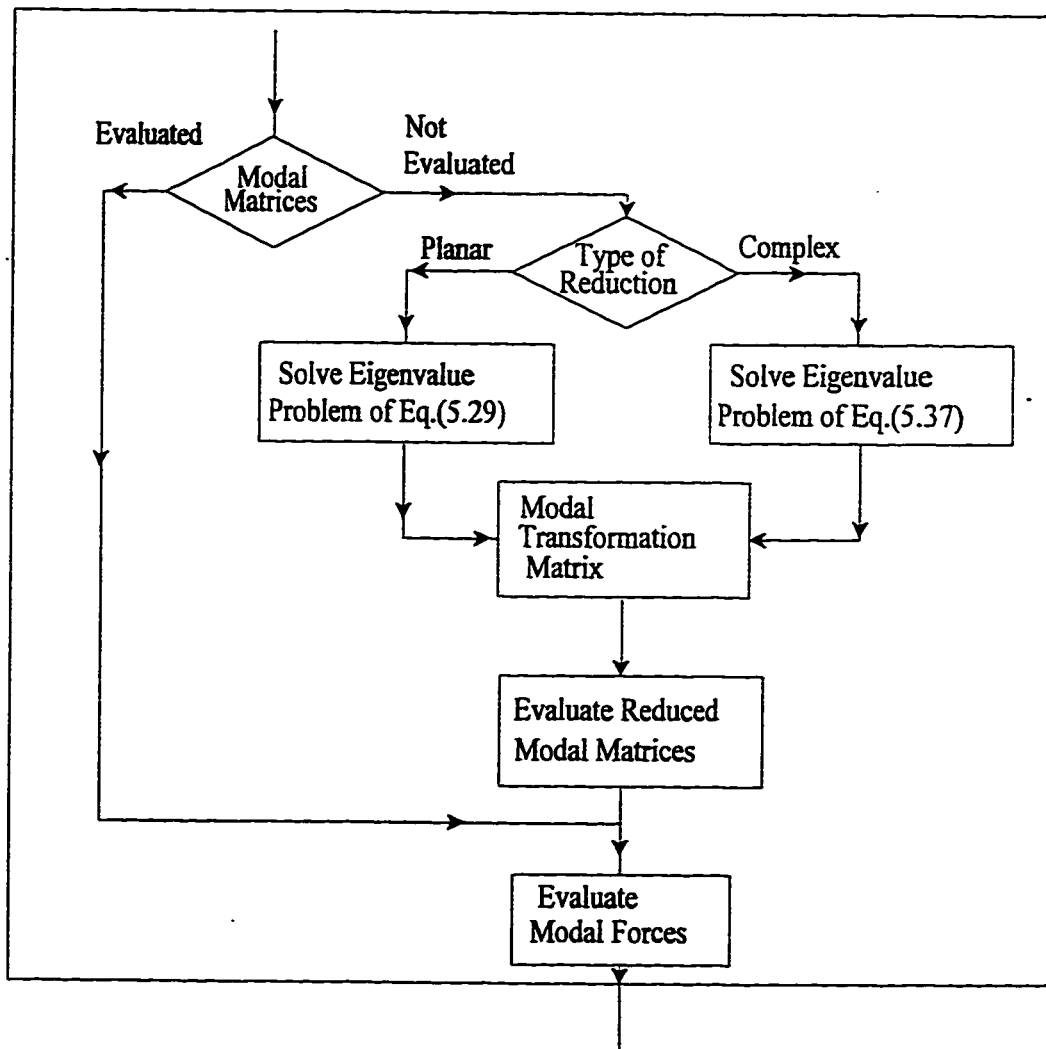


Figure 6-4: Control flow diagram for the implementation of the modal reduction scheme

for the whole system is assembled from the element matrices. Accordingly, the forcing vector for the whole system is updated at every time step. The assembly procedure has to be implemented at every time step which makes the numerical integration of the inertia coupled equations time consuming. The control flow diagram for the evaluation of the forcing vector is shown in Figure 6-5. In Figure 6-6 the procedure to evaluate the nodal coordinate vector from the modal vector is presented.

6.2 Modal Characteristics

This section is divided into two subsections. In the first subsection, the natural frequencies obtained using the developed finite element model will be compared to the results available in the literature. In the second subsection, the natural frequencies obtained using the planar and complex modal reduction schemes will be compared to the natural frequencies obtained using the full order finite element model.

6.2.1 Natural Frequencies

To validate the present finite element model, some numerical comparisons with analytical results published in the literature are presented.

Example 1

As a first example, the cantilever shaft considered in reference [14] with the following data: radius $R = 0.1m$, length $L = 1m$, Young's modulus of Elasticity $E = 2.1 \times 10^{11}N/m^2$,

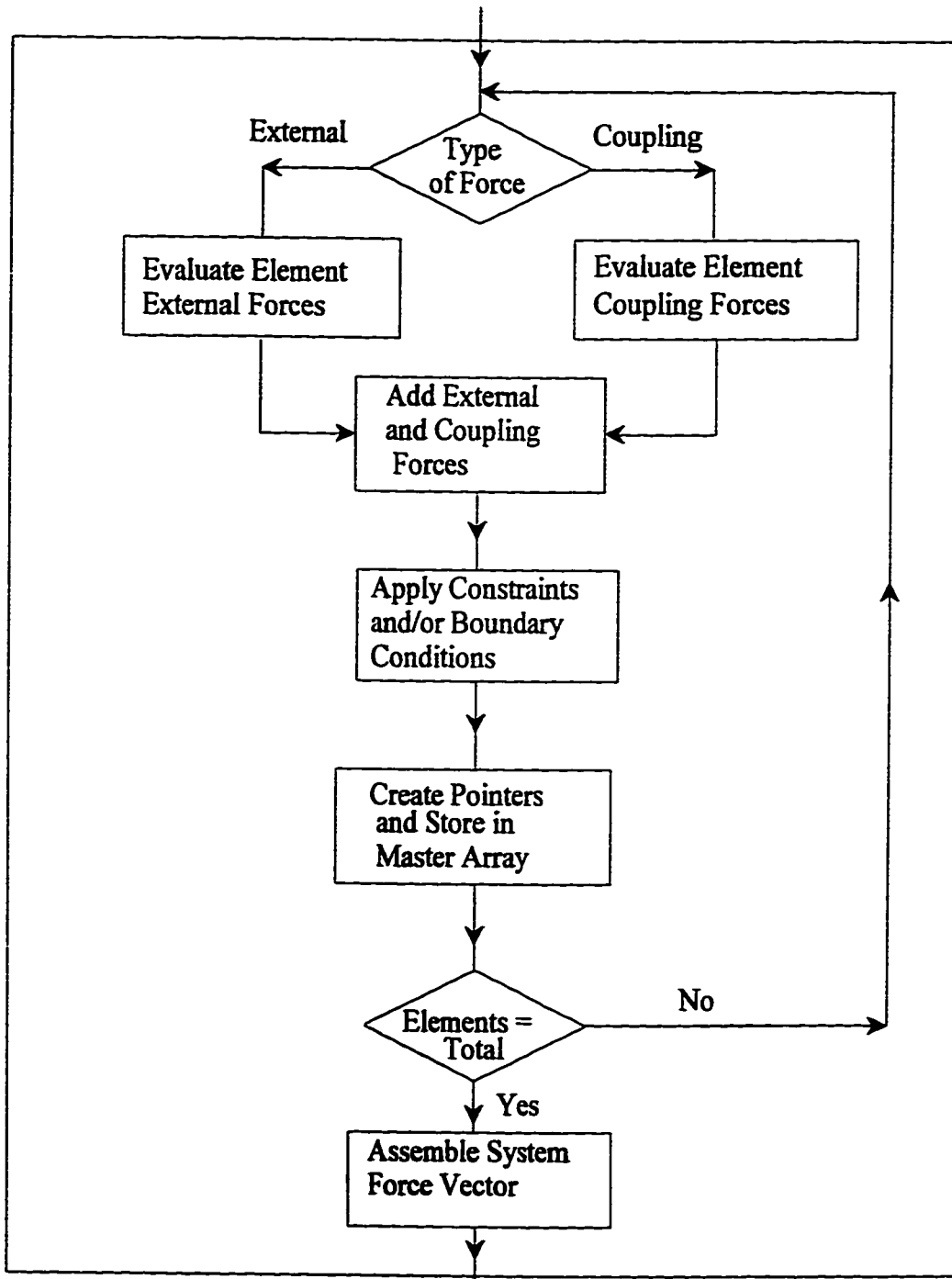


Figure 6-5: Control flow diagram to compute the time dependent forcing vector
133

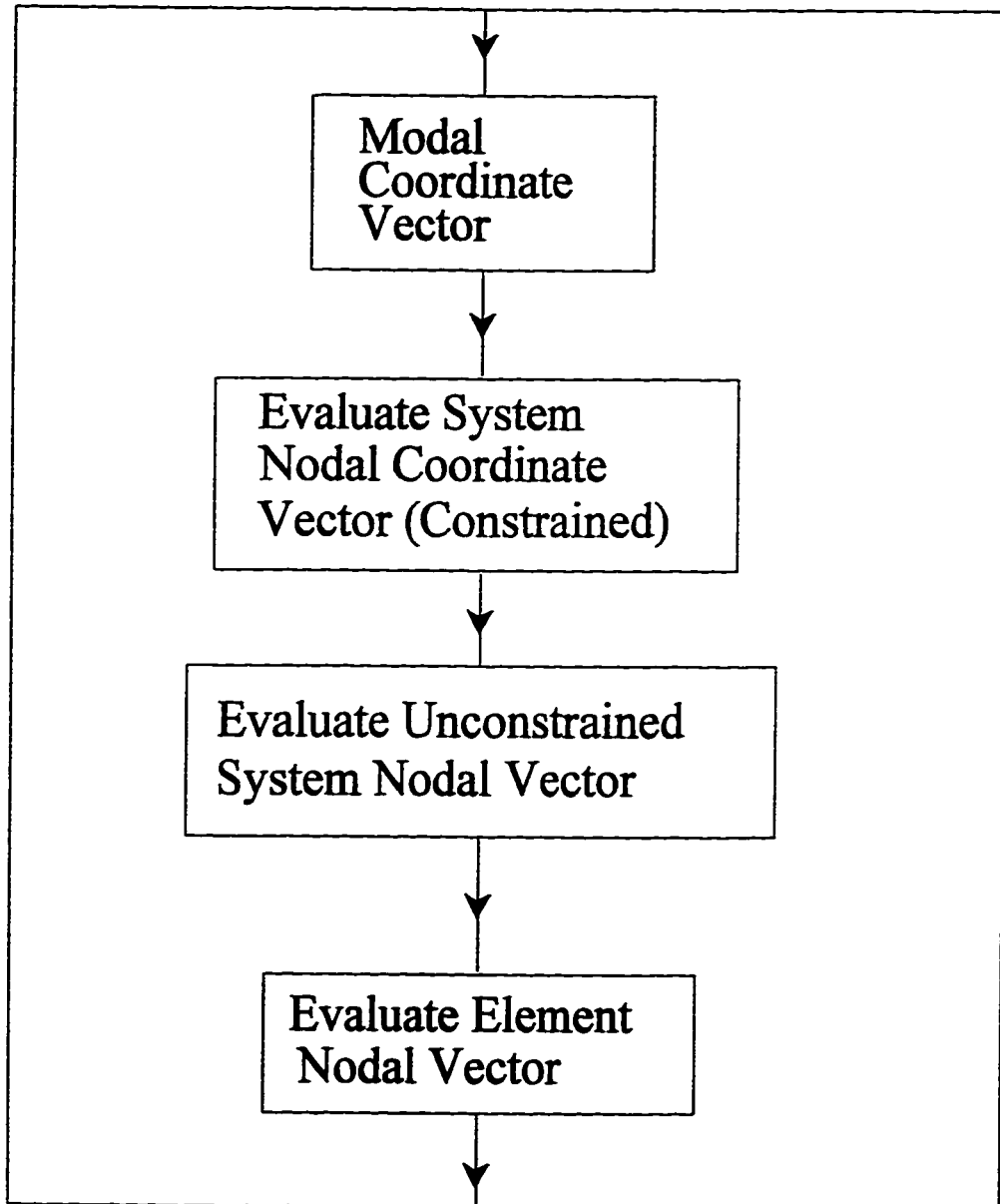


Figure 6-6: Control flow diagram to evaluate the nodal coordinates from the modal coordinates

mass density $\mu = 7860 \text{ kg/m}^3$ and Poisson ratio $\nu = 0.3$ is simulated. The change in the first bending natural frequency is studied for different slenderness ratios η , position of the crack ρ and crack depth Δ . The above parameters are defined as follows:

$$\text{slenderness ratio } \eta = \frac{R}{L} \quad (6.1a)$$

$$\text{position of the crack } \rho = \frac{L_1}{L} \quad (6.1b)$$

$$\text{crack depth } \Delta = \frac{a}{D} \quad (6.1c)$$

where R is the radius, L is the length, D is the diameter, L_1 is the distance of the crack from one end of the shaft and a is the depth of the crack. The change in the bending natural frequency is measured by the frequency ratio f_{nr} , which is defined as

$$f_{nr} = \frac{\omega_{ic}}{\omega_i} \quad (6.2)$$

where ω_{ic} and ω_i are the i^{th} frequency of the cracked and uncracked shaft, respectively. The change of the natural frequency due to the presence of a crack for different η and crack depths Δ is given in Table 6.1. The results are compared to those published in reference [14]. One must note that the results available in the literature are reported only in graphical form. For comparisons, numerical values are depicted from such graphs. Nevertheless, Table 6.1 shows a very good agreement.

Table 6.1: Frequency Ratio f_{nr} of Cylindrical Cantilever Shaft ($\rho = 0.2$)

Δ	$\eta = 0.1$	$\eta = 0.06$	$\eta = 0.02$
0.2	0.96	0.98	0.99
	0.94*	0.97*	0.98*
0.3	0.90	0.94	0.98
	0.88*	0.93*	0.97*
0.4	0.78	0.85	0.95
	0.79*	0.83*	0.92*
0.5	0.64	0.75	0.90
	0.63*	0.72*	0.86*

* Reference [14]

Example 2

A simply supported shaft of material properties similar to that of example 1 is considered. Here, the change in the natural frequency is measured by an index called the natural frequency index f_n which is defined as

$$f_n = \frac{\omega_i - \omega_{ic}}{\omega_i} \quad (6.3)$$

where ω_{ic} and ω_i are as defined earlier. The behavior of the natural frequency index is studied for different crack depths Δ and crack positions ρ . The results are presented in Table 6.2 which show a good agreement with those depicted values from graphs published in reference [7].

Example 3

In the previous examples, non-rotating beams were considered. As a third example, the simply supported shaft of example 2 is rotated at a speed of $\Omega = 1000 \text{ rad/sec}$. The resulting eigenvalue problem is solved using Eq.(3.24). The frequency index f_n for the first frequency is plotted against crack depth Δ , for different crack positions in Figure 6-7. The natural frequency of the rotor decreases as the position of the crack moves away from the bearings, i.e. towards the middle of the rotor. It is also observed that as the crack depth increases the difference in f_n for either forward or backward whirl speed also increases.

Table 6.2: Frequency Index f_n of Cylindrical Simply Supported shaft ($\eta = 1$)

Δ	$\rho = 0.3$	$\rho = 0.5$
0.1	0.01	0.01
	0.01*	0.015*
0.2	0.04	0.06
	0.04*	0.06*
0.3	0.12	0.14
	0.12*	0.14*
0.4	0.23	0.283
	0.24*	0.28*
0.5	0.40	0.45
	0.42*	0.45*

* Reference [7]

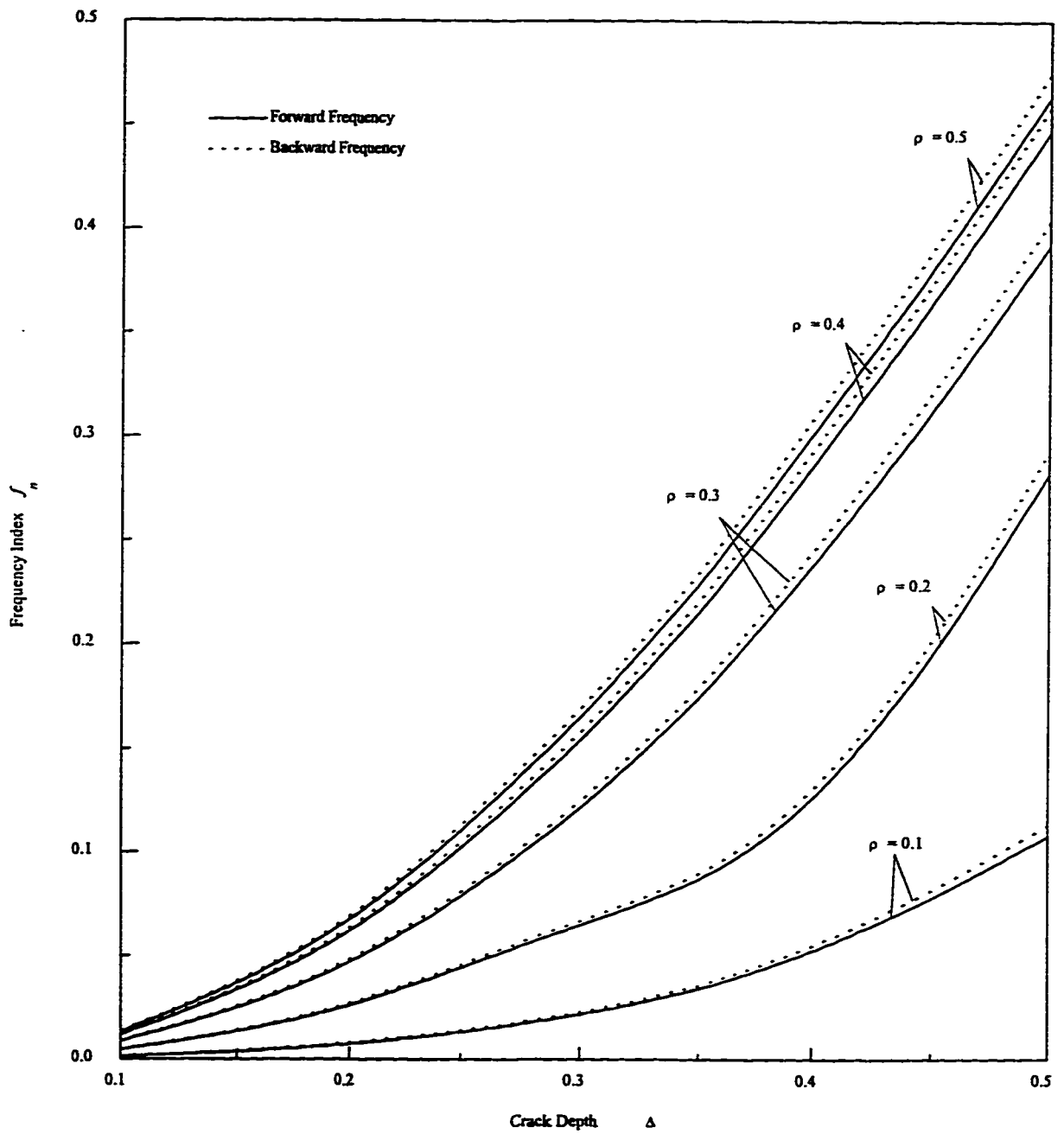


Figure 6-7: Frequency Index f_n of Cylindrical Simply Supported Shaft Rotating at $\Omega = 1000$ rad/sec ($\eta = 0.1$)

Example 4

The available literature falls short of presenting adequate results for the case of cracked rotating tapered shafts. The efficient numerical scheme developed in this thesis has been utilized to produce the first ten natural whirl speeds of a short conical solid shaft. The dimensions of the tapered shaft are $R_1/L = 0.125$ and $L = 1m$. The obtained natural frequencies are presented for the first time in Table 6.3 and 6.4 at different values of whirl ratio λ . In Table 6.3, the frequency parameter f of a tapered Timoshenko shaft overhang of taper ratio equal to 0.5 and rigid journal bearings at the widest end is presented. The frequency parameter f is defined as

$$f = \left(\frac{\mu AL^4 \omega^2}{EI} \right)^{\frac{1}{4}} \quad (6.4)$$

where μ is the mass density, A is the cross-sectional area, L is the length, ω is the natural frequency, E is the modulus of elasticity and I is the moment of inertia of the shaft. In Table 6.4, the frequency parameter of a tapered Timoshenko simply-supported shaft of taper ratio equal to 0.5 and supported by rigid bearings at both ends is presented.

In Figure 6-8, the effect of taper ratio on the frequency of the cracked rotor is presented. In this case of shaft overhang, the crack is present at a distance $\rho = 0.3$ from the rigid journal bearing. The results show that the frequency parameter f decreases as the crack depth increases. It is also observed that the rate of decrease grows as the taper ratio decreases (i.e. as taperness increases). In Figure 6-9, the effect of taper ratio on the

Table 6.3: Frequency parameter f of tapered Timoshenko shaft overhang
(taper ratio = 0.5; $\rho = 0.3$; rigid journal bearing at widest end)

λ	Δ	f_1	f_2	f_3	f_4	f_5	f_6	f_7	f_8	f_9	f_{10}
0.0	0.0	4.4856	17.2112	37.8979	63.3996	92.4837	124.5094	159.3874	194.9848	207.0685	235.1958
	0.1	4.4385	17.1939	37.6196	63.2963	92.2349	123.7556	159.1824	194.8224	206.1463	234.9456
	0.3	3.9569	17.0408	35.1403	62.5175	90.1255	117.8696	157.7989	192.8741	203.1463	229.3229
	0.5	2.9945	16.7769	31.9482	61.6095	87.3429	112.4276	156.1745	190.8625	203.8301	216.5360
1.0	0.0	4.5373	17.9427	40.7391	69.8769	103.5734	140.7416	181.1213	223.4499	266.0084	301.9229
	0.1	4.4899	17.9239	40.4707	69.8379	103.3619	140.3344	181.0812	223.3001	265.7815	301.8839
	0.3	4.0056	17.7519	38.1331	69.4888	101.7339	137.5288	180.9373	222.3016	264.5039	301.7925
	0.5	3.0356	17.4612	35.2527	69.0428	100.2002	135.5365	180.6310	221.9854	263.8940	301.5328
-1.0	0.0	4.4355	16.5477	35.4350	57.7605	82.2616	106.9787	122.9354	137.1748	154.9036	166.9515
	0.1	4.3886	16.5315	35.1557	57.5953	81.9795	106.1319	122.5983	136.4144	154.8823	166.5408
	0.3	3.9099	16.3951	32.6178	56.3973	79.6287	99.4326	120.7543	132.7488	154.8056	164.8661
	0.5	2.9549	16.1571	29.2579	55.0304	76.2440	93.7205	120.1342	130.4184	154.7695	163.0729

Table 6.4: Frequency parameter f of tapered Timoshenko shaft
(taper ratio = 0.5; $\rho = 0.3$; rigid journal bearing at both ends)

λ	Δ	f_1	f_2	f_3	f_4	f_5	f_6	f_7	f_8	f_9	f_{10}
0.0	0.0	6.6736	25.4504	50.8223	80.4492	113.2839	149.1624	172.2307	188.0682	227.3348	229.6645
	0.1	6.6345	25.1553	50.7078	80.3050	112.5890	148.8769	171.8373	187.9642	225.9655	229.1376
	0.3	6.6115	22.1109	49.7009	78.8766	106.2775	146.5024	169.7798	186.9984	214.1292	227.4202
	0.5	4.4472	17.6684	48.5389	76.7718	99.7246	144.0206	168.2493	185.4405	203.2677	227.5021
1.0	0.0	6.8284	26.9204	55.0895	88.1305	124.3901	163.5732	205.3019	248.8343	290.0152	323.6926
	0.1	6.7897	26.6286	54.9953	88.0431	123.9430	163.4469	205.2471	248.5412	289.9418	323.6819
	0.3	6.2721	23.6171	54.1003	87.2048	120.4496	162.5359	204.8654	246.7473	289.5166	323.6327
	0.5	4.6005	19.1218	53.0945	86.2813	117.5749	161.9101	204.6492	245.8866	289.3269	323.6284
-1.0	0.0	6.5279	24.1465	47.0014	73.1427	101.0574	103.1527	133.2097	137.5662	164.2639	167.5871
	0.1	6.4885	23.8523	46.8782	72.9460	100.5625	102.5259	132.8568	136.9478	164.0173	167.2936
	0.3	5.9679	20.8245	45.8609	70.8988	92.8298	101.2479	128.5129	135.3211	163.3138	165.0491
	0.5	4.3071	16.5057	44.6751	67.4722	85.4529	101.3668	124.9414	135.1872	161.4553	163.7010

frequency of a cracked simply supported rotor is studied. In this case, as the taper ratio increases, the frequency parameter also increases. There is a greater change in frequency at higher taper ratios as crack depth increases. The behavior of the rotor overhang is shown to be in contrast with that of simply supported rotor. In Figure 6-10, the effect of crack position on the frequency of a rotor overhang is studied. The crack has a greater effect on the frequency of the rotor as its position gets closer to the bearing. The farther away the crack position is from the bearing, the lesser the effect it has on the overhanging rotor. In Table 6.5, the frequency parameter f of a tapered simply supported rotor is tabulated for different crack positions.

Example 5

To demonstrate the capability of the developed finite element formulation, a complex rotor-bearing system as shown in Figure 6-11 is simulated. The rotor-bearing system has stepped cylindrical geometry with hollow elements, in addition to the presence of elastic bearings and disks. The data of the rotor-bearing system is given in Table 6.6. The first three natural frequencies of the rotor-bearing system are tabulated in Table 6.7 for different whirl ratios and crack depths. The natural frequency of the rotor-bearing system decreases as the depth of the crack increases, as expected.

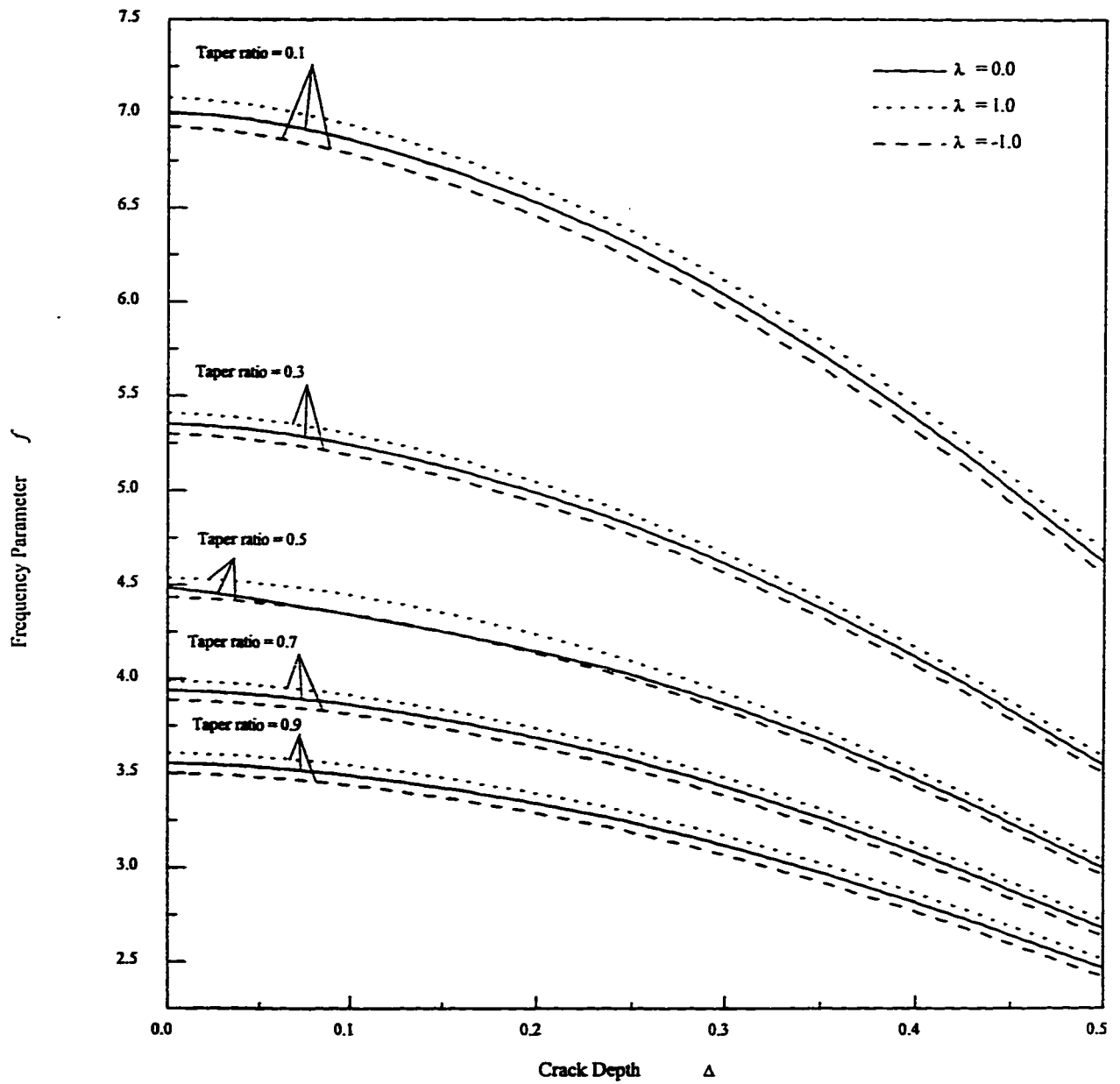


Figure 6-8: Frequency Parameter f of a Shaft overhang, ($\rho = 0.3$)

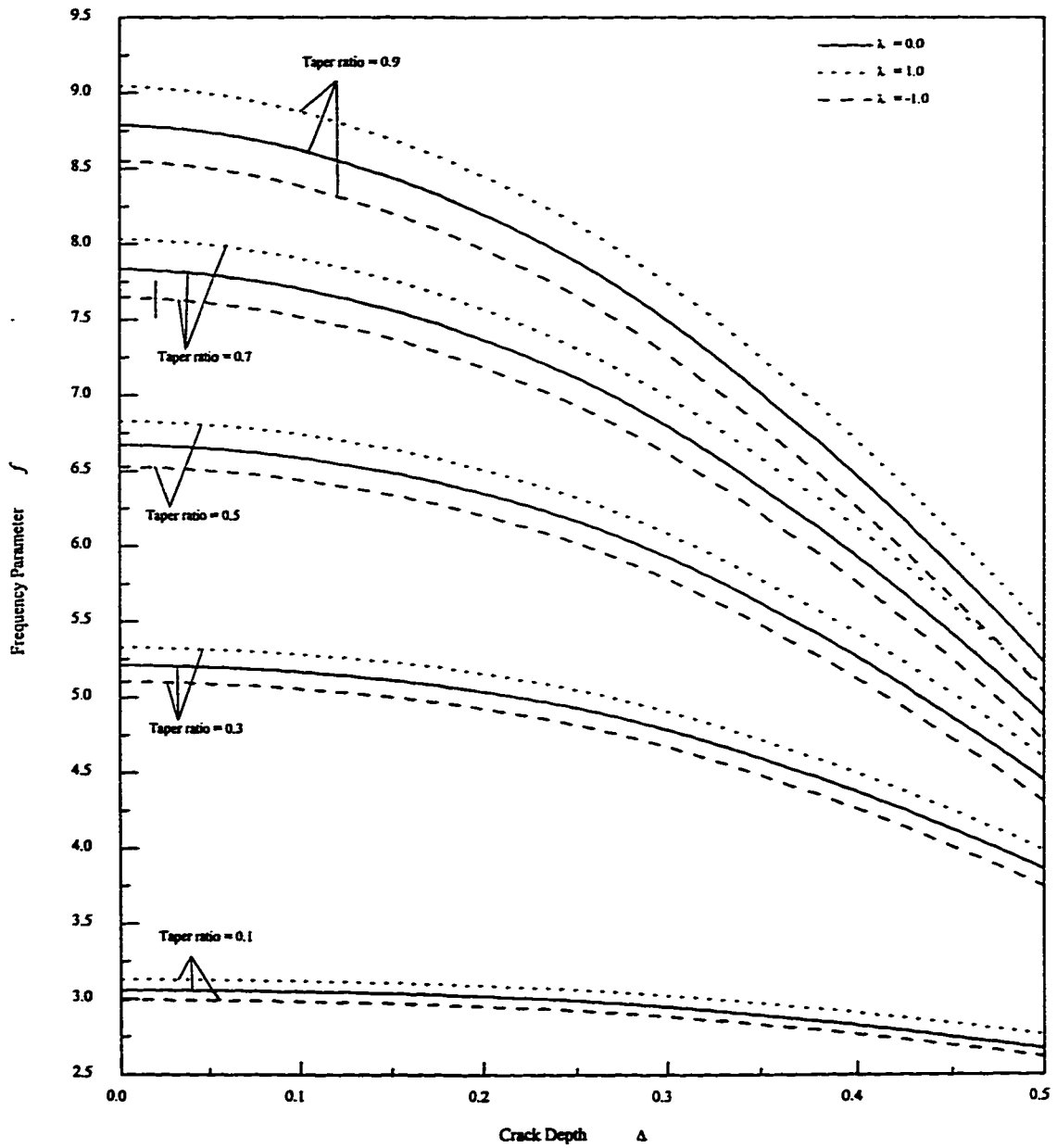


Figure 6-9: Frequency Parameter f of Simply Supported Shaft

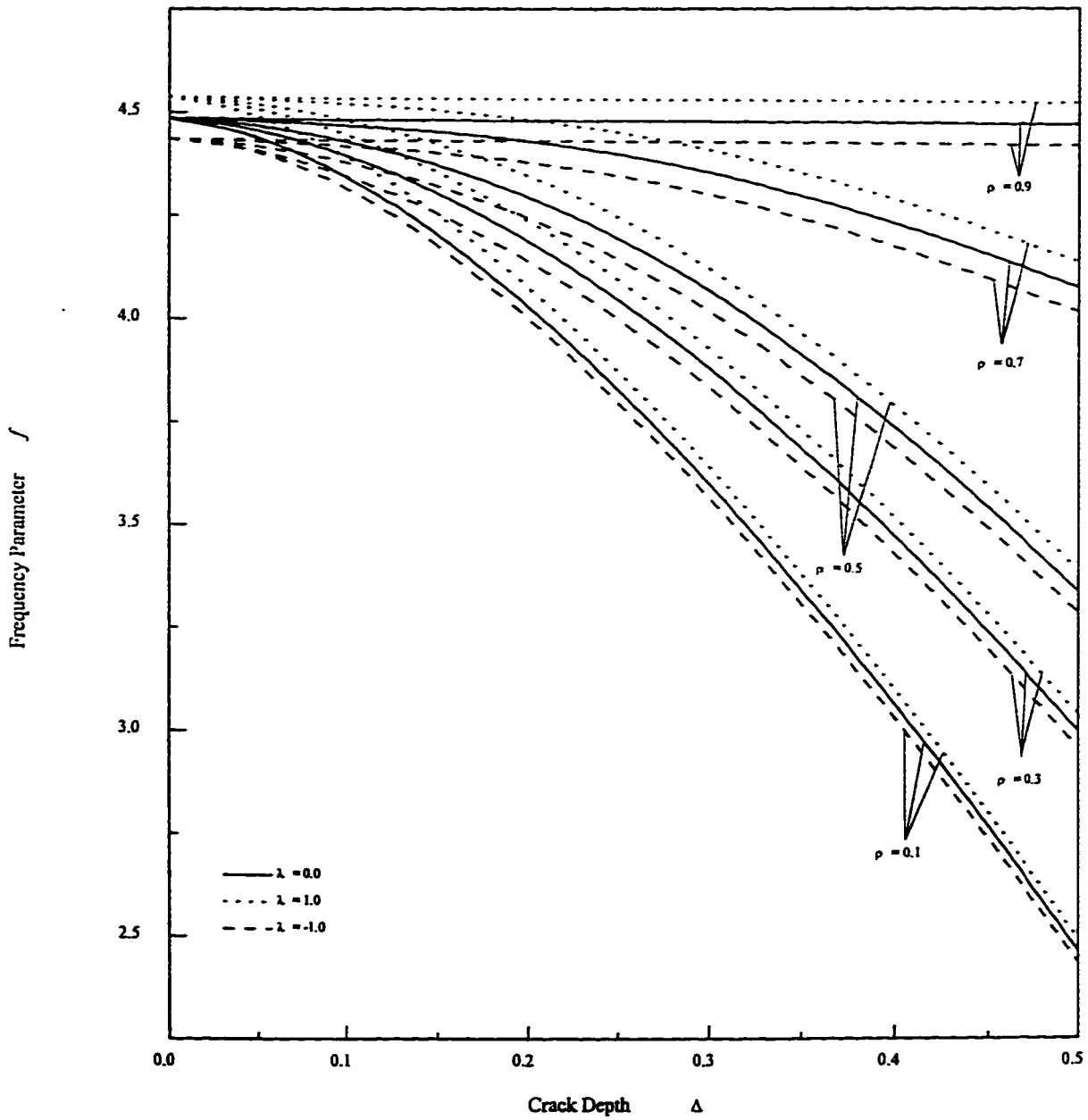


Figure 6-10: Frequency Parameter f of a Shaft Overhang (Taper Ratio = 0.5)

Table 6.5: Frequency parameter f of tapered Timoshenko shaft
(Rigid Bearing at both ends; Taper ratio = 0.5)

λ	Δ	ρ		
		0.1	0.3	0.5
0.0	0.1	6.6661	6.6345	6.5941
	0.3	6.6083	6.1149	5.6617
	0.5	6.2547	4.4472	3.5996
1.0	0.1	6.8222	6.7897	6.7478
	0.3	6.7687	6.2721	5.8017
	0.5	6.4353	4.6005	3.7021
-1.0	0.1	6.5193	6.4885	6.4496
	0.3	6.4577	5.9679	5.5308
	0.5	6.0849	4.3071	3.5049

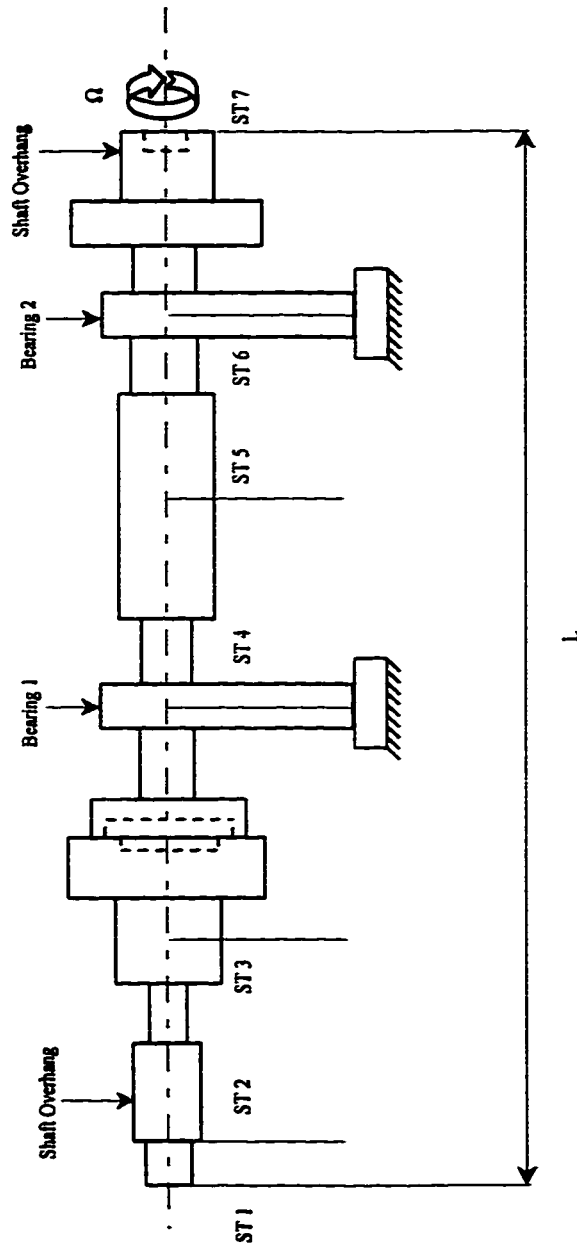


Figure 6-11: The Multi-Stepped rotor-bearing shaft

Table 6.6: Multi-stepped rotor configuration data

Element Node no.	Node Location (cm)	Bearing/ Disk	Outer radius (cm)	Inner radius (cm)
1	-17.90		0.51	
2	-16.63		1.02	
3	-12.82		0.76	
4	-10.28		2.03	
5	-9.01	Disk no. 1	2.03	
6	-7.74		3.30	
7	-7.23		3.30	1.52
8	-6.47		2.54	1.78
9	-5.20		2.54	
10	-4.44		1.27	
11	-1.39	Bearing no. 1	1.27	
12	1.15		1.52	
13	4.96		1.52	
14	8.77		1.27	
15	10.80	Bearing no. 2	1.27	
16	12.58		3.81	
17	13.60		2.03	
18	16.64		2.03	1.52
19	17.91			

Table 6.7: Natural frequencies (rpm) of uniform stepped shaft with bearings and disks

Mode	Δ	Whirl ratio λ		
		0	1	-1
1	0.0	16269	17432	15260
	0.1	16250	17413	15241
	0.3	15978	17148	14969
	0.5	14788	15973	13788
2	0.0	47706	49303	45907
	0.1	47648	49229	45837
	0.3	46840	48623	44854
	0.5	43530	45934	41105
3	0.0	76220	100241	62630
	0.1	76087	100061	62579
	0.3	74362	97356	61916
	0.5	69239	86258	60117

6.2.2 Reduction Schemes

The natural frequencies presented in Tables 6.1-6.5 and 6.7 are found using the actual full order matrices obtained from the finite element formulation. In this section, the natural frequencies obtained by implementing the modal reduction schemes will be compared to the actual natural frequencies obtained from the full-order finite element formulation.

Example 1

The modal reduction schemes, planar and complex, are applied to a tapered rotating shaft with a crack at $\rho = 0.3$. The shaft is rotating at a spin speed of $\Omega = 3000$ rad/sec. The tapered rotating shaft is divided into 11 equal finite elements. Hence, the total number of degrees of freedom of the shaft is 60. The shaft is simply supported at both ends. The simply supported boundary conditions require the deflections and moments at both ends to be specified as zeros. After applying the boundary conditions, the coefficient matrices of the equations of motion become of order (56×56) . A subset of eigenvalues spanning the lower part of the frequency spectrum of the actual finite element model is presented in Table 6.8. The planar or real eigenvalues are computed by using the Eq.(5.29), where the matrices are of order (56×56) resulting in 56 real eigenvalues. The complex eigenvalues are computed using Eq.(5.37), where the matrices are of order (112×112) resulting in 112 complex conjugate eigenvalues. The complex parts of the eigenvalues give the natural frequencies of the shaft.

The first natural frequency in both columns of Table 6.8 is zero. The zero natural

frequency corresponds to the rigid body mode of the tapered shaft. In Table 6.9, the eigenvalues of the reduced system are presented. The lowest six eigenvalues excluding the rigid body mode are retained in the reduced system for comparison with the eigenvalues obtained using full order system. The eigenvalues representing the planar modal reduction scheme which are presented in the second column of Table 6.9 are computed using Eq.(5.32). In this case, the eigenvectors corresponding to the lowest six eigenvalues which are presented in the second to seventh rows of the second column of Table 6.8 are used to form the planar modal transformation matrix of Eq.(5.30). The eigenvalues representing complex modal reduction which are presented in the third column of Table 6.9 are computed using Eq.(5.41). Here, the complex eigenvectors corresponding to the lowest six complex conjugate eigenvalues which are presented in the second to seventh rows of the third column of Table 6.8 are used to form the complex modal transformation matrices of Eq.(5.40). The constituent matrices of Eq.(5.32) which are used in the computation of eigenvalues of the reduced system (using planar modes) are given in Table 6.10. On the other hand, the matrices of Eq.(5.35) used to compute the complex frequencies of the reduced system (using complex modes) are given in Tables 6.11 and 6.12.

6.3 Time Response

In this section the time response of the rotor-bearing system will be evaluated. To validate the numerical integration procedure and the modal reduction scheme used in

Table 6.8: The lowest thirty eigenvalues of actual finite element model

No	Planar $\times 10^5$	Complex $\times 10^5$
1	0.0	$0 \pm 0i$
2	0.0164154947	$0 \pm 0.0163213471i$
3	0.0215594259	$0 \pm 0.0216746157i$
4	0.0608982377	$0 \pm 0.0607611444i$
5	0.0822192867	$0 \pm 0.0823956876i$
6	0.1169403329	$0 \pm 0.1169403329i$
7	0.1576532413	$0 \pm 0.1568350997i$
8	0.1641846489	$0 \pm 0.1649875968i$
9	0.2120893874	$0 \pm 0.2120893874i$
10	0.2499529147	$0 \pm 0.2490694259i$
11	0.2598963655	$0 \pm 0.2607166561i$
12	0.2936281149	$0 \pm 0.2936281149i$
13	0.3274772047	$0 \pm 0.3270869371i$
14	0.3659711790	$0 \pm 0.3662860096i$
15	0.4279436565	$0 \pm 0.4279436565i$
16	0.4662195901	$0 \pm 0.4654591656i$
17	0.4818788691	$0 \pm 0.4824776762i$
18	0.5448149492	$0 \pm 0.5228359033i$
19	0.5564023518	$0 \pm 0.5676328998i$
20	0.5676328997	$0 \pm 0.5785165331i$
21	0.6023423874	$0 \pm 0.6016633521i$
22	0.6075662745	$0 \pm 0.6094748314i$
23	0.6496314061	$0 \pm 0.6496314059i$
24	0.6612497069	$0 \pm 0.6572952699i$
25	0.7327582632	$0 \pm 0.7158384281i$
26	0.7344195405	$0 \pm 0.7418661493i$
27	0.7419460442	$0 \pm 0.7563515149i$
28	0.8133527288	$0 \pm 0.8133527289i$
29	0.8466765034	$0 \pm 0.8390969999i$
30	0.8682133909	$0 \pm 0.8515084686i$

Table 6.9: Eigenvalues of the reduced modal matrices

No	Planar Reduction $\times 10^4$	Complex Reduction $\times 10^4$
1	$0 \pm 0.1632382848i$	$0 \pm 0.1632134706i$
2	$0 \pm 0.2167715785i$	$0 \pm 0.2167461569i$
3	$0 \pm 0.6077676536i$	$0 \pm 0.6076114441i$
4	$0 \pm 0.8239568757i$	$0 \pm 0.8238009352i$
5	$0 \pm 1.1694033291i$	$0 \pm 1.1694033291i$
6	$0 \pm 1.5765439220i$	$0 \pm 1.5683509967i$

Table 6.10: Reduced matrices obtained after applying planar modal reduction scheme

$$M_r = \text{diag} \begin{bmatrix} 1.7107 \\ 1.6224 \\ 6.4767 \\ 0.5136 \\ 0.0342 \\ 0.2751 \end{bmatrix}$$

$$K_r = \text{diag} \begin{bmatrix} 4.609899176 \\ 7.541046601 \\ 17.67813394 \\ 34.71854369 \\ 4.674722414 \\ 68.36783589 \end{bmatrix} \times 10^6$$

$$G_r = \begin{bmatrix} 0 & -2.4629346 & 0 & 1.1748973 & 0 & 0 \\ 2.4629346 & 0 & -0.4051377 & 0 & 0 & -0.0604384 \\ 0 & 0.4051377 & 0 & -1.74761154 & 0 & 0 \\ -1.1748973 & 0 & 1.74761154 & 0 & 0 & 0.19086445 \\ 0 & 0 & 0 & 0 & 0 & 0 \\ 0 & 0.0604384 & 0 & -0.19086445 & 0 & 0 \end{bmatrix} \times 10^2$$

this investigation, the time response will be predicted and compared to the time response evaluated using ANSYS. This comparison is presented in the first subsection. In the second subsection, the time response of a uniform non-rotating cracked shaft is presented. In the third subsection, the time response of the tapered non-rotating cracked shaft is studied. The fourth subsection is devoted to the study of the time response of cracked rotating tapered shaft. The last subsection is devoted to demonstrate the capability of the developed computer scheme in simulating large-scale rotor-bearing systems which are often found in real life.

In this investigation, the time response is expressed as a nondimensional generalized displacement parameter ζ plotted against time. The time response can be evaluated either by applying external force or by specifying initial conditions. When the time response is due to external forces, it is normalized with respect to the static deflection. When it is evaluated by specifying initial conditions, the static deflection cannot be used for normalizing, instead the maximum value of deflection in the time response of the uncracked shaft is used. For the transverse deflections, the nondimensional generalized displacement parameter ζ is defined as

$$\zeta_v = \frac{v}{\Lambda} \quad (6.5)$$

where v is the deflection and Λ is the maximum static deflection of the shaft in the direction of the force. For the torsional deflection the nondimensional generalized displacement

parameter is defined as

$$\zeta_{\phi} = \frac{\phi}{2\Lambda/d} \quad (6.6)$$

where ϕ is the torsional deformation and d is the diameter of the shaft at the point of measurement. The impulse response is evaluated for some initial velocity input while the forcing vector is zero. In this investigation the impulse response is normalized with respect to the maximum value of deflection in the unit impulse response of the uncracked shaft.

6.3.1 Comparison with ANSYS

Example 1

A uniform steel shaft rotating at a spin speed of $\Omega = 400$ rad/s and supported at the two ends by rigid ball bearings (simply supported) is considered. The shaft is of diameter $d = 10.16$ cm and length $l = 127$ cm. The density and elastic modulus of the shaft material are $\mu = 7833$ kg/m³ and $E = 2.068 \times 10^{11}$ N/m², respectively. This particular example is selected to validate the results of the dynamic analysis code developed during this study by comparing them to the results from the commercially available finite element software ANSYS. The rotating shaft is divided into six equal finite elements and is excited by a unit step force in Y-direction at the midpoint of the shaft. The response of the system is computed using both the programs. Figure 6-12 gives a comparison of the deflection in Y-direction of the midpoint of the rotating shaft, when the response is computed using

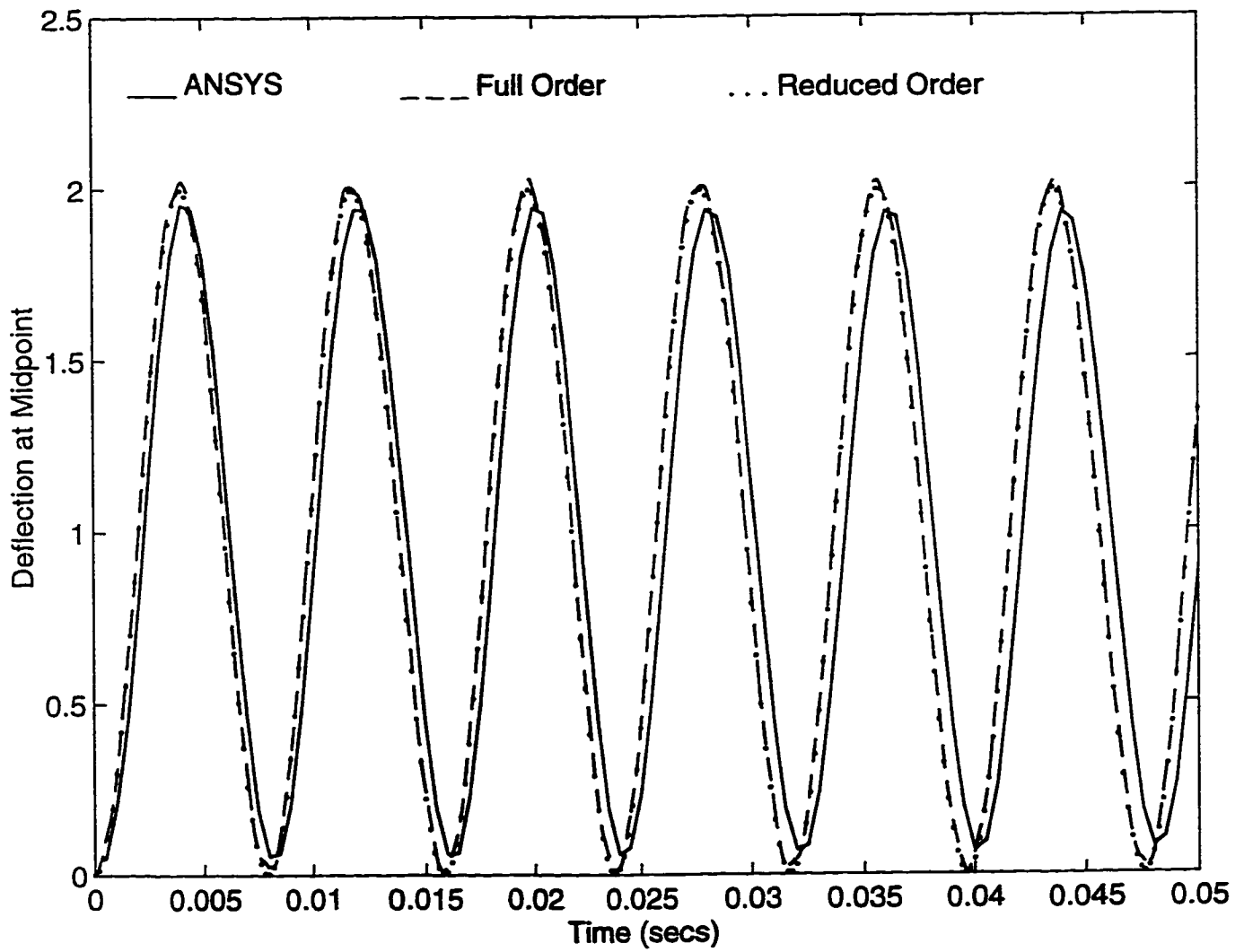


Figure 6-12: Comparison of the deflections of the rotating shaft due to unit step force.

- (a) the currently developed code with full dimension state space matrices
- (b) the currently developed code with (4×4) reduced dimension state space matrices
and
- (c) ANSYS software with full dimension matrices

The response of the shaft using the dynamic analysis code developed during this study is in a good agreement with the response computed using ANSYS software. Hence, the validation of the developed dynamic analysis code using the complex modal reduction technique can be established.

6.3.2 Non-Rotating Uniform Shaft

Example 1

To study the effect of a crack on the time response of the rotor-bearing system, a cracked short cylindrical solid shaft is simulated. The dimensions of the uniform cylindrical non-rotating shaft are $R/L = 0.1$ and $L = 0.1$ m. A crack of depth $\Delta = 0.5$ is present at location $\rho = 0.3$ from the left end of the shaft. The left end of the shaft is supported on a rigid journal bearing such that the end conditions is similar to that of a clamped end. The material properties of the shaft are exactly the same as mentioned in example 1 of section 6.3.1. The uniform shaft is divided into 11 equal finite elements. Each finite element has two nodes at its ends with five degrees of freedom for each node. Hence, the total number of degrees of freedom is 60. When the equations of motion are written

in state space form, the order of equations of motion doubles to 120. Applying modal reduction schemes (complex and planar), only the first three lowest natural frequencies are retained. Therefore, the 120 order state space system is reduced to a sixth order system. The shaft is excited by a unit step force at node 5. The time response of the cracked shaft using full order equations of motion, reduced order equations of motion as well as the uncracked shaft response are plotted in Figures 6-13 and 6-14. The time response predicted by either reduced order scheme is comparable to the time response predicted using the full order equations of motion. An increase in the time period of the cracked shaft is observed. The increase in the time period, or in other words, the decrease in the natural frequency of the cracked shaft is due to the additional flexibility of the crack. Figure 6-15, gives a comparison of the time responses of cracked and uncracked shafts when evaluated at the free end. As expected, the amplitudes of vibration of the cracked shaft are larger than the amplitudes of vibration of the uncracked shaft. Figure 6-16 gives a comparison of the time response of the cracked shaft measured at different locations on the shaft due to unit step force at node 5. As expected, the amplitude of vibration of the cantilever shaft increases as the location of measurement moves away from the clamped end. The amplitude of vibration is comparatively larger for the part of the cantilever which lies between the crack and the free end.

In Figure 6-17, the time response of node 5 due to unit impulse applied at node 5 is plotted. It is observed that the amplitudes of vibration of the cracked shaft are comparable to that of the uncracked shaft. In Figure 6-18, the time response of the free

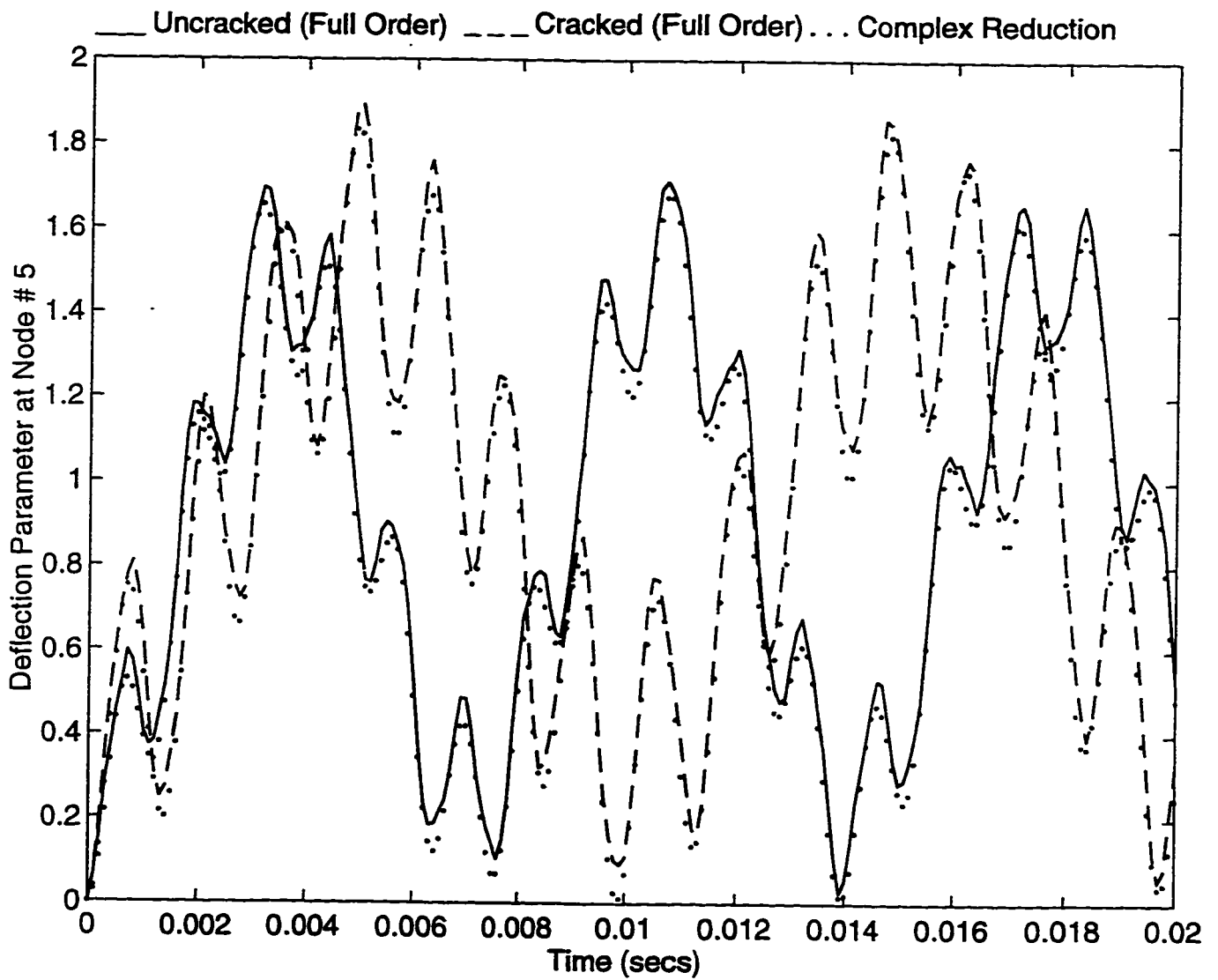


Figure 6-13: Step response of cracked non-rotating cantilever shaft using complex modal reduction

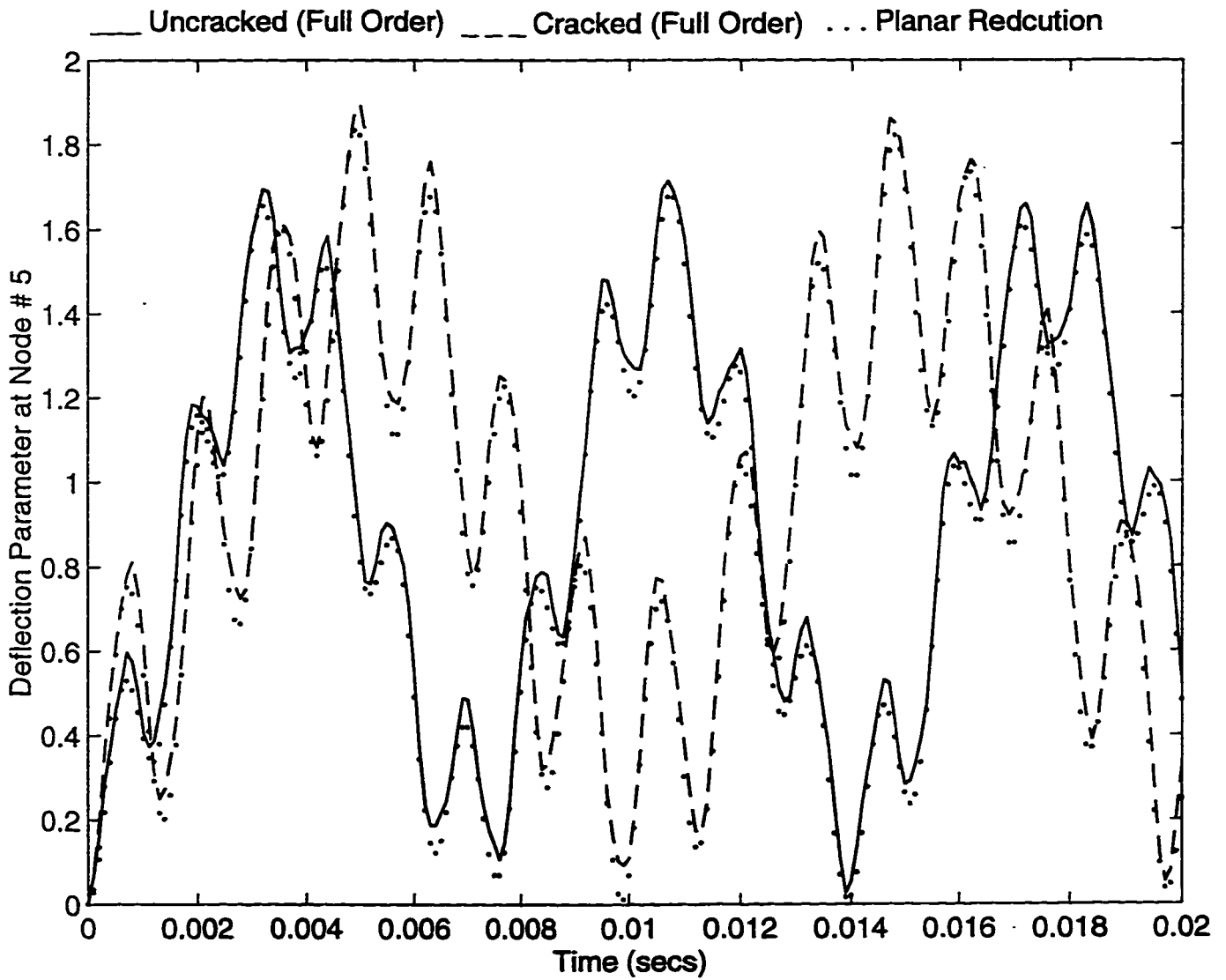


Figure 6-14: Step response of cracked non-rotating cantilever shaft using planar modal reduction

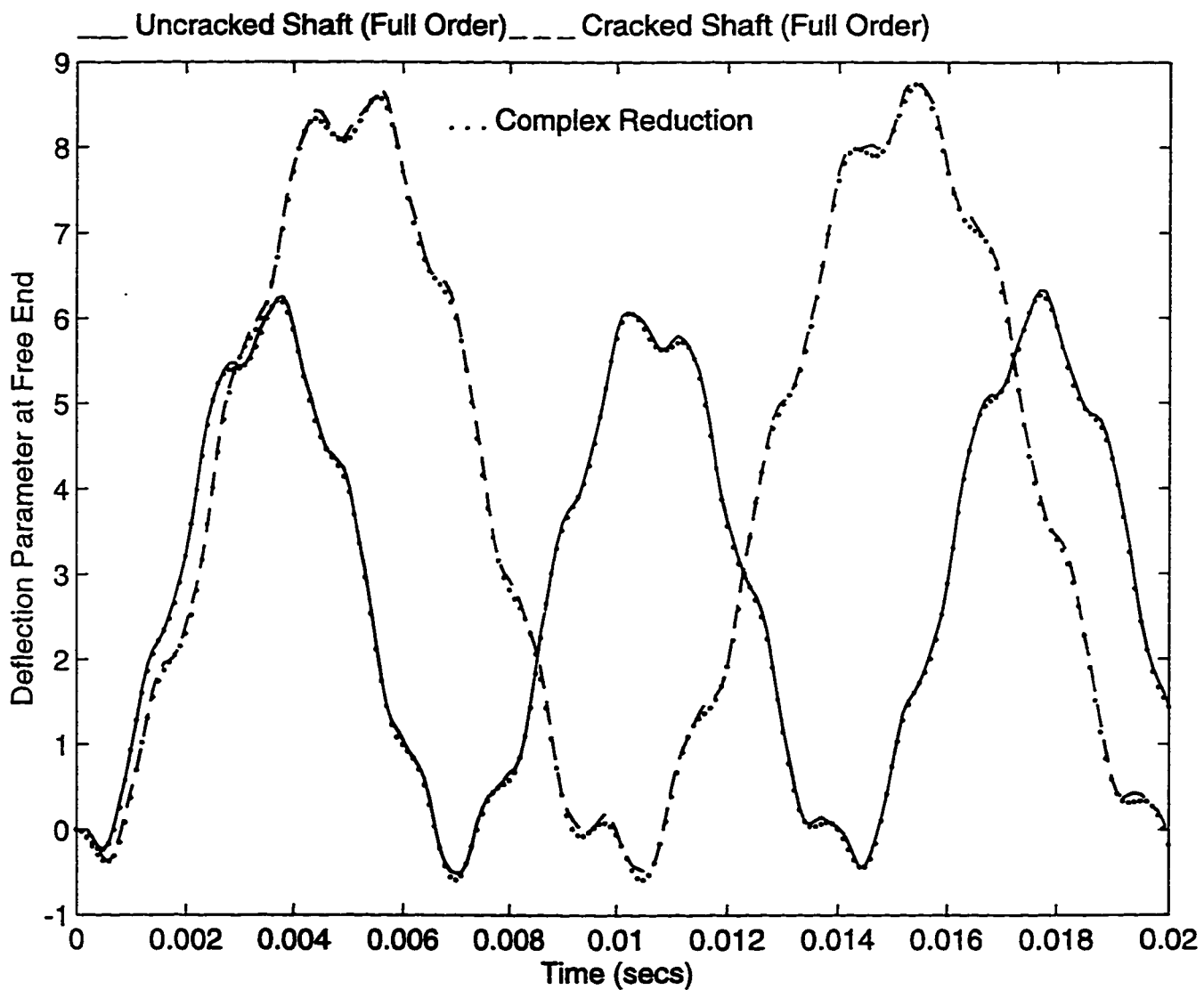


Figure 6-15: Comparison of time response of cracked and uncracked non-rotating cantilever shaft at the free end

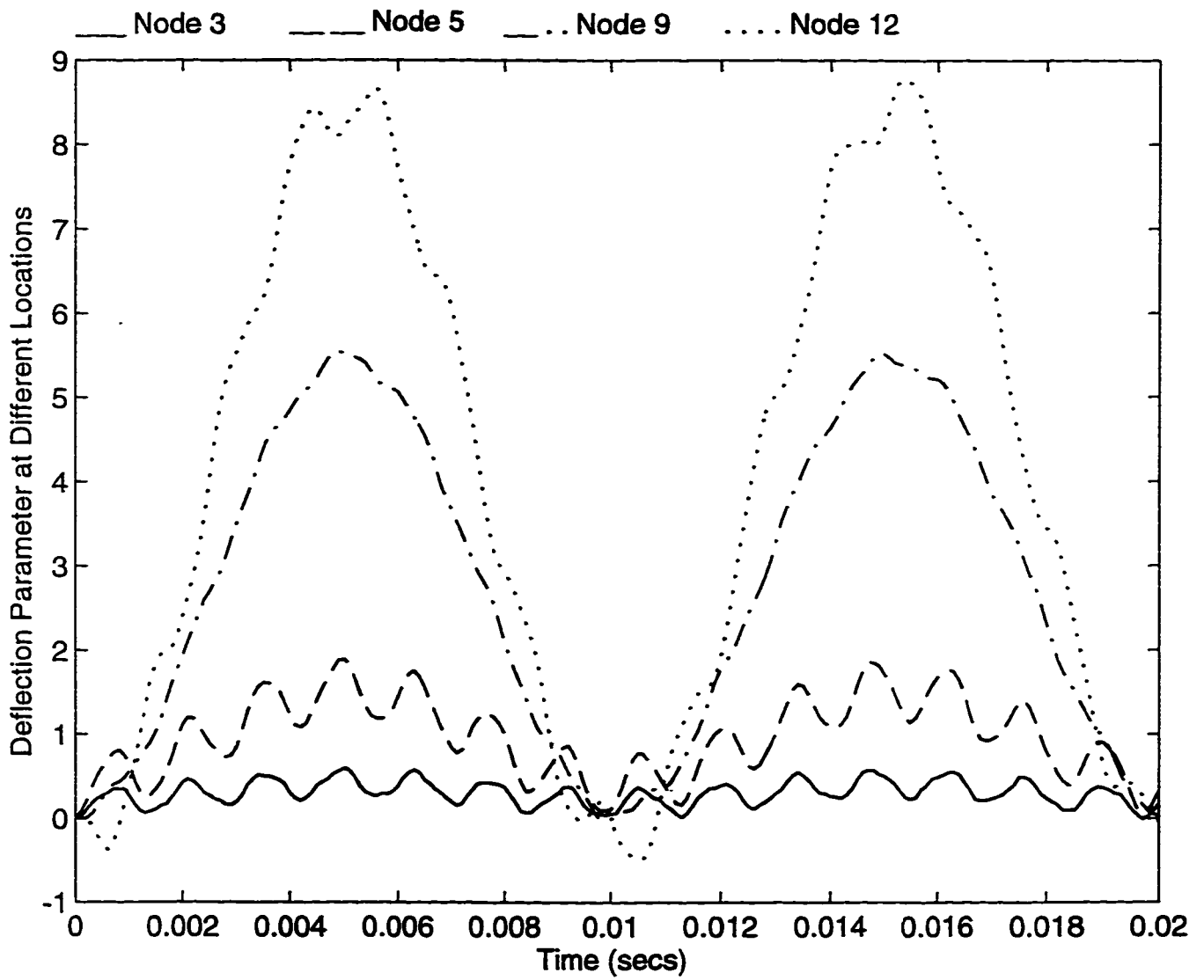


Figure 6-16: Time response of the cracked non-rotating cantilever shaft at different locations along its length

end i.e. node 12 due to unit impulse applied at node 5 is plotted. It is observed that the amplitudes of vibration of the cracked shaft are almost equal to the amplitudes of vibration of the uncracked shaft. Figures 6-17 and 6-18 simply imply that the effect of crack on the impulse response of a cracked uniform cantilever shaft is more pronounced near the location of crack.

Example 2

A uniform cylindrical shaft with a crack at $\rho = 0.3$ is supported by rigid ball bearings at both ends. This is equivalent to simply supported end conditions. The cracked simply supported shaft is excited by a unit step force at node 5. In Figures 6-19 and 6-20, the time responses at node 5 of the cracked and uncracked shafts are plotted. The time response of the cracked shaft predicted using full-order equations of motion is compared to the time response predicted using reduced order equations of motion. The amplitude of vibration of the cracked simply supported shaft is about four times that of the uncracked shaft. Figure 6-21 gives a comparison of the time responses at different locations on the simply supported cracked shaft. As expected, the amplitude of vibration is highest at the point of application of force and decreases as one moves away from the location of the applied force.

The simply supported uniform cylindrical shaft considered in example 2 of this section is excited by a unit impulsive force at node 5. The time responses of node 5 for the cracked shaft as well as uncracked shaft are drawn in Figure 6-22. The amplitudes of vibration of

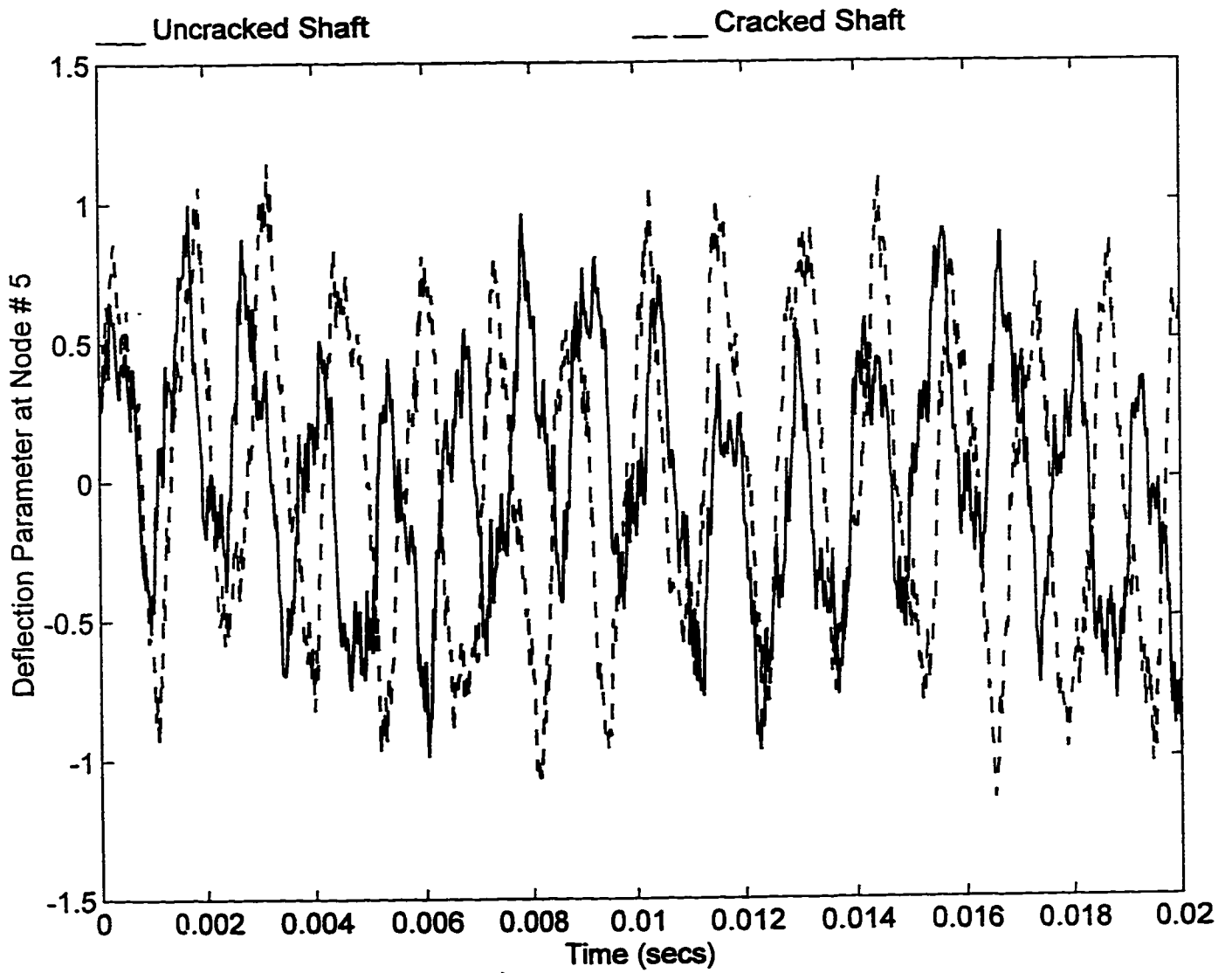


Figure 6-17: Comparison of impulse response of cracked and uncracked non-rotating cantilever shaft

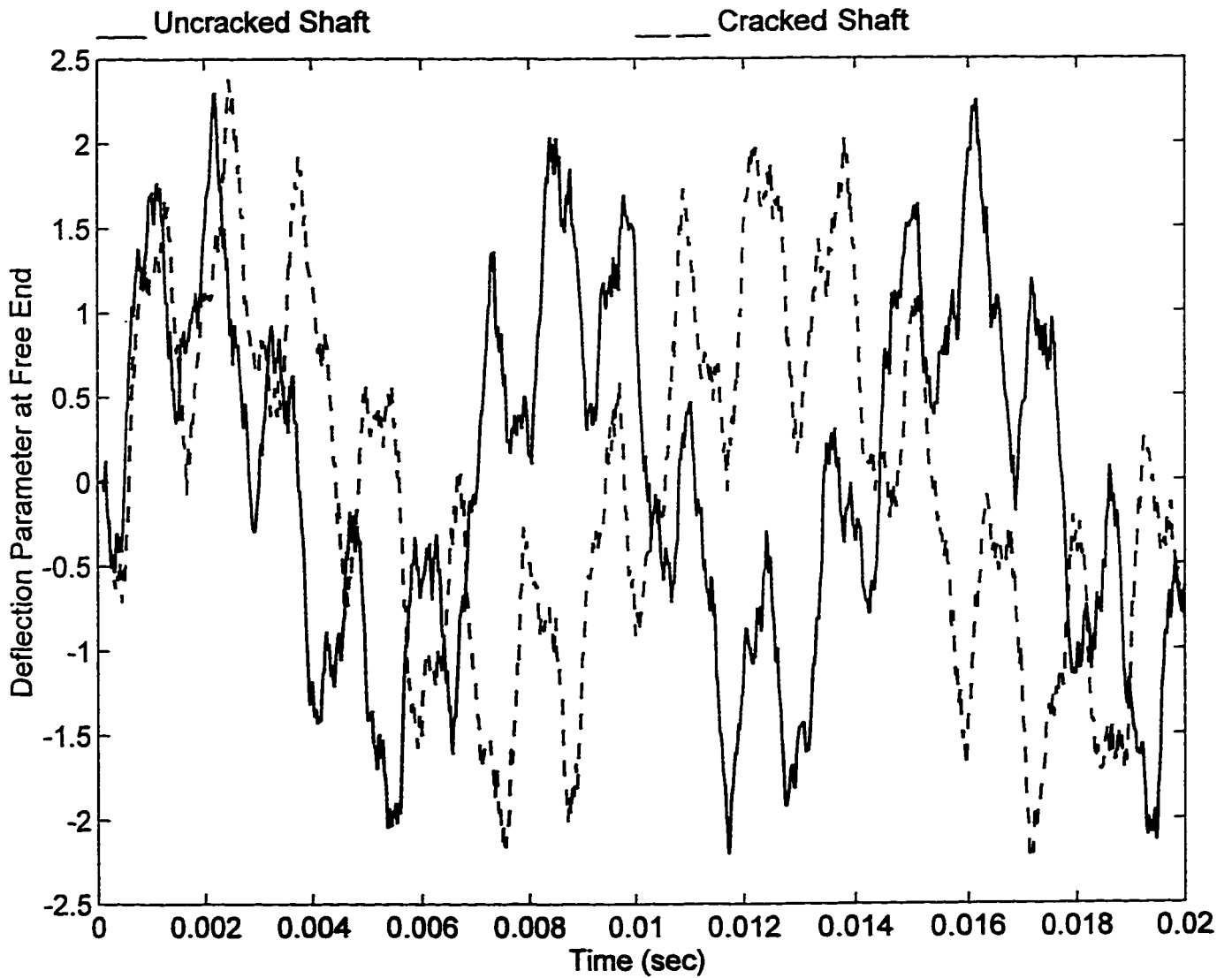


Figure 6-18: Comparison of impulse response of cracked and uncracked non-rotating cantilever shaft at its free end

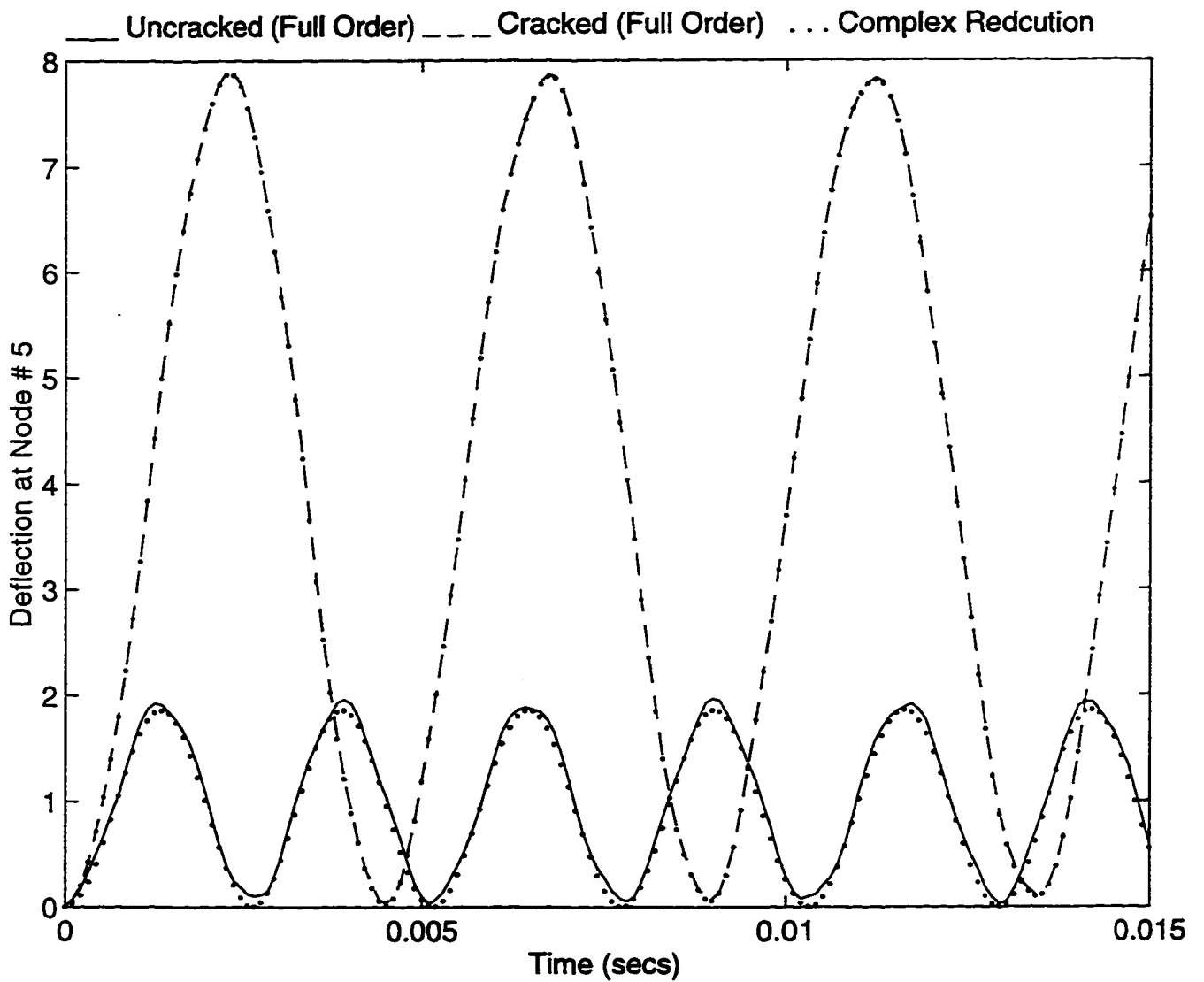


Figure 6-19: Step response of non-rotating simply supported shaft using complex modal reduction

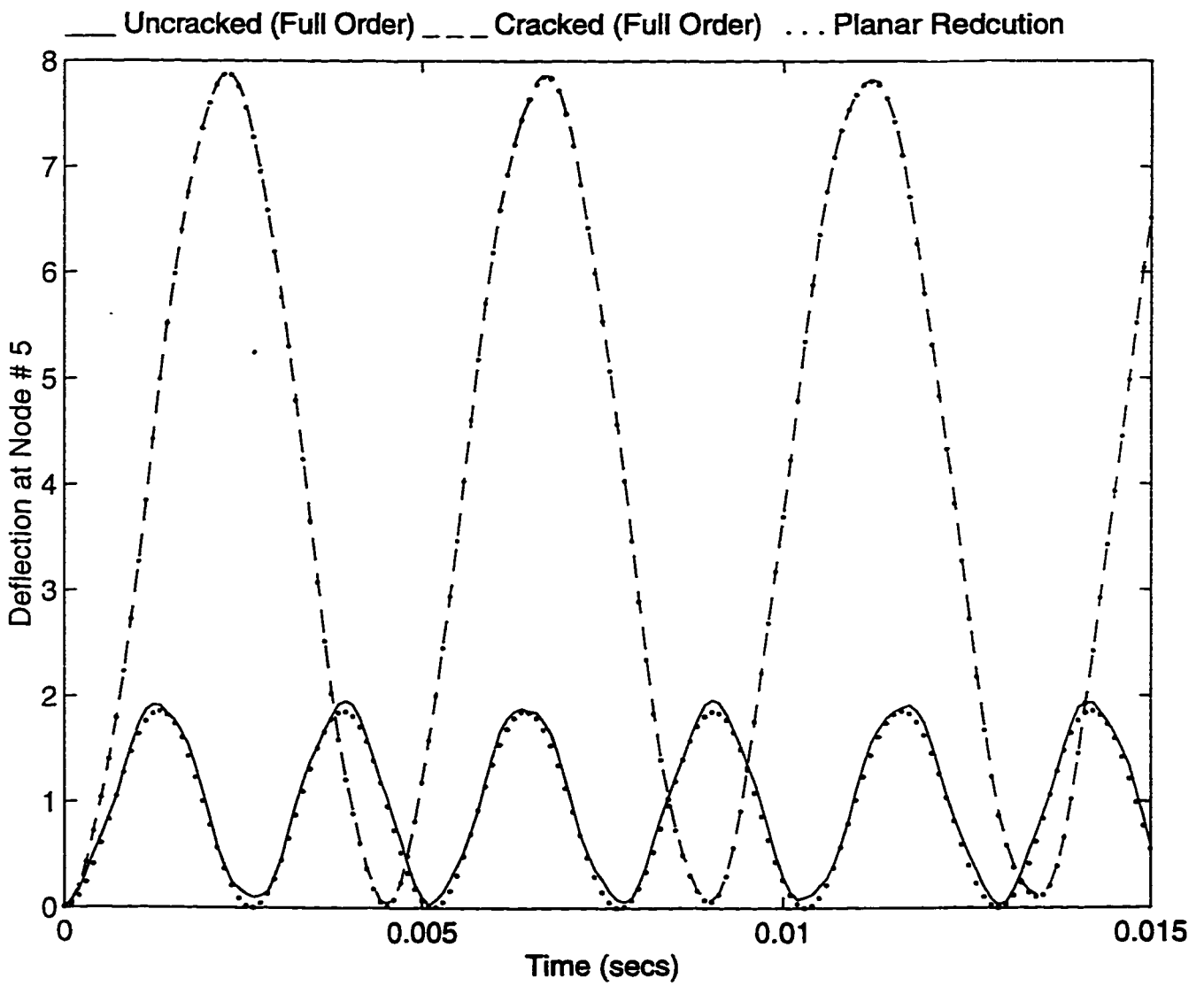


Figure 6-20: Step response of non-rotating simply supported shaft using planar modal reduction

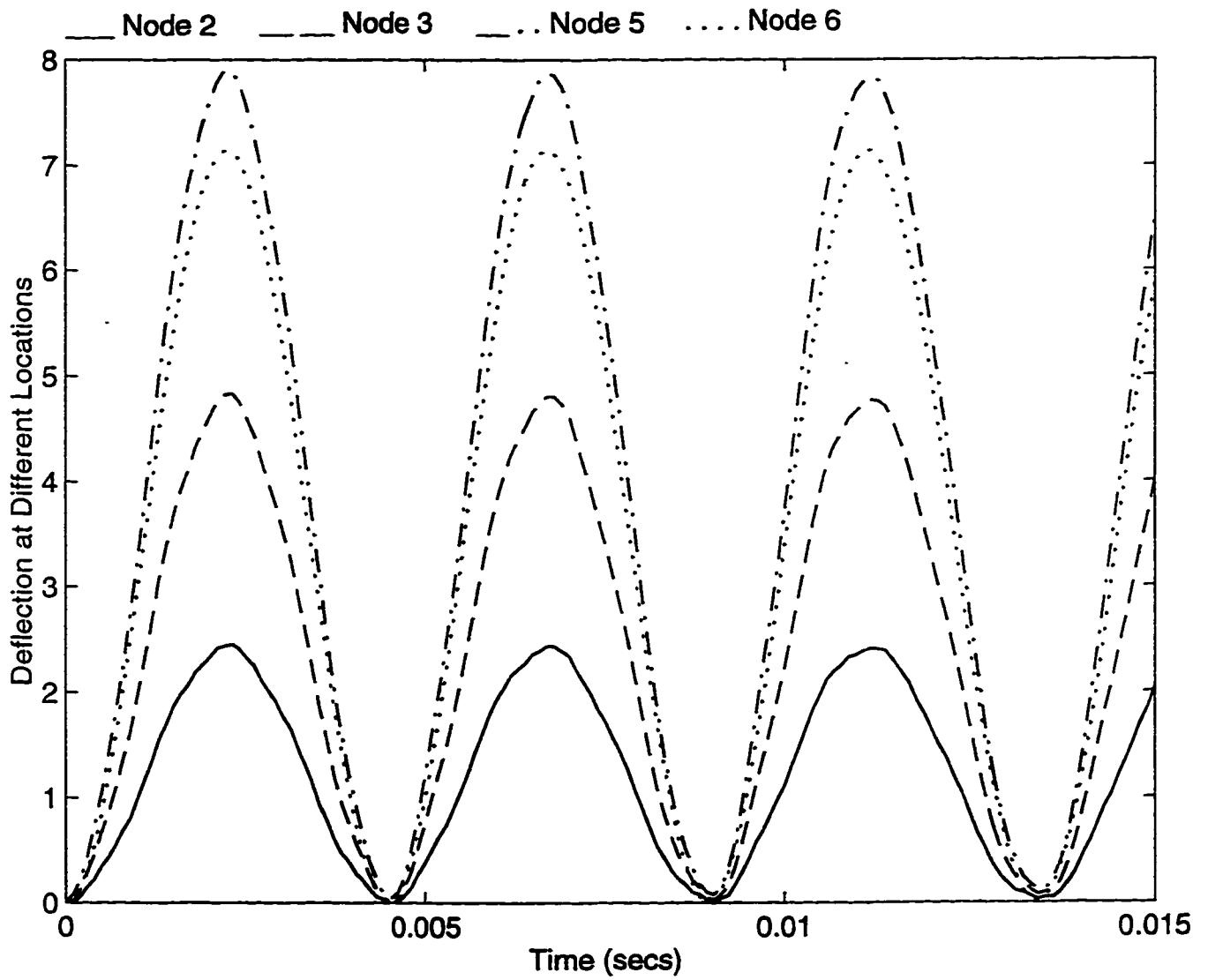


Figure 6-21: Step response of the cracked simply supported shaft at different locations along its length due to unit step force at node 5

the cracked shaft are greater than the amplitudes of vibration of uncracked shaft. Figure 6-23 gives a comparison of the time responses of different locations on the cracked shaft due to a unit impulse. It can be observed that the amplitude of vibration at the point of application of unit impulse is greater although it is not at the middle of the shaft (the shaft midpoint is node 6).

6.3.3 Non-Rotating Tapered Shaft

Example 1

In the previous examples, the effect of a crack on the time response of uniform cylindrical shafts is studied. Now, a cracked tapered short solid shaft is simulated. The dimension of the tapered shaft are $R_1/L = 0.125$ and $L = 1m$. The taper ratio is 0.5. A crack of depth $\Delta = 0.5$ is present at location $\rho = 0.3$ from the widest end. Both the ends of the cracked tapered shaft are supported on rigid journal bearings. The shaft is divided into 11 equal elements and is excited at the fifth node by a unit step force in Y-direction. The deflections of the cracked as well as uncracked shaft at the fifth node are shown in Figures 6-24 and 6-25. The amplitudes of vibration of the cracked shaft are about three times that of the amplitudes of vibration of the uncracked shaft.

The time response of the cracked shaft is also simulated using the complex and planar modal reduction schemes. Similarly, the shaft is divided into 11 equal finite elements. Each finite element has two nodes with five degrees of freedom for each node. Hence, the total number of degrees of freedom is 60. When the equations of motion are transformed

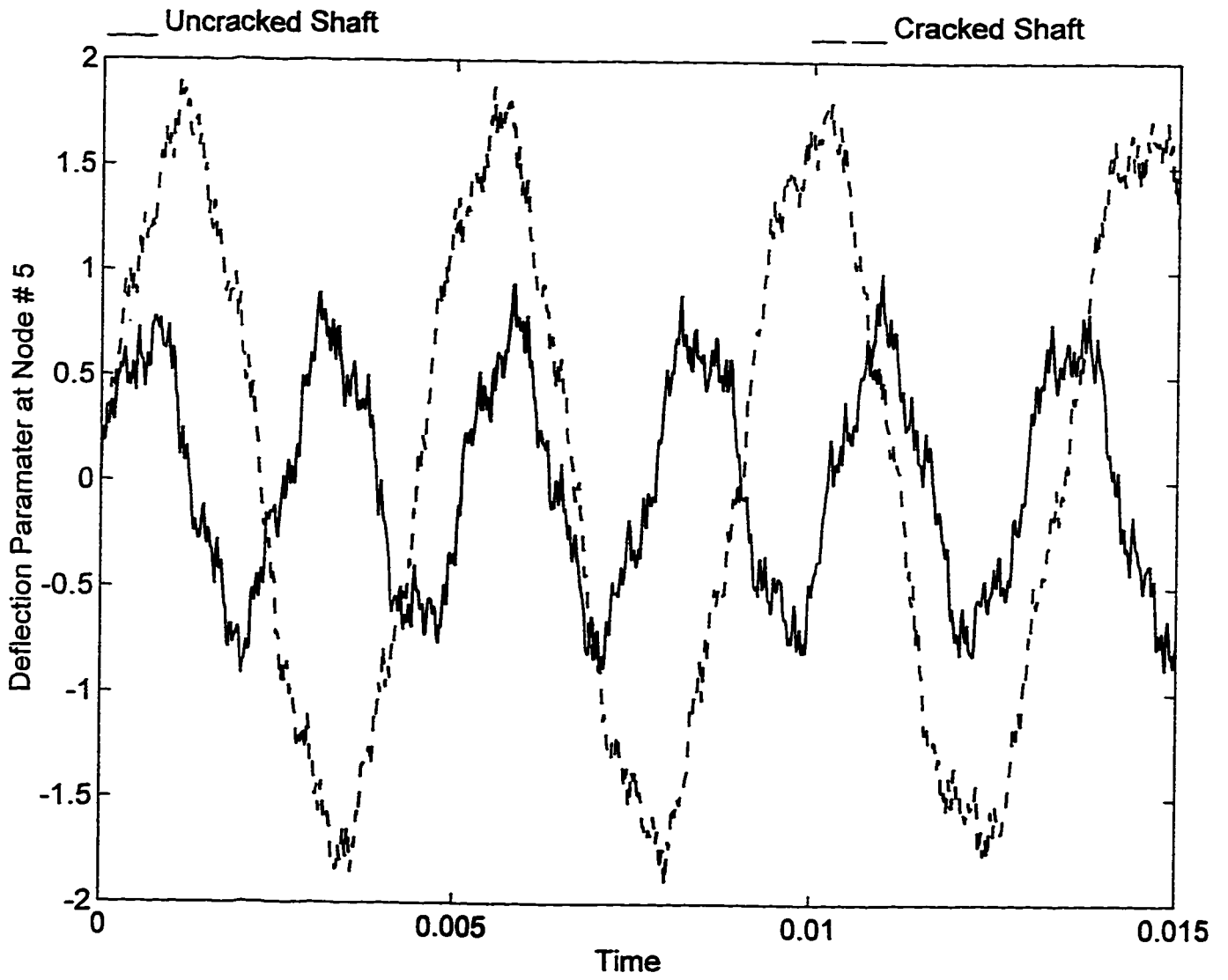


Figure 6-22: Impulse response of non-rotating simply supported shaft

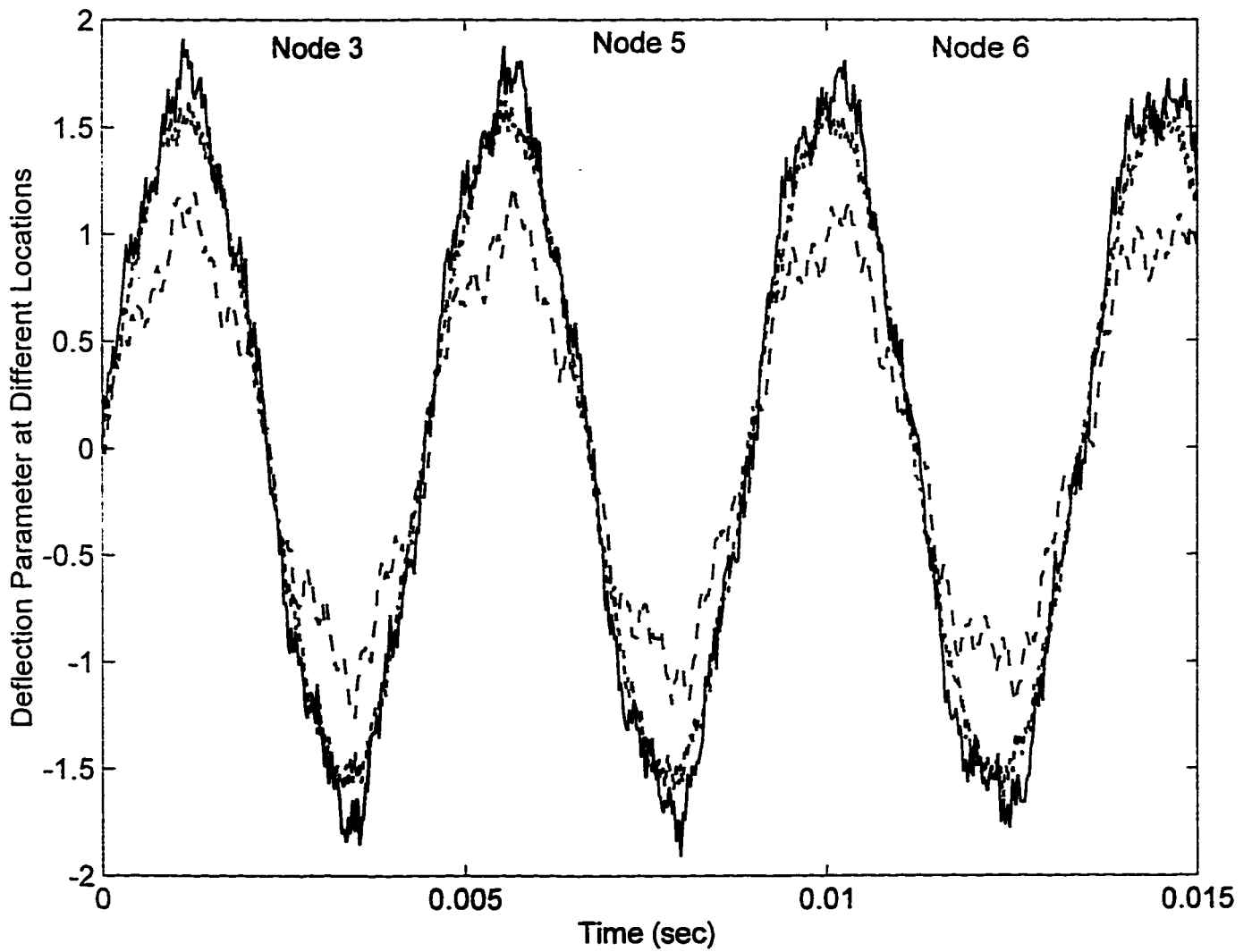


Figure 6-23: Deflection of the cracked non-rotating simply supported shaft at different locations along its length due to unit impulse at node 5

into the state space form, the order of the equations is doubled to 120. By invoking either the complex or planar modal reduction, only the first three lowest frequencies are selected and retained. Therefore, the reduced state space modal equations are of order (6×6) . Figures 6-24 and 6-25 show that the time responses predicted using complex as well as planar modal reductions agree well with that of the full order equations of motion. This comparison validates the modal reduction schemes. Figures 6-26 and 6-27 show the response of the cracked tapered shaft at different locations on the shaft when excited by a unit step force at the fifth node. Figure 6-26 gives a comparison of the time responses at node 2 of uncracked shaft to that of the cracked shaft modelled by full order equations of motion as well as reduced order equation of motion. Figure 6-27 gives a similar comparison for the time responses at node 6. It is noted that node 2 is to the left of the crack and node 6 is to the right of the crack. In both the figures the amplitude of vibration of the cracked shaft is about three times the amplitude of vibration of uncracked shaft.

The cracked tapered shaft considered in the present example is excited by an impulse at the fifth node in the Y-direction. Figures 6-28 and 6-29 compare the impulse responses at node 5 of the uncracked shaft to that of the cracked shaft. The time responses predicted using the reduced order schemes are also plotted in the same figure. Again, the time responses predicted using the reduced order schemes are in close agreement with that of the full order model. It is observed that the amplitudes of vibration of the cracked shaft are about two times that of the amplitudes of vibration of uncracked shaft. In

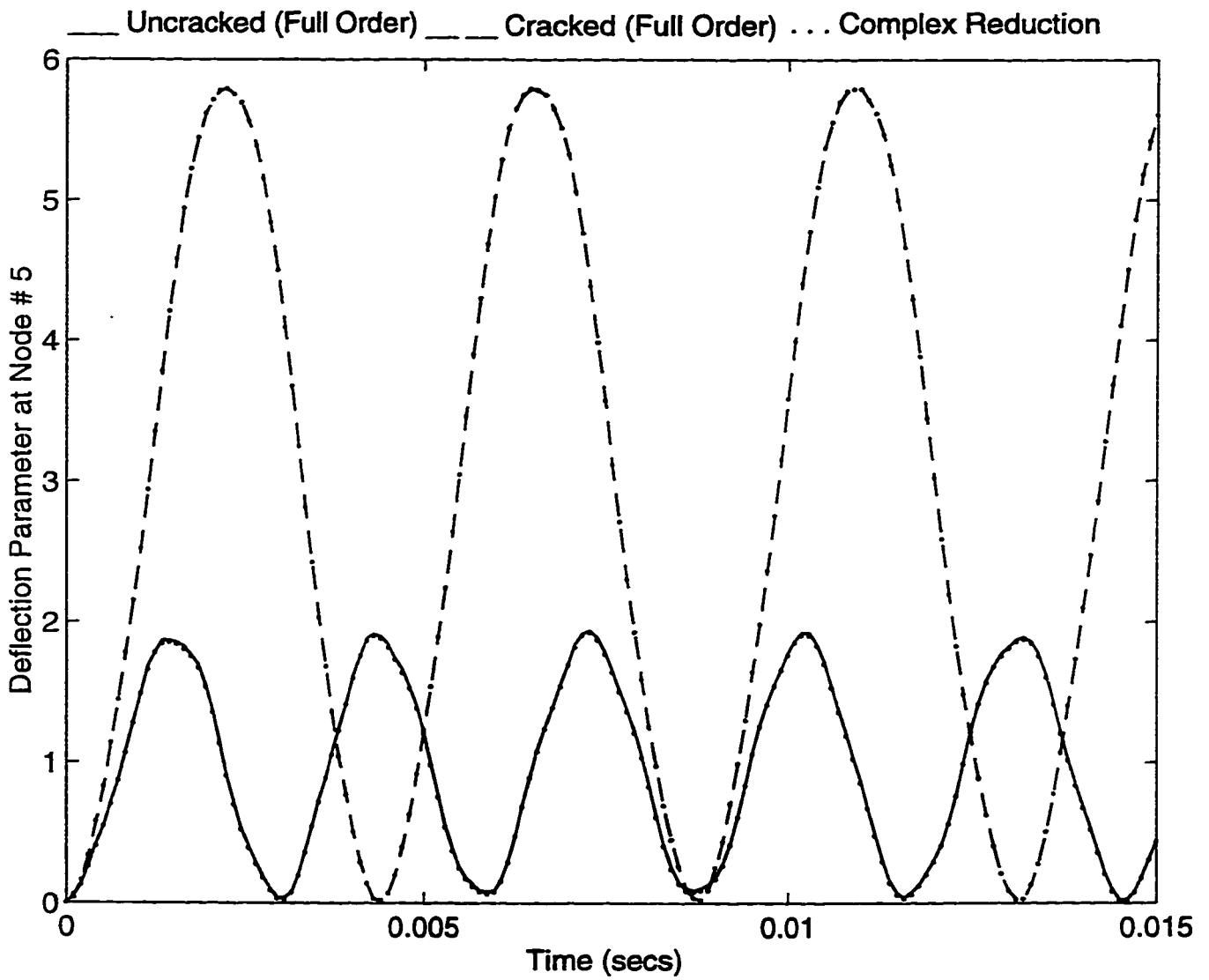


Figure 6-24: Step response of non-rotating tapered simply supported shaft using complex modal reduction

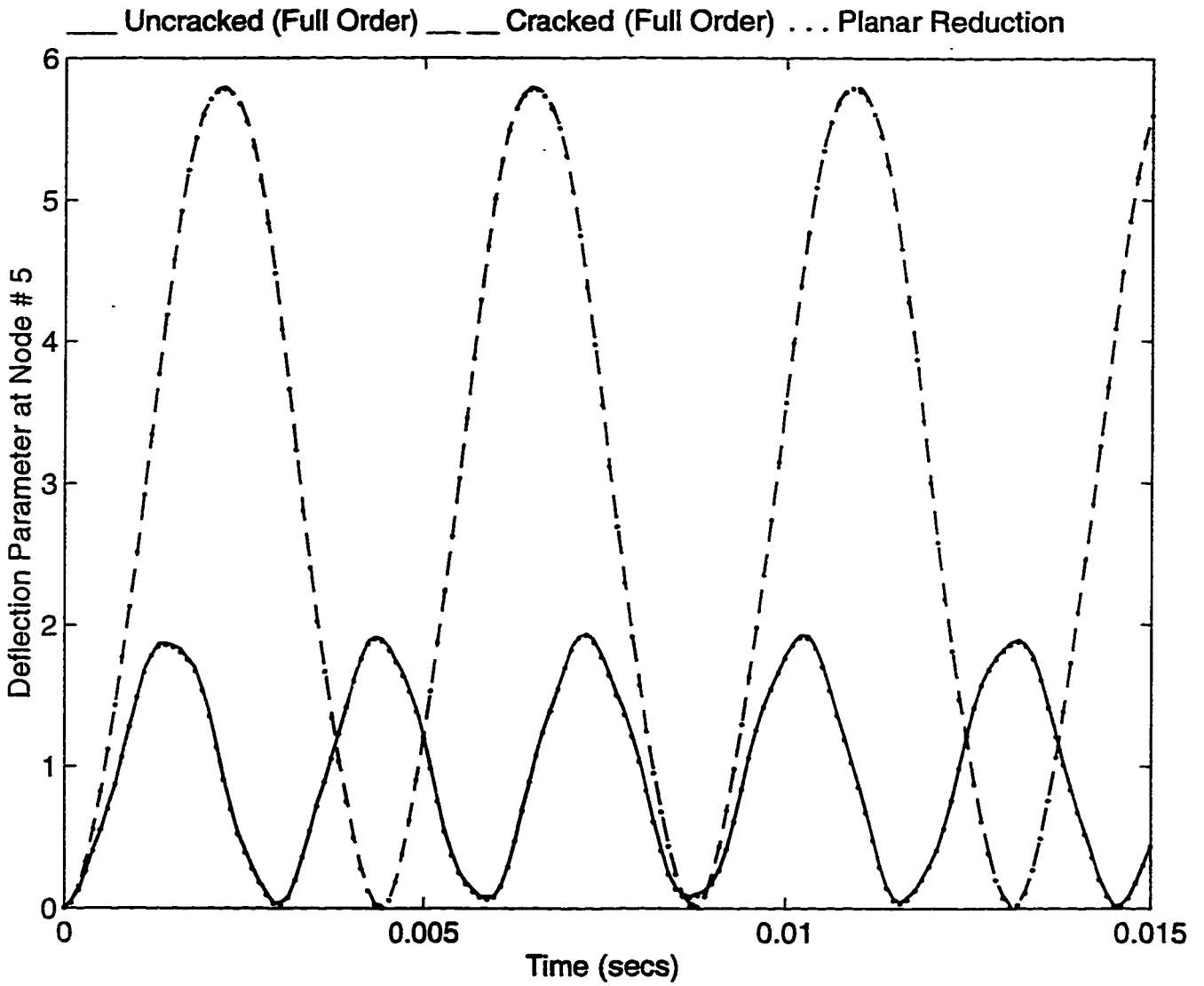


Figure 6-25: Step response of non-rotating tapered simply supported shaft using planar modal reduction

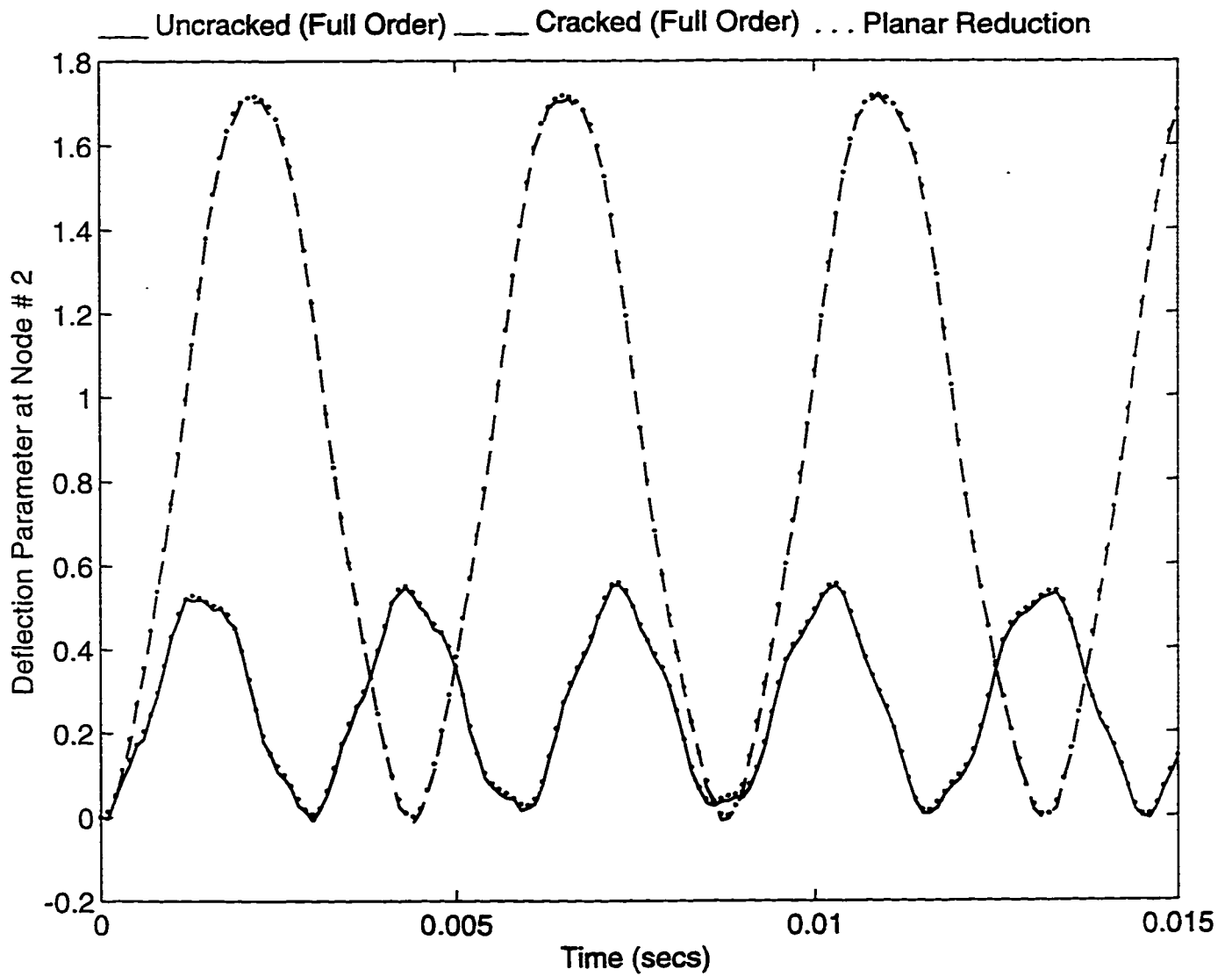


Figure 6-26: Step response of the non-rotating tapered shaft near the widest end

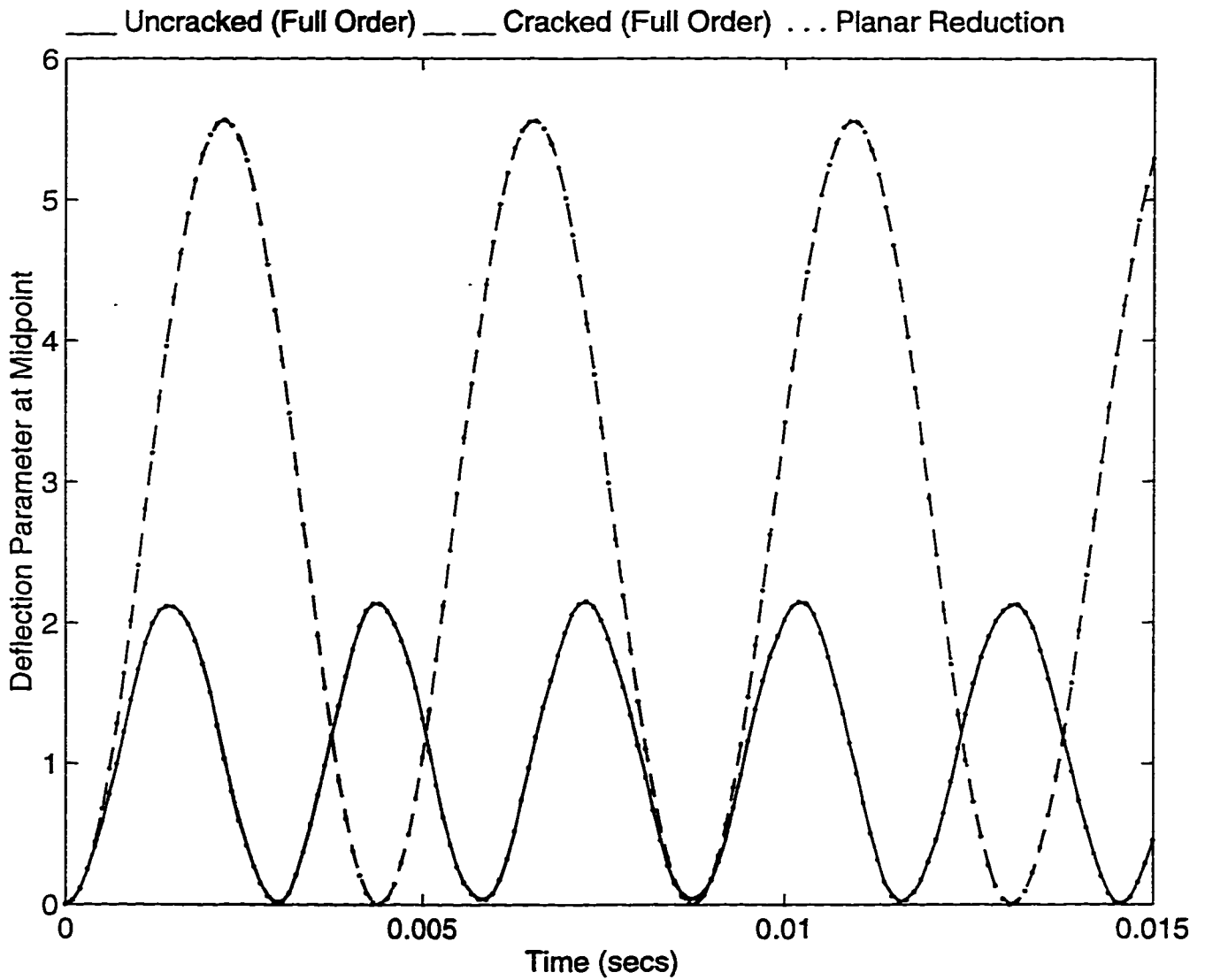


Figure 6-27: Step response of non-rotating tapered shaft near the narrow end

Figure 6-30, the impulse responses at different locations on the cracked tapered shaft are plotted. It is observed that amplitude is smallest at node 2 which is adjacent to the rigid journal bearing and largest at node 5 which is the point of excitation.

Example 2

Consider a non-rotating cantilever tapered shaft as another example. The material properties of the shaft are similar to that of the previous example. The widest end of the shaft is supported by rigid journal bearing. The shaft is excited by a unit step force at the fifth node. The time responses of the shaft at the fifth node are shown in Figures 6-31 and 6-32. The time responses of the cracked shaft predicted using full order and reduced order equations of motion are compared to that of the uncracked shaft. The accuracy of the modal reduction schemes, complex as well as planar is then validated by comparing the time response predicted using the full order and reduced order models. In Figure 6-33, the time responses of the free end of the cracked as well as uncracked cantilever are plotted. The amplitudes of vibration at the free end are comparatively larger than the amplitudes of vibration at node 5. In Figure 6-34, the time responses at different locations of the cracked non-rotating cantilever are plotted to compare the corresponding amplitudes of vibration.

In Figures 6-35 and 6-36, the impulse responses of the free end and node 5, respectively, of the cracked non-rotating cantilever is compared to that of uncracked cantilever shaft. The cantilever shaft is excited by an impulse at node 5. It is observed that ampli-

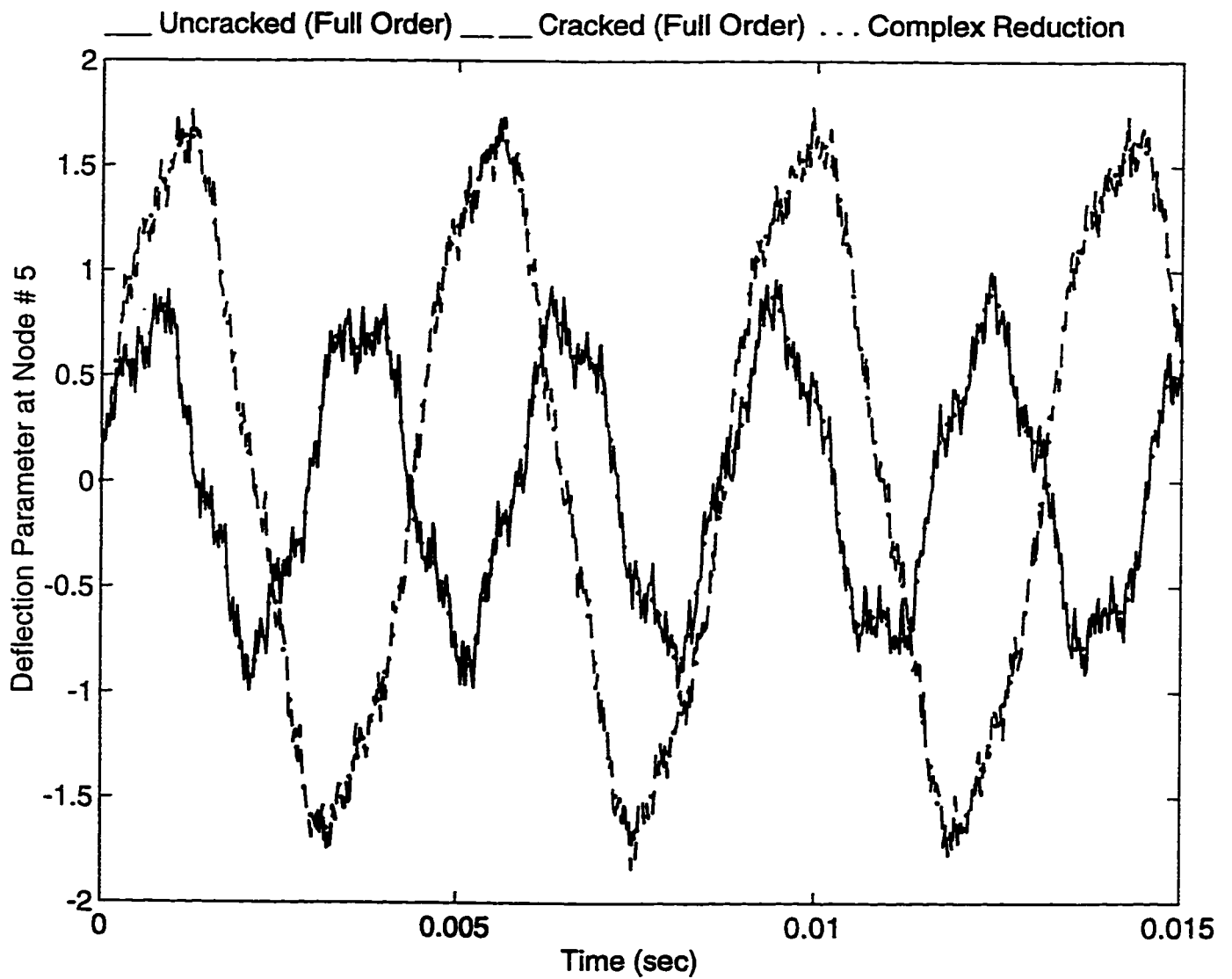


Figure 6-28: Impulse response of non-rotating simply supported shaft using complex modal reduction

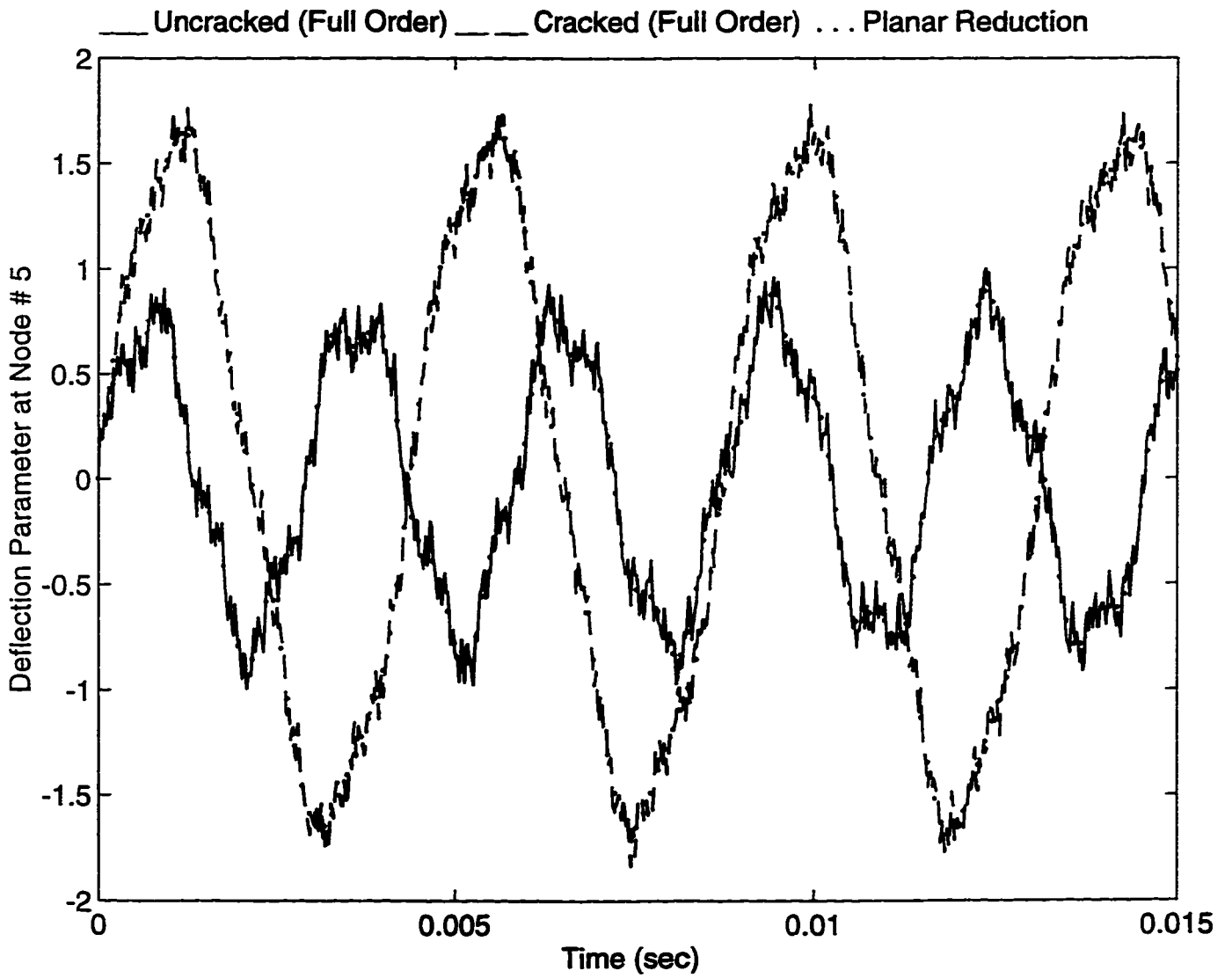


Figure 6-29: Impulse response of non-rotating simply supported shaft using planar modal reduction

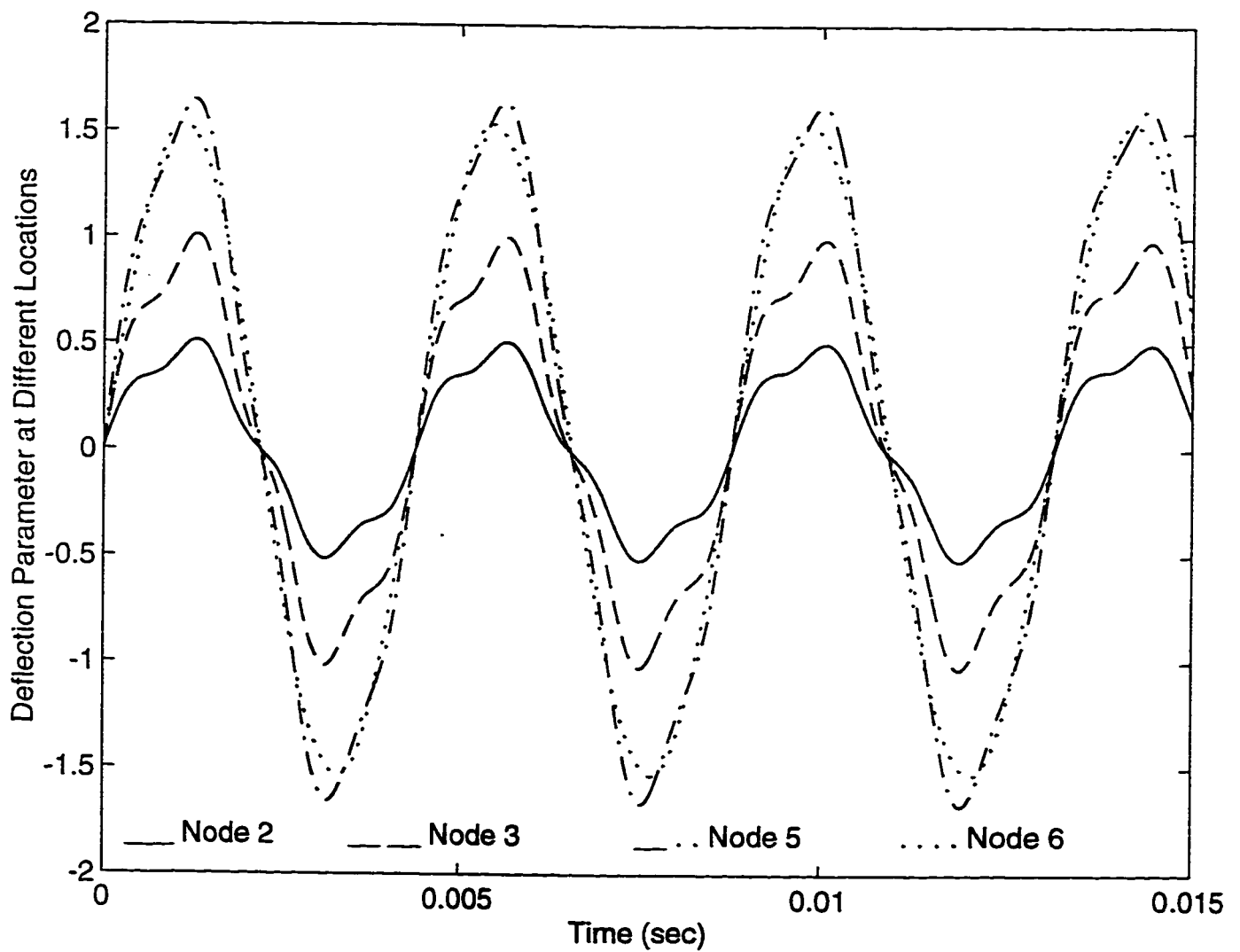


Figure 6-30: Deflection of cracked non-rotating simply supported shaft at different locations along its length due to unit impulse at node 5

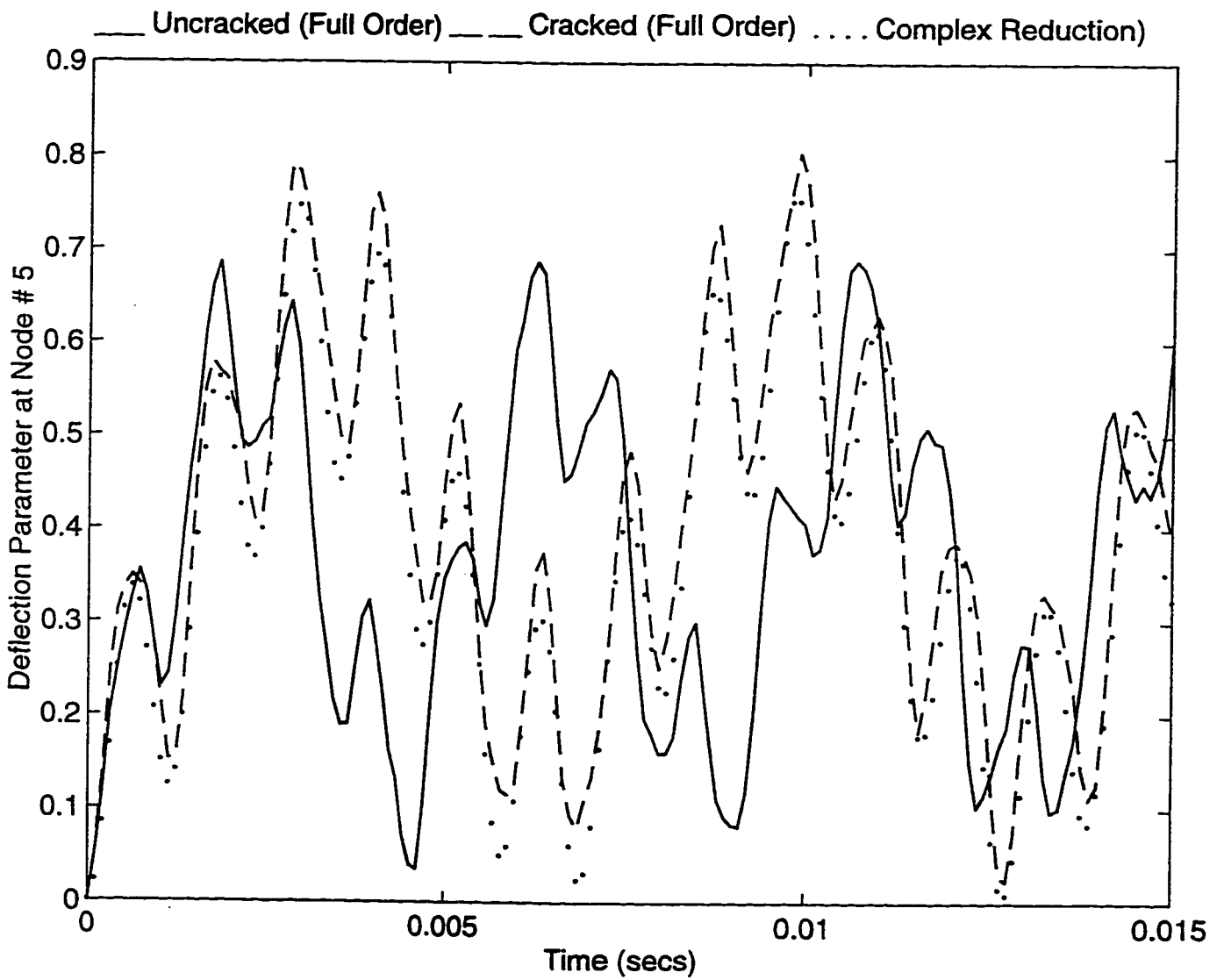


Figure 6-31: Step response of non-rotating tapered cantilever shaft using complex modal reduction

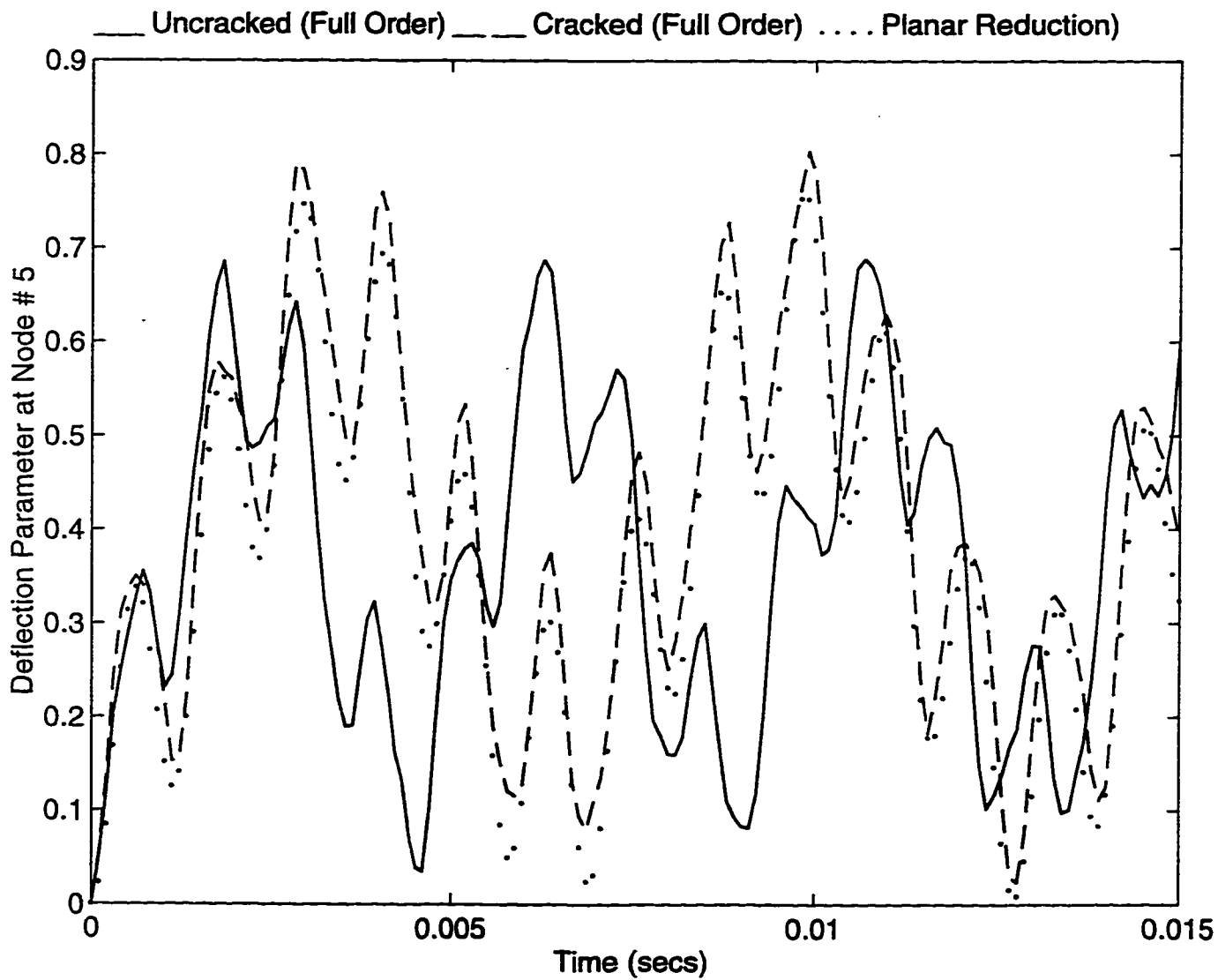


Figure 6-32: Step response of non-rotating tapered cantilever shaft using planar modal reduction

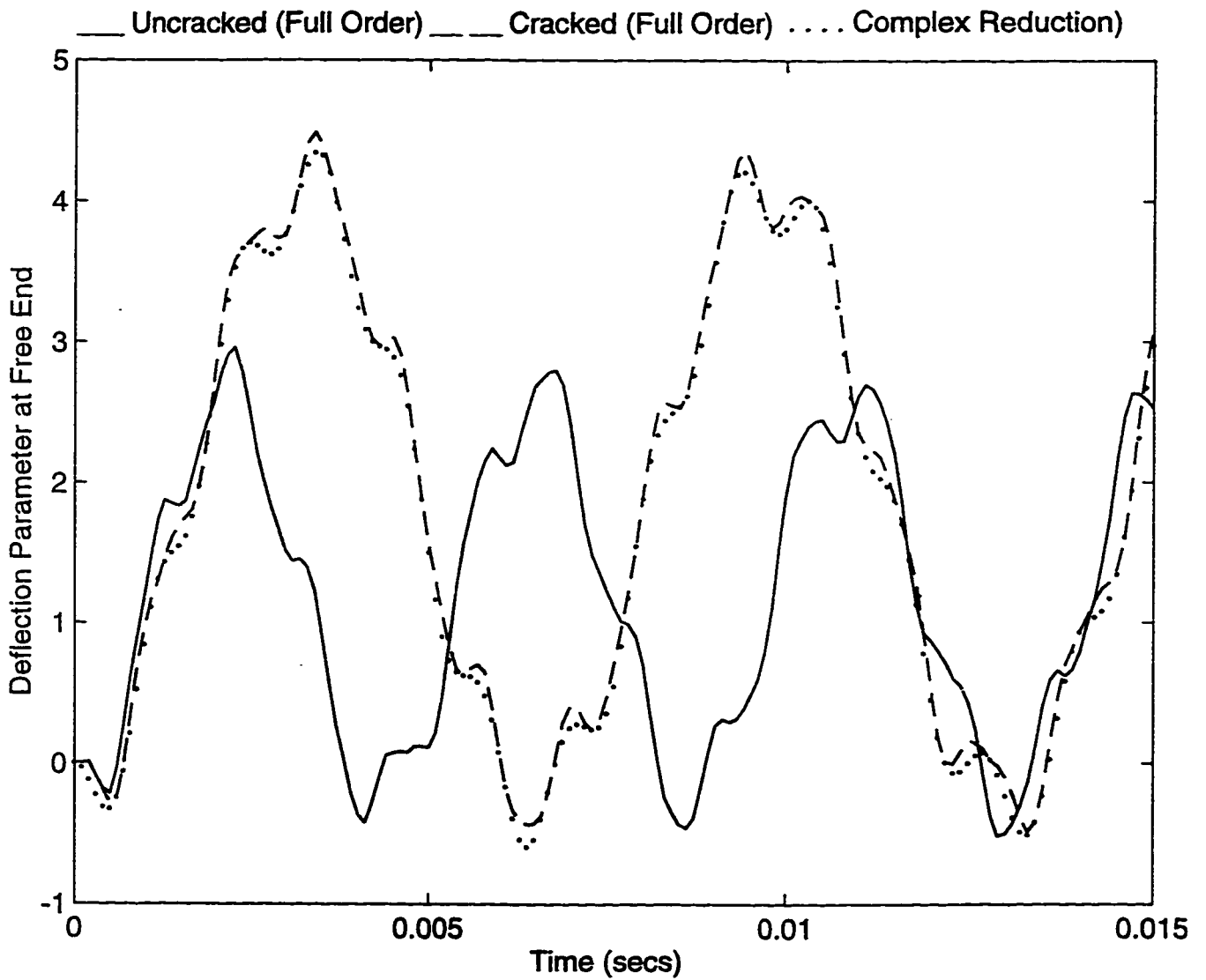


Figure 6-33: Comparison of step response of the cracked and uncracked non-rotating tapered cantilever shaft at the free end

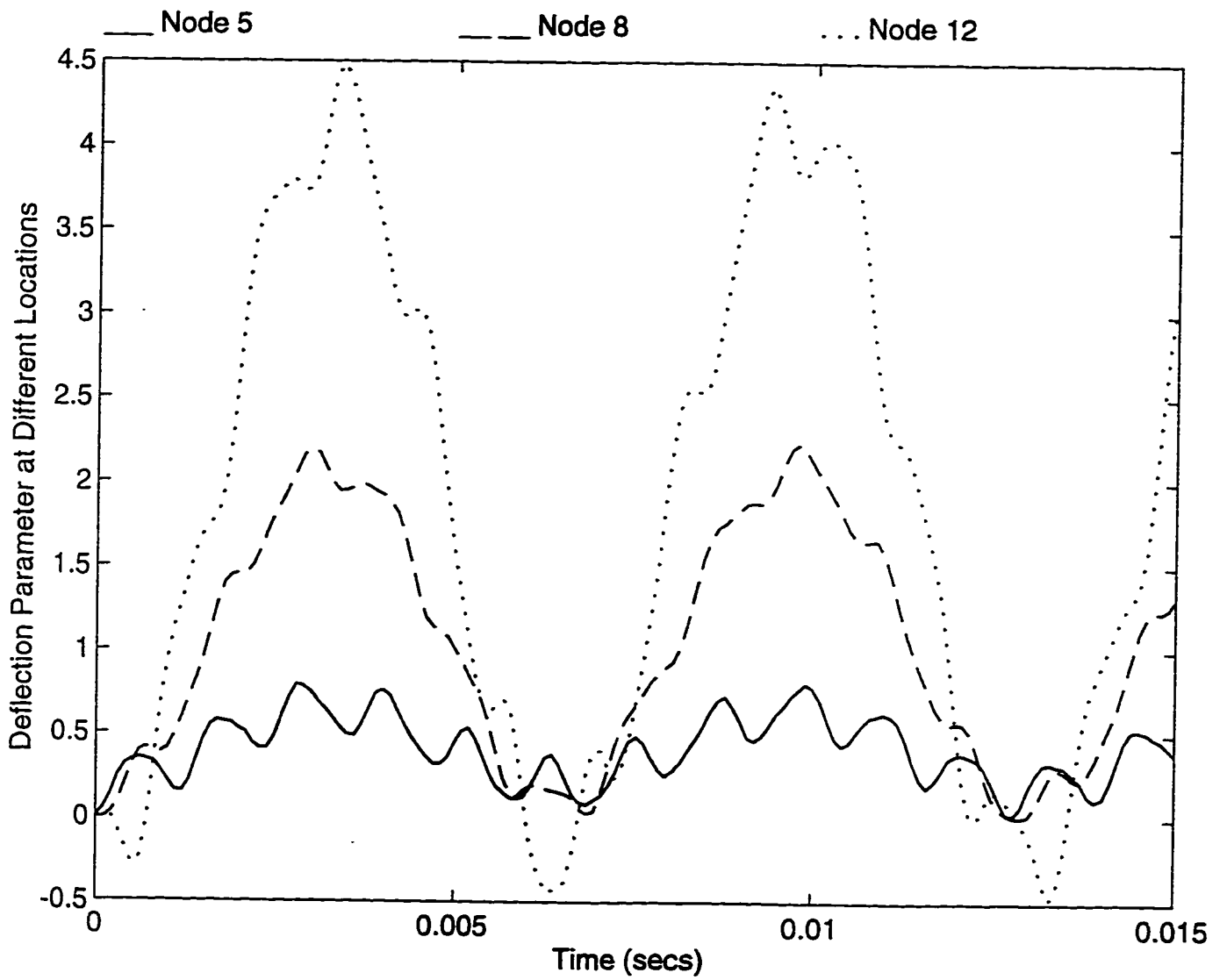


Figure 6-34: Step response of cracked non-rotating tapered cantilever shaft at different locations along the length of the shaft

tudes of vibration of the impulse responses are comparable for the cracked and uncracked non-rotating tapered cantilever shafts.

6.3.4 Rotating Tapered Shaft

Example 1

In the previous examples, the effect of a crack on the time response of non rotating shafts was studied. Consider a cracked tapered shaft rotating at a spin speed of $\Omega = 3000$ rad/sec with a crack of depth $\Delta = 0.5$ at $\rho = 0.3$ and taper ratio equal to 0.5, which is supported at the widest end by a rigid journal bearing, is excited by a step force near the crack. Again the tapered shaft is of length $L = 1m$ and slenderness ration $R_1/L = 0.125$. The shaft is divided into 11 equal finite elements. The excitation is at node 5. The time responses of the rotating tapered shaft in the two planes of vibration obtained using the full order models are plotted in Figure 6-37. In this example, the unit step force is acting in the direction of vibration along which the crack is present. It is clearly shown in the figure that the deflection in the plane in which the crack is present is greater than that in the other plane. Although the excitation is only in one plane we record a deflection in the other plane because the two flexural motions are coupled by the gyroscopic moments. The response computed using the complex reduction scheme is also shown in the figure. In Figure 6-38 the time responses at node 5 of an uncracked tapered rotating shaft excited by unit step at node 5 is plotted. It is observed that the vibration of the shaft in the two planes is exhibiting out of phase beating phenomenon. Comparing Figures 6-37 and

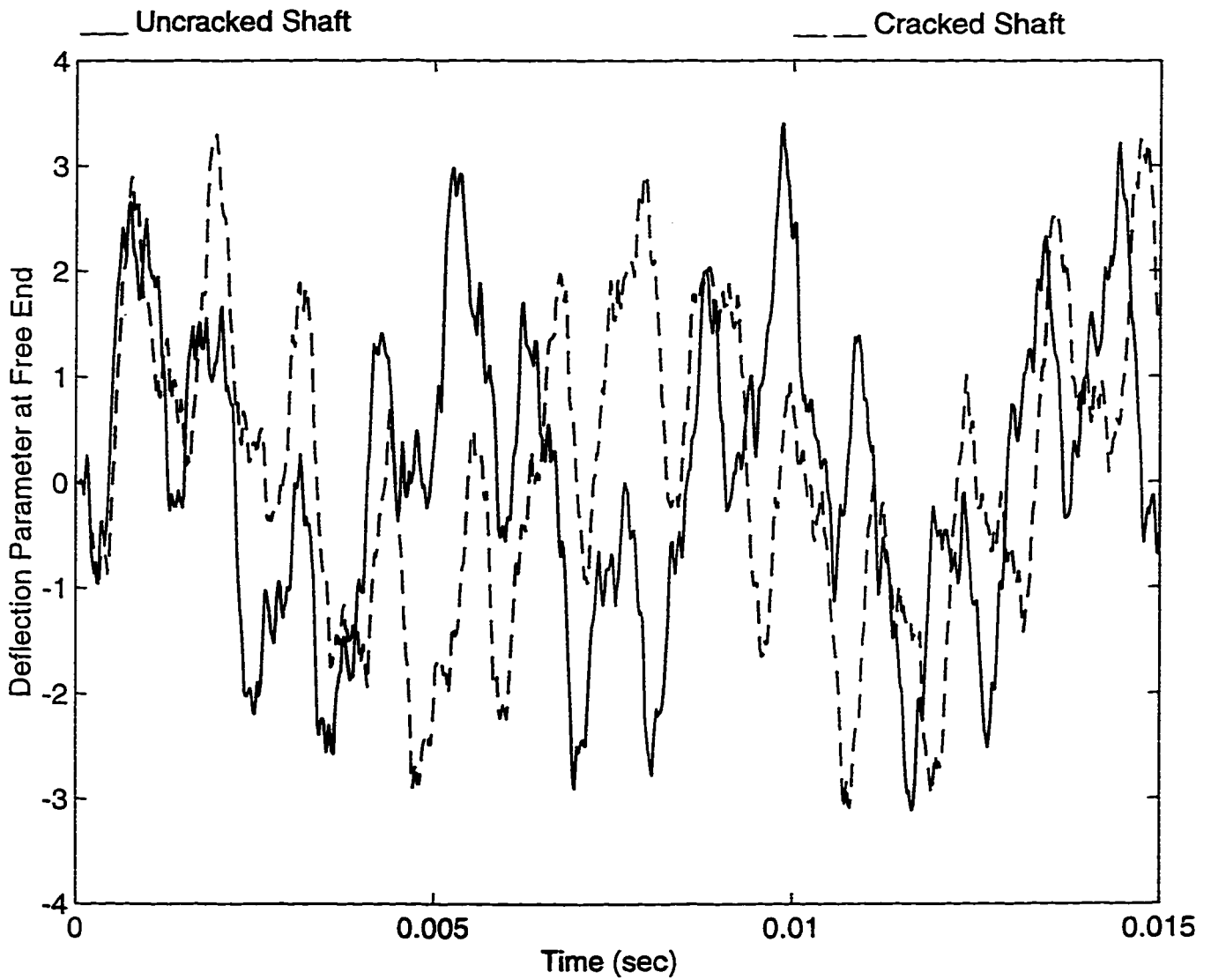


Figure 6-35: Comparison of impulse response of the cracked and uncracked tapered cantilever shaft at the free end

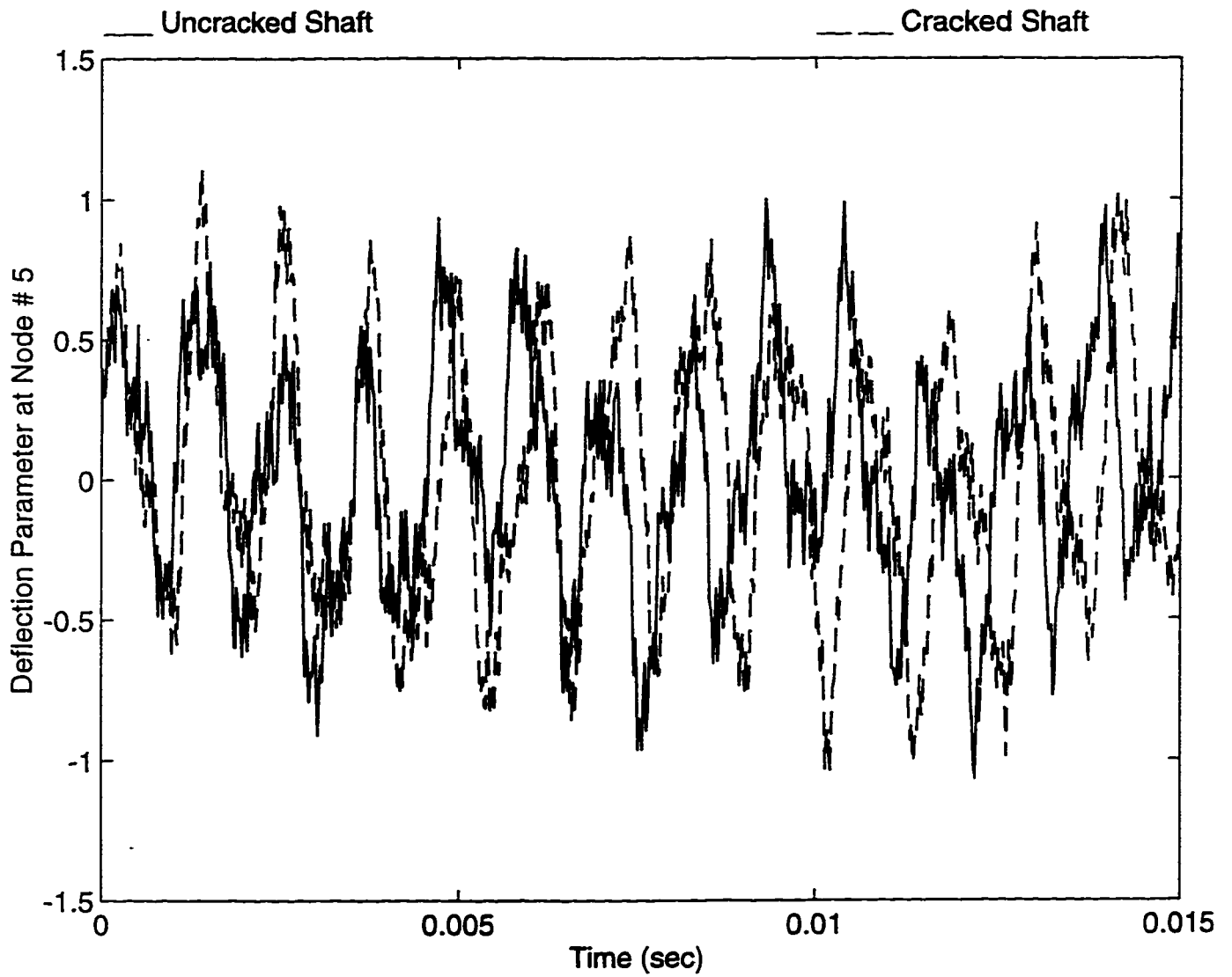


Figure 6-36: Comparison of impulse response of the cracked and uncracked tapered cantilever shaft at node 5

6-38 one can infer that the amplitudes of vibration of the cracked shaft have increased in the plane of crack.

In Figure 6-39, the deflection of the rotating shaft at the free end is shown. In this figure, the response computed using planar reduction scheme is compared to the one computed using full order matrices. In Figure 6-40, the response of the cracked rotating shaft at node 5, when excited by a unit impulse at node 5 is shown. The response computed using full order matrices is compared to the response computed using the planar reduction model. The compared responses are in good agreement.

Example 2

A simply supported rotating tapered cracked shaft is considered. Other details of the shaft are similar to those of example 1. The response of the simply supported rotating shaft to unit step force is shown in Figure 6-41. The amplitudes of vibration in the plane in which the crack is present are much higher when compared to the amplitudes of vibration in the other plane of vibration. This is due to the inertial coupling matrix which couples the flexural and torsional vibrations of the shaft. In Figure 6-42 the torsional deflection of the simply supported shaft due to a unit step force in the flexural direction is shown. The torsional deflection is solely due to coupling with the flexural motion because no torsional load is applied to the shaft. In addition, the response due to a unit step force computed using planar reduction model is in good agreement with that computed using full order matrices.

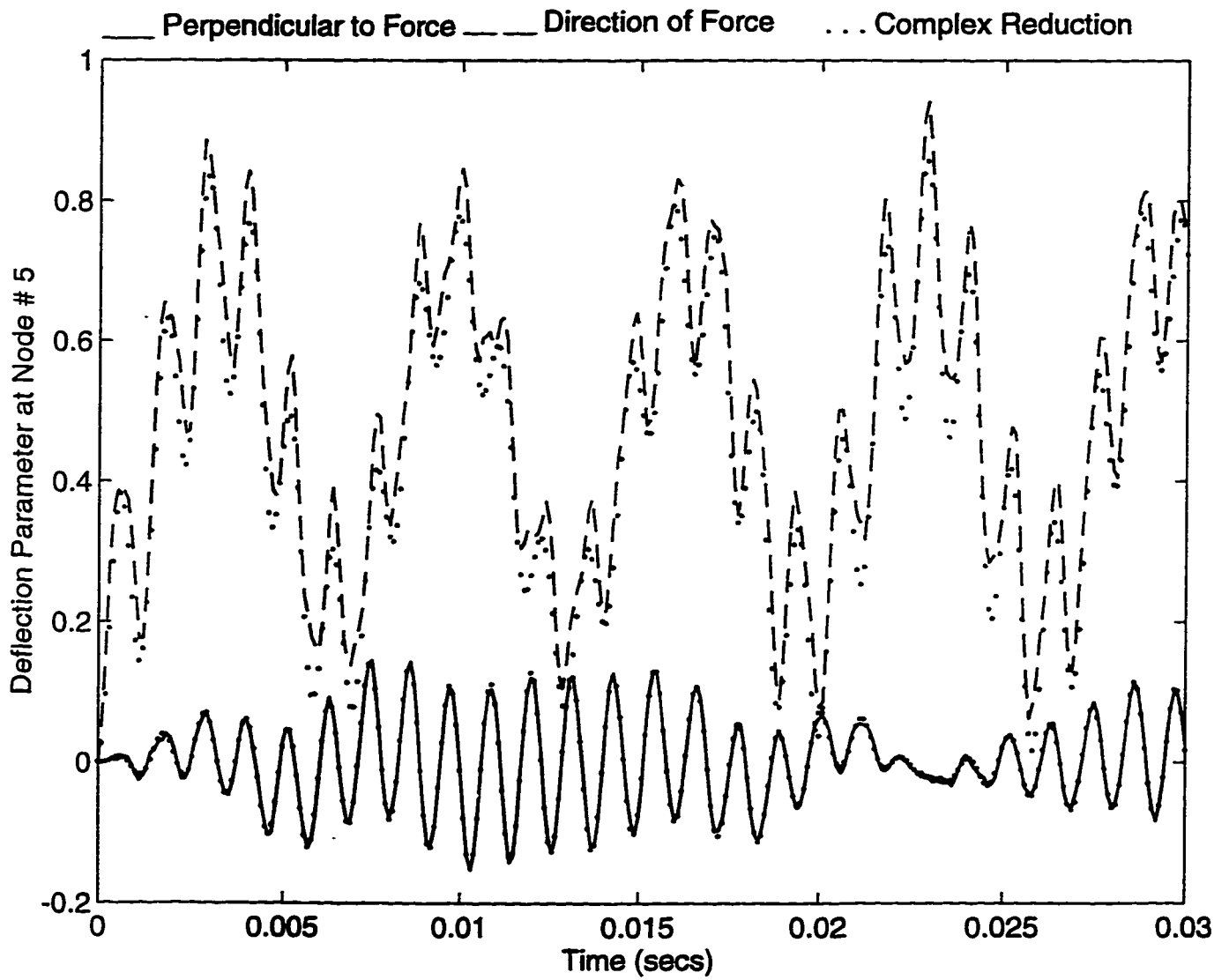


Figure 6-37: Step response of the rotating tapered cracked cantilever shaft using complex modal reduction

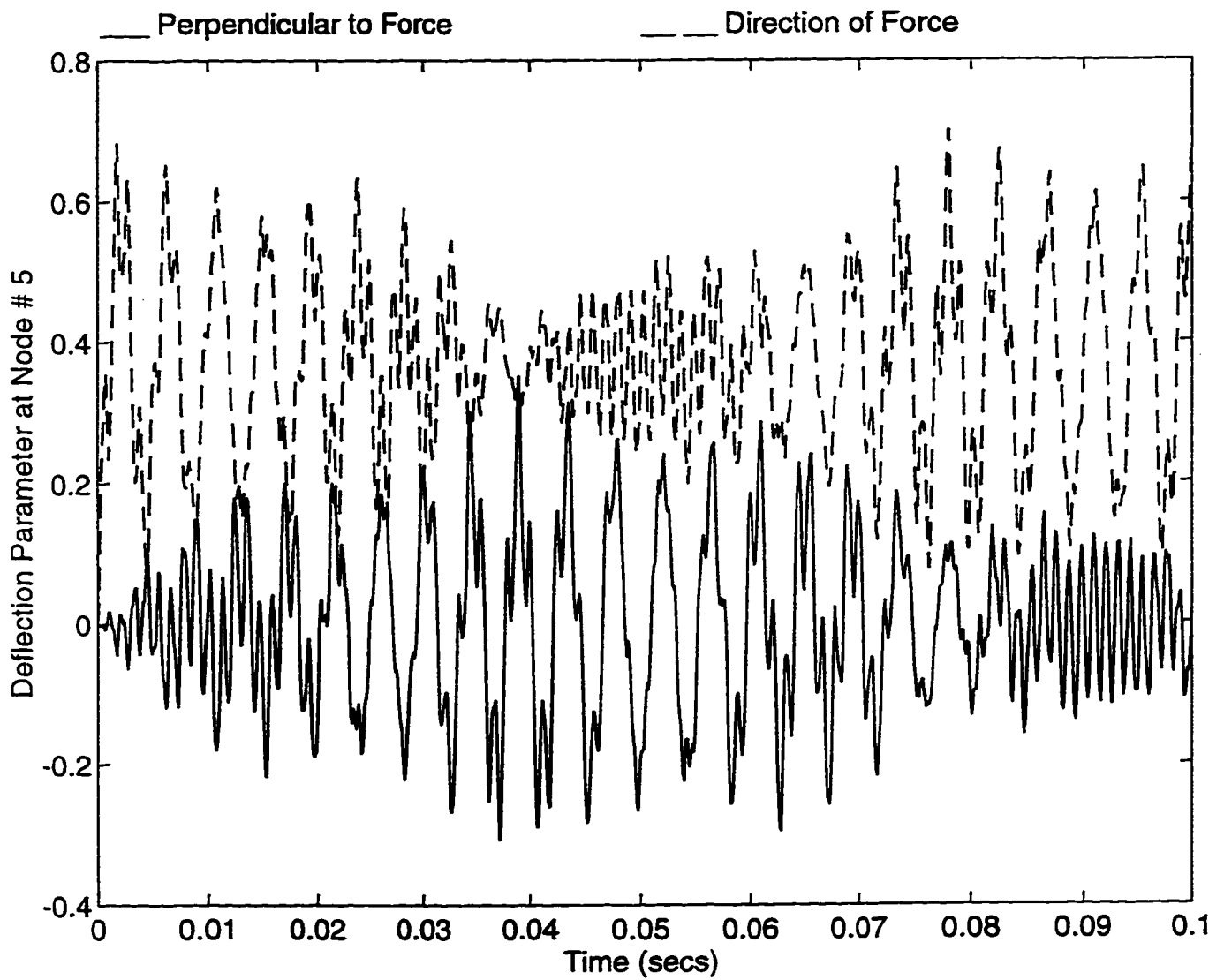


Figure 6-38: Step response of the rotating tapered uncracked cantilever shaft

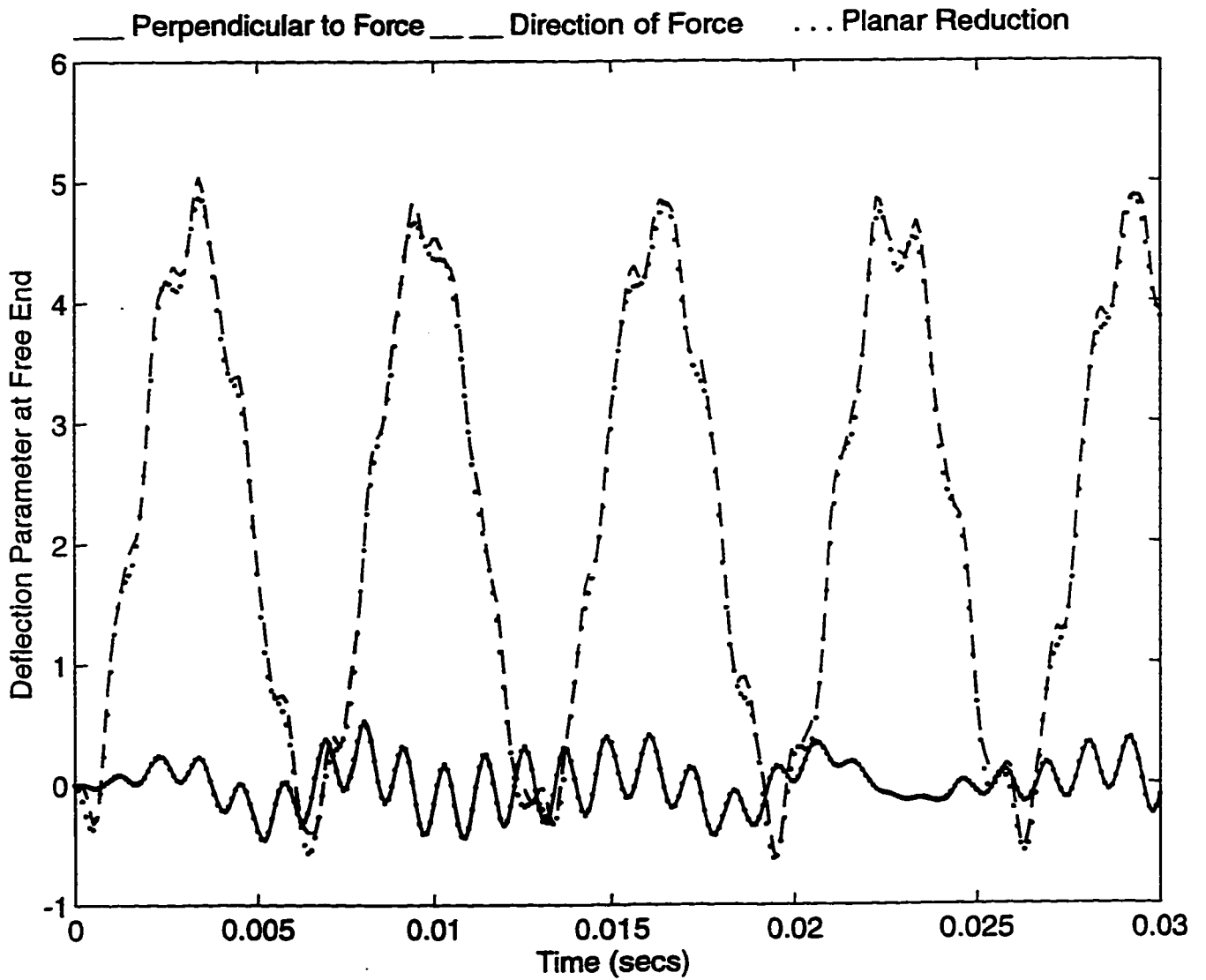


Figure 6-39: Step response of the rotating tapered cracked cantilever shaft using planar modal reduction

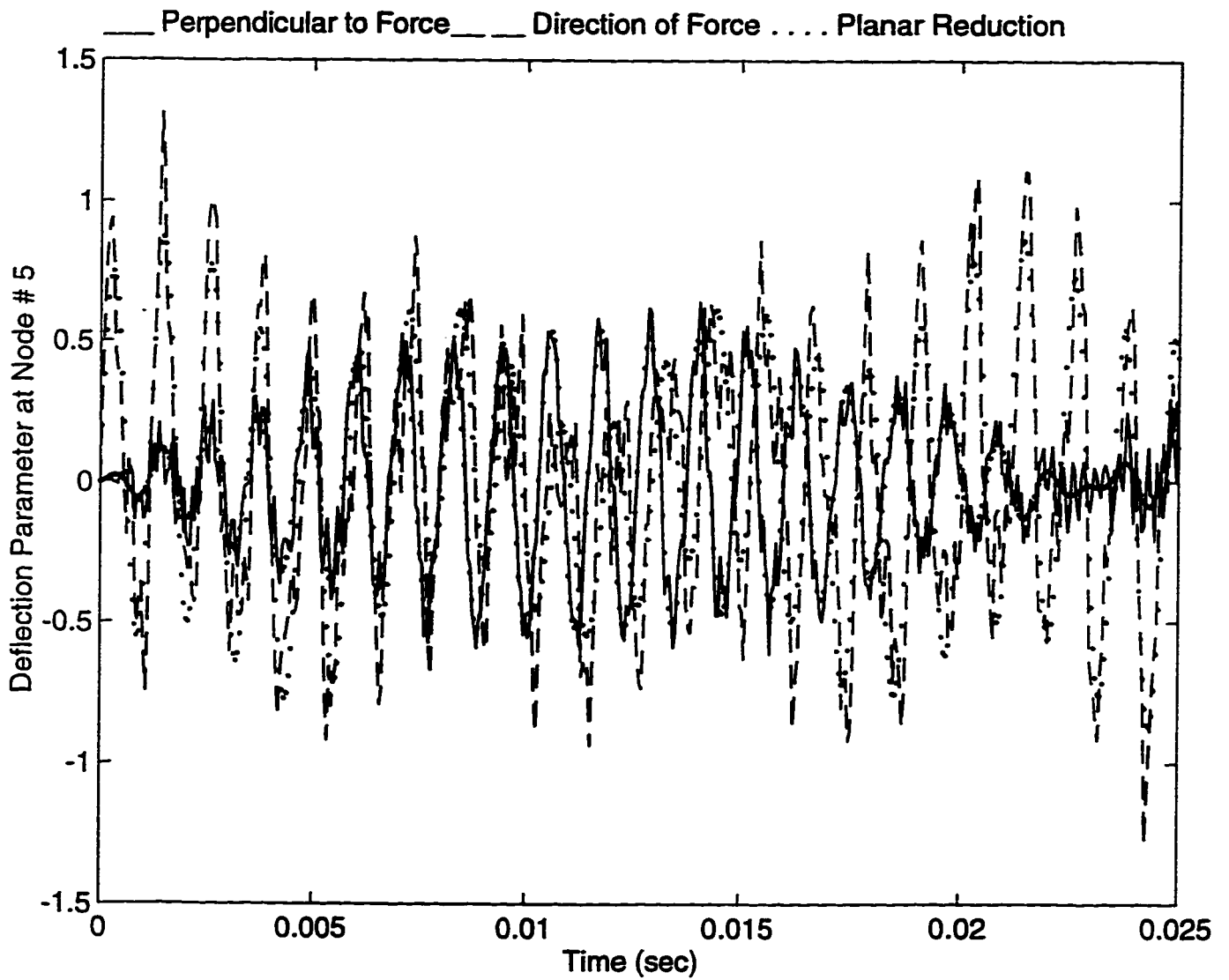


Figure 6-40: Impulse response of the rotating tapered cracked cantilever shaft using planar modal reduction

In Figure 6-43 the step response of a tapered rotating uncracked shaft is plotted. The tapered shaft is simply supported at both ends and is rotating at a spin speed of $\Omega = 3000$ rad/sec. The comparison of Figures 6-41 and 6-43 show the difference in the behavior of the rotating shaft due to the presence of crack. The time responses of the uncracked rotating shaft have out-of-phase vibrations exhibiting the beating behavior. The step response of the cracked rotating shaft does not exhibit the above characteristics. The deflection in the plane of crack is much higher when compared to the deflection in the other plane.

The response at node 5 due to unit impulse is shown in Figure 6-44. Once again, the amplitude of vibration in the plane of crack is higher than the amplitude of vibration in the other plane. Moreover, the comparison of impulse responses computed using planar reduction and using full order matrices is excellent.

Example 3

The rotating cantilever shaft of example 1 is excited by cyclic forces. In Figure 6-45, the response at node 5 of the cantilever shaft due to a force of the form $\sin(1000t)$ applied at node 5 is shown. It is observed that the behavior of the shaft when excited by a cyclic force is completely different compared to the behavior when excited by step or impulse forces. The amplitudes of vibration exhibit in-phase beating unlike the behavior of the uncracked shaft shown in Figure 6-43.

In Figure 6-46, the response at node 5 of the cantilever shaft due to a force $\sin(3000t)$

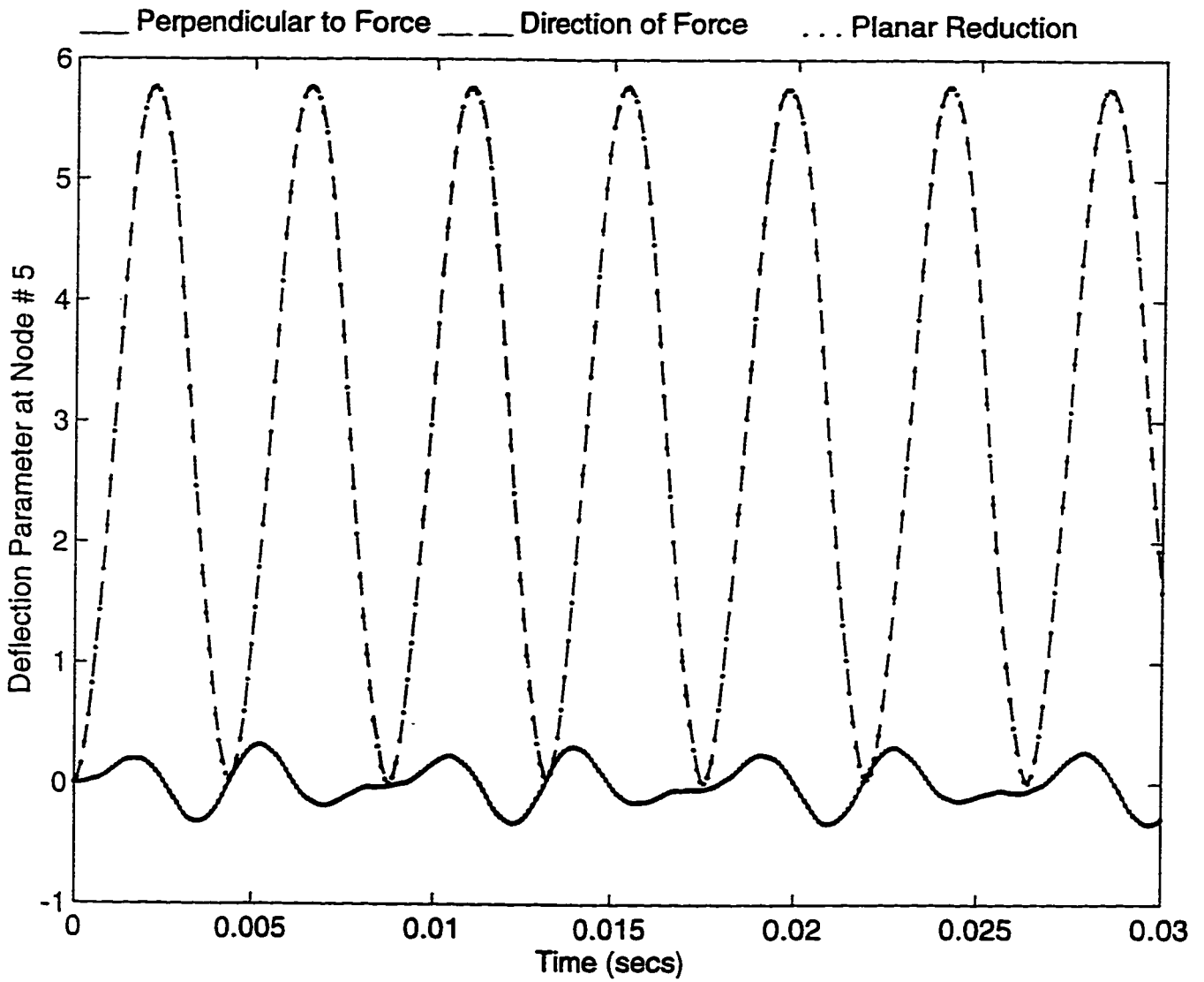


Figure 6-41: Step response of a cracked rotating tapered simply supported shaft using planar modal reduction

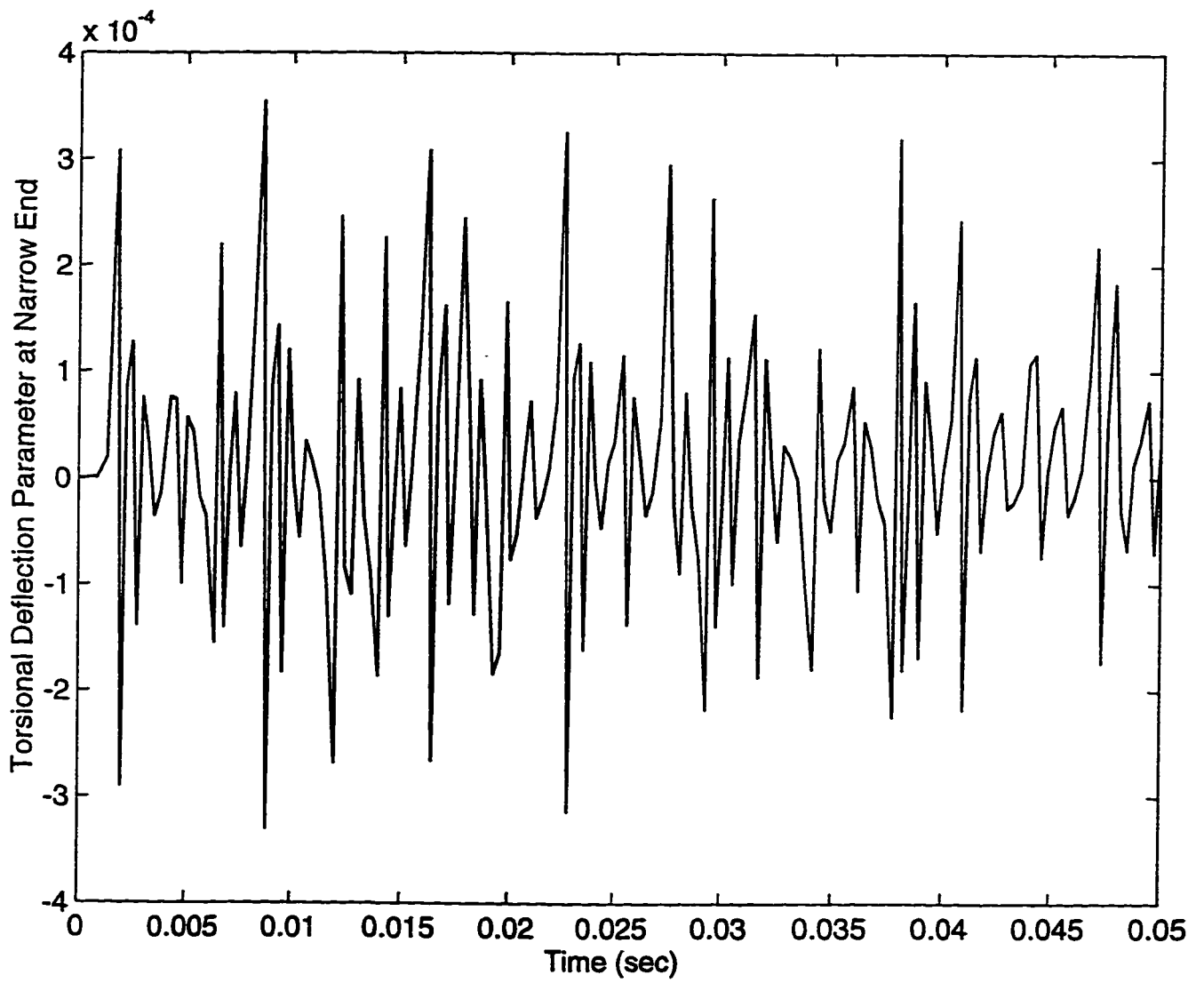


Figure 6-42: Torsional response of a cracked rotating tapered simply supported shaft due to inertial coupling

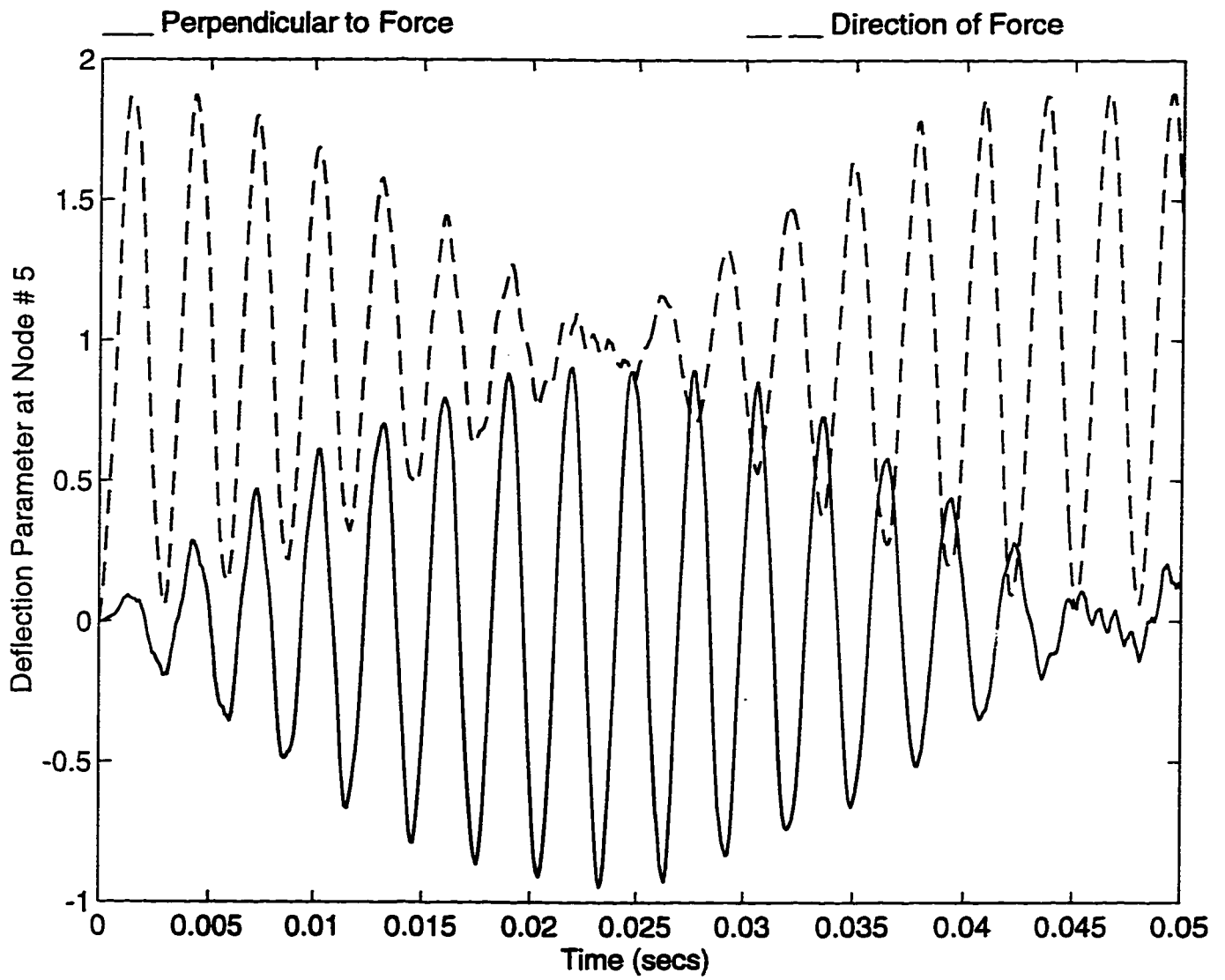


Figure 6-43: Step response of an uncracked rotating tapered simply supported shaft

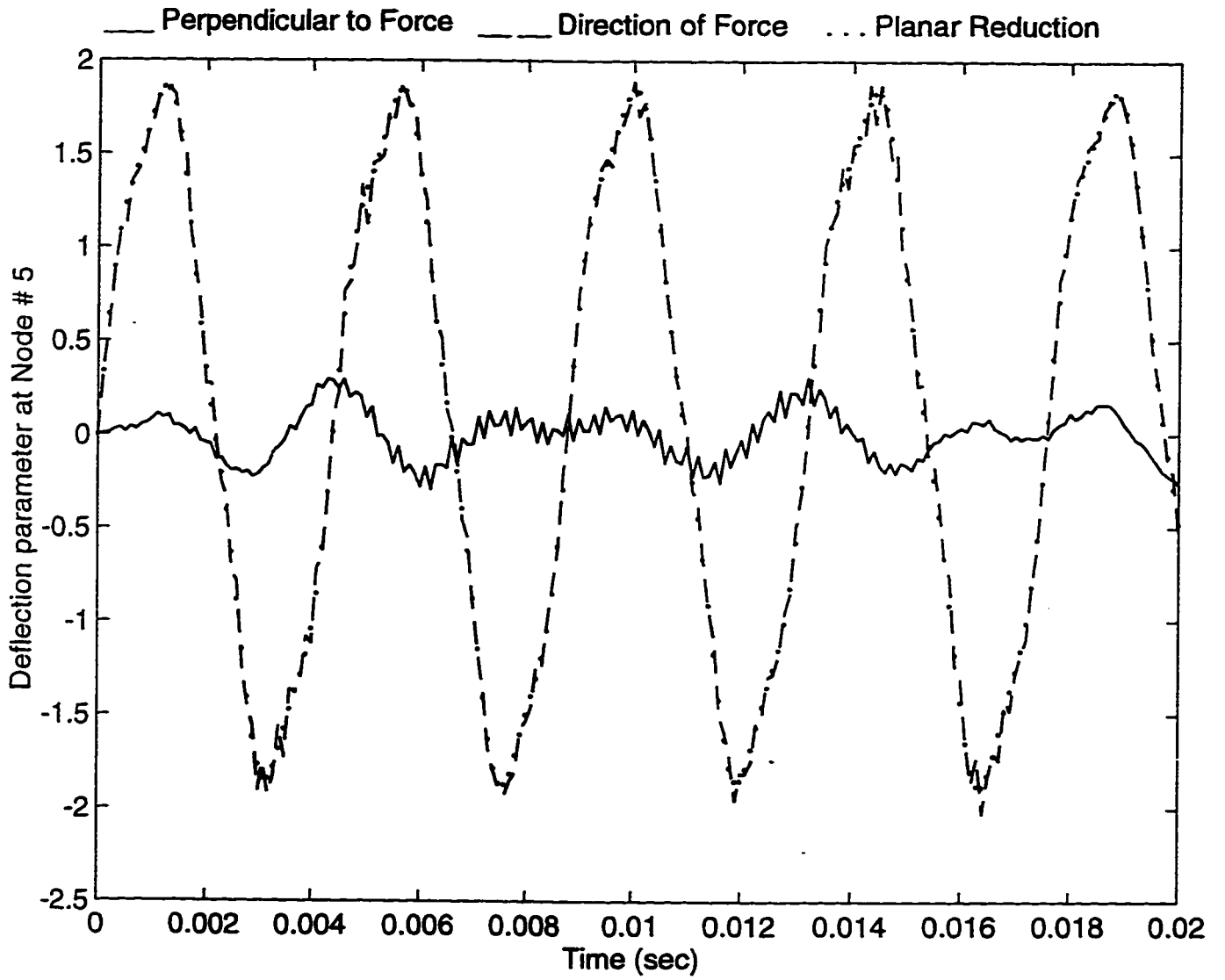


Figure 6-44: Impulse response of cracked rotating tapered simply supported shaft using planar modal reduction

applied at node 5 is shown. In this case, the frequency of the applied force is selected far from the lowest natural frequency of the shaft, hence the phenomenon of beating will not take place, however, this is a case of unbalance response because the frequency of applied force is equal to the spin speed of the rotor shaft. It is also observed that the amplitude of vibration in the plane of crack is higher than the amplitude of vibration in the other plane.

In Figure 6-47, the shaft is excited by a force $\sin(965t)$ at node 5. The lowest frequency of vibration of the shaft in the plane of crack is 965 rad/sec. Hence resonance occurs. It is observed from the figure that the amplitude of vibration in the other plane also increases, though the forcing frequency is not near the frequency of vibration of the other plane. In Figure 6-48, the excitation force is $\sin(1425t)$ at node 5, where 1425 rad/sec is the frequency of vibration of the shaft in the plane in which crack is not present. From the figure it is clear that the resonance occurs in the plane in which crack is not present, even though the force is acting in the plane of the crack.

Example 4

The simply supported rotating cracked tapered shaft considered in example 2 of the present section is excited by cyclic loads. The response of the simply supported shaft due to a force of $\sin(3000t)$ is shown in Figure 6-49. The response of the shaft due to a force of $\sin(2167t) + \cos(1632t)$ applied at node 5 is shown in Figure 6-50. The frequencies of excitation are equal to the two lowest natural frequencies of the simply

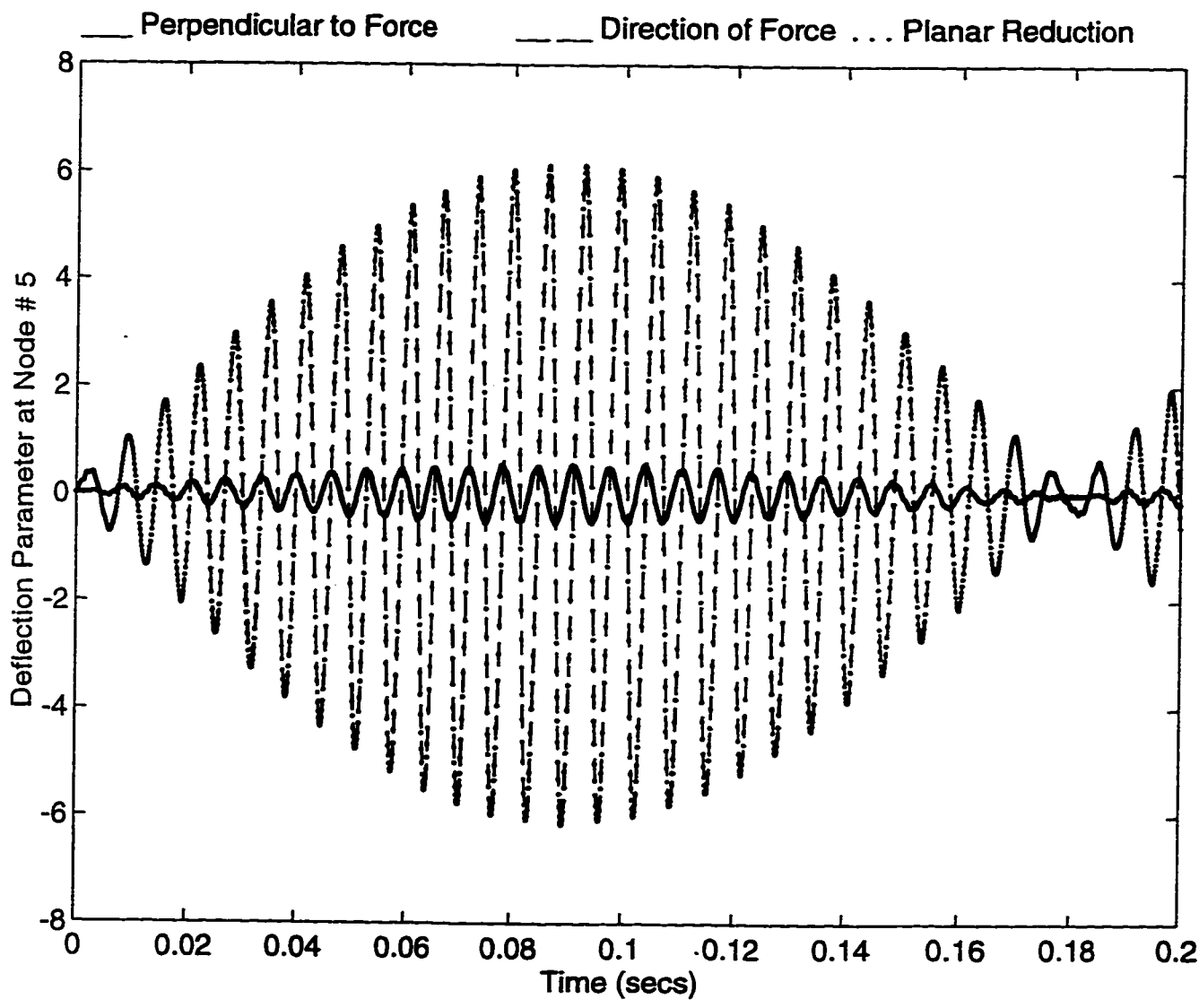


Figure 6-45: Time response of cracked rotating tapered cantilever shaft due to a force $\sin(1000 t)$

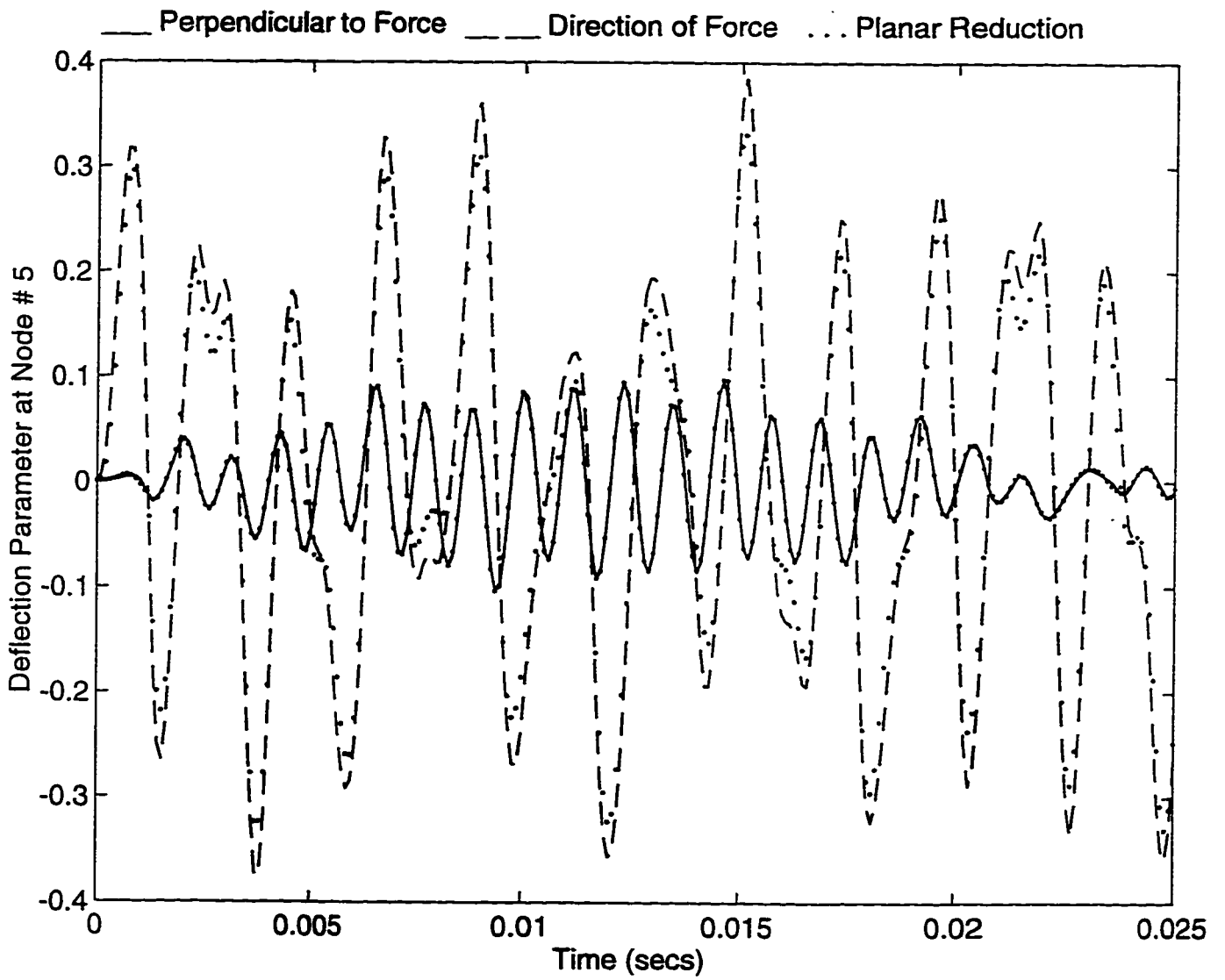


Figure 6-46: Time response of cracked rotating tapered cantilever shaft due to a force $\sin(3000 t)$

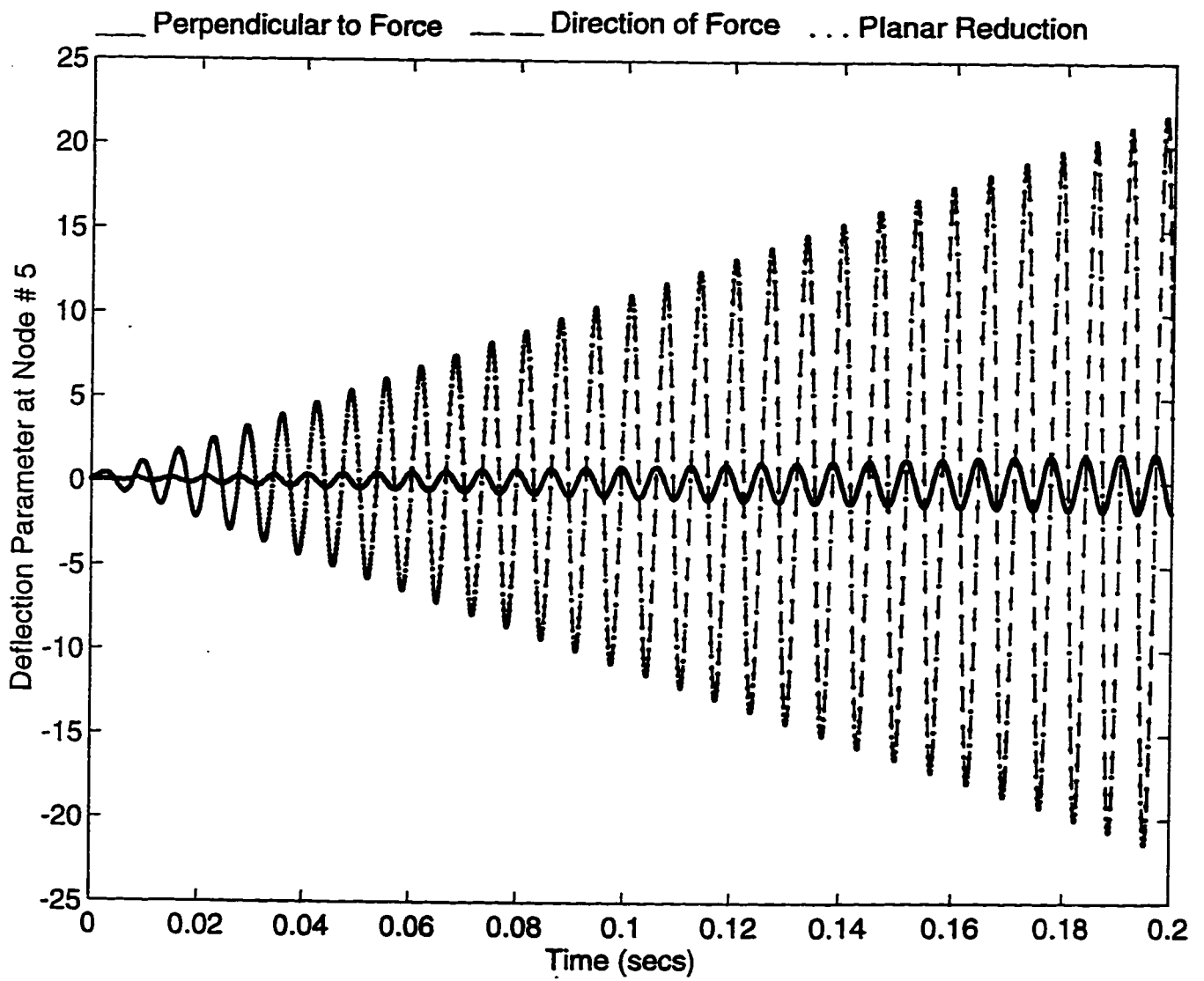


Figure 6-47: Time response of cracked rotating tapered cantilever shaft due to a force $\sin(965 t)$

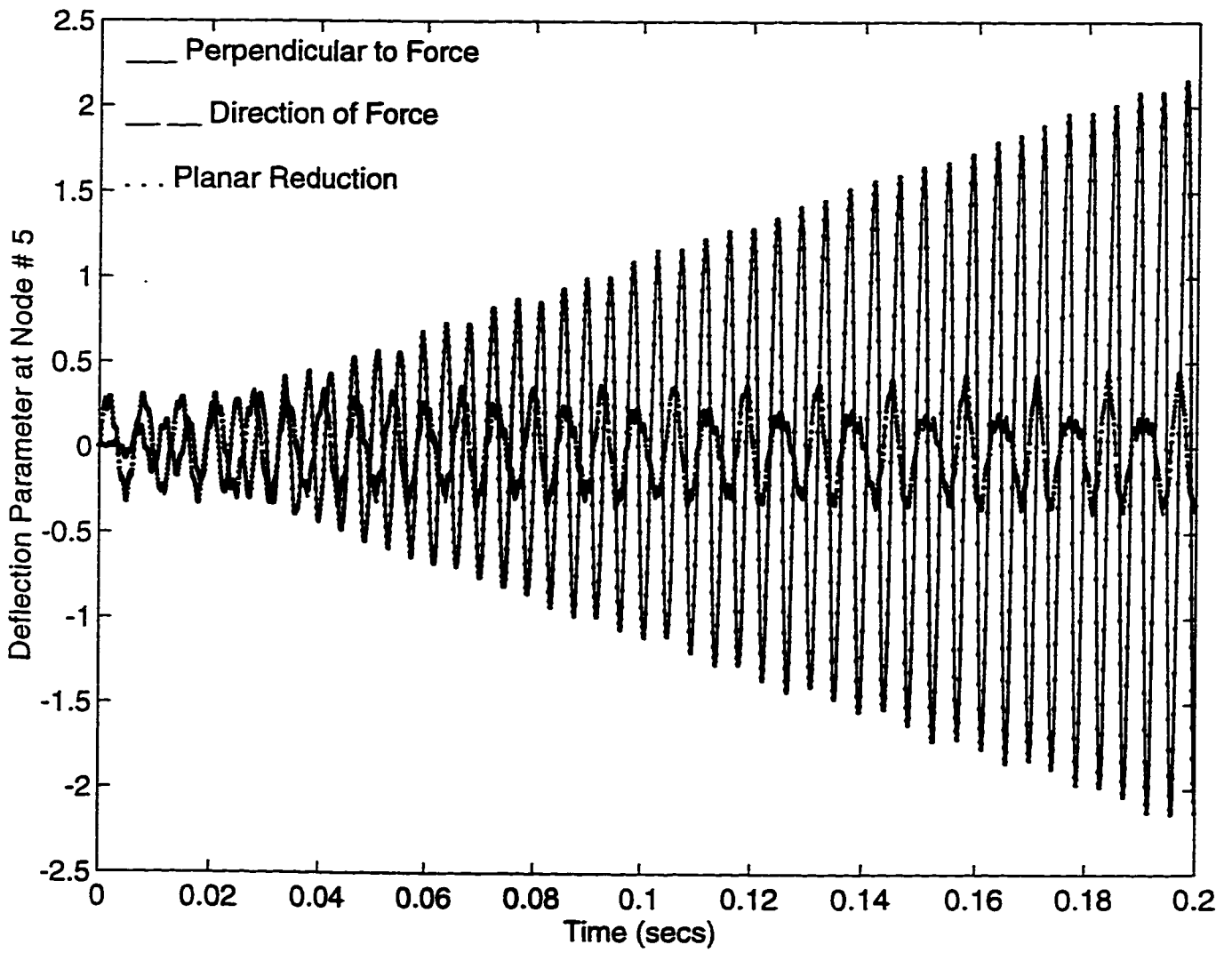


Figure 6-48: Time response of cracked rotating tapered cantilever shaft due to a force $\sin(1425 t)$

supported shaft. It is seen that resonance occurs in both the planes of vibration. In all the cases in which the shaft is excited by cyclic forces, the response evaluated using modal reduction schemes is found to be in excellent agreement when compared to the full order finite element model.

6.3.5 Rotating Multi-Stepped Shaft

Example 1

The complex multi-stepped rotor-bearing system shown in Figure 6-11 is now simulated to study the time response of an actual large-scale rotor system. The rotor-bearing system is rotating at a spin speed of $\Omega = 2000 \text{ rad/sec}$. The shaft is supported by two bearings which are flexible and damped. The stiffness coefficients of the bearings are $K_{yy} = K_{zz} = 3.503 \times 10^7 \text{ N/m}$ and $K_{yz} = K_{zy} = -8.756 \times 10^6 \text{ N/m}$. The damping coefficients are $C_{yy} = C_{zz} = 1.752 \times 10^3 \text{ N.s/m}$ and $C_{yz} = C_{zy} = 0$. The mass properties of the disk are mass 1.401 kg , polar moment of inertia 0.002 kg/m^3 , and diametral inertia $0.00136 \text{ kg} - \text{m}^2$. The shaft is excited by a step force applied at the disk. The multi-stepped shaft is divided into 18 elements of which some are hollow. The total number of degrees of freedom of the shaft are 95, therefore the state space full order model is of order (190×190) . The full order model is reduced to an order of (20×20) by retaining the first ten complex conjugate modes of the full order model. The time responses at the disk evaluated using the full order model and the reduced order model are plotted in Figure 6-51. It is observed that the comparison of the time responses of the full and

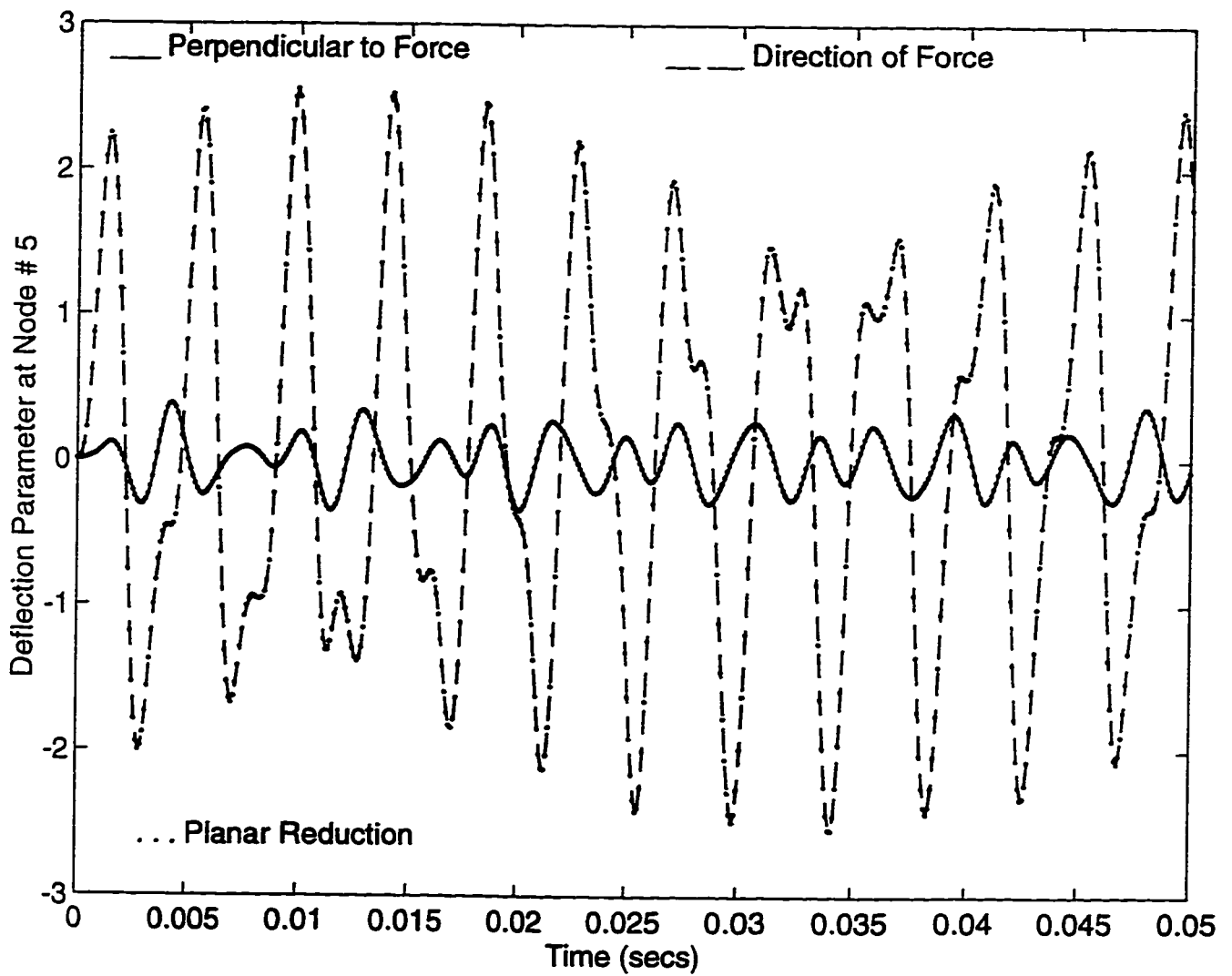


Figure 6-49: Time response of cracked rotating tapered simply supported shaft due to a force $\sin(3000 t)$

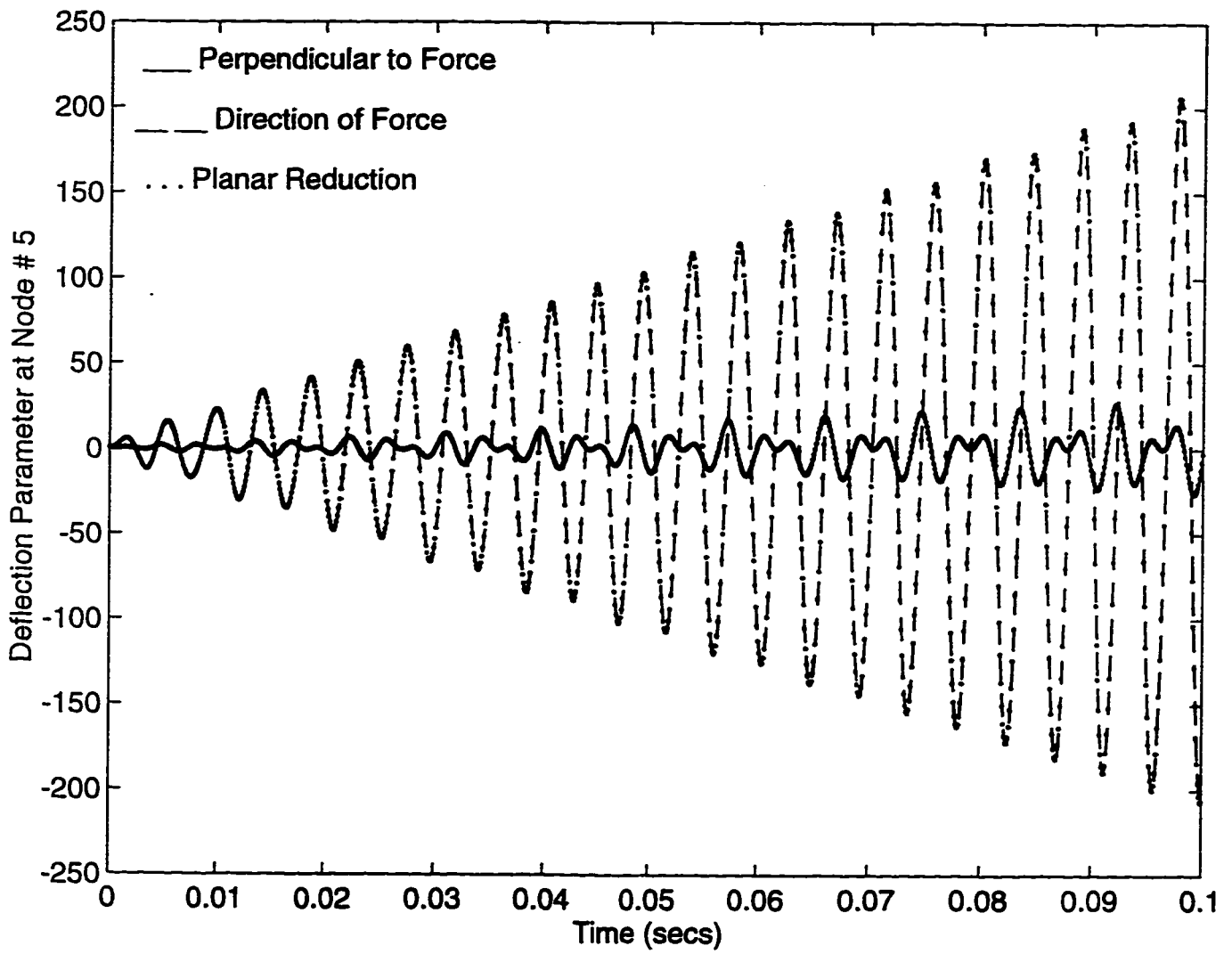


Figure 6-50: Time response of cracked rotating tapered simply supported shaft due to a force $\sin(2167 t) + \cos(1632 t)$

reduced order models is excellent.

Let a crack of depth $\Delta = 0.5$ be present at element 4 to the left of the disk. The time response of the cracked shaft due to step force at the disk is plotted in Figure 6-52. By comparing the time responses of uncracked (Figure 6-51) and cracked (Figure 6-52) shafts one can infer that the amplitudes of vibration are comparable, although the behavior of the cracked shaft exhibits longer settling time. This could be attributed to the fact that the crack, in some situations, was found to have a destabilizing effect on the rotor response.

Now, the uncracked multi-stepped shaft is excited at the middle of the two bearings, i.e. at node 13. The deflection of the shaft at node 13 evaluated using full and reduced order models is plotted in Figure 6-53. In Figure 6-54, the deflection of node 1 (tip of overhang) due to step force at node 13 is plotted. In Figure 6-55, the deflection of node 1 is plotted for expanded simulation time. Figures 6-53-6-55, show that the comparison of responses evaluated using full and reduced order models is excellent.

Let a crack of depth $\Delta = 0.5$, be present near mode 13 and the shaft be excited by a unit step force at node 13. The deflection at node 13 of the cracked shaft due to step force is plotted in Figure 6-56. Comparison of Figures 6-53 and 6-56 show that the amplitudes of vibration in the direction of force have increased appreciably for the cracked shaft. The deflection at node 1 of the cracked shaft due to excitation at node 13 is plotted in Figure 6-57. Comparison of Figures 6-54 and 6-57 show that the amplitudes of vibration of the cracked shaft have increased. Hence, one can infer that when the crack is present

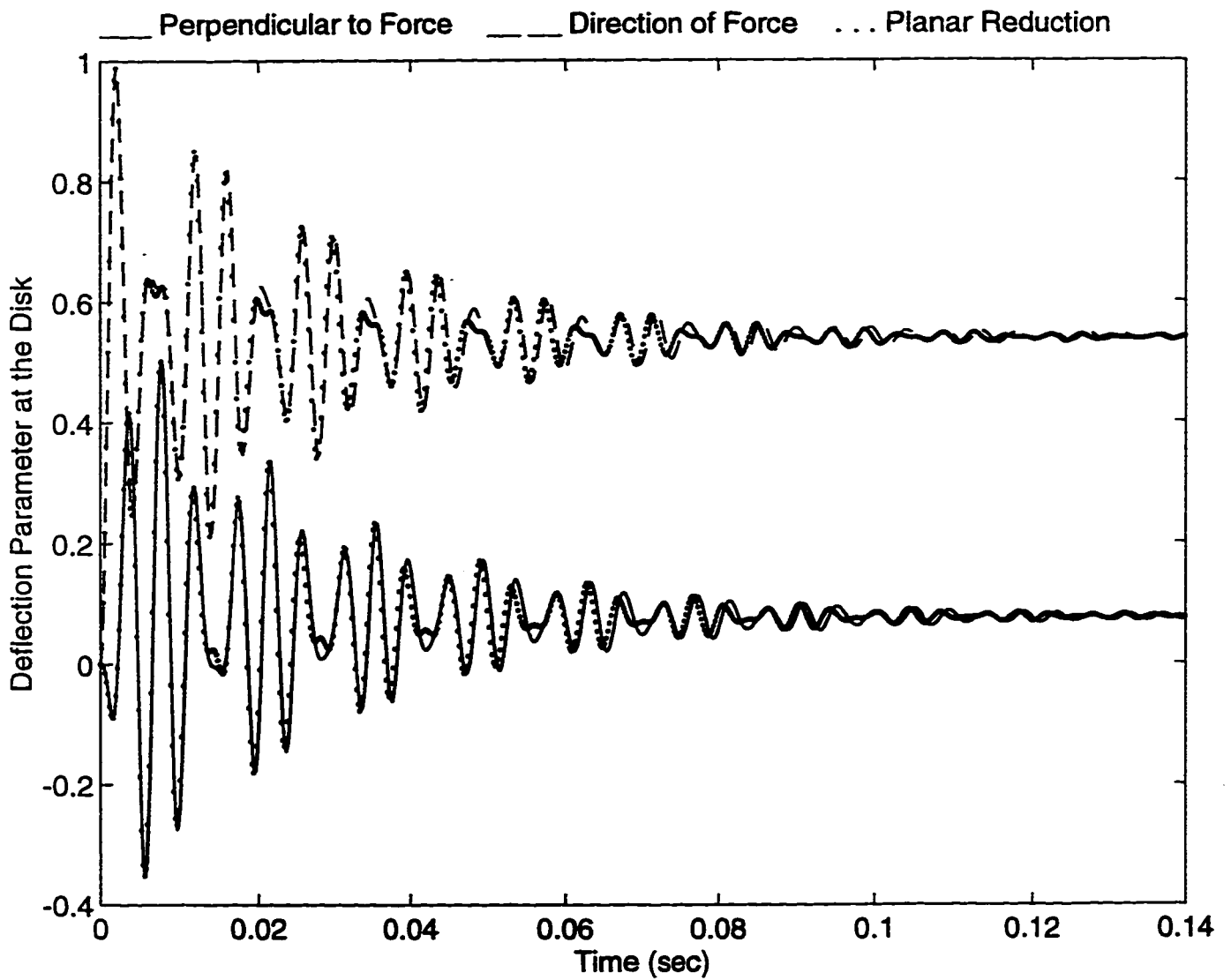


Figure 6-51: Time response of uncracked multi-stepped shaft due to unit force at the disk

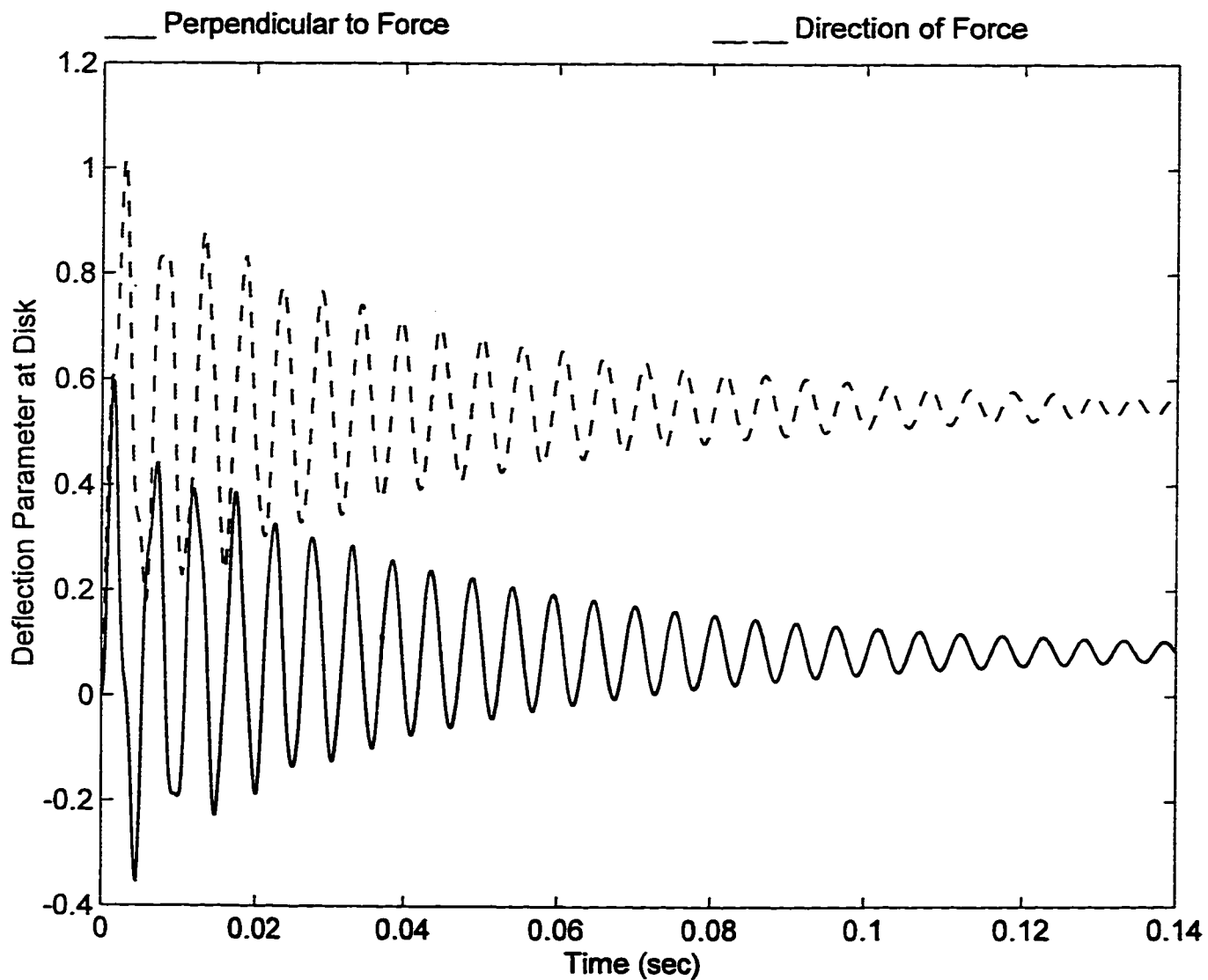


Figure 6-52: Time response of cracked multi-stepped shaft due to unit force at the disk

in the span between the bearings, it has appreciable effect over the time response, whereas, if it is present in the shaft overhang, the amplitudes of vibration of the cracked and uncracked shafts are comparable.

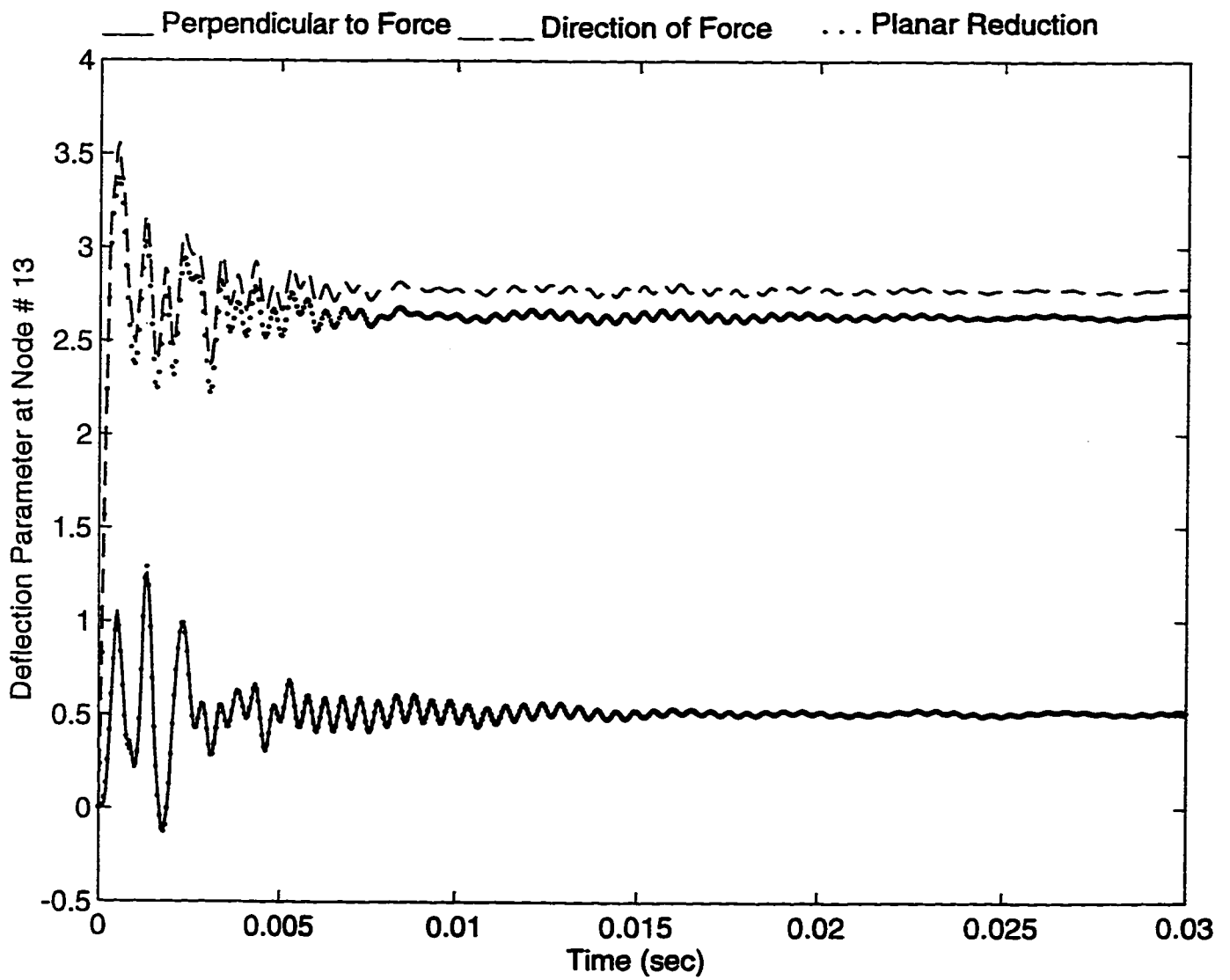


Figure 6-53: Step response of the multi-stepped uncracked rotor-bearing system using planar modal reduction

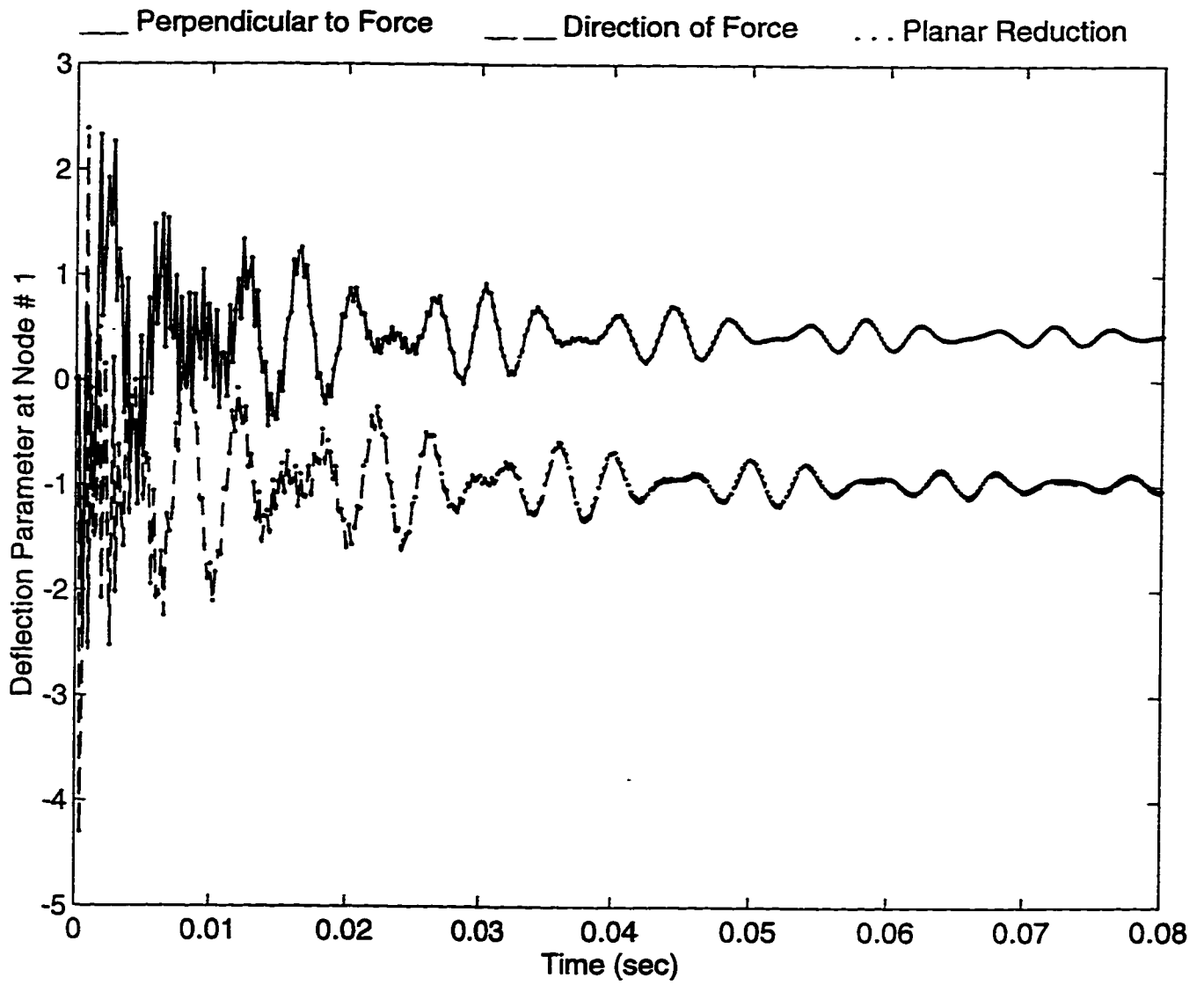


Figure 6-54: Step response of uncracked multi-stepped system an node 1 due to excitation at node 13

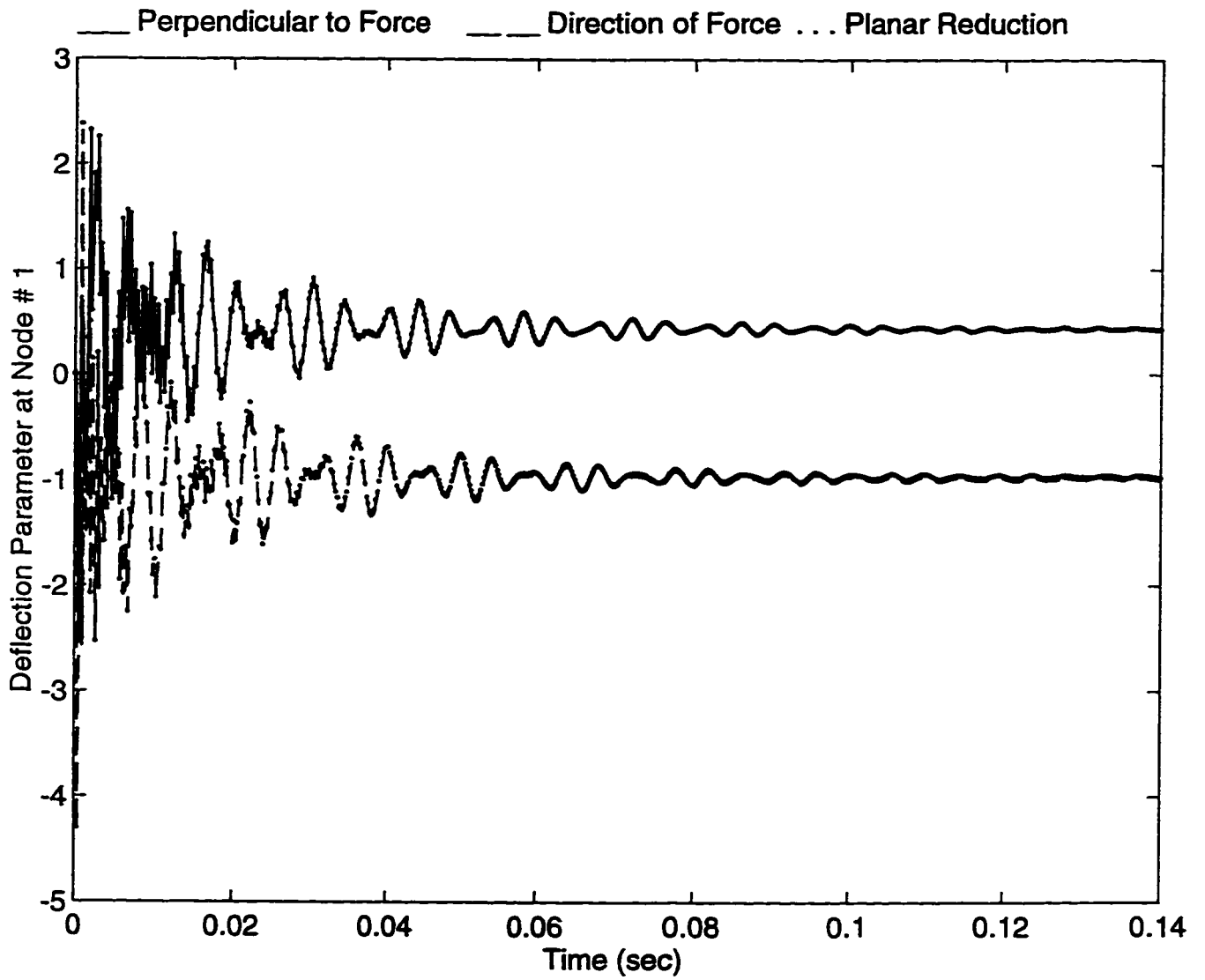


Figure 6-55: Step response of multi-stepped shaft at node 1 with expanded simulation time

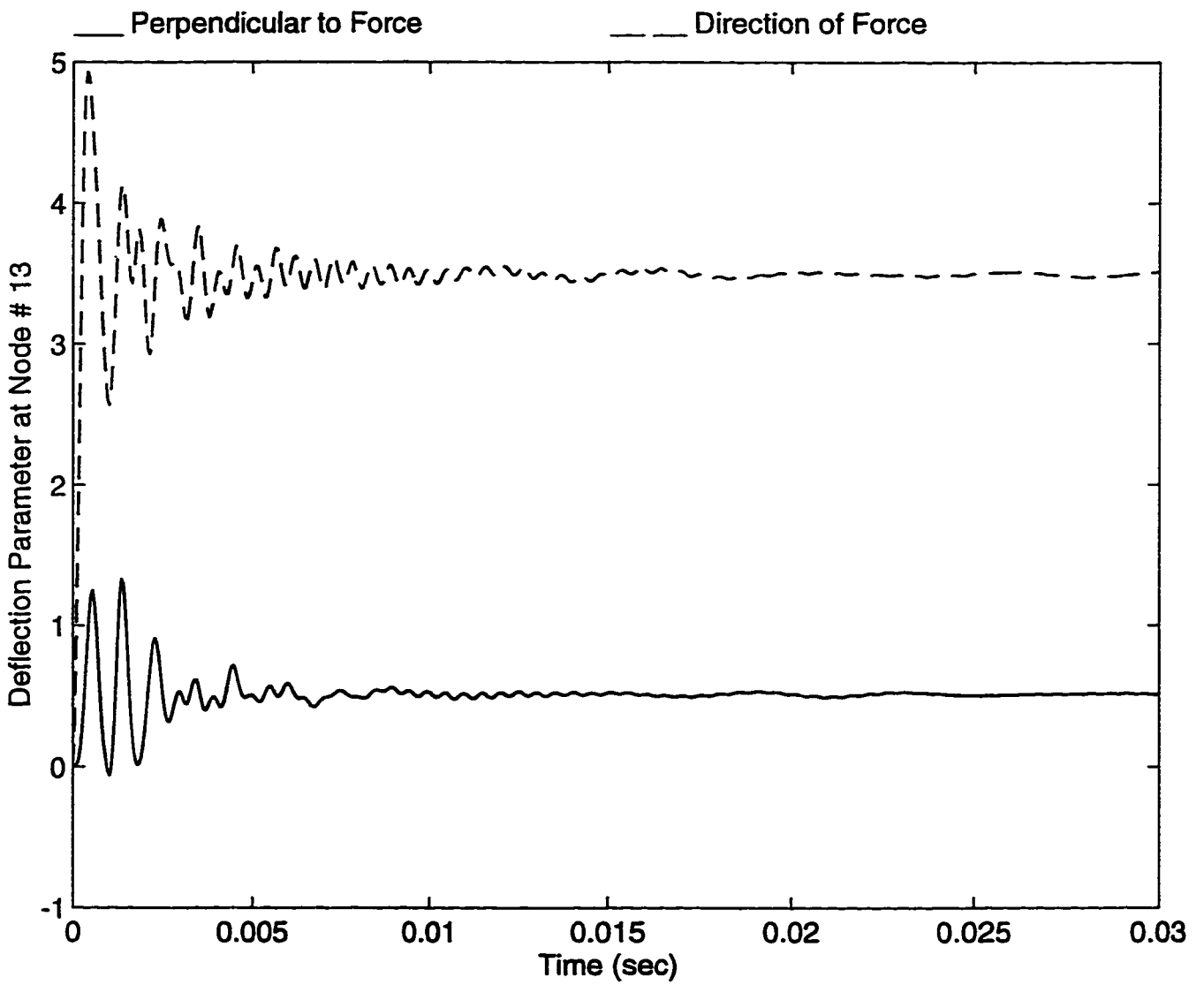


Figure 6-56: Step response of cracked multi-stepped system due to excitation at node 13

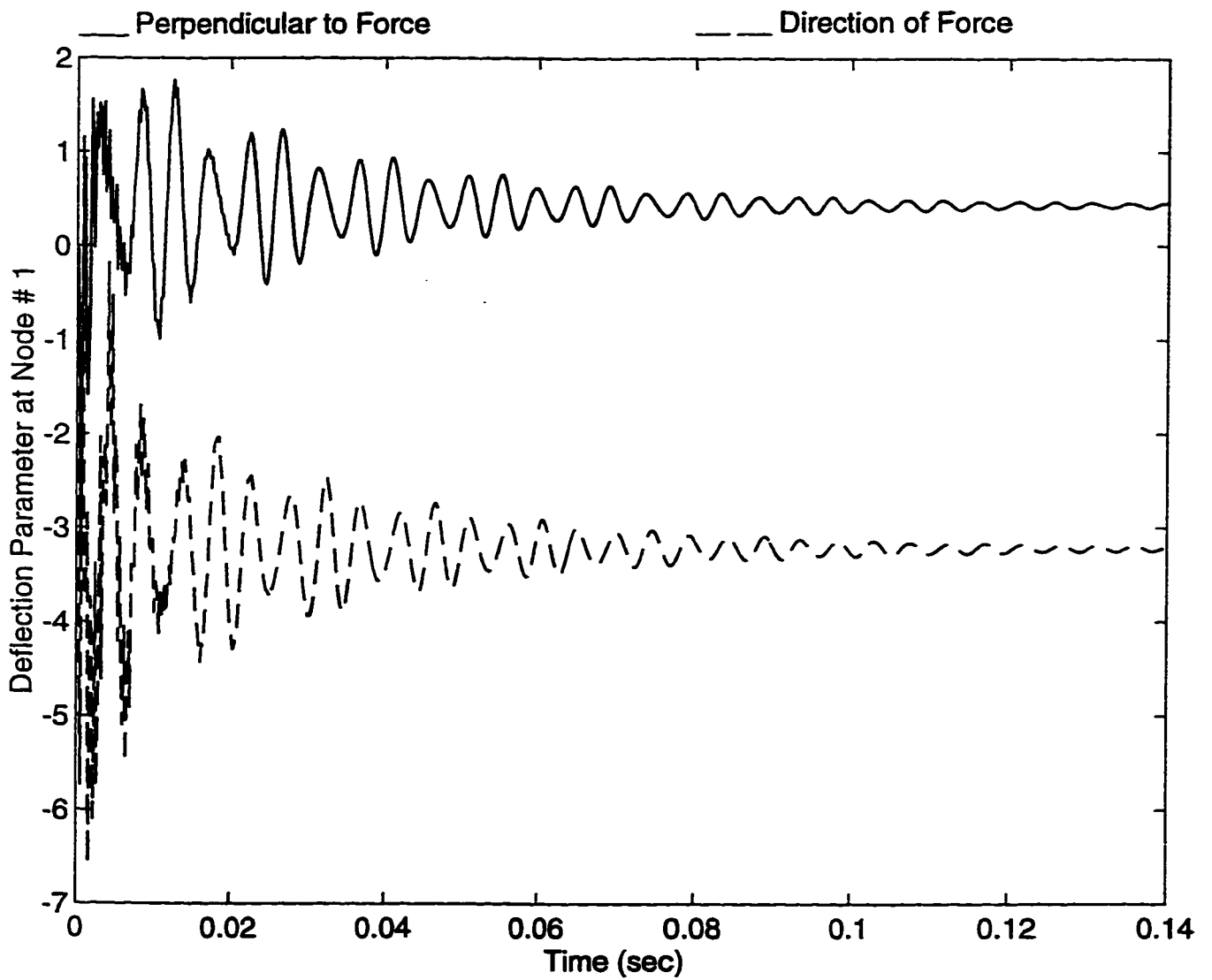


Figure 6-57: Step response of cracked multi-stepped shaft at node 1 due to excitation at node 13

Chapter 7

Conclusions and Recommendations

7.1 Conclusions

The shape functions for the rotating tapered cracked shaft finite element with shear deformation are derived. Expressions for the element mass, stiffness and gyroscopic matrices are formulated. The explicit form of the element matrices offers a computational advantage by eliminating the loss of computer time and round-off errors associated with extensive matrix operations which are necessary for their numerical evaluation. It is noteworthy to observe that these matrices are easily reducible to those of the Euler-Bernoulli theory by equating the shear deformation and the local crack flexibility parameters to zero. The developed finite element is integrated into a computational scheme for calculating natural frequencies and transient dynamic behavior of cracked rotor-bearing systems. The computational scheme accounts for any hollow portion in the shaft, as well as the

presence of disks and bearings.

As anticipated, the study shows that the frequency of the rotor decreases with the increase in the crack depth. The effect of the position of the crack on the natural frequencies of the rotor is also studied. For simply supported rotor, the frequencies decrease as the position of the crack moves away from the end bearing to the middle of the rotor. In this case, the largest decrease in frequency occurs when the crack is at the middle of the rotor. The effect of the crack position on the natural frequencies of the overhanging rotor is in contrast to that of a simply supported rotor, i.e. the frequency decreases as the crack moves closer to the support bearing.

The transient dynamic behavior of the cracked rotor-bearing system is studied for different types of end conditions and excitations. It has been observed that among the different types of excitations studied in this thesis, the step force produces larger deflections of the cracked shaft. The effect of the impulsive force is more pronounced on the time response of the cracked shaft if the impulse is applied near the crack. The application of cyclic forces exhibit the interesting phenomenon of beating if the frequency of applied force is near the first natural frequency of the shaft. If the frequency of the applied cyclic force is equal to the first natural frequency, resonance occurs as expected.

It is observed that the difference in amplitudes of vibrations of cracked and uncracked shafts is large for the case of a simply supported shaft. However, the time responses of cracked and uncracked cantilever shafts are comparable. This observation is applicable to uniform, tapered, non-rotating and rotating shafts. The amplitude of vibration of

rotating and non-rotating shafts is almost equal. For the non-rotating shaft the two planes of vibrations are not coupled, while for the rotating shaft, the vibrations in the two planes of vibrations are coupled by the gyroscopic moments. If the rotating shaft is excited in one plane, it deflects in the other plane as well.

The modal reduction techniques, both complex and planar reduction schemes, are used to reduce the order of the equations of motion. The time responses predicted using the reduction schemes are in excellent agreement with those predicted using actual full-order finite element model.

In conclusion, the contributions of the investigation presented in this thesis are manifested by the following:

- (a) Development of a new tapered finite shaft element with a crack.
- (b) Explicit expressions of the elemental mass, stiffness, gyroscopic matrices are derived.
- (c) The complex modal reduction scheme is numerically implemented for the first time, to the best knowledge of the investigator, to obtain a reduced order model of the equations of motion for dynamic response analysis of rotor-bearing systems.
- (d) Equations of motion of a general rotor-bearing system that includes disks and bearings are computer generated
- (e) A numerical scheme to integrate the equations of motion in either its full-order form or reduced-order form (using either planar or complex modal reductions) is

established. Time responses of any general rotor system can be easily obtained due to any general forcing function.

7.2 Recommendations for Future Research

The following recommendations are made for future research:

- In this investigation the equations of motion of the general multibody system are derived for all the three reference rotations of the body axis. While deducing the equations of motion of the the rotor-bearing system, only the reference rotation about the axis of the shaft is considered. One can include the reference rotation about other axes. The inclusion of the rotation about other perpendicular axes is like simulating a rotor shaft of an aircraft or a ship engine during any turning manoeuvres.
- The rate of change of body reference rotation i.e. the spin speed of the shaft is assumed to be constant. This assumption yields a constant gyroscopic matrix. During startup and shutdown, the spin speed of the shaft is not constant. If a variable spin speed is considered, it yields a time dependent gyroscopic matrix. The effect of time dependent gyroscopic matrix on the stability and dynamic analysis of the rotor-bearing system can be studied.
- It is well known that the bearing properties are function of spin speed of the shaft. If a variable spin speed is assumed, better models of the bearings, which accommodate

the variation of its properties with speed, will have to be considered.

- The disks are assumed as rigid in the present investigations. A multibody formulation of the rotor-bearing system can be developed considering flexible disks.
- It is assumed that the crack remains open. This assumption is valid for most of the shafts found in real life. But if the shaft is heavy and the static deflection of the shaft is large compared with the vibration amplitudes, the crack opens and closes periodically with the shaft rotation. The periodic opening and closing of the crack makes its stiffness a function of time. Moreover, a switching function will have to be defined to signal the opening and closing of the crack. The crack opening could be gradual with shaft rotation. Therefore, instead of having an on-off switching function a continuous function of time can be considered.
- An analytical solution to the equations of motion of a uniform rotating Timoshenko shaft can be investigated.
- Another extension to this work is to investigate the development of an alternative approach for modeling the crack flexibility by assuming discontinuity in the slope together with the resulting Dirac delta functions in the moments and shear forces at the crack location. In such a case, however, the physical integrity of the structure should be preserved.

Appendix A

Fracture Mechanics

A.1 Fracture Modes

A crack in a solid can be stressed in three different modes as shown in Figure A-1 [24]. Normal stresses give rise to the “opening mode” denoted as Mode I. The inplane shear results in Mode II or “sliding mode” of fracture. The “tearing mode” or Mode III is caused by out of plane shear.

A.2 Stress Analysis of Cracks

If we define a polar coordinate axis with the origin at the crack tip (Figure A-2), it can be shown that the stress field in any linear elastic cracked body is given by [23]

$$\sigma_{ij} = \frac{k}{\sqrt{r}} f_{ij}(\theta) + \text{other terms} \quad (\text{A.1})$$

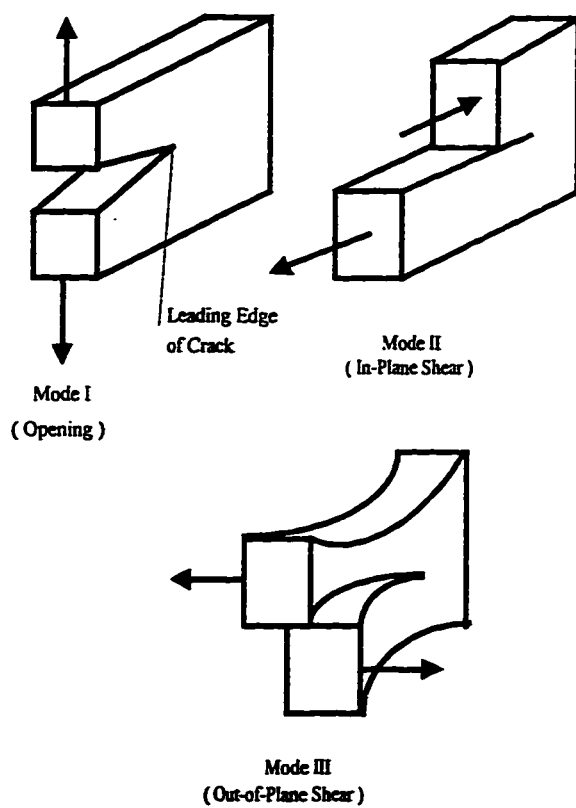


Figure A-1: The different modes of fracture of a solid

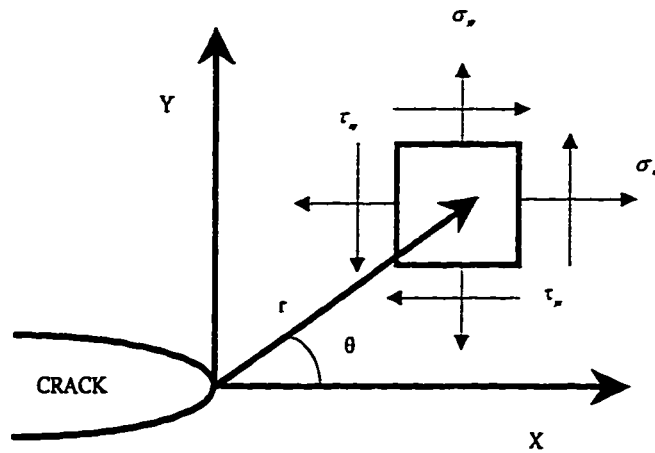


Figure A-2: Definition of the coordinate axis ahead of a crack tip. The Z direction is normal to the page

where σ_{ij} is the stress tensor, r and θ are as defined in Figure A-2, k is a constant, and f_{ij} is a dimensionless function of θ .

A.2.1 The Stress Intensity Factor

It is convenient at this point to replace k by the stress intensity factor K , where $K = k\sqrt{2\pi}$. The stress intensity factor is usually given a subscript to denote the mode of fracture; i.e., K_I , K_{II} , or K_{III} . Detailed expressions for the singular stress fields for Modes I and II are given in Table A.1. Displacement relationships for Modes I and II are listed in Table A.2. Table A.3 lists the nonzero stress and displacement components for Mode III.[24]

A.2.2 Relationship Between K and Global Behavior

In order for the stress intensity factor K to be useful, one must be able to determine K from remote loads and the geometry. Closed-form solutions for an infinite plate subjected to a remote tensile stress (Figure A-3) is given by [24]

$$K_I = \sigma\sqrt{\pi a} \quad (\text{A.2})$$

Thus the amplitude of the crack tip singularity for this configuration is proportional to the remote stress and the square root of crack size.

A related solution is that of a semi-infinite plate with an edge crack (Figure A-4).

Table A.1: Stress fields ahead of a crack tip for Mode I and Mode II in a linear elastic, isotropic material

	Mode I	Mode II
σ_{xx}	$\frac{K_I}{\sqrt{2\pi r}} \cos\left(\frac{\theta}{2}\right) \left[1 - \sin\left(\frac{\theta}{2}\right) \sin\left(\frac{3\theta}{2}\right)\right]$	$-\frac{K_{II}}{\sqrt{2\pi r}} \sin\left(\frac{\theta}{2}\right) \left[2 + \cos\left(\frac{\theta}{2}\right) \cos\left(\frac{3\theta}{2}\right)\right]$
σ_{yy}	$\frac{K_I}{\sqrt{2\pi r}} \cos\left(\frac{\theta}{2}\right) \left[1 + \sin\left(\frac{\theta}{2}\right) \sin\left(\frac{3\theta}{2}\right)\right]$	$\frac{K_{II}}{\sqrt{2\pi r}} \sin\left(\frac{\theta}{2}\right) \cos\left(\frac{\theta}{2}\right) \cos\left(\frac{3\theta}{2}\right)$
τ_{xy}	$\frac{K_I}{\sqrt{2\pi r}} \cos\left(\frac{\theta}{2}\right) \sin\left(\frac{\theta}{2}\right) \cos\left(\frac{3\theta}{2}\right)$	$\frac{K_{II}}{\sqrt{2\pi r}} \cos\left(\frac{\theta}{2}\right) \left[1 - \sin\left(\frac{\theta}{2}\right) \sin\left(\frac{3\theta}{2}\right)\right]$
σ_{zz}	0 (Plane Stress) $\nu(\sigma_{xx} + \sigma_{yy})$ (Plane Strain)	0 (Plane Stress) $\nu(\sigma_{xx} + \sigma_{yy})$ (Plane Strain)
τ_{xz}, τ_{yz}	0	0

Table A.2: Crack tip displacement fields for Mode I and Mode II (linear elastic, isotropic material).

	Mode I	Mode II
u_x	$\frac{K_I}{2G} \sqrt{\frac{r}{2\pi}} \cos\left(\frac{\theta}{2}\right) \left[\kappa - 1 + \sin^2\left(\frac{\theta}{2}\right)\right]$	$\frac{K_{II}}{2G} \sqrt{\frac{r}{2\pi}} \sin\left(\frac{\theta}{2}\right) \left[\kappa + 1 + \cos^2\left(\frac{\theta}{2}\right)\right]$
u_{yy}	$\frac{K_I}{2G} \sqrt{\frac{r}{2\pi}} \sin\left(\frac{\theta}{2}\right) \left[\kappa + 1 - \cos^2\left(\frac{\theta}{2}\right)\right]$	$-\frac{K_{II}}{2G} \sqrt{\frac{r}{2\pi}} \cos\left(\frac{\theta}{2}\right) \left[\kappa - 1 - \sin^2\left(\frac{\theta}{2}\right)\right]$

$$\kappa = 3 - 4\nu \text{ (plane strain)}$$

$$\kappa = (3 - \nu) / (1 + \nu) \text{ (plane stress)}$$

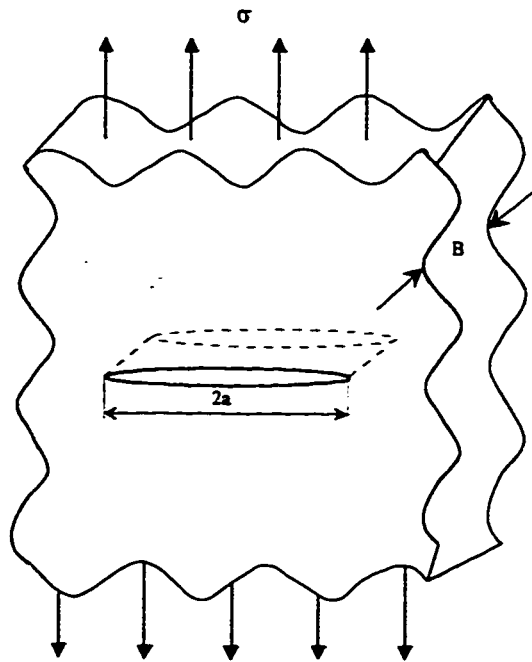


Figure A-3: A through-thickness crack in an infinitely wide plate subjected to a remote tensile stress

Table A.3: Non-zero stress and displacement components in Mode III
(linear elastic, isotropic material)

τ_{xz}	$\frac{K_{III}}{\sqrt{2\pi r}} \sin\left(\frac{\theta}{2}\right)$
τ_{yz}	$\frac{K_{III}}{\sqrt{2\pi r}} \cos\left(\frac{\theta}{2}\right)$
u_z	$\frac{K_{III}}{G} \sqrt{\frac{r}{2\pi}} \sin\left(\frac{\theta}{2}\right)$

The stress intensity factor for the edge crack is given by [24]

$$K_I = 1.12\sigma\sqrt{\pi a} \quad (\text{A.3})$$

which is similar to Eq.(A.2).

A.2.3 Effect of Finite Size

Figure A-5 schematically illustrates the effect of finite width on the crack tip stress distribution, which is represented by lines of force; the local stress is proportional to the spacing between lines of force. Since a tensile stress cannot be transmitted through a crack, the lines of force are diverted around the crack, resulting in a local stress concentration. In the infinite plate, the line of force at a distance W from the crack center line has force components in the x and y directions. If the plate width is restricted to $2W$, the x force must be zero on the free edge; this boundary condition causes the lines of

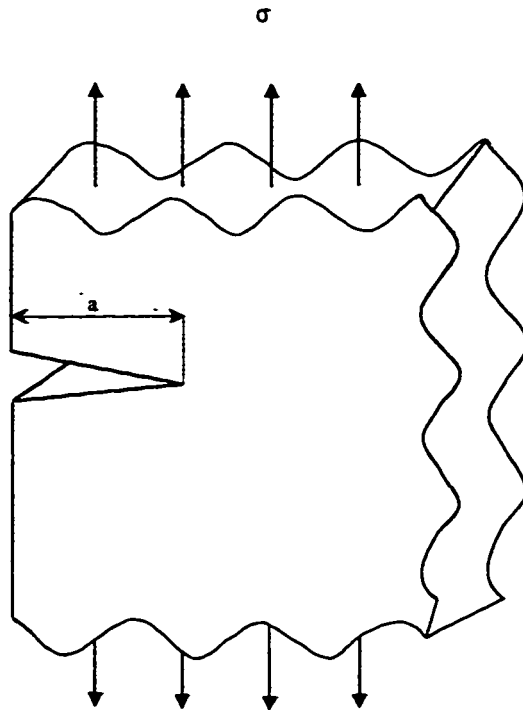


Figure A-4: Edge crack in a semi-infinite plate subjected to a remote tensile stress

force to be compressed, which results in a higher stress intensification at the crack tip.

The Mode I stress intensity factor for this situation is given by [24]

$$K_I = \sigma \sqrt{\pi a} \left[\frac{2W}{\pi a} \tan \left(\frac{\pi a}{2W} \right) \right]^{\frac{1}{2}} \quad (\text{A.4})$$

More accurate solutions for a through crack in a finite plate have been obtained from finite element analysis. Solutions of this type are usually fit to polynomial expressions.

One such solution [25] is given by

$$K_I = \sigma \sqrt{\pi a} \left[\sec \left(\frac{\pi a}{2W} \right) \right]^{\frac{1}{2}} \left[1 - 0.025 \left(\frac{a}{W} \right)^2 + 0.06 \left(\frac{a}{W} \right)^4 \right] \quad (\text{A.5})$$

Equation (A.4) agrees with the finite element solution to within 7% for $\frac{a}{W} < 0.6$. The secant correction is much closer to the finite element solution; the error is less than 2% for $\frac{a}{W} < 0.9$.

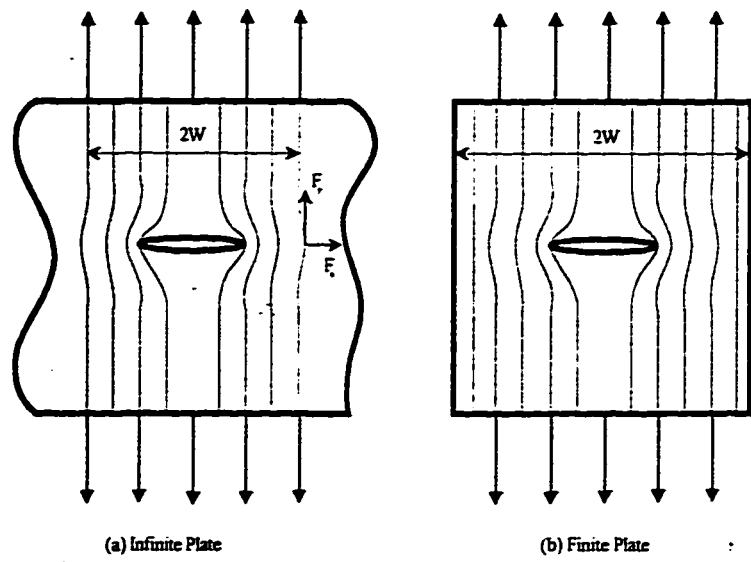


Figure A-5: Stress concentration effects due to a through crack in finite and infinite width plates.

NOMENCLATURE

A^{ij}	Cross-sectional area of element ij
\hat{B}^{ij}	Curvature matrix
E^{ij}	Young's modulus
e^{ij}	Nodal coordinates of element ij
G^{ij}	Shear modulus
I^{ij}	Second moment of the cross-sectional area
K	Stress intensity factor
K^{ij}	Composite stiffness matrix of element ij
K_e^{ij}	Element stiffness matrix due to flexure
K_s^{ij}	Element stiffness matrix due to shear
K_ϕ^{ij}	Element stiffness matrix due to torsion
K^i	Stiffness matrix of the body i
L	Lagrangian
l^{ij}	Length of element ij
l_c^{ij}	Location of the crack
M^{ij}	Composite mass matrix of element ij
M^i	Mass matrix of the body i
N^{ij}	Shape functions of element ij
Q^{ij}	Generalized forces acting on element ij
q^{ij}	Generalized coordinate vector of element ij
q^i	Generalized coordinate vector of body i
q	Generalized coordinate vector of the system
R	Outer radius of shaft finite element
r	Inner radius of shaft finite element
T^{ij}	Kinetic energy of element ij
T^i	Kinetic energy of body i
U^{ij}	Strain energy of element ij
U^i	Strain energy of body i
V^{ij}	Volume of element ij
v^{ij}	Deflection in Y^{ij} direction
W^{ij}	Virtual work done on element ij
w^{ij}	Deflection in Z^{ij} direction
$X^{ij}Y^{ij}Z^{ij}$	Coordinate axes of element ij
$X^iY^iZ^i$	Coordinate axes of body i
XYZ	Inertial axes

Γ^{ij}	Transformation matrix from $\overline{X}^{ij}\overline{Y}^{ij}\overline{Z}^{ij}$ to $X^iY^iZ^i$
Φ^{ij}	Shear deformation parameter
Ψ^i	Transformation matrix from $X^iY^iZ^i$ to XYZ
Θ	Holonomic constraints
Ω	Spin speed
ε^{ij}	Strain
μ^{ij}	Mass density of element ij
ϕ^{ij}	Torsional rotation about X_1^{ij}
β^{ij}	Elastic rotation about Y_2^{ij}
γ^{ij}	Elastic rotation about Z_3^{ij}
θ_x^i	Rigid body rotation about X^i
κ	Shear coefficient
ν	Poisson's ratio
ω	Natural frequency
λ	Whirl ratio

Bibliography

- [1] A. Muszynska, *Shaft Crack Detection*, Seventh Machinery Dynamics Seminar, Canada, 1982.
- [2] H. J. Petroski, *Simple Static and Dynamic Models for the Cracked Elastic Beam*, International Journal of Fracture, Vol. 17, pp. R71-R76, 1981.
- [3] S. Christides and A. D. S. Barr, *One-Dimensional Theory of Cracked Bernoulli-Euler Beams*, International Journal of Mechanical Sciences, Vol. 26, No. 11/12, pp. 639-648, 1984.
- [4] M. -H. H. Shen and C. Pierre, *Natural Modes of Bernoulli-Euler Beams with Symmetric Cracks*, Journal of Sound and Vibration, Vol. 138, No. 1, pp. 115-134, 1990.
- [5] M. -H. H. Shen and C. Pierre, *Free Vibrations of Beams with a Single-Edge Crack*, Journal of Sound and Vibration, Vol. 170, No. 2, pp. 237-259, 1994.
- [6] C. A. Papadopoulos and A. D. Dimarogonas, *Coupling of Bending and Torsional Vibration of a Cracked Timoshenko Shaft*, Ingenieur-Archiv, Vol. 57, pp. 257-266, 1987.

- [7] M. D. Rajab and A. Al-Sabeeh, *Vibrational Behavior of Cracked Shafts*, Journal of Sound and Vibration, Vol. 147, 1991, pp. 467-473.
- [8] G. Gounaris and A. Dimarogonas, *A Finite Element of a Cracked Prismatic Beam for Structural Analysis*, Computers & Structures, Vol. 28, No. 3, pp. 309-313, 1988.
- [9] B. S. Haisty and W. T. Springer, *A General Beam Element for Use in Damage Assessment of Complex Structures*, Journal of Vibration, Acoustics, Stress, and Reliability in Design, Vol. 110, pp. 389-394, July 1988.
- [10] W. M. Ostachowicz and M. Krawczuk, *Vibration Analysis of a Cracked Beam*, International Journal of Computers & Structures, Vol. 36, No. 2, pp. 245-250, 1990.
- [11] M. Krawczuk, *Finite Timoshenko-Type Beam Element with a Crack*, Engineering Transactions, Vol. 40, No. 2, pp. 229-248, 1992.
- [12] L-W Chen and C-L Chen, *Vibration and Stability of Cracked Thick Rotating Blades*, Computers & Structures, Vol. 28, No. 1, pp. 67-74, 1988.
- [13] J. Wauer, *Dynamics of Cracked Rotating Blades*, Applied Mechanics Review, Vol. 44, No. 11, Part 2, pp. s273-s278, Nov 1991.
- [14] M. Krawczuk, *Natural Vibration of Cracked Rotating Beams*, Acta Mechanica, Vol. 99, pp. 35-48, 1993.

- [15] W. G. R. Davies and I. W. Mayes, *The Vibrational Behavior of a Multi-Shaft, Multi-Bearing System in the Presence of a Propagating Transverse Crack*, Journal of Vibration, Acoustics, Stress, and Reliability in Design, Vol. 106, pp. 146-153, January 1984.
- [16] B. Grabowski, *The Vibrational Behavior of a Turbine Rotor Containing a Transverse Crack*, Journal of Mechanical Design, Vol. 102, pp. 140-146, January 1980.
- [17] C. A. Papadopoulos and A. D. Dimarogonas, *Coupled Longitudinal and Bending Vibration of a Rotating Shaft with an Open Crack*, Journal of Sound and Vibration, Vol. 117, No. 1, pp. 81-93, 1987.
- [18] C. A. Papadopoulos and A. D. Dimarogonas, *Coupled Longitudinal and Bending Vibrations of a Cracked Shaft*, Journal of Vibration, Acoustics, Stress, and Reliability in Design, Vol. 110, pp. 1-8, January 1988.
- [19] J. Wauer, *Modelling and Formulation of Equations of Motion for Cracked Rotating Shafts*, International Journal of Solids Structures, Vol. 26, No. 8, pp. 901-914, 1990.
- [20] H. D. Nelson and C. Nataraj, *The Dynamics of a Rotor System with a Cracked Shaft*, Journal of Vibration, Acoustics, Stress, and Reliability in Design, Vol. 108, pp. 189-196, April 1986.
- [21] L. Hamidi, J. B. Piau, H. Pastorel, W. M. Mansour and M. Masoud, *Modal Parameters for Cracked Rotors: Models and Comparisons*, Journal of Sound and Vibration, Vol. 175, No. 2, pp. 265-278, 1994.

- [22] A. A. Griffith, *The Phenomena of Rupture and Flow in Solids*, Philosophical Transactions, Series A, Vol. 221, pp. 163-198, 1920.
- [23] H. M. Westergaard, *Bearing Pressures and Cracks*, Journal of Applied Mechanics, Vol. 6, pp. 49-53, 1939.
- [24] T. L. Anderson, Fracture Mechanics - Fundamentals and Applications, CRC Press, 1991.
- [25] H. Tada, P. C. Paris, and G. R. Irwin, The Stress Analysis of Cracks Handbook, (2nd Edition) Paris Productions Inc., St. Louis, 1985.
- [26] A. D. Dimarogonas and S. A. Paipetis, Analytical Methods in Rotor Dynamics, Applied Science Publishers, 1983.
- [27] L. M. Greenhill, W. B. Bickford and H. D. Nelson, *A Conical Beam Finite Element for Rotor Dynamics Analysis*, Journal of Vibration and Acoustics, Vol. 107, Oct 1985, pp. 421-430.
- [28] M. A. Mohiuddin and Y. A. Khulief, *Modal Characteristics of Rotors Using a Conical Shaft Finite Element*, Computer Methods in Applied Mechanics and Engineering, Vol. 115, pp. 125-144, 1994.
- [29] Y. A. Khulief and A. A. Shabana, *Impact Responses of Multi-Body Systems with Consistent and Lumped Masses*, Journal of Sound and Vibration, Vol. 104, No. 2, pp. 187-207, 1986.

- [30] Y. A. Khulief and A. A. Shabana, *Dynamic Analysis of Constrained System of Rigid and Flexible Bodies with Intermittent Motion*, ASME Journal of Mechanisms, Transmission, and Automation in Design, Vol. 108, March 1986, pp. 38-45.
- [31] P. W. Likins, *Finite Element Appendage Equations for Hybrid Coordinate Dynamic Analysis*, International Journal of Solids and Structures, Vol.8, pp.709-731, 1972.
- [32] E. J. Gunter, K. C. Choy and P. E. Allaire, *Modal Analysis of Turborotors Using Planar Modes - Theory*, Journal of Franklin Institute, Vol.305(4), pp.221-243, 1978.
- [33] R. M. Laurenson, *Modal Analysis of Rotating Flexible Structures*, AIAA Journal, Vol.14(10), pp.1444-1450, 1976.
- [34] L. Meirovitch, *A New Method of Solution of the Eigenvalue Problem for Gyroscopic Systems*, AIAA Journal, Vol.12, pp.1337-1342, 1972.
- [35] R. W. Stephenson and K. E. Rouch, *Modeling Rotating Shafts using Axisymmetric Solid Finite Elements with Matrix Reduction*, Journal of Vibration and Acoustics, Vol.115, pp.484-489, 1993.
- [36] S. V. Neriya, R. B. Bhat and T. S. Sankar, *Coupled Torsional-Flexural Vibration of a Geared Shaft System Using Finite Element Analysis*, 55th Shock and Vibration Symposium, pp.13-25, Dayton, OH, 1984.

- [37] R. Subbiah, R. B. Bhat and T. S. Sankar, *Dynamic Response of Rotors using Modal Reduction Techniques*, Journal of Vibrations, Acoustics, Stress and reliability in Design, Vol.111, pp.360-365, 1989.
- [38] D. M. Ku, *Stability and Whirl Speeds of Rotating Shaft under Axial Loads*, International Journal of Analytical and Experimental Modal Analysis, Vol.9(2), pp.111-123, 1994.
- [39] G. Sauer and M. Wolf, *Finite Element Analysis of Gyroscopic Effects*, Journal of Finite Elements in Analysis and Design, Vol.5, pp.131-140, 1989.
- [40] W. H. Sundada and S. Dubowsky, *On The Dynamic Analysis and Behavior of Industrial Robotic Manipulators with Elastic Links*, ASME Journal of Mechanisms, Transmission and Automation in Design, Vol.105, pp.42-51, 1983.
- [41] A. A. Shabana and R. Wehage, *Variable Degree of Freedom Compact Mode Analysis of Inertia Variant Flexible Machine Systems*, ASME Journal of Mechanisms, Transmission and Automation in Design, Vol.105(3), pp.370-378, 1983.
- [42] T. J. Spanos and W. S. Tsuha, *Selection of Component Modes for Flexible Multibody Simulations*, Journal of Guidance, Vol.14(2), pp.260-267, 1991.
- [43] Y. A. Khulief, *On The Finite Element Dynamic Analysis of Flexible Mechanisms*, Computer Methods in Applied Mechanics and Engineering, Vol.97, pp.23-32, 1992.

- [44] K. Kane and B. J. Torby, *The Extended Modal Reduction Method Applied to Rotor Dynamic Problems*, Journal of Vibration and Acoustics, Vol.113, pp.79-84, 1991.
- [45] J. H. Wilkinson, *The Algebraic Eigenvalue Problem*, Clarendon Press, Oxford, 1965.

Vita

- Mohammed Ahmed Mohiuddin
- Born on June 24, 1968, at Hyderabad, India.
- Received Bachelor of Technology degree in Mechanical Engineering from Jawahar Lal Nehru Technological University, Hyderabad, India in 1989.
- Received Master of Science degree in Mechanical Engineering from King Fahd University of Petroleum & Minerals, Dhahran, KSA in 1992.
- Received Doctor of Philosophy degree in Mechanical Engineering from KFUPM, Dhahran, KSA in 1997.
- Worked as Assistant Engineer (Drilling), Singareni Collieries Company Limited, Kothagudem, India, July 1989-August 1990.
- Worked as Research Assistant in Mechanical Engineering Department, KFUPM, September 1990-December 1992.
- Worked as Lecturer in Mechanical Engineering Department, KFUPM, January 1992-August 1997.